

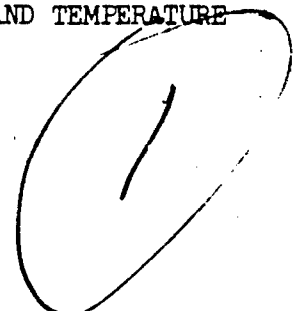
INSTITUTE  
FOR  
AEROSPACE STUDIES

UNIVERSITY OF TORONTO

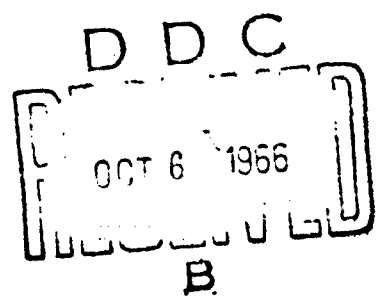
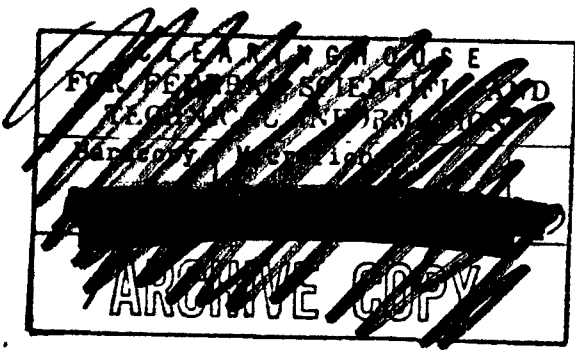
ROCKET MEASUREMENTS OF UPPER ATMOSPHERE DENSITY AND TEMPERATURE  
OVER FORT CHURCHILL, MANITOBA

by

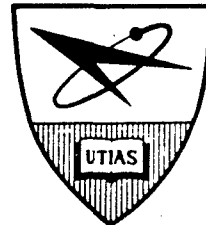
R. N. Grenda



AD 639607



20050218010





### ACKNOWLEDGEMENTS

The author wishes to express his thanks to Dr. J. H. de Leeuw for his supervision and encouragement throughout the course of this investigation.

The author wishes to thank Dr. G. N. Patterson for making the facilities of the Institute for Aerospace Studies available for this research.

A number of persons were instrumental in making this rocket experiment a success. Thanks are due to Messrs. J. Burt, W.B. Feyrer, J. Hager, G. Martens, B. Sherman, and H. Treial for their work on various aspects of the electronics required for the experiment. Thanks are due to Mr. J. Leffers, who constructed and assisted in testing many of the payload components. Thanks are extended to Mr. A. Staniforth, who provided the liason with the Churchill Research Range, and to the many members of the Space Electronics Section of the National Research Council who aided in the launching. The assistance provided by Pan American World Airways, Inc. personnel, who operated the range during the launching, is greatly appreciated.

Financial support to carry out this research was provided by the National Research Council under grant NRC SRA-1, and by the U.S. Air Force Office of Scientific Research under grant AFOSR 276-66.

## SUMMARY

This report describes a rocket experiment designed to measure density and molecular scale temperature above 100 km by means of a free molecule flow analysis of the data. In addition, pressure, temperature, and density were measured in the lower atmosphere by conventional methods.

A theoretical analysis under conditions of continuum and free-molecule flow is included. The desired atmospheric parameters are given in terms of the quantities measured by the rocket-borne instruments.

The mechanical design of the payload, and the electronics and electrical system are discussed.

The data is reduced, and the atmospheric parameters based on the data are presented. The experiment is discussed, and modifications are suggested to improve the experiment and obtain better data.

**BLANK PAGE**

## TABLE OF CONTENTS

	<u>Page</u>
NOTATION	vi
1. INTRODUCTION	1
2. THEORETICAL BASIS	3
2.1 Continuum Flow Theory	3
2.1.1 Atmospheric Density	4
2.1.2 Atmospheric Pressure	5
2.2 Rarefied Gas Flow Theory	7
2.2.1 Free Molecule Orifice Probe Theory	8
2.2.2 Theory for a Pressure Gauge Mounted on a Spinning Rocket	9
2.2.3 Time Response of Free Molecule Gauges	18
2.2.4 Near-Free-Molecule Flow Corrections	20
2.2.5 Relations Between Atmospheric Pressure, Density and Temperature	20
3. DESCRIPTION OF THE ROCKET VEHICLE AND PAYLOAD	22
3.1 Mechanical Configuration	22
3.1.1 Black Brant IIA Rocket	22
3.1.2 Mechanical Design Considerations	22
3.1.3 Nose Cone Sealing	23
3.2 Instrumentation	24
3.2.1 Selection of Gauges	24
3.2.2 Stagnation and Cone Surface Pressure Transducers	27
3.2.3 Mounting of the Cold Cathode Ionization Gauges	30
3.2.4 Separation Mechanism	31
3.2.5 Extension and Braking System	33
3.2.6 Testing of the Separation, Extension, and Braking Systems	34
3.2.7 Cable Holder	36
3.2.8 Pumping System	36
3.2.9 Sun Sensors	38
3.2.10 Magnetometers	40
4. ELECTRICAL AND ELECTRONIC SYSTEMS	40
4.1 Telemetry	41
4.2 Radar Beacon	41
4.3 Ionization Gauge Circuits	42
4.4 H.P. and M.P. Gauge Amplifiers	43
4.5 Timers and Firing Circuit	43
4.6 Batteries	43
4.7 Temperature Sensors	44
4.8 Magnetometers	44
4.9 Miscellaneous Instrumentation	44
4.10 Electronics Frame	44

5.	PRESSURE GAUGE CALIBRATION	45
	5.1 Strain Gauge and Thermocouple Pressure Transducer Calibration	45
	5.2 Ionization Gauge Calibration	45
6.	THE ROCKET LAUNCHING	47
	6.1 Churchill Research Range	47
	6.2 Payload Preparation and Rocket Launching	48
7.	DATA REDUCTION AND DISCUSSION	49
	7.1 Rocket Orientation Measurements	49
	7.2 Trajectory Information	53
	7.3 Low Altitude Properties	54
	7.4 Upper Atmosphere Properties	56
	7.4.1 Upper Atmosphere Wind	56
	7.4.2 Upper Atmosphere Density	57
	7.4.3 Atmospheric Molecular Scale Temperature	61
8.	RECOMMENDATIONS	62
9.	CONCLUSIONS	64
	APPENDIX A	65
	APPENDIX B	67
	REFERENCES	70
	TABLE	
	FIGURES	

## NOTATION

a	$\frac{Mg + F}{k}$
$a_1$	$\frac{mg + F}{k}$
A	gauge orifice area
$B_0$	strength of the earth's magnetic field
$B_\perp$	measured magnetic field component perpendicular to the rocket axis
$B_\parallel$	measured magnetic field component parallel to the rocket axis
$\Delta B_\perp$	change in the magnetic field due to the presence of the rocket
C	proportionality factor
$C_m$	most probable molecular speed
d	diameter of an impact pressure probe, or initial compression of the extension system spring
$d_1$	diameter of a capillary in a pressure measuring system
$\bar{e}_x, \bar{e}_y, \bar{e}_z$	unit vectors pointing south, east, and vertically upward respectively
F	friction force
g	acceleration of gravity
k	spring constant
$K_D$	pressure coefficient, $\frac{p_c - p_1}{\rho_1 V^2}$
Kn	Knudsen number
L	characteristic length in flow problems
$L_1$	length of a capillary
m	mass of parts in the extension system
$m_1$	local molecular weight in the atmosphere
$m_0$	molecular weight of air at sea level
M	mass of the ejected tip cone plus m
$M_c$	flow Mach number on the surface of a cone

$M_g$	mass of moving extension system parts in the test frame
$M_1$	flight Mach number
$n_b$	emitted molecule number density
$p$	static pressure
$p_f$	steady state pressure in a measuring system
$p_m$	mean pressure in a capillary of a measuring system
$p_s$	measured nose cone surface pressure
$P$	stagnation pressure
$r$	radius of a capillary
$R$	universal gas constant
$R_o$	specific gas constant for dry air
$R_1$	local atmospheric specific gas constant
$Re_c$	Reynolds number based on conditions at the surface of a cone
$Re_d$	Reynolds number based on impact probe diameter
$S$	speed ratio
$S_N$	speed ratio component directed into the orifice probe
$\Delta t$	time difference
$T$	static temperature
$T_b$	body temperature in a gas flow
$T_M$	molecular scale temperature, $\frac{R_1 T_1}{R_o}$
$U_c$	flow velocity on the surface of a cone
$v$	ionization gauge volume
$v_x, v_y, v_z$	components of $\bar{V}_w$ in the $\bar{e}_x, \bar{e}_y, \bar{e}_z$ directions respectively
$\bar{V}$	relative velocity of the atmosphere with respect to the rocket
$V_1$	volume of the capillary in a pressure measuring system
$V_H$	horizontal component of the rocket velocity with respect to the ground
$V_m$	volume of the gauge in a pressure measuring system

$V_N$	maximum component of $\bar{V}_R$ perpendicular to the rocket axis during a spin cycle
$\bar{V}_R$	rocket velocity with respect to the ground
$V_V$	vertical component of the rocket velocity with respect to the ground
$\bar{V}_w$	atmospheric wind velocity with respect to the ground
$V_x, V_y, V_z$	components of $\bar{V}_R$ in the $\bar{e}_x, \bar{e}_y, \bar{e}_z$ directions respectively
$V, V_R, V_w$	magnitudes of the corresponding vectors
$x$	displacement from a reference position $x_0$
$X_c$	distance of the surface pressure orifice from the vertex of the cone
$(a, b, c)$	direction cosines of the rocket axis
$(i, j, k)$	direction cosines of $\bar{V}_R$
$(l, m, n)$	direction cosines of the earth's magnetic field
erf S	error function, $\frac{2}{\sqrt{\pi}} \int_0^S e^{-x^2} dx$
$\alpha$	angle between $\bar{V}$ and the rocket axis
$\beta$	angle between the rocket axis and the normal to the gauge orifice
$\gamma$	ratio of the specific heats (1.4 for dry air)
$\Gamma$	$\pm(90^\circ - \Gamma)$ defines the acceptance angle of a sun sensor
$\theta$	angle between the sun's direction and the plane perpendicular to the rocket axis
$\theta_R$	angle between $\bar{V}_R$ and the vertical
$\lambda$	mean free path
$\mu$	viscosity
$\xi$	angle between $\bar{V}$ and the normal to the gauge orifice
$\rho$	density
$\Delta\rho_2$	maximum change in gauge volume density during a spin cycle
$\tau$	time constant
$\tau_0$	time constant at standard atmospheric pressure

$\varphi$	phase difference
$\varphi_R$	azimuth angle of the rocket trajectory
$\Delta\varphi_w$	phase shift caused by wind
$\Delta\varphi_{S,V}$	angle between two planes
$\Phi$	angle between the rocket axis and the earth's magnetic field
$\Phi_0$	angle between the rocket axis and the earth's magnetic field far from the rocket
$\Delta\Phi_0$	change in $\Phi_0$ due to distortion of the magnetic field by the rocket
$\chi(S)$	$e^{-S^2} + S\sqrt{\pi} (1 + \operatorname{erf} S)$
$\omega$	angular spin rate of the rocket
$(\alpha, \beta, \gamma)$	direction cosines of the sun's direction

#### Subscripts

1	refers to the free stream conditions
2	refers to ionization gauge volume conditions
c	refers to conditions on the surface of a cone if there is no boundary layer
max.	refers to gauge volume conditions when the orifice is oriented to collect the maximum mass flux
min.	refers to gauge volume conditions when the orifice is oriented to collect the minimum mass flux.

## 1. INTRODUCTION

The past 20 years has seen the increasing use of the rocket as a vehicle for carrying experiments into the earth's atmosphere. Atmospheric parameters such as pressure, density, temperature and composition, to name a few, have all been successfully measured with rocket borne experiments. The sounding rocket provides a means of making measurements at altitudes which, while they are too high to be reached by balloons, are too low to be probed by satellites (Refs. 1, 2, 3, 4, and 5).

Early rocket measurements of pressure, density, and temperature provided much of the data which was used in establishing the first standard atmosphere tables. More recently, satellites have provided new information for extension of the standard atmosphere to higher altitudes. However, quite large deviations from these standard values can result depending on the time of day, the season of the year, and the degree of solar activity. For this reason many rocket experiments have been flown, and many more should be flown, to empirically determine the effect of these various factors. In this way enough data will be accumulated to enable the various proposed atmospheric models to be properly evaluated.

While there are many ways of measuring pressure, density and temperature, certain standard rocket experiments have evolved for making these measurements. Pressure and density, up to approximately 80 to 90 km, have generally been determined with pitot-static pressure probes, or by measurement of impact pressure and a surface pressure on the body of the rocket. Continuum aerodynamic theory and test data from supersonic wind tunnels provide the means for relating the measured pressures to the ambient conditions. Since the low altitude rocket motion is generally free from large angles of attack, this approach yields acceptable values of pressure and density (Refs. 6, 7, 8, 9, and 10).

In the falling sphere experiment, the deceleration of a sphere ejected from a rocket is measured as it falls freely through the atmosphere. Since the drag coefficient for a sphere is well known from wind tunnel tests, the deceleration can be related to the atmospheric density. Sensitive accelerometers and accurate radar tracking of the sphere are necessary for this type of experiment. Using large inflatable spheres, these density measurements have been carried to an altitude of 130 km. (References 11, 12, and 13).

A method which has been used quite frequently for making temperature and wind velocity measurements up to approximately 100 km is the rocket grenade technique. In this experiment the rocket carries a number of explosive grenades and releases them one at a time above 40 km. By knowing the time and position of the explosion, and the time of arrival of the sound waves at an array of ground microphones, it is possible to compute the temperature and wind velocity profile in the atmosphere. This method requires knowledge of the pressure and temperature in the lower atmosphere up to the first grenade explosion from radio-sonde data (Refs. 14, 15, 16, and 17).

These brief descriptions summarize the more important rocket experiments which have been used for making atmospheric structure measurements below 90 km. At higher altitudes the mean free paths of the atmospheric particles become of the same order or larger than the rocket dimensions. When this happens the nature of the flow field around the rocket is changed considerably. Under conditions of free molecule flow, kinetic theory must be used to analyze the motion of the gas particles in order to interpret the readings of gauges within the rocket.

There are two methods which have generally been used to measure the atmospheric density at high altitudes. A method which has produced a considerable amount of density information in recent years involves relating changes in the orbit of a satellite to the aerodynamics drag on it, and hence to the atmospheric density. (Refs. 18,19,20,21, and 22). This method has resulted in a considerable amount of density information above 200 km, which has enabled the validity of proposed model atmospheres to be tested. However, this satellite data is generally restricted to altitudes above 170 km. Below this altitude, the atmospheric structural parameters are usually determined by some type of rocket experiment.

A second method of measuring density employs free molecule flow theory to relate the gauge volume conditions, of vacuum gauges mounted in a rocket, to the ambient density (Refs. 10, 23, 24 and 25). By allowing the rocket to spin, and orienting a gauge with its opening facing perpendicular to the rocket axis, it is theoretically possible to derive the atmospheric density and molecular scale temperature from the readings of a single gauge. With accurate measurements of rocket velocity and angular orientation it is even possible to obtain the velocity and direction of upper atmosphere winds. However, this is an ideal situation which encounters practical difficulties in an actual rocket experiment. Previous high altitude rocket experiments of this type have encountered a common problem in attempting to make their measurements. This has been the presence of a gas cloud surrounding the rocket which was of higher density than the undisturbed atmosphere. As a result the measured gauge density is much higher than the theory predicts. Unless the effect of this gas cloud can be subtracted from the gauge reading, the results can not be properly interpreted. Fortunately, spinning the rocket imposes a modulation on the gauge density which is due solely to the free stream conditions. With this measurement, the theory permits only the atmospheric density to be computed. This method still permits wind velocity and direction to be computed (Ref. 10).

This gas cloud is believed to have a number of possible sources. One of these may be the outgassing of rocket surfaces close to the gauge opening. Normally, this might not be of importance if the surface was cold. However, aerodynamic heating raises the surface temperature and hence increases the outgassing rate by orders of magnitude. Since the normal flight time is so short, the surfaces do not have sufficient time to clean themselves. In some of the experiments there has probably been outgassing within the gauge volume itself. The gauge has started at atmospheric pressure and then has been required to measure pressures between  $10^{-5}$  to  $10^{-6}$  mm Hg within 2 or 3 minutes. It has generally been found that the density of the gas cloud decreases with time during the flight.

Another possible source of the gas is leakage from pressurized compartments in the rocket nose cone. Unless great care is taken to seal the nose cone, even very small leaks could be important if they happened to be close to the gauge openings.

A third source, and possibly an important one, is the rocket motor itself. The hot internal and external surfaces of the burnt-out motor could generate large quantities of gas which could be scattered forward to the vicinity of the gauges. Pfister and Ulwick in Ref. 26 indicate the importance of the effect of motor outgassing on their electron density measurements. This indicates that motor outgassing probably contributes a large part of the total gas cloud around the rocket.

The rocket experiment designed at the Institute for Aerospace Studies was intended to measure atmospheric pressure and density at the lower altitudes, and density and molecular scale temperature above 100 km. During the lower part of the rocket trajectory, this was done by making impact and nose cone surface pressure measurements. Above 100 km the density was determined by the method of making measurements with a pressure gauge oriented with its orifice facing perpendicular to the axis of a spinning rocket. While this method had been used previously, it was proposed to extend it and measure the molecular scale temperature by using a pressure gauge oriented with its orifice at an angle of  $45^\circ$  to the rocket axis. Free molecule flow theory indicated that this method of measuring molecular scale temperature directly was possible. The normal method of determining the scale temperature is to employ the hydrostatic equation for the atmosphere and the density vs altitude information obtained from the experiment (Ref. 27). The method used in the UTIAS experiment for measuring molecular scale temperature still requires the use of a spinning rocket. This is still the only way of separating the effect of the free stream from that of the gas cloud which is certain to be present.

While the experiment was designed to provide density and scale temperature even though a gas cloud existed, an attempt was made to try and reduce the magnitude of the gas cloud. The high altitude ionization gauges were sealed within the nose cone and pre-evacuated to a low pressure in order to outgas them. At 76 km the nose cone was opened and the gauges extended forward, away from the effects of nose cone surface outgassing. Great care was also observed in sealing the pressurized section of the nose cone. Little could be done about the effect of the rocket motor since the best way to eliminate this effect would be to separate the nose cone from the motor. As this was the first rocket experiment designed by the Institute for Aerospace Studies, it was considered to present too many complications to be attempted. In order to determine the effectiveness of the measures taken to reduce outgassing, an ionization gauge was located in the aft portion of the nose cone. The gauge was open to the atmosphere from ground level and hence was subjected to the maximum outgassing effect.

## 2. THEORETICAL BASIS

During its flight the rocket passed through the continuum, transition, and free molecule flow regimes in turn. As the theoretical basis for the experiment is completely different for the continuum and free molecule flow regimes, these have been treated separately in the following sections. The transition flow regime requires corrections to be made to both the high altitude and low altitude measurements when the Reynolds number and Knudsen number indicate the presence of transition flow.

### 2.1 Continuum Flow Theory

Ambient pressure and density for the lower atmosphere were determined by making measurements of impact pressure,  $P$ , and nose cone surface pressure,  $p_s$ . These two measurements can be related to the atmospheric density, and temperature or pressure with compressible flow theory.

### 2.1.1 Atmospheric Density

The density is obtained essentially from the measurement of the impact pressure at the nose of the rocket. If the pressure probe is not inclined to the free stream, and if the Reynolds number is large enough to make viscous effects negligible, then the measured impact pressure can be considered to be the same as the stagnation pressure behind a normal shock wave whose strength is given by the flight Mach number. The relation between this stagnation pressure  $P$ , the ambient static pressure  $p_1$ , and the flight Mach number  $M_1$  is given by

$$\frac{P}{p_1} = \left[ \frac{(\gamma-1) M_1^2}{2} \right]^{\frac{\gamma}{\gamma-1}} \cdot \left[ \frac{\gamma+1}{2\gamma M_1^2 - (\gamma-1)} \right]^{\frac{1}{\gamma-1}}$$

or

$$\frac{P}{p_1} = M_1^2 \left[ \frac{\gamma+1}{2} \right]^{\frac{\gamma+1}{\gamma-1}} \cdot \gamma^{-\frac{1}{\gamma-1}} \left[ 1 - \frac{\gamma-1}{2\gamma M_1^2} \right]^{-\frac{1}{\gamma-1}} \quad (2.1)$$

This is the Rayleigh supersonic pitot tube formula given in Ref. 28. Newell in Ref. 1 puts Eq. 2.1 in a form which is more useful in reducing rocket data. By replacing  $M_1^2$  with  $\rho_1 v^2 / \gamma p_1$  and expanding the term  $\left[ 1 - \frac{\gamma-1}{2\gamma M_1^2} \right]^{-1/(\gamma-1)}$

as a series, Eq. 2.1 becomes :

$$P = 0.92 \rho_1 v^2 + 0.46 p_1 + \dots, \quad (\gamma = 1.4) \quad (2.2)$$

Table I indicates the relative importance of the terms in the series by comparing the exact solution for  $P/p_1$  with the first term,  $0.92 \rho_1 v^2 / p_1$ , and also with the first two terms,  $0.92 \rho_1 v^2 / p_1 + 0.46$ , for a series of Mach numbers. It can be seen that there is no significant difference between the exact solution and the sum of the first two terms of the series for Mach numbers greater than 1.5. The second term provides a correction whose importance decreases as the Mach number increases. As a result the expression for the ambient density as determined with only the first two terms of Eq. 2.2 is

$$\rho_1 = \frac{1.087 (P - 0.46 p_1)}{v^2} \quad (2.3)$$

An accurate value of  $\rho_1$  can be obtained from Eq. 2.3 without knowing  $p_1$  accurately. Substitution of a value of  $p_1$  from standard atmosphere tables (Ref. 29) will result in an error in  $\rho_1$  of less than 1% for  $M_1 > 2$ , even if the assumed  $p_1$  is in error by 10%. Since in an actual rocket flight the Mach number quickly reaches a value greater than 5, the  $0.46 p_1$  term becomes insignificant.

Equation 2.3 indicates that the atmospheric density can be determined if:

- (1) the impact pressure is measured,
- (2) an approximate value of static pressure is known, and
- (3) the free stream velocity can be measured.

Using Eq. 2.1 and the predicted rocket performance figures, the expected impact pressures were calculated. On this basis gauges were selected to cover the anticipated range of impact pressures. These are described in more detail in Section 3.2. The U.S. Standard Atmosphere (Ref. 29) provides a sufficiently accurate value of  $p_1$  for an initial determination of  $\rho_1$ . When the actual  $p_1$  is determined (see Section 2.1.2), then this value can be used if it is significantly different.

Radar tracking of the rocket provides velocity and position information with respect to the ground. However, the rocket velocity is great enough (i.e. up to 6000 ft/sec) to be influenced very little by atmospheric wind during the lower part of its trajectory. For this reason, the radar determination of rocket velocity can be used in data reduction.

Since Eq. 2.3 is only accurate for small angles of attack an indication of the angular orientation of the rocket is desirable. For this purpose sun sensors were employed in the rocket to measure the angle between the rocket spin axis and the sun's direction. This information was sufficient to indicate that the rocket was not yawed significantly during the lower part of the trajectory.

These measurements will all be dealt with in more detail when the experimental results are examined.

The validity of Eq. 2.3 depends on the magnitude of the Reynolds number, which is a parameter describing the importance of viscosity on the flow field. Normally in the case of measurements with an impact probe, the probe diameter is significant and the Reynolds number is defined by

$$Re_d = \frac{\rho_1 V d}{\mu_1}$$

where  $d$  is the probe diameter and  $\mu_1$  is the free stream viscosity. In Refs. 30, 31, and 32 the variation of impact pressure with Reynolds number for various Mach numbers is examined both theoretically and experimentally. Reference 30 indicates that the correction is negligible for Reynolds numbers greater than 1000, and is only 2% or 3% for Reynolds numbers as low as 60. If the Reynolds number computed from the flight data becomes small enough then the necessity of applying these corrections must be considered.

### 2.1.2 Atmospheric Pressure

The theory developed by Taylor and Maccoll for the supersonic flow around a cone at zero angle of attack can be used to relate the free stream static pressure to the pressure measured at the surface of a cone. Reference 33 contains tabulated values of the function

$$K_D = \frac{p_c - p_1}{\rho_1 V^2} \quad (2.4)$$

where  $p_c$  is the surface pressure on the cone, in the ideal case of no boundary layer on the surface. The value of  $K_D$  depends on the free stream Mach number  $M_1$ , and the vertex angle of the cone. Figure 1 is the result of using Ref. 33

to evaluate  $K_D$  as a function of  $M_1$  for the Black Brant II nose cone angle of  $11^\circ 24'$ .

By making use of the normal shock relations and tabulated flow parameters in Ref. 28, the quantity  $P/\frac{1}{2}\rho_1 V^2$  can be determined as a function of free stream Mach number,  $M_1$ . Combining the equation

$$\frac{P}{\frac{1}{2}\rho_1 V^2} = F(M_1)$$

with Eq. 2.4 the following expression results:

$$\frac{P}{p_c} = \frac{1}{\frac{2 K_D}{F(M_1)} + \frac{P_1}{P}} \quad (2.5)$$

Equation 2.5 now expresses the quantity  $P/p_c$  as a function of  $M_1$  alone for the particular cone angle being considered. Figure 2 is a graph of the ratio of the measured pressures,  $P$  and  $p_c$ , as a function of free stream Mach number. From the value of  $P/p_c$  the value of  $M_1$  can be determined, and hence the value of  $R_1 T_1$ , from which the temperature can be determined when  $R_1$  is known, since

$$M_1 = \frac{V}{\sqrt{\gamma R_1 T_1}} \quad (2.6)$$

where

- $V$  = free stream velocity
- $\gamma$  = ratio of the specific heats
- $R_1$  = specific gas constant, given by  $R/m_1$
- $R$  = universal gas constant
- $m_1$  = local molecular weight of the atmosphere
- $T_1$  = free stream temperature

Since the value of  $K_D$  used in Eq. 2.5 is that for the cone at zero angle of attack, the angle of attack should be checked in the actual experiment to insure that Eq. 2.5 is applicable.

When the value of  $R_1 T_1$  is determined, the atmospheric pressure can be calculated from the equation of state

$$p_1 = \rho_1 R_1 T_1 \quad (2.7)$$

The previous analysis is valid only when the boundary layer on the cone surface is thin. As the Reynolds number becomes smaller during the rocket ascent, the boundary layer thickens causing an increase in the surface pressure over the ideal value. This necessitates applying theoretical or empirical corrections to the measured surface pressure to enable the atmospheric temperature to be correctly calculated. Many theoretical and experimental investigations of the boundary layer effect on the surface pressure of a cone in supersonic flow have been carried out (Refs. 32, 34, 35, and 36). Figure 3, as obtained from Ref. 35, indicates the deviation of the surface pressure from the ideal value in terms of a correlation factor

$$M_c^3 \sqrt{\frac{C}{Re_c}}$$

where  $M_c$  = Mach number on the surface of the cone  
 $C$  = proportionality factor in the relation between viscosity and temperature,  $\mu_1/\mu_2 = C(T_1/T_2)$

$$Re_c = \frac{\rho_c U_c X_c}{\mu_c}$$

$\rho_c$  = gas density on the cone surface,  
 $U_c$  = gas velocity on the cone surface,  
 $\mu_c$  = gas viscosity on the cone surface,  
 $X_c$  = distance of the pressure orifice from the vertex of the cone (measured along the surface).

The use of this empirical data to apply corrections to the measured surface pressure will be considered in Section 7.

## 2.2 Rarefied Gas Flow Theory

As the rocket ascends to higher altitudes, the atmosphere becomes so rarefied that the nature of the flow around the rocket is completely different from that at low altitude. The approach of this transition flow regime is signalled by the need to make the previously discussed corrections to the impact and cone pressure measurements. Probstein and Kemp in Ref. 37 discuss the criterion for determining the degree of rarefaction of the flow around a body moving at hypersonic speed. The parameter which describes the flow is the Knudsen number, defined as

$$Kn = \frac{\lambda}{L}$$

The mean free path  $\lambda$ , is the average distance which the air molecules travel between collisions with each other, and  $L$  is a characteristic length for the problem being considered. For a highly rarefied flow the value of  $\lambda$  is generally evaluated for the free stream conditions, and the length  $L$  is the diameter or length of the body in the flow. Free molecule flow is generally considered to exist when  $Kn \geq 10$ . This is a condition in which the body does not affect the free stream molecules until they strike it, and there is no significant interference between free stream molecules and molecules reflected from the surface after collision. In this case kinetic theory can adequately describe the flux of molecules reaching the surface of the body. However, one should be careful in applying this definition to the free molecule flow regime. In Ref. 37 it was pointed out that the body temperature has an effect on the flow field. If one calculates the mass flux of particles emitted from the body surface using kinetic theory, it is found to be proportional to  $n_b \sqrt{T_b}$  (Ref. 38), where  $n_b$  is an effective emitted molecule number density, and  $T_b$  is the body temperature. For a given incident flux of molecules,  $n_b$  is inversely proportional to  $\sqrt{T_b}$ . If the body is cold  $n_b$  will be larger than if the body is hot, and thus there will be more interference with the incoming stream. As a result there may still be significant interference between the incident and reflected molecules even though  $Kn$  has a value of 10 or greater based on free stream conditions.

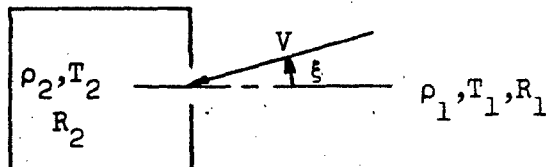
While free molecule flow theory has been thoroughly described by Patterson (Refs. 38, 39) and Tsien (Ref. 40), the near free molecule flow regime is not as well described. For this type of flow, analyses have been carried out which take into account single collisions between molecules of the incoming and reflected streams (Ref. 41). The applicability of these is limited by the simplifying assumptions made in order to permit a solution of the problem. However, this does allow first order corrections to be made in the absence of any experimental data.

### 2.2.1 Free Molecule Orifice Probe Theory

The free molecule orifice pressure probe provides a means of relating the measured conditions inside a pressure gauge mounted in the rocket, to the flow parameters in the free stream. It is possible, in principle to measure  $\rho_1$ ,  $R_1 T_1$ , and even obtain some information concerning wind velocity, by using a number of gauges oriented at different angles to the free stream velocity.

Since the basic theory behind the operation of the orifice probe has been adequately treated in Refs. 38, 39, only the relevant results of the analysis will be included here.

Consider a gauge volume exposed to a uniform rarefied gas flow through an opening with zero length (i.e. an orifice). The free stream velocity  $V$ , makes an angle,  $\xi$ , with the normal to the orifice. The free stream and gauge volume density, temperature and gas constant are as shown below.



The free molecule analysis assumes the following:

- 1) The mean free path in the ambient stream is much greater than the gauge dimensions, implying that the incident and reflected streams of molecules do not interfere.
- 2) There is an equilibrium between the mass flux of molecules entering and leaving the gauge volume.
- 3) The distribution functions describing the velocities of the entering and leaving molecules are Maxwellian.

Under these conditions the expression relating the gauge volume conditions to the free stream parameters is

$$\frac{\rho_2 \sqrt{R_2 T_2}}{\rho_1 \sqrt{R_1 T_1}} = \chi (S_N) \quad (2.9)$$

where the following symbols are used:

$$\chi(S_N) = e^{-S_N^2} + \sqrt{\pi} S_N (1 + \operatorname{erf} S_N) \text{ for } S_N > 0 \quad (2.10)$$

$$\chi(S_N) = e^{-S_N^2} - \sqrt{\pi} |S_N| (1 - \operatorname{erf} |S_N|) \text{ for } S_N < 0 \quad (2.11)$$

$$S_N = \frac{V}{\sqrt{2 R_1 T_1}} \cos \xi, \quad 0 \leq \xi \leq 180^\circ \quad (2.12)$$

and

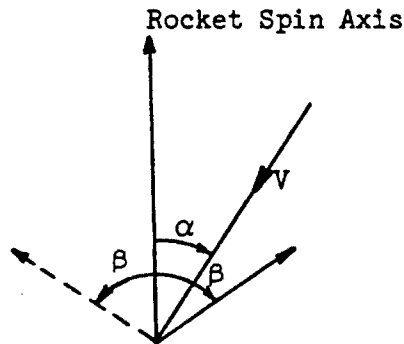
$$\operatorname{erf} x = \frac{2}{\sqrt{\pi}} \int_0^x e^{-y^2} dy \quad (2.13)$$

Since  $V/\sqrt{2R_1T_1}$  is the definition of the speed ratio  $S$ , then  $S_N$  is the component of  $S$  directed into the gauge orifice.

It is evident that Eq. 2.9 contains both  $\rho_1$  and  $R_1T_1$  as variables. If measurements could be made simultaneously with a second gauge making a different angle with the free stream, then, in principle, it is possible to obtain 2 equations to be solved for  $\rho_1$  and  $R_1T_1$ . In an ideal rocket flight all of the other parameters in the equations would be measurable. However, this implies that there is no gauge outgassing or atmospheric wind. If outgassing is present, there is no way of distinguishing between the outgassing pressure and the pressure due to the free stream molecules, unless the rocket is performing a motion which produces a modulation of the gauge signal caused solely by the free stream molecules. Similarly, if significant atmospheric winds are present, there are now too many unknown parameters to permit a solution for the wind velocity, even if data obtained during ascent and descent are compared.

### 2.2.2 Theory for a Pressure Gauge Mounted on a Spinning Rocket

The preceding discussion is only true in the ideal case of no rocket or gauge outgassing. When this is present a different technique must be used, although it is still based on the validity of Eq. 2.9. For this situation, consider the case of a gauge mounted on a rocket spinning about its longitudinal axis.



The angle between the rocket spin axis and the relative velocity vector,  $V$ , is given by  $\alpha$ . The angle between the rocket spin axis and the direction perpendicular to the plane of the gauge orifice is given by  $\beta$ .

As the rocket spins, the gauge volume density changes in a cyclic manner because of the changing value of  $S_N$ . When the rocket axis, the velocity vector, and the normal to the gauge orifice all lie in the same plane, then the function  $\chi(S_N)$ , and hence the gauge density  $\rho_2$ , assumes a maximum or minimum value. This value depends on which direction the gauge orifice is facing.

a) Gauge Oriented With  $\beta = 90^\circ$

Let us first consider the information which can be derived from this type of rocket experiment when the gauge is oriented with  $\beta$  having a value of  $90^\circ$ . In this form the experiment has been carried out several times by a number of different experimenters (Refs. 23 and 42). For this case the maximum and minimum values of  $S_N$  are

$$S_{N(\max)} = \frac{V}{\sqrt{2R_1T_1}} \sin \alpha$$

and

$$S_{N(\min)} = -\frac{V}{\sqrt{2R_1T_1}} \sin \alpha.$$

The gauge volume densities corresponding to these two limiting values of  $S_N$  are

$$\frac{\rho_{2(\max)} \sqrt{R_2T_2}}{\rho_1 \sqrt{R_1T_1}} = e^{-\frac{(V \sin \alpha)^2}{2 R_1 T_1}} + \frac{\sqrt{\pi} V \sin \alpha}{\sqrt{2 R_1 T_1}} \left[ 1 + \operatorname{erf} \left( \frac{V \sin \alpha}{\sqrt{2 R_1 T_1}} \right) \right] \quad (2.14)$$

and

$$\frac{\rho_{2(\min)} \sqrt{R_2T_2}}{\rho_1 \sqrt{R_1T_1}} = e^{-\frac{(V \sin \alpha)^2}{2 R_1 T_1}} - \frac{\sqrt{\pi} V \sin \alpha}{\sqrt{2 R_1 T_1}} \left[ 1 - \operatorname{erf} \left( \frac{V \sin \alpha}{\sqrt{2 R_1 T_1}} \right) \right]. \quad (2.15)$$

The maximum gauge density variation,  $\Delta \rho_2$  over a single spin cycle is therefore given by

$$\frac{\Delta \rho_2 \sqrt{R_2T_2}}{\rho_1} = \sqrt{2\pi} V \sin \alpha \quad (2.16)$$

or

$$\rho_1 = \frac{\Delta \rho_2 \sqrt{R_2T_2}}{\sqrt{2\pi} V \sin \alpha} \quad (2.17)$$

where

$$\Delta \rho_2 = \rho_{2(\max)} - \rho_{2(\min)}$$

It is evident from Eq. 2.17 that a gauge oriented with  $\beta = 90^\circ$  can be employed to determine the free stream density if the following measurements can be made:

- 1) Gauge volume density.
- 2) Gauge volume temperature.
- 3) Composition of the gas in the gauge volume.
- 4) Relative velocity of the rocket with respect to the atmosphere.
- 5) Orientation of the rocket spin axis.

Let us consider each of these quantities in turn and see what problems each measurement might pose.

The measurement of  $\rho_2$ , in principle, requires a vacuum gauge calibrated for the particular atmospheric composition to be encountered. In practice the gauge is calibrated against a McLeod gauge for dry air of normal composition. At altitudes above 100 km the composition does start to change, due mainly to dissociation of molecular oxygen, resulting in an atmospheric molecular weight of 26.81 at 155 km (apogee for the UTIAS rocket) (Ref. 29). Some experimenters have attempted to correct for this by measuring or calculating the gauge sensitivities for each of the atmospheric components (Refs. 42 and 43). This could also present problems since the gas composition in the gauge volume may not be the same as in the atmosphere due to recombination within the gauge. Depending on the rocket altitude, these factors affecting the gauge calibration must be considered in order to provide an estimate of the error possible in measuring  $\rho_2$ .

The temperature of the molecules within the gauge should be essentially the temperature of the walls of the gauge volume. This can be easily measured with some type of thermistor temperature probe.

As mentioned previously, one's knowledge of  $R_2$  or the gas composition within the gauge volume may be in doubt. Unless the atmospheric composition is known, along with the degree of recombination within the gauge, then  $R_2$  cannot be stated definitely. However, by comparing the value of the molecular weight for normal dry air, and the atmospheric value given by standard atmosphere tables as the two limiting values of  $R_2$ , an estimate of the possible error can be made. By assuming  $R_2$  to have the sea level value, the calculated value of  $\rho_1$  can be too small by the factor  $\sqrt{m_1/m_0}$ , where  $m_0$  is the molecular weight at sea level and  $m_1$  is the molecular weight at the altitude under consideration.

The determination of the rocket velocity relative to the atmosphere presents problems because it cannot be directly measured. The only velocity measured during the experiment is the velocity of the rocket with respect to the ground, as determined by radar tracking. Since upper atmosphere winds greater than 300 feet per second have been measured (Ref. 44) the relative rocket velocity could be significantly different, in magnitude and direction, from the value determined by radar. The quantities  $V$  and  $\alpha$  can be expressed explicitly as functions of the unknown wind velocity components.

$$\bar{V}_R = \bar{e}_x V_x + \bar{e}_y V_y + \bar{e}_z V_z \quad (2.18)$$

where  $\bar{e}_x$  is a unit vector pointing south,  
 $\bar{e}_y$  is a unit vector pointing east,  
 $\bar{e}_z$  is a unit vector pointing vertically upward, and  
 $V_x, V_y, V_z$  are the corresponding rocket velocity components with respect to the coordinate system fixed to the earth.

In this same coordinate system the wind velocity is given by

$$\bar{V}_w = \bar{e}_x v_x + \bar{e}_y v_y + \bar{e}_z v_z \quad (2.19)$$

As a result the relative velocity of the atmosphere with respect to the rocket is

$$\bar{V} = -(\bar{V}_R - \bar{V}_w) \quad (2.20)$$

If (a,b,c) are the direction cosines of the rocket axis and

$$\left( \frac{V_x - v_x}{V}, \frac{V_y - v_y}{V}, \frac{V_z - v_z}{V} \right)$$

are the direction cosines of the velocity vector, then from Ref. 45, the angle of attack is given by

$$\alpha = \cos^{-1} \left( \frac{V_x - v_x}{V} \cdot a + \frac{V_y - v_y}{V} \cdot b + \frac{V_z - v_z}{V} \cdot c \right) \quad (2.21)$$

where

$$V = \sqrt{(V_x - v_x)^2 + (V_y - v_y)^2 + (V_z - v_z)^2} \quad (2.22)$$

If there are no atmospheric winds, then the maximum or minimum gauge signal must occur when the normal to the gauge orifice lies in the plane defined by the rocket axis and the velocity vector  $\bar{V}_R$ . If winds are present, then the time of maximum or minimum gauge signal is shifted, because the normal to the gauge orifice now must lie in a different plane defined by the rocket axis and the velocity vector  $\bar{V}$ . The amount of phase shift in the signal is given by the angle between the two planes defined above. Using the methods of analytic geometry (Ref. 45), the phase shift  $\Delta\phi_w$  is expressed by

$$\cos \Delta\phi_w = \frac{X_a Y_a + X_b Y_b + X_c Y_c}{\sqrt{X_a^2 + X_b^2 + X_c^2} \cdot \sqrt{Y_a^2 + Y_b^2 + Y_c^2}} \quad (2.23)$$

where

$$X_a = \begin{vmatrix} b & c \\ \frac{v_y}{V_R} & \frac{v_z}{V_R} \end{vmatrix}$$

$$X_b = \begin{vmatrix} c & a \\ \frac{v_z}{V_R} & \frac{v_x}{V_R} \end{vmatrix}$$

$$X_c = \begin{vmatrix} a & b \\ \frac{v_x}{V_R} & \frac{v_y}{V_R} \end{vmatrix}$$

$$Y_a = \begin{vmatrix} b & c \\ \frac{V_y - v_y}{V} & \frac{V_z - v_z}{V} \end{vmatrix}$$

$$Y_b = \begin{vmatrix} c & a \\ \frac{V_z - v_z}{V} & \frac{V_x - v_x}{V} \end{vmatrix}$$

$$Y_c = \begin{vmatrix} a & b \\ \frac{V_x - v_x}{V} & \frac{V_y - v_y}{V} \end{vmatrix}$$

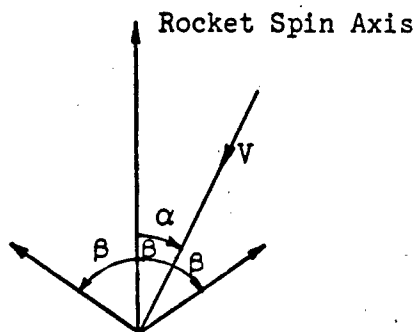
In order to make use of these general expressions containing the wind velocity components, one must make some simplifying assumptions. First, the wind must be assumed to be horizontal; second, the wind and other atmospheric parameters remain constant over the horizontal range of the flight. There is evidence to suggest that winds at an altitude of 100 km are essentially horizontal, having fluctuating vertical components with root-mean-square values of vertical speed of 1 to 2 meter/sec. (Ref. 46). However, the same reference indicates the possibility of having horizontal changes in the wind due to large wind eddies. There is a possibility that the wind conditions may not be the same during ascent and descent. Since the wind eddies have a vertical extent of only a few kilometers, their presence would be apparent in the calculated wind pattern. By measuring the phase shift at a given altitude during ascent and descent, one obtains two equations from substitution of the known parameters in Eq. 2.23. While this illustrates that the wind components can be found, it is certainly difficult to solve the equations. Ainsworth, Fox and LaGow (Ref. 10) describe a graphical method of solution for the wind velocity which is still based on making measurements of the phase shift in the gauge signal, and using ascent and descent data at the same altitude. To simplify the solution the wind is still assumed to be horizontal and the rocket axis is also considered to be vertical. In the case of the UTIAS rocket, the angle between the rocket axis and the vertical was never more than  $15^\circ$ , which was small enough to permit the type of solution in Ref. 10 to be used. Since errors arise in the measurement of phase shift, rocket velocity, and orientation, the wind which can be detected by this method may be subject to large errors in magnitude and direction. This question of detecting the wind velocity will be examined more fully when the experimental data is considered in Section 7.4.

The final quantity which must be determined if the data is to be interpreted is the angular orientation of the rocket axis. In principle this can be done if one measures the angle between the rocket axis and the known direction of the earth's magnetic field, and also the angle between the rocket axis and the sun's direction. The angle with respect to the magnetic field can be measured with two single component magnetometers oriented parallel and perpendicular to the rocket axis. An analog type of sun sensor was selected to provide the means of measuring the angle between the rocket axis and the sun's direction. If the phase relation between the sun sensor signals and the lateral magnetometer output is also considered, then the orientation of the rocket axis can be uniquely determined.

Each of the measurements necessary for the interpretation of the flight data will be dealt with in some detail in the sections devoted to the rocket payload and data reduction.

The free molecule flow analysis is based on the assumption that the free stream parameters do not change significantly during a single spin cycle. So long as the spin rate is sufficiently high, and the rocket motion does not become unstable, this is a valid assumption. When the high altitude gauges first gave useful readings at an altitude of 320,000 feet, the rocket travelled a vertical distance of 1080 feet during a spin cycle. Over this distance the free stream density changes by only 6% (Ref. 29). At higher altitudes the change becomes insignificant since the rocket velocity decreases and the scale height increases. In addition, it will be shown that the change in the rocket axis orientation during a spin cycle is also insignificant.

b) Gauge Oriented at an Arbitrary Angle  $\beta$



In this general case the maximum and minimum components of the speed ratio are given by

$$S_{N(\max)} = S \cos (\beta-\alpha) \quad (2.25)$$

and

$$S_{N(\min)} = S \cos (\beta+\alpha) \quad (2.26)$$

The corresponding gauge volume densities, obtained by substitution in Eq. 2.9 are

$$\frac{\rho_2(\max) \sqrt{R_2 T_2}}{\rho_1 \sqrt{R_1 T_1}} = e^{-S^2 \cos^2 (\beta-\alpha)} + \sqrt{\pi} S \cos (\beta-\alpha) \{1 + \operatorname{erf} S \cos (\beta-\alpha)\} \quad (2.27)$$

and

$$\frac{\rho_2(\min) \sqrt{R_2 T_2}}{\rho_1 \sqrt{R_1 T_1}} = e^{-S^2 \cos^2 (\beta+\alpha)} + \sqrt{\pi} S \cos (\beta+\alpha) \{1 + \operatorname{erf} S \cos (\beta+\alpha)\} \quad (2.28)$$

The gauge density difference,  $\Delta \rho_2$ , over a single spin cycle is given by

$$\frac{\Delta \rho_2 \sqrt{R_2 T_2}}{\rho_1 \sqrt{R_1 T_1}} = e^{-S^2 \cos^2(\beta-\alpha)} + \sqrt{\pi} S \cos(\beta-\alpha) [1 + \operatorname{erf} S \cos(\beta-\alpha)]$$

$$- e^{-S^2 \cos^2(\beta+\alpha)} - \sqrt{\pi} S \cos(\beta+\alpha) [1 + \operatorname{erf} S \cos(\beta+\alpha)]$$

$$= F(S, \alpha, \beta) \quad (2.29)$$

Equation 2.29 indicates that  $\Delta \rho_2 \sqrt{R_2 T_2} / \rho_1$  is a function of  $R_1 T_1$  of the form

$$\frac{\Delta \rho_2 \sqrt{R_2 T_2}}{\rho_1} = \sqrt{R_1 T_1} F(S, \alpha, \beta) \quad (2.30)$$

In principle it is possible to solve for  $R_1 T_1$  if  $\rho_1$  can be determined from Eq. 2.17 which is the special case for  $\beta = 90^\circ$  and if  $\Delta \rho_2$ ,  $R_2 T_2$ ,  $V$ ,  $\alpha$ , and  $\beta$  are known. In actual practice there are certain limitations to this method of obtaining  $R_1 T_1$ . If  $\sqrt{R_1 T_1} F(S, \alpha, \beta)$  is a slowly varying function of  $S$ , it is evident that large errors in the calculated value of  $R_1 T_1$  are possible even though the measured values of the other parameters are quite accurate. It is therefore necessary to examine Eq. 2.29 to determine its range of usefulness.

Consider Eq. 2.29 for the two limiting cases of values of  $S$  which are small or very large.

Case (a):  $S \ll 1$

For this case the following approximations can be used:

$$\operatorname{erf} x \approx \frac{2}{\sqrt{\pi}} x \quad \text{for } (x \ll 1)$$

and

$$e^y \approx 1 + y \quad \text{for } (y \ll 1)$$

With these approximations, Eq. 2.29 becomes

$$\frac{\Delta \rho_2 \sqrt{R_2 T_2}}{\rho_1 \sqrt{R_1 T_1}} = \sqrt{\pi} S [\cos(\beta-\alpha) - \cos(\beta+\alpha)]$$

when second order terms are neglected. The expression  $\Delta \rho_2 \sqrt{R_2 T_2} / \rho_1$  is therefore not dependent on  $R_1 T_1$  and hence the method is not useful for very small values of  $S$  no matter what values  $\alpha$  and  $\beta$  are used.

Case (b):  $S \gg 1$

For this case there are three possibilities depending on  $\alpha$  and  $\beta$ :

- (1)  $S \cos (\beta-\alpha) \gg 1$  and  $S \cos (\beta+\alpha) \gg 1$ .
- (2)  $S \cos (\beta-\alpha) \gg 1$  and  $S \cos (\beta+\alpha) \ll -1$ .
- (3)  $S \cos (\beta-\alpha) \ll -1$  and  $S \cos (\beta+\alpha) \ll -1$ .

Using the approximations

$$\operatorname{erf}(\pm x) \approx \pm 1 \quad \text{for } x \gg 1$$

and

$$e^{-y} \approx 0 \quad \text{for } y \gg 1$$

each of the above possibilities can be examined in turn. The resulting expressions for  $\Delta \rho_2 \sqrt{R_2 T_2} / (\rho_1 \sqrt{R_1 T_1})$  are the following:

$$(1) \quad \frac{\Delta \rho_2 \sqrt{R_2 T_2}}{\rho_1 \sqrt{R_1 T_1}} \approx 2 \sqrt{\pi} S \{ \cos (\beta-\alpha) - \cos (\beta+\alpha) \}$$

$$(2) \quad \frac{\Delta \rho_2 \sqrt{R_2 T_2}}{\rho_1 \sqrt{R_1 T_1}} \approx 2 \sqrt{\pi} S \{ \cos (\beta-\alpha) \}$$

$$(3) \quad \frac{\Delta \rho_2 \sqrt{R_2 T_2}}{\rho_1 \sqrt{R_1 T_1}} \approx 0$$

In each case  $\Delta \rho_2 \sqrt{R_2 T_2} / \rho_1$  is not a function of  $S$ , and hence these combinations of  $S$ ,  $\alpha$  and  $\beta$  will not yield solutions for  $R_1 T_1$ .

In general it can be said that solutions for  $R_1 T_1$  will not be possible if  $S_{N(\max)}$  and  $S_{N(\min)}$  are very small, or if they are very large.

Between these limits the sensitivity of the function  $\sqrt{R_1 T_1} F(S, \alpha, \beta)$  to changes in  $S$  will depend on  $\alpha$ , and  $\beta$  and well as  $S$ . Since the values of  $\alpha$  and  $S$  for a rocket flight are difficult to predict in advance, it is necessary to choose a gauge orientation whose  $\beta$  will provide a possibility of solution of Eq. 2.29 for a major part of the trajectory. Of course, if the value of  $S$  becomes very small near apogee, then an accurate solution for  $R_1 T_1$  will not be possible no matter what value of  $\beta$  is chosen.

The choice of a value of  $\beta$  involves a certain amount of compromise. One requirement for  $\beta$  is that it produces a large value of  $\Delta \rho_2$  since this will allow greater accuracy in the gauge measurements if outgassing is present. The second requirement is that Eq. 2.29 be soluble for  $R_1 T_1$  over a wide range of values of  $S$  and  $\alpha$ . These two requirements are not necessarily compatible since the value of  $\beta$  which produces the largest value of  $\Delta \rho_2 \sqrt{R_2 T_2} / (\rho_1 \sqrt{R_1 T_1})$  for a given  $S$  and  $\alpha$  is not in general the one which permits a solution of Eq. 2.29 over a suitable range of values of  $S$  and  $\alpha$ . Figure 4 compares the values of  $\Delta \rho_2 \sqrt{R_2 T_2} / (\rho_1 \sqrt{R_1 T_1})$  for  $0 < \alpha < 180^\circ$  and  $S = 1$  for  $\beta = 20^\circ, 30^\circ, 45^\circ, 60^\circ$  and  $90^\circ$ . The case for  $\beta = 90^\circ$  is simply Eq. 2.16 which cannot be solved for  $R_1 T_1$ . Hence

it is evident that values of  $\beta$  close to  $90^\circ$  will not be useful even though these would produce relatively high values of  $\Delta p_2$ . At the other end of the range where  $\beta$  is small, the value of  $\Delta p_2$  is also relatively small. In addition, for values of  $\alpha$  close to  $90^\circ$  Eq. 2.29 cannot be solved for  $R_1 T_1$  since  $S_N$  is small. As a result  $\beta$  was chosen to be  $45^\circ$  since this value gave good sensitivity, and as will be shown, enabled Eq. 2.29 to be solved over a sufficiently large part of the trajectory. While this is not the only value which could be used, it is certainly within the band of useful values.

c) Pressure Gauge Oriented at  $\beta = 45^\circ$

Substitution of  $\beta = 45^\circ$  in Eq. 2.29 results in the following expressions:

(1) For  $0 \leq \alpha \leq 45^\circ$

$$\frac{\Delta p_2 \sqrt{R_2 T_2}}{\rho_1 \sqrt{R_1 T_1}} = \frac{-\frac{S^2}{2}(1 + \sin 2\alpha)}{e} - \frac{\frac{S^2}{2}(1 - \sin 2\alpha)}{-e} + \sqrt{2\pi} S \sin \alpha$$

$$+ \sqrt{\frac{\pi}{2}} S (\cos \alpha + \sin \alpha) \operatorname{erf} \left\{ \frac{S}{\sqrt{2}} (\cos \alpha + \sin \alpha) \right\}$$

$$- \sqrt{\frac{\pi}{2}} S (\cos \alpha - \sin \alpha) \operatorname{erf} \left\{ \frac{S}{\sqrt{2}} (\cos \alpha - \sin \alpha) \right\} \quad (2.31)$$

(2) For  $45^\circ \leq \alpha \leq 135^\circ$

$$\frac{\Delta p_2 \sqrt{R_2 T_2}}{\rho_1 \sqrt{R_1 T_1}} = \frac{-\frac{S^2}{2}(1 + \sin 2\alpha)}{e} - \frac{\frac{S^2}{2}(1 - \sin 2\alpha)}{-e} + \sqrt{2\pi} S \sin \alpha$$

$$+ \sqrt{\frac{\pi}{2}} S (\cos \alpha + \sin \alpha) \operatorname{erf} \left\{ \frac{S}{\sqrt{2}} (\cos \alpha + \sin \alpha) \right\}$$

$$- \sqrt{\frac{\pi}{2}} S (\sin \alpha - \cos \alpha) \operatorname{erf} \left\{ \frac{S}{\sqrt{2}} (\sin \alpha - \cos \alpha) \right\} \quad (2.32)$$

(3) For  $135^\circ \leq \alpha \leq 180^\circ$

$$\frac{\Delta p_2 \sqrt{R_2 T_2}}{\rho_1 \sqrt{R_1 T_1}} = \frac{-\frac{S^2}{2}(1 + \sin 2\alpha)}{e} - \frac{\frac{S^2}{2}(1 - \sin 2\alpha)}{-e} + \sqrt{2\pi} S \sin \alpha$$

$$- \sqrt{\frac{\pi}{2}} S (\cos \alpha + \sin \alpha) \operatorname{erf} \left\{ -\frac{S}{\sqrt{2}} (\cos \alpha + \sin \alpha) \right\}$$

$$- \sqrt{\frac{\pi}{2}} S (\sin \alpha - \cos \alpha) \operatorname{erf} \left\{ \frac{S}{\sqrt{2}} (\sin \alpha - \cos \alpha) \right\} \quad (2.33)$$

The expressions for  $\Delta p_2 \sqrt{R_2 T_2} / (\rho_1 \sqrt{R_1 T_1})$  are plotted in Fig. 5 as a function of  $\alpha$

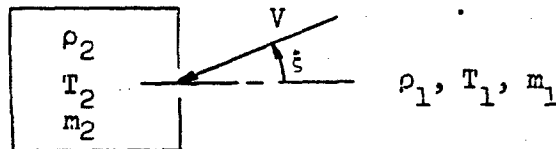
for a number of values of  $S$ . To determine the range of values of  $\alpha$  for which a solution for  $R_1 T_1$  is possible, Eqs. 2.31 to 2.33 are plotted as a function of  $S$  for the full range of values of  $\alpha$  (Figs. 6a, b). For values of  $\alpha$  between  $0^\circ$  and  $100^\circ$ , the quantity  $\Delta \rho_2 \sqrt{R_2 T_2} / (\rho_1 \sqrt{R_1 T_1})$  is very nearly proportional to  $S$  and hence solutions for  $R_1 T_1$  over this range will not be accurate. For values of  $\alpha > 120^\circ$  (Fig. 6b) the curves are no longer proportional to  $S$  except for small values of  $S$ . Since the angle of attack is roughly in the range  $0 < \alpha < 90^\circ$  during ascent, it is evident that solutions with a gauge oriented with  $\beta = 45^\circ$  will only be possible during descent.

In order to determine the values of  $R_1 T_1$  during the rocket's ascent it is necessary to orient a second gauge with  $\beta = 135^\circ$ . In this way a comparison can be made of results obtained over most of the rocket trajectory above 100 km. The symmetry of the orientations  $\beta = 45^\circ$  and  $135^\circ$  results in Eqs. 2.31 to 2.33 being applicable to the case of  $\beta = 135^\circ$ , if  $180-\alpha$  is substituted wherever  $\alpha$  appears.

### 2.2.3 Time Response of Free Molecule Gauges

Since the experiment requires the measurement of a rapidly varying gauge volume density, it is necessary to investigate the time response of the gauge volume for a given orifice area. The time response must be fast enough to allow the gauge volume conditions to reach essentially the values predicted for an equilibrium condition at any instant of time.

Consider the gauge volume,  $v$ , exposed to the free molecule gas flow through an orifice of area,  $A$ .



The free stream conditions are described by density  $\rho_1$ , temperature  $T_1$ , and molecular weight  $m_1$ . The flow velocity is  $V$  and is inclined at an angle  $\xi$  to the normal to the orifice area. The gauge volume conditions are given by  $\rho_2$ ,  $T_2$  and  $m_2$ .

From Ref. 39 the mass entering the gauge volume per unit time at any time,  $t$ , is

$$\frac{\rho_1 C_{m_1}}{2 \sqrt{\pi}} AX(S_N) \quad (2.34)$$

where  $C_{m_1}$  = most probable molecular speed

$$\begin{aligned} C_{m_1} &= \sqrt{\frac{2 R T_1}{m_1}} \\ &= \sqrt{2 R_1 T_1} \end{aligned} \quad (2.35)$$

and  $R$  is the universal gas constant.

At the time  $t$ , the mass leaving the gauge volume per unit time is

$$\frac{\rho_2 C_{m2}}{2\sqrt{\pi}} A$$

where  $C_{m2} = \sqrt{2 \frac{R}{m_2} T_2} = \sqrt{2R_2 T_2}$  .

The rate of change of mass in the gauge volume  $v(dp_2/dt)$  can be expressed as the difference between the mass flux entering and leaving the volume

$$v \frac{dp_2}{dt} + \frac{\rho_2 C_{m2} A}{2\sqrt{\pi}} = \frac{\rho_1 C_{m1} A}{2\sqrt{\pi}} \chi(S_N) \quad (2.36)$$

or

$$\frac{dp_2}{dt} + \frac{\rho_2}{\tau} = \frac{1}{\tau} \rho_1 \frac{C_{m1}}{C_{m2}} \chi(S_N) \quad (2.37)$$

where

$$\tau = \frac{2\sqrt{\pi} v}{C_{m2} A} \quad (2.38)$$

For low speed ratios ( $S < 2$ ) the function  $\chi(S_N)$  for the spinning rocket can be approximated by a Fourier series of the form

$$\chi(S_N) = k_1 + k_2 \cos \omega t + k_3 \cos 2\omega t \quad (2.39)$$

where  $\omega$  is the angular frequency of spin.

Using this expression for  $\chi(S_N)$ , the steady state solution for Eq. 2.37 is

$$\rho_2 = \rho_1 \frac{\sqrt{R_1 T_1}}{\sqrt{R_2 T_2}} \left[ k_1 + \frac{k_2}{\sqrt{1+\omega^2 \tau^2}} \cos(\omega t - \varphi_1) + \frac{k_3}{\sqrt{1+4\omega^2 \tau^2}} \cos(2\omega t - \varphi_2) \right] \quad (2.40)$$

where

$$\varphi_1 = \tan^{-1} \omega \tau \quad (2.41)$$

and

$$\varphi_2 = \tan^{-1} 2\omega \tau \quad (2.42)$$

Equation 2.40 shows that there is attenuation and distortion of the gauge density waveform over the ideal value which is a function of  $\omega \tau$  . The magnitude of this effect will be discussed further when the experimental data is reduced.

#### 2.2.4 Near-Free-Molecule Flow Corrections

The analysis in Sections 2.2.1 and 2.2.2 have been performed under the assumption that the gauges are in free molecular flow. This of course will depend on the relevant value of the Knudsen number at the altitude being considered. Reference 29 gives the following values of mean free path at the altitudes noted:

<u>Altitude (km)</u>	<u>Mean Free Path (cm)</u>
85.0	1.02
97.5	10.5
112.0	111.7

It is evident that the mean free path very quickly becomes large enough to consider that free molecular conditions exist around the gauges in the extended gauge package. For the gauge mounted farther back on the body of the rocket this condition will not be reached until a higher altitude is attained.

The package containing the pressure gauges is a complicated shape and makes a varying angle of attack with the free stream. As a result it is virtually impossible to make exact corrections for the transition flow regime. Enkenhus in Ref. 47 performed experiments with orifice probes in supersonic flows at Knudsen numbers in the near free molecule flow regime. An empirical relation was obtained which gave the variation of orifice probe impact pressure with Mach number and Knudsen number. Although Enkenhus' experiments were performed for cylindrical orifice probes placed perpendicular to the flow, and hence do not duplicate the flow about the rocket gauges exactly, there is enough similarity to permit an approximate correction to the gauge readings to be made. In Enkenhus' experiments the probe temperature was higher than the stream temperature, while in the rocket experiment the gauge temperatures were approximately equal to the stream temperature. As a result of the effect mentioned in Section 2.2, the corrections from Enkenhus' work may be too small if the Knudsen number is based on free stream conditions in each case. Fortunately, Enkenus' work shows that for Knudsen numbers greater than 2 the correction may be of the order of 10% or less depending on the Mach number and Knudsen number.

Since the mean free path increases so rapidly with increasing altitude, corrections to the measured gauge conditions need only be applied over a narrow altitude range. The necessary corrections will be discussed later when the data is reduced and computations of the mean free path and Knudsen number can be made.

#### 2.2.5 Relations Between Atmospheric Pressure, Density and Temperature

As a general rule rocket experiments do not measure atmospheric pressure, density, temperature and molecular weight during a single flight. One, or perhaps two of these parameters may be measured during a typical flight. Thus a means of relating the measured parameter to the others must be found. The two basic relations which permit an interrelation between the atmospheric parameters are the equation of state for an ideal gas and the hydrostatic equation for a fluid at rest (Ref. 1). The equation of state is simply Eq. 2.7.

$$p_1 = \rho_1 R_1 T_1 \quad (2.7)$$

The hydrostatic equation makes use of the fact that in an atmosphere at rest the pressure at a specific altitude is equal to the weight of the air in a vertical cylinder of unit cross section above that altitude. Thus,

$$dp_1 = \rho_1 g dz \quad , \quad (2.43)$$

where  $dp_1$  is the pressure change across the infinitesimal altitude change  $dz$ , and  $\rho_1$  and  $g$  are the density and acceleration of gravity at that altitude. In integral form the hydrostatic equation can be written as

$$p_1(z) = p_1(z_0) - \int_{z_0}^z \rho_1 g dz \quad , \quad (2.44)$$

where  $p_1(z)$  is the atmospheric pressure at some arbitrarily chosen altitude  $z$ , and  $p_1(z_0)$  is the pressure at an altitude  $z_0$  chosen at a reference altitude where the properties are known.

Combining the equation of state with either Eq. 2.43 or 2.44, the following relations between pressure, density, and temperature result:

$$p_1(z) = p_1(z_0) e^{-\int_{z_0}^z \frac{m_1 g}{RT_1} dz} \quad (2.45)$$

$$\rho_1(z) = \rho_1(z_0) \cdot \frac{T_1(z_0) m_1(z)}{T_1(z) m_1(z_0)} e^{-\int_{z_0}^z \frac{m_1 g}{RT_1} dz} \quad (2.46)$$

$$T_1(z) = \frac{\rho_1(z_0) m_1(z)}{\rho_1(z) m_1(z_0)} \left[ T_1(z_0) - \frac{m_1(z_0)}{\rho_1(z_0) R} \int_{z_0}^z \rho_1 g dz \right] \quad (2.47)$$

$$\frac{d(\ln p_1)}{dz} = -\frac{m_1 g}{R T_1} \quad (2.48)$$

The quantity  $RT_1/(m_1 g)$  has the dimensions of length and is defined as the scale height. Since it provides an indication of how rapidly  $p_1$  and  $\rho_1$  change as a function of altitude, the scale height is a fundamental parameter in upper atmosphere study.

Atmospheric pressure, temperature, and density have all been determined by different types of rocket experiments. If one of these quantities has been determined as a function of altitude then from Eqs. 2.45 to 2.48 the remaining two can be calculated, but only as functions of  $m_1$ . If two of the parameters can be determined then the relations between the quantities can be used to check the consistency of the measurements. Since the UTIAS rocket experiment permits two of the parameters to be measured, the equations will be used to ensure that the measurements are self-consistent.

### 3. DESCRIPTION OF THE ROCKET VEHICLE AND PAYLOAD

#### 3.1 Mechanical Configuration

In the UTIAS rocket experiment, the nose cone was meant to be more than just a covering for the payload, as it is in most other rocket experiments. It was required to perform as a high vacuum chamber, which meant that a number of modifications were necessary before it was suitable. The sections to follow describe the rocket itself, the design requirements for the nose cone and the changes which had to be made to fulfill them.

##### 3.1.1 Black Brant IIA Rocket

The Black Brant IIA rocket is a Canadian designed and built, high altitude sounding rocket. The single stage, solid propellant motor has a burning time of approximately 15 seconds and a peak acceleration of 15 g, which permits the vehicle to carry a payload of 200 pounds to an altitude of 500,000 feet. Of course, the actual peak altitude depends on the launcher elevation angle, the actual payload weight, and the fin design used on the rocket. Figure 7 provides the weights and dimensions of the vehicle components.

Although this rocket is normally fired with the fins set for a nominal spin rate of zero, the UTIAS experiment required a spin rate of the order of 1 cps or higher. This spin was necessary for both the measurement of upper atmosphere density and scale temperature, and also for the operation of the sun sensors. The 1 cps spin rate was found to be inadvisable due to anticipated aerodynamic instability problems. A nominal spin rate of 3 cps was finally recommended by the rocket manufacturer. A 4-fin configuration, with fins designed by Canadair Limited, was provided for the UTIAS rocket. Although these fins decreased the peak altitude, they were believed to provide better aerodynamic stability of the vehicle.

Figure 8 illustrates the payload space provided by the standard Black Brant II nose cone. With the exception of the steel cone for the tip, the forward cone, the aft cone, the cylindrical section, and the extension body, are all magnesium castings. This gives the basic nose cone a weight of approximately 130 pounds.

##### 3.1.2 Mechanical Design Considerations

The basic obstacle to a direct rocket measurement of upper atmosphere density above 100 km has been the presence of a relatively high density gas cloud surrounding the rocket and moving with it. For this reason the prime consideration in the mechanical design of the experiment has been an attempt to eliminate possible sources of such a contaminating gas cloud. The sources of contamination that could be controlled included outgassing within gauge volumes, outgassing of surfaces close to gauge orifices, and leakage of gas from pressurized compartments. However, it was considered that the extensive modifications required to prevent outgassing from the motor were too cumbersome to be attempted for this first experiment.

The elimination or reduction of outgassing of gauge volumes, and surfaces close to gauge orifices was achieved by sealing the high altitude gauges in the conical section of the nose cone, and then evacuating this compartment to as low a pressure as possible. This required the design of a system for opening

the nose cone at the desired altitude and exposing the gauges to the atmosphere. It was decided to separate and eject the forward section of the nose cone at station 30.0 (Fig. 8) to provide an opening through which the gauges could be projected. The four gauges, oriented with  $\beta$  values of 0, 45, 90 and 135 degrees, were enclosed in a stainless steel shell. This gauge package was mounted atop a set of spring-loaded, telescoping tubes which provided the force for pushing the nose cone away when it was separated, as well as extending the gauges forward through the opening. This system also required a friction brake to dissipate the energy in the spring and hold the gauge package in the extended position. Finally, a portable vacuum system was designed to evacuate the nose cone even while the rocket was on the launcher. Each part of the system is described in some detail in Section 3.2.

By evacuating the high altitude gauges in this way it was believed that the internal gauge surfaces as well as the gauge package surfaces could be outgassed sufficiently to allow the gauges to follow the atmospheric pressure changes with minimized outgassing problems.

Since only one rocket was being instrumented, an effort was made to duplicate untried equipment whenever possible. For example, two sun sensors were constructed even though only one was required to provide the necessary orientation information. In addition the high altitude gauge outputs were arranged in such a way that some quantitative information could still be obtained in the event that certain mechanical and electrical systems should fail to operate properly.

### 3.1.3 Nose Cone Sealing

Nose cone sealing was accomplished by using the same vacuum techniques which one employs in sealing laboratory high vacuum systems. O-rings were used in all instances since they were the most reliable, if they were properly installed. The seals on the nose cone were finally subjected to testing with a mass spectrometer, helium leak detector before they were acceptable. Since the final assembly at the rocket range could not be tested for leaks, it was important that the number of seals made on final assembly be kept to a minimum. In this way, many of the joints and holes could be sealed and tested in the laboratory without having to be taken apart again.

The nose cone, as received from the manufacturer, was not well suited for sealing to the required degree of leak-tightness. In normal use the nose cones were only required to maintain the pressure within them above a certain minimum value. This could generally be done by sealing holes with RTV silicone rubber. However, this degree of sealing was not acceptable for a high vacuum system, and hence O-ring seals had to be designed for each joint and hole in the nose cone sections.

For sealing purposes the nose cone was divided into three compartments. A bulkhead at station 86.0 (see Fig. 9) provided a compartment forward of this station which was required to be capable of evacuation to  $10^{-5}$  mm Hg. A second bulkhead at station 110.5 isolated the cylindrical section. This was to be maintained at ground level pressure since it contained the electronics for the experiment. The same requirements for leak tightness were demanded for this section as for the evacuated conical section. A short cylindrical extension body was the transition piece between the motor and the pressurized compartment. Holes in the outer surface of this section provided rapid escape of the air within as the ambient pressure decreased during the flight.

One of the first tests performed on the large aft cone section, which was to be evacuated, was a check for porosity or cracks in the casting. The castings had been painted by the manufacturer, and this was first stripped from the casting by chemical means. It was then thoroughly washed with water and rinsed with acetone. Steel plates were machined to cap the ends of the casting and all threaded holes were plugged with "Sealskrews". These are machine screws with O-rings under the heads manufactured by the AFM-Hexseal Corporation of Englewood, N.J. The casting was then mounted on a high vacuum pumping stand to determine the ultimate pressure which could be attained. With a pumping speed of approximately 20 litre/second it was found that an ultimate pressure of  $4 \times 10^{-6}$  mm Hg was possible after a week of pumping, if no attempt was made to accelerate the outgassing by heating the cone. By measuring the rate of pressure rise in the cone section when the pumping line was closed, the leak rate or internal outgassing rate was calculated to be  $6.8 \times 10^{-5}$  mm-litre/second. This corresponded to an effective surface outgassing rate of  $4.8 \times 10^{-9}$  mm-litre/sec/cm<sup>2</sup>, which was quite acceptable from the standpoint of rate of pressure rise in the sealed cone. The ultimate pressure obtained was an ideal value which could not be attained in practice because the nose cone was later filled with numerous other parts and wires which all increased the internal sources of outgassing.

The test demonstrated that the nose cone could be evacuated to a low pressure if O-ring seals were designed for the joints between sections and if the numerous screw holes in the casting could be sealed. More than 100 holes were eventually sealed using various types and sizes of "Sealskrews". In all cases Viton O-rings were employed since virtually all of the O-rings were in contact with the aerodynamically heated rocket skin.

### 3.2 Instrumentation

Figure 9 provides a schematic view of the layout of the various payload components within the nose cone. There was more involved in the design of the payload than just the rigid mounting of instruments within the nose cone. For the experiment to fulfill expectations a number of active mechanical systems had to operate properly. Considerable efforts were expended in the design and development of these systems to ensure their operation in a reliable manner. This section deals with the details of the instrumentation and the development of the necessary mechanical systems.

#### 3.2.1 Selection of Gauges

Since the experiment depended on the measurement of pressures and densities, the selection of the gauges was of primary importance. Since the rocket flight imposes some harsh environmental conditions on the instruments, the gauges were mainly selected for their ability to withstand the rocket environment. The environmental tests specified by the National Research Council as being adequate for equipment in the Black Brant II Rockets were the following:

- (1) Shock: A Shock of 25g in each of three mutually perpendicular axes for a duration of 10 milliseconds.
- (2) Acceleration: A 25g forward acceleration and 10g rearward acceleration for 1 minute each.

- (3) Vibration: A vibration amplitude of 0.06 inches peak-to-peak from 10 to 50 cps; and 10g maximum acceleration from 50 to 2000 cps on each of three mutually perpendicular axes, using a one hour cycling period and remaining 1 minute at each resonance.
- (4) Temperature : A temperature range of  $-20^{\circ}\text{C}$  to  $+75^{\circ}\text{C}$ .

In practice not all of the payload components were given the environmental tests listed above. In some cases test data was supplied by the manufacturer for his instruments. Only if there was some doubt that the component would not function in the expected environment was the appropriate test made.

From previous measurements of upper atmosphere properties (Ref. 29) it was known that the ambient pressure would vary from approximately 760 mm Hg to  $10^{-6}$  mm Hg. In order to cover this pressure range adequately, three types of pressure gauges were selected.

Preliminary rocket performance data supplied by Canadian Bristol Aerojet Ltd., provided the information for calculation of the stagnation and cone surface pressures to be expected. On the basis of these performance figures and the theory in Section 2.1, stagnation pressures from 0 to 8250 mm Hg and cone surface pressures from 0 to 930 mm Hg. were anticipated.

The high pressure range, starting at ground level, was covered by strain gauge pressure transducers supplied by the Fairchild Controls Corporation, Hicksville, N.Y. In this type of transducer, diaphragm deflection from the applied pressure produces strain in a semiconductor bridge causing a linear voltage unbalance at the bridge output. The full scale output of the transducer was 250 millivolts. A supply regulation module built into the transducer allowed operation from unregulated supplies with variation from 26 to 32 volts D.C.

The medium pressure range from 20 mm to 0.1 mm Hg was covered by subminiature thermocouple gauges manufactured by Hastings-Raydist Inc., Hampton, Virginia. This type of gauge operates on the principle that at low pressure, the equilibrium temperature of a heated wire depends on the pressure, since the heat transfer from the wire depends on the pressure. A power supply provided a regulated heating current for the gauge elements. This power supply could be operated from an unregulated 28 volt D.C. supply. The gauge output varied between 1.5 millivolts at atmospheric pressure and 10 millivolts at high vacuum. These outputs could be changed slightly by making adjustments in the gauge heating current.

The manufacturers supplied environmental specifications for both the strain gauge pressure transducers and the thermocouple gauges. However, mechanical test data for vacuum gauges suitable for measuring in the range  $10^{-3}$  to  $10^{-6}$  mm Hg was not available from the manufacturers of these gauges. Three commercial gauges were selected for testing to the vibrational specifications. These were a Balzers UMR1, an Edwards High Vacuum Ltd. IG-2HB, and a Consolidated Vacuum Corporation GFH-001.

The first two gauges named have a triode electrode structure consisting of a heated cathode surrounded by a wire grid, which is in turn surrounded by a collector (Fig. 10). In the hot cathode gauges, electrons

emitted from a hot tungsten filament are accelerated toward the positive wire grid. Some of the electrons are accelerated into the space between the grid and the negative collector where they may collide with the gas molecules to produce positive ions. If the electrode potentials and the grid current are kept constant, the positive ion current drawn by the collector will be proportional to pressure, below  $10^{-3}$  mm Hg. This type of gauge is generally considered to be an accurate continuous indicator of pressure below  $10^{-3}$  mm Hg (Ref. 48).

The third gauge has a diode structure which relies on the measurement of the ion current produced by a high voltage glow discharge (Fig. 10). The electrons emanating from the cathode, which is the body of the gauge tube, are caused to spiral as they move across a magnetic field to the anode. This spiral action increases the possibility of collisions with the gas molecules present and produces more sensitivity by increasing the number of positive ions formed. The magnetic field also sustains the discharge at low pressures where the electron mean free path greatly exceeds the distance between the electrodes. In using this gauge, one must be careful not to contaminate the internal surfaces since they form the gauge cathode.

The vibration tests on the three gauges were performed according to the specifications using facilities provided by the Canadian General Electric Company. Each gauge was encapsulated for support in a 4 inch cube of epoxy casting compound. This mounting block also provided a means of orienting the gauge on the shaker table. Figure 11 shows the Balzers and the CVC gauges mounted in their blocks and the type of failure which occurred in each case.

The results of the tests were as follows:

(1) Balzers UMR1:

The supports for the grid, collector and filament failed, making the gauge completely inoperative. If the electrode structure had been supported this complete failure would probably not have occurred. The failure probably was the result of resonance in the electrodes.

(2) Edwards IG-2HB:

This gauge had a glass envelope and the collector and grid received some support from the glass enclosure. Although the grid and collector remained intact, the tungsten filament cathode was found to be broken. Both of the triode type ionization gauges failed before the testing along one axis had been completed.

In each case the testing axis along which failure occurred was perpendicular to the longitudinal axis of the gauge structure.

(3) Consolidated Vacuum Corporation GPH-001:

This gauge fared better in the test than the other two because of its more rugged construction. It survived the vibration test along one axis perpendicular to the gauge tube axis but the anode broke during the test along the second axis perpendicular to the gauge tube axis. A soft-solder joint on the anode was the cause of failure, but it was believed that this joint could easily be strengthened to solve the problem.

Since both of the hot cathode ionization gauges had failed in a way which would have made them completely inoperative, it was decided to use the cold cathode gauge because of its inherently more rugged construction. This type of gauge has the advantage of having a higher current output at the same pressure, and also it requires only a single high voltage power supply for its operation. While its current vs pressure characteristic is essentially linear at low pressure, it becomes non-linear above  $3 \times 10^{-4}$  mm Hg with a resultant loss in sensitivity. If the gauge surfaces are not contaminated by exposure to hydrocarbons in the vacuum system, adequate reproducibility of the calibration results. Some of the gauges exhibited two stable modes of operation for the glow discharge with sudden jumps from one mode to the other depending on the pressure. This operation was believed to be due to small changes in the internal magnetic field caused by the magnetic shields installed around the gauge magnets. More will be said about the two mode operation in Section 5 when gauge calibration is discussed.

### 3.2.2 Stagnation and Cone Surface Pressure Transducers

The transducers for measuring stagnation and cone surface pressures were located in the tip section of the cone which was to be separated and ejected. Two problems arose in connection with the high and medium pressure transducers. Since the skin temperature in this section had been found to exceed  $200^{\circ}\text{C}$  insulating the transducers was necessary. In addition, the passage between the gauge volume and the pressure orifice had to be large enough to provide adequate time response.

#### a) Mounting of Transducers:

Figure 12 illustrates the location and mounting method employed with the thermocouple and strain gauge transducers. A single thermocouple and strain gauge transducer were connected to a common pressure manifold for each of the stagnation and cone surface pressure measurements. Figure 13 indicates the size and the interconnection of the two transducers. Thin wall stainless steel tubing formed the connecting passage between the gauge volume and the opening in the nose cone surface. Little heat could be transferred to the gauges through the tubing. The stagnation pressure gauges were positioned in the tip section and then Dow Corning RTV-601 silicone rubber was poured around them, filling the space between the gauges and the inner wall. The liquid rubber was vacuum de-aired both before and after pouring to remove gas mixed into the rubber. After the rubber had hardened the gauges were held firmly in position. The use of mold release on the internal surfaces of the nose cone and the gauges meant that the gauges could be removed from the rubber, and the cast rubber plug could be removed from the nose cone. This  $\frac{1}{2}$  inch thickness of rubber provided sufficient thermal protection during the short time between lift off or the rocket and ejection of the tip section. The rubber plug was held in place by a circular shelf fastened to the nose cone.

The surface pressure transducers were mounted in a similar manner on a circular shelf within the tip section (Fig. 14). The gauges were positioned in a cylindrical shell with a  $\frac{1}{4}$  inch thickness of silicone rubber cast around them for mechanical support and thermal protection.

Both of the cast rubber plugs were removed from the nose cone, and preconditioned to the high temperatures anticipated by baking for several hours at 500°F. In this way any volatile material remaining within the rubber would be driven off and not hamper future evacuation of the nose cone.

#### b) Time Response of Gauge Tubulations

The second consideration in the design of the impact and surface pressure measuring systems was the response time of the tubing leading to the transducers. Since the placement of the gauges was dictated by the space available, the length of the tubulation was fixed but the diameter could be varied to find an acceptable response time. Figure 12 illustrates the configuration of the impact and surface pressure orifices and the dimensions of the tubing leading to the gauge volumes. References 49, 50 and 51 provide a theoretical and experimental study of time response in pressure measuring systems which was used in the analysis of the experimental configuration.

The flow in the pressure measuring capillary is assumed to be laminar. In the practical case of the changing pressure in a measuring system, this is generally true, since the capillary walls are smooth and the flow velocities are low enough to prevent transition to a turbulent flow. For pressures above approximately 5 mm Hg (at which rarefied gas effects begin to appear) an analysis of the system based on the assumption of Poiseuille flow permits the time response to be calculated. Reference 50 derives the following expression for the time constant of a system at pressures where a Poiseuille flow analysis is valid.

$$\tau = \frac{256 \mu L_1 (V_m + \frac{1}{2} V_1)}{d_1^4 p_f} \quad (3.1)$$

where  $\mu$  = viscosity of the air in the system  
 $L_1$  = length of the tube  
 $V_m$  = gauge volume  
 $V_1$  = volume of the tube  
 $d_1$  = diameter of the tube  
 $p_f$  = final or steady state pressure.

The percentage error in any measurement falls to  $\frac{1}{2}\%$  after time  $3\tau$  has elapsed.

The time constants for the impact and surface pressure probes were evaluated at standard atmospheric pressure using Equation 3.1.

a) Impact pressure probe response:

The gauge dimensions provide the following parameters for use in Eq. 3.1:

$$\begin{aligned}L_1 &= 15 \text{ in.} \\d_1 &= 0.150 \text{ in.} \\V_m &= 0.065 \text{ in}^3. \\ \frac{1}{2}V_1 &= 0.1325 \text{ in}^3. \\p_f &= 2116 \text{ lbs/ft}^2 \\ \mu &= 4.7 \times 10^{-7} \text{ slug/ft-sec at } 212^\circ\text{F}\end{aligned}$$

With these values,  $\tau$  is  $1.06 \times 10^{-4}$  seconds which certainly provides adequate time response at high pressures.

b) Surface pressure probe response:

In this case the gauge dimensions are the following:

$$\begin{aligned}L_1 &= 3.0 \text{ in.} \\d_1 &= 0.085 \text{ in.} \\V_m &= 0.035 \text{ in}^3. \\ \frac{1}{2}V_1 &= 0.0085 \text{ in}^3.\end{aligned}$$

Using the same values of  $p_f$  and  $\mu$ ,  $\tau$  has a value of  $4.54 \times 10^{-5}$  seconds. At the surface of the nose cone the surface pressure capillary ends in an 0.040 inch diameter hole. However, Ref. 51 concludes that an orifice has little effect on the response time when its diameter is greater than  $\frac{1}{4}$  of the diameter of the capillary to which it is attached.

As the value of  $p_f$  decreases, the response time correspondingly increases. Davis (Ref. 49) derives an expression for the time constant which takes into account rarefied gas effects. According to this theory the ratio of the time constant at low pressure to the value at atmospheric pressure is given by

$$\frac{\tau}{\tau_0} = \frac{2116 r}{p_m r + .00278} \quad (3.2)$$

where  $\tau$  = time constant at low pressures

$\tau_0$  = time constant at atmospheric pressure

$p_m$  = mean pressure in the capillary (lbs/ft<sup>2</sup>)

$r$  = radius of the capillary (ft).

The minimum pressures measured by the impact and surface pressure gauges were 1.25 mm Hg and 0.06 mm Hg respectively. Using Eq. 3.2, the time constants corresponding to these pressures are 0.0571 seconds and 0.101 seconds respectively. At an altitude of 240,000 feet where these pressures were measured, the rocket velocity was 4100 feet per second. In a time of 0.3 seconds or 3 times the maximum value of  $\tau$  the rocket has moved 1230 feet vertically. The ambient pressure change over this altitude interval is only 6% (Ref. 29).

Thus in the very worst case the error in the gauge pressure due to time lag in the system would be 6%.

### 3.2.3 Mounting of the Cold Cathode Ionization Gauges

#### a) Gauge Package

The gauge package design was dictated by the requirement of having cleaned, outgassed surfaces close to the gauge orifices. Since attachment points for the separation mechanism (to be described in Section 3.2.4) were located close to the upper end of the aft cone, the opening through which the gauges could be projected was restricted. The size and shape of the opening dictated the configuration of the gauge package shown in Fig. 15.

The gauge tubes were shortened to an overall length of 5 inches to enable them to fit within the space available for the gauge package. Reducing the length also reduced the gauge volume and hence improved the time response for the gauge. The design values of  $v$ ,  $A$  and  $C_{m2}$  were the following:

$$v = 1.50 \text{ in}^3.$$

$$A = 0.1255 \text{ in}^2.$$

$$C_{m2} = 1360 \text{ ft/sec (corresponding to } T_2 = 80^\circ\text{F)}.$$

With these values in Eq. 2.38 the time constant for the system is  $2.6 \times 10^{-3}$  seconds. If the nominal spin rate for the rocket is 3 cps, then the signal attenuation factor  $1/\sqrt{1+(\omega\tau)^2}$  is 0.9988.

Teflon insulated coaxial cable carried the high voltage to the gauge anode. The surface of the Teflon insulation was treated with a solution produced by Chemplast Inc., East Newark, N.J., which permitted epoxy adhesives to adhere to it. After soldering the centre conductor to the gauge anode, a coating of epoxy resin (Emerson and Cummings, Stycast 1264) was put on the anode to provide electrical insulation. In addition the anode was strengthened with the same epoxy at the joint which the vibration tests had demonstrated to be weak. In order to measure the gauge volume temperature, bead thermistors were cemented to the steel barrel of each gauge tube. It was necessary to shield the gauge magnets to prevent interference with the magnetometers by enclosing them in thin-wall mild steel containers. These completely enclosed the magnet but had openings for the ends of the gauge tube to protrude. This was found to be sufficient to reduce the flux leakage outside the shields to a level which was undetectable by the magnetometers when the gauge package was in its extended position. Figure 16 illustrates the details of the final gauge configuration.

After all electrical connections to the gauges had been made, they were fitted into the stainless steel mountings which formed the ends of the gauge package. These pieces had the gauge orifices machined into them, and they determined the angular orientation of the gauges with respect to the rocket axis (Fig. 17). Leakage from the interior of the gauge package into the gauge volume was prevented by an O-ring seal between the barrel of the gauge tube and the steel mounting plates. The shell of the gauge package was formed from 0.025 inch thick stainless steel sheet. This shell was

welded to the steel gauge mountings. The completed assembly was tested with a helium leak detector to ensure that each gauge volume was free from leakage from within the gauge package. The interior of the package was then filled with Dow Corning Silastic RTV-601 in order to provide mechanical support and electrical insulation for the gauges. The silicone rubber was poured into the package in 3 layers with approximately 24 hours being allowed for hardening before the next layer was poured. By working at temperatures of 45°F, the viscosity of the rubber remained low enough to allow complete vacuum de-airing of the rubber after it was poured into the gauge package. After this had been completed, the gauges were given a final test with the leak detector.

The method of "potting" the gauges within the gauge package was found to be of prime importance. It was necessary to completely rebuild the gauge package after it was constructed for the first time when it was found that a high voltage breakdown occurred inside the package after it had been under high vacuum for approximately 3 days. When the first gauge package was constructed, the electrical connection at the anode was not given an insulating layer of epoxy. A different type of silicone rubber was poured into the package at one pouring, and as a result, it was difficult to properly de-air the liquid rubber before it hardened. It was intended that the rubber alone would provide the high voltage insulation. When the high voltage breakdown occurred and the package was dismantled, many gas bubbles were found in the rubber. In the second, and successful design, the epoxy coating provided the necessary high voltage insulation and any electrical insulation supplied by the silicone rubber merely provided a larger margin of safety.

#### b) Outgassing Comparison Gauge

As a check on how effective the outgassing reduction measures had been, a fifth ionization gauge was located in the cylindrical section. The gauge was fitted into a mounting, which was then fastened to the inner wall of the cylindrical section. Figures 18a, and b give details of the construction and sealing method. The orifice into the gauge volume was of the same dimensions as for the gauge package.

#### 3.2.4 Separation Mechanism

In order to allow the package containing the vacuum gauges to be exposed to the atmosphere at high altitude, a method of removing the tip section of the nose cone forward of station 30.0 (see Fig. 9) had to be devised. A system was designed which employed four ball-and-race quick-release fasteners (Fig. 19). In its use in the rocket, the races were fastened to a collar in the aft cone close to Station 30 and the ball guides were fitted into the separation mechanism, which was fastened to the cone section to be separated. The four fasteners were released simultaneously by depressing the plungers with a rotating cam, driven by four bellows actuators (hercules Powder Company, Type BA31K2). These actuators provided a powerful linear stroke and also kept the combustion products sealed within themselves. Circular guides in the cam and the actuator supports translated the essentially linear motion of the bellows actuators into a rotary motion of the cam. Figures 20a,b and c illustrate the parts of the system and the mounting in the nose cone. In order to prevent the cam from rotating too far and possibly causing the ball-and-race fasteners to lock again, the cam motion was stopped,

with the plungers depressed, by projecting scoops which gouged into diametrically situated Teflon blocks. Ease of rotation for the cam was assured by the use of a ball bearing on the central shaft and a circular Teflon pad beneath the cam. Construction of the separation mechanism parts was mainly from aluminum since it closely matched the expansion of the magnesium cone but had a higher thermal heat capacity. It was expected that the mass of aluminum used would provide a sufficiently large heat sink to prevent the temperature of the separation mechanism and the bellows actuators from reaching an unacceptable level. Stainless steel was used for the central shaft for the cam, and hardened tool steel was used for the fasteners and the ramps fitted to the cam.

Considerable effort was expended before the ball and race fasteners were made to release reliably under tensile loads. Tests were performed on a number of designs and materials before the proper combination was discovered. For test purposes the quick-release fasteners were mounted in a fixture in the UTIAS tensile testing machine. This fixture made possible the release of the fastener in the same way that the cam would release it in the separation mechanism. The release force normal to the plunger was measured by adding weights to the test rig until the plunger was depressed (Fig. 21). The four fasteners finally made for the separation mechanism were each tested under a tensile load of 500 pounds, and gave release forces varying from 10 to 18 pounds. This was considered to be adequate since a single bellows actuator was able to drive the cam in the system tests which were performed later.

The tests showed that the hardness and surface finish of the plunger were very important. Atlas Keewatin steel was finally used for the plunger. The surface on which the ball bearings would slide was case hardened and all sliding surfaces were highly polished. Both the race and the ball guide were constructed from Atlas Nutherm steel. After hardening, the race was still soft enough for the ball bearings to leave an impression when the fastener was under load. It was found that the radius of the channel cut into the inner surface of the race was quite an important factor in determining the release force.

It was realized that differences in thermal expansion of the various components could subject the fasteners to bending as well as tensile loads. Provision for this was made by tapering the ball guide by 1 degree to enable it to pivot slightly in the race. Release forces were measured for combined bending and tensile loads and found to be not significantly different from those for tensile loads alone.

The action of the cam and fasteners after the bellows actuators were fired was observed with a high framing rate Fastex camera. With framing rates of the order of 3000 frames per second it was possible to observe the cam motion, the depression of the plungers and the stopping of the cam motion with the plungers depressed. The complete sequence required only approximately 10 milliseconds.

### 3.2.5 Extension and Braking System

The purpose of this system was to provide a means of pushing the separated nose cone free of the rocket, extending the gauge package forward through the opening, and then stopping the extension stroke after a suitable length of stroke. Figures 22a, and b give details of the various components. The extension system consists of two telescoping aluminum tubes, the outer one fixed to the aft cone and the inner one sliding on two Teflon bushings. A beryllium copper coil spring, with one end fixed to the base of the outer tube and the other end fixed in the inner tube, provided the thrust to push off the nose cone and extend the gauges. The force exerted by the fully compressed spring was approximately 650 pounds. A large spring force was chosen to push the cone apart since it was considered possible that differential thermal expansion might cause some of the parts to bind. Later high temperature tests allayed these fears.

The braking system (Fig. 23) consisted of an aluminum plate pivoted at one end. The inner tube slid through a hole cut into this plate. Two nylon pads fitted to the inner edge of the hole pressed against the sliding inner tube. These pads provided the friction which dissipated the energy of the spring and held the gauge package in an extended position. An adjustable spring which depressed one end of the aluminum plate allowed the friction force to be varied to yield optimum extension.

The circular plate on which the braking system was constructed provided lateral support for the tubes. A Viton O-ring around the outer edge of the plate cushioned the plate against the inner surface of the nose cone. A short cylindrical section was machined into the inner surface of the cone on which the O-ring could seat and also to centre the tubes in the nose cone. This arrangement provided lateral support for the tubes but permitted them to float in the longitudinal direction as the nose cone expanded during the flight.

Appendix A provides an analysis of the motion of the gauge package and the ejected nose cone when the separation mechanism is activated. The analysis indicates that there is a relation between the amount of spring compression and the braking force which will permit the gauge package to be stopped and held at the peak of its extension stroke. This relation as given by Eq. A.12 is

$$\frac{2F}{k} = \sqrt{\frac{m}{M}} \cdot \sqrt{(d-a)^2 - (a-a_1)^2}$$

where  $F$  = braking friction force  
 $k$  = spring constant of the spring in the extension system  
 $m$  = mass of the moving parts which remain with the rocket  
 $M$  = mass of the ejected tip section plus  $m$   
 $d$  = initial compression of the spring from its neutral position with no external forces acting on it  
 $a = (Mg + F)/k$

and  $a_1 = (mg + F)/k$  .

Once the relation between  $d$  and  $F$  has been determined for the actual values of  $k$ ,  $m$ , and  $M$ , then from Eq. A.10 the length of the compression plus extension stroke can be calculated. This is given by

$$d - a_1 + \sqrt{\frac{m}{M}} \cdot \sqrt{(d-a)^2 - (a-a_1)^2} \quad (3.3)$$

One can then select the value of  $d$  which gives a compression plus extension stroke which is safely below the maximum stroke of 33.4 inches, which is determined by the position of the Teflon bushings.

### 3.2.6 Testing of the Separation, Extension, and Braking Systems

The best way to verify the reliability and operation of the mechanical systems was to test them under the same conditions that they would experience in the rocket. For this purpose, a mock-up of the nose cone was constructed and the parts fitted into it as they would be in the actual nose cone.

This mock-up consisted of an aluminum angle frame, topped by an aluminum casting machined to the internal dimensions of the nose cone (Figs. 24a, b). The tip section of the cone was simulated by using an aluminum casting at the base of the cone, a steel tip, and a wooden section between the two. This combination produced the proper weight and centre of gravity. The aluminum casting was machined to permit the separation mechanism to be fitted into it. In addition, a mock-up of the gauge package, constructed from wood and weighted with lead, was mounted on the tubes of the extension system.

Initial tests were performed on the extension system using a steel coil spring which had a spring constant of 23.5 pounds per inch and which permitted a total compression of 21 inches. It was intended that this spring would provide the data concerning the friction force applied by the braking system, which could then be used to determine the specifications for the spring to be used in the rocket. The tests performed to determine the friction force were done without the tip section in place. The gauge package was compressed in the test frame and then allowed to be extended forward by the force of the spring. By measuring the length of the initial compression and the subsequent position of maximum extension, it was possible to calculate an effective braking force for the system. Equation A.2 gives the magnitude of the compression plus extension as

$$2(d-a) = 2\left(d - \frac{M_g \cdot g + F}{k}\right) \quad , \quad (3.4)$$

where  $M_g$  is the effective mass of the moving parts in the test frame (i.e., the mock-up of the gauge package, the tube, and the extension spring). The remaining symbols are defined in Appendix A. With tests of this type it was possible to determine the variation of  $F$  as the strength of the adjustable spring in the braking system was varied.

In order to determine the effect of vacuum conditions on the braking friction, the test frame was mounted horizontally in the UTIAS low density wind tunnel. The gauge package was compressed in the test frame and held in position by a cable which was held at one end with a ball-and-race fastener. To extend the gauge package, the fastener was released by depressing the plunger with a bellows actuator which was controlled from outside the tunnel. With the tunnel pressure at  $3 \times 10^{-4}$  mm Hg, the calculated friction

force was 20% higher than previously measured at atmospheric pressure. This amount of variation was not considered to be significant since the tests at atmospheric pressure had shown variations of this order.

With the separation mechanism mounted in the cone mock-up, and the extension and braking systems mounted in the test frame, a series of test firings were conducted to verify the reliability of the complete system. In general only one bellows actuator was used in the separation mechanism, rather than the four which could have been installed. In order to observe the action at the instant of separation and the subsequent motion of the cone, all tests were photographed with a Fastex camera at framing rates of approximately 3000 frames per second. It was observed that the gauge package always pushed the tip cone straight up, with no observed tendency for it to tip sideways. Since the rocket would be spinning in flight, this condition was also simulated for one test. The frame was mounted on a turntable spinning at  $2\frac{1}{2}$  cycles per second and the separation mechanism was fired. Under these conditions the operation of the complete system was not noticeably different from the case with no spin.

On the basis of the information obtained from the preliminary tests with the steel spring, a new beryllium copper spring was installed in the extension system. Since the magnetometers were mounted on the outer tube of the extension system close to the spring it was necessary to select this non-magnetic material for the spring. Increases in the expected weight of parts such as the gauge package and tip cone necessitated making some increase in the strength of the spring. The specifications for this final spring were as follows

Free length	57.38 in.
Possible compression	25.50 in.
Wire diameter	0.315 in.
Outside diameter	1.846 in.
Spring constant	27.9 lb/in.

100 turns with 5 close wound turns at each end.

A nominal spring constant of 25 lb/in. had been specified, as for the steel test spring, but the actual measured value was 27.9 lb/in. The purpose of the close wound turns at each end was to permit the spring to be threaded onto a machined plug, which could then be fastened in the telescoping tubes.

The parts were again assembled in the test frame to allow the friction force to be adjusted with the spring in the braking system. When this had been set at a value as close as possible to that indicated by Eq. A.12 the parts were then installed in the nose cone. Figures 25a, and b illustrate a typical test of the completed system, although the mock-up of the tip cone was still used for these experiments to prevent possible damage to the actual tip section. If the friction force had been set at the optimum value of 173 pounds, then the spring compression of 24.5 inches should have produced a compression plus extension stroke of 30.5 inches. The test illustrated in Fig. 25b indicates that the length was 29 inches which shows satisfactory agreement. Under the free fall conditions experienced during the flight, the length of the stroke should have been lengthened by approximately 1 inch. This experimental value of the length of the extension stroke was close to the limit of 33.4 inches determined by the length of the telescoping tubes. In all, three tests of the complete system were performed successfully in this configuration.

Since the nose cone would become heated during the flight, this condition was simulated by wrapping the nose cone near the separation joint with electrical heating tapes. Three tests were performed at temperatures of up to 300°F. These pointed out some potential problem areas in the separation system which had to be corrected to ensure reliable operation. Teflon caps were originally used on the plungers for the ball-and-race fasteners (Fig. 19). While these were suitable at room temperature, they seemed to soften at high temperature and become deformed when subjected to the action of the ramps on the cam. Since this prevented the fasteners from releasing properly, the Teflon caps were replaced by caps made from hardened tool steel. This softening of the Teflon also resulted in larger blocks of Teflon being used to stop the rotation of the cam at the proper position.

When the necessary changes had been made, the separation mechanism was fitted into the forward section of the actual nose cone.

### 3.2.7 Cable Holder

A certain amount of slack had to be left in the electrical cables from the ionization gauges to allow for the gauge package extension. This excess cable was laced into a single bundle, and then tied with thread to a sheet aluminum frame. The cable was thus secured during the powered portion of the flight, but was free to tear loose when the gauge package was extended (Fig. 26). Event oscillators in the telemetry link were employed to tell whether the extension had actually taken place. If the input to the event oscillator was short circuited, a continuous signal was relayed by the telemetry. This short circuit was provided by lengths of 36 gauge magnet wire tied to the laced cable at three points. When the gauge package was extended, the wires would be broken, causing the output from the three event oscillators to fall to zero.

### 3.2.8 Pumping System

Since evacuation of the nose cone was required before the launching, a high vacuum pumping system was designed. The system was intended to provide pumping for the nose cone in the preparation area, while the nose cone was transported to the launcher, and also after the rocket was mounted on the launcher. This pumping action had to continue until 90 seconds before launch, at which time, the nose cone was sealed and the vacuum system detached from the rocket. Figures 27a and 27b provide details of the pumping system.

The diffusion pump used was an Edwards air cooled pump with a rated pumping speed of 150 litres per second. To reduce backstreaming of oil vapour, the diffusion pump was topped by a baffle valve cooled by thermoelectric cooling modules. Three D.C. power supplies rated at 3 volts D.C. and 20 amperes provided the power for the thermoelectric cooling units. The vacuum line to the nose cone consisted of a 3 foot length of stainless steel flexible hose with an inside diameter of  $3\frac{1}{2}$  inches. An adaptor chamber was sealed against the outer surface of the nose cone around the pumping hole in the cone surface. The flexible hose was sealed to the chamber on one end, and a curved O-ring seal on the other end was sealed against the nose cone. Atmospheric pressure forces were not sufficient to keep the pumping line sealed to the nose cone. A nylon strap with turnbuckles on the ends allowed the adaptor chamber to be secured to the nose cone to prevent it from jarring

loose and causing leaks. This nylon strap was held together at one point with one of the ball-and-race fasteners designed for the separation system. A single bellows actuator caused the release of the fastener when the release of the pumping system from the nose cone was required (Fig. 28).

Ninety seconds before the rocket was launched, the pumping hole in the nose cone was to be sealed to allow the pumping system to be released. In order to achieve this, a valve was designed which was operated by a bellows actuator (Figs. 29a,b, and c). A modified ball and race device was used to keep a spring-loaded cover plate extended in front of the pumping hole. When the actuator was fired the cover plate was retracted and sealed the pumping hole flush with the nose cone surface.

It was found that the pressure in the nose cone could be reduced to almost  $10^{-5}$  mm Hg after pumping for a week. No attempt was made to accelerate the outgassing by moderate heating of the nose cone. This pressure level was considered to be satisfactory for the experiment. The nose cone pumped down very slowly because of the long lengths of stranded wire inside the cone. More than 200 feet of teflon insulated stranded wire and 60 feet of teflon insulated coaxial cable contributed to the outgassing.

The thermoelectrically cooled baffle valve performed very well. With a cooling air temperature of  $75^{\circ}\text{F}$  for the heat exchanger, the interior surface temperature of the valve was  $5^{\circ}\text{F}$ .

For use in the nose cone preparation area, an auxiliary mechanical backing pump and air blowers for the diffusion pump and thermoelectric baffle valve were provided. This equipment was also used while the nose cone was transported from the preparation area to the launcher building.

In the launcher room, a second mechanical pump was located. Here, a pre-evacuated backing manifold was installed. This consisted of two 40 foot lengths of  $3/4$  inch and  $1\frac{1}{4}$  inch inside diameter PVC plastic pipe. The end of the pipe was capped with a valve, and it was kept evacuated for a day before the launch. During the arming of the rocket all power had to be turned off. This meant installing manual or solenoid operated valves in the pumping line at a number of places. Figure 30 is a schematic drawing of the pumping system for the rocket mounted on the launcher. Figure 31 shows the actual equipment during the launch operation.

A solenoid actuated, air admittance valve allowed air to be let into the pumping line after the nose cone valve was shut. This removed the pressure forces which tended to keep the pumping system attached to the rocket. The sequence of operations just before launch was as follows:

- 1) Close valve inside nose cone.
- 2) Open the air admittance valve and release the nylon strap holding the pumping system.

### 3.2.9 Sun Sensors

Two sun sensors were constructed and mounted in the extension body (see Figs. 41b,d) to measure the angle between the sun's direction and the rocket spin axis. Although these were both of similar construction, one had a nominal angular field of view of 130 degrees and the other had a field of view of 90 degrees. Specification of the angular field of view of the sensors was made on the basis of angular orientation information from other flights. If the rocket motion was unstable then a large acceptance angle would be necessary to permit the sensor to view the sun; if the motion was stable then the narrow angle sensor would be adequate and would also have better sensitivity. These sensors were similar to those previously used by NASA for orientation information of spinning vehicles.

Figure 32 illustrates the principle behind the construction and operation of the sun sensor. Six narrow slits form 3 planes oriented as shown. The plane formed by slits 1 and 2 passes through the rocket spin axis. The planes formed by the other slits both make an angle  $\Gamma$  with the first plane. The acceptance angle of the sensor is governed by the angle  $\Gamma$ . Light sensors are placed behind the back set of slits at A, B, and C. On a spinning rocket the sun's direction will lie in each plane at different times and hence light pulses will be received by the light sensors at different instants. For the sensor positions shown, sensor B would receive light only when  $\theta$  was positive, sensor C only when  $\theta$  was negative, but sensor A would receive light for the full range of angles. For a given value of  $\Gamma$ , the angle  $\theta$  can be calculated in terms of the time difference between the pulse outputs of the light sensors. In the analysis it may be assumed that the angle  $\theta$  does not change appreciably while the rocket rotates through 360 degrees and also that the spin rate is essentially constant. If the time difference between pulses is  $\Delta t$  and the angular frequency of rocket spin is  $\omega$ , then the angle through which the rocket must rotate between the time the central slit views the sun and the time an angled slit views the sun is given by

$$\varphi = \omega \Delta t \quad (3.5)$$

The relationship between  $\theta$  and  $\varphi$  can be shown to be

$$\varphi = \tan^{-1} \frac{\sin \theta \tan \Gamma}{(\cos^2 \theta - \sin^2 \theta \tan^2 \Gamma)^{1/2}} \quad (3.6)$$

For small values of  $\theta$

$$\frac{d\varphi}{d\theta} \approx \tan \Gamma \quad (3.7)$$

This gives an indication of the sensitivity of the two sensors for small values of  $\theta$ . For the values of  $\Gamma$  used the sensitivity is

$$\left[ \frac{d\varphi}{d\theta} \right]_{\Gamma=25^\circ} \approx 0.466$$

and

$$\left[ \frac{d\varphi}{d\theta} \right]_{\Gamma=45^\circ} \approx 1.000$$

This means that the sensor with  $\Gamma = 45^\circ$  will have approximately twice the sensitivity of the other sensor. Figure 33 plots the theoretical relation between  $\theta$  and  $\phi$  for  $\Gamma = 25$  and  $45$  degrees.

Figures 34 and 35 show the type of construction which was used for both sun sensors. The body of the sensor was machined from a magnesium block to minimize any problem of differential thermal expansion between it and the magnesium extension body. To this block were fastened the plates which formed the slits on the surface of the rocket, and also on the back of the mounting block. These slit plates were constructed from 0.078 inch thick stainless steel sheet, with sharply ground edges forming the slits. This gave a uniform slit width with little chance of damage from normal handling. By making the mounting block tent shaped, it was possible to achieve a more compact design with the same resolution that would have been obtained with a larger flat-topped block. In order to reduce internal reflection, the magnesium mounting block was given an alkaline dichromate treatment which produced a dull black surface coating (Ref. 52).

In order to resolve the pulses at small values of  $\theta$ , it was desirable to design the slits in such a way that the pulse obtained would be as narrow as possible. Since the sun itself subtends an angle of  $\frac{1}{2}$  degree of arc, a pulse width of 1 degree was chosen as a practical limit. This means that the slit width must be quite narrow. A slit width of 0.010 inches was selected to provide enough light for the light sensors, and a reasonably small sun sensor.

The extension body was accurately machined with cutouts to receive the sun mounting blocks. This allowed the sensors to be placed to within  $\frac{1}{4}$  degree of their calculated angular positions. Fairings fore and aft removed the sharp corners projecting into the flow. Figures 41b and f illustrate the mounting in the extension body.

Type 1N2175 photo-diodes were used to respond to the light pulses. These photo-diodes have a very directional response to light, their sensitivity being reduced by a factor of 2 if the light direction is 20 degrees off the sensor axis. This necessitated using more than one photo-diode to cover the full acceptance angle of each set of slits.

The photo-diodes were mounted in a magnesium block in holes which had been drilled at the proper angle to allow each photo-diode to cover part of the total acceptance angle of the sensor slits. The diodes were held in place by a clear epoxy resin which provided electrical and thermal insulation (Fig. 36). Since it was expected that the slit block would become heated during the flight, care was taken to minimize the heat transfer to the photo-diode mounting block by leaving a narrow space between the two parts and keeping the number of contact points to a minimum.

The theoretical calibration for the sun sensors was verified by mounting the extension body, with the sun sensors in place, on an outdoor turntable. It was found that the turntable could be levelled to within  $\frac{1}{2}$  degree even while rotating. Knowing the latitude, longitude, and the time, the sun's elevation could be accurately calculated. By measuring the rotational speed of the turntable and the time difference between pulses, the angle  $\phi$  was calculated for various values of  $\theta$ . Some experimental points are shown in Fig. 33. Figure 37 is a typical oscilloscope trace of the light sensor

outputs. The light sensors were connected electrically in a way which produced positive pulses from the centre slit and negative pulses from the angled slits. By observing whether the negative pulse was leading or trailing the positive pulse, it was possible to tell whether the value of  $\theta$  was positive or negative. The agreement between the theoretical calibration curves and the experimental points was within  $1^\circ$ . Since the construction of the sensors and the mounting in the extension body was considered to be very accurate, it is believed that most of the observed disagreement was due to such things as errors in levelling the turntable and measuring the time difference between pulses.

### 3.2.10 Magnetometers

While the sun's direction provided one reference for use in determining the orientation of the rocket axis, a second independent reference was necessary to uniquely determine the direction of the rocket axis. The second reference was the direction of the earth's magnetic field over Churchill, Manitoba. From measurements made by the Defence Research Northern Laboratories at Fort Churchill, the direction was known with sufficient accuracy. Two single component magnetometers were installed in the rocket to measure the magnetic field components parallel and perpendicular to the rocket axis. These magnetometers were type RAM-3 manufactured by the Schonstedt Instrument Company of Silver Spring, Maryland. The field sensing units were mounted in teflon blocks on a shelf fastened to the outer tube of the extension system (Fig. 23). They were positioned as far forward as possible in order to minimize the effect of the rocket motor casing on the magnetic field direction. If  $\Phi$  is the angle between the rocket axis and the magnetic field direction, then the magnitude of  $\Phi$  is given by

$$\tan \Phi = \frac{B_{\perp}}{B_{\parallel}} \quad (3.8)$$

where  $B_{\perp}$  is the magnitude of the maximum magnetic field components perpendicular to the rocket axis over a single spin cycle (see Section 7.0) and  $B_{\parallel}$  is the magnitude of the magnetic field component parallel to the rocket axis.

## 4. ELECTRICAL AND ELECTRONIC SYSTEMS

The electronics required for the experiment could be divided into two categories. The first of these included the components which the National Research Council had developed or supplied for the Black Brant II rockets; the second comprised the components which were designed and constructed at UTIAS specifically for this experiment. The electronic circuits developed by UTIAS personnel were of the following types:

- 1) DC amplifiers for the outputs of the high and medium pressure (HP and MP) gauges.
- 2) High voltage power supplies for the cold cathode ionization gauges.
- 3) AC and DC amplifiers for the outputs of the ionization gauges.
- 4) Automatic voltage-level sensing, and gain switching circuitry for all of the AC and DC amplifiers.

In addition to this the wiring of the equipment in the nose cone was done at UTIAS. NRC advice on wiring and construction techniques proved to be extremely valuable in this work. A block diagram of the electrical system is shown in Fig. 38.

The design and development of the circuits required the efforts of a number of people. Once the rocket instrumentation had been specified, the initial layout of the electrical system was performed by Mr. W.B. Feyrer, who also constructed prototypes of the high voltage power supply, DC amplifier, and automatic range switching for the ionization gauges. Further development of these circuits was carried on by Messrs. G. Martens, H. Treial and B. Sherman. Final development and testing of all the circuits was performed by Mr. J. Burt. The wiring of instrumentation in the nose cone was done by Mr. J. Hager, who also assisted in the construction of the final circuits for the payload. Figure 39 illustrates some of the circuits which comprised the payload.

#### 4.1 Telemetry

The Space Electronics Section of the National Research Council supplied the telemetry system for the experiment. This telemetry system, which was of the FM/FM type, was provided by NRC for all of the Black Brant rocket experiments being performed by Canadian universities. It contained 10 subcarrier oscillators with frequencies covered by the IRIG channels 9 to 18 inclusive (Fig. 41a). The outputs of the subcarrier oscillators were combined and transmitted by a crystal-stabilized FM transmitter with a 5 watt output. An in-flight calibrator applied short duration pulses of 0 and 5 volts amplitude to the input of the subcarrier oscillators, with the amplitude alternating every 10 seconds. One of the subcarrier oscillators carried the signal from a 30 channel commutator which permitted sampling of slowly varying signals at a rate of 10 times per second.

In order to monitor all of the signals, a subcommutator was found to be necessary. This permitted each of 20 very slowly varying signals to be monitored every 2 seconds. One of the commutator channels carried the sub commutator signal, and a second channel carried an indicator voltage to tell which sub commutator channel was being read out. The indicator voltage was in the form of 20 voltage steps between 0.0 and 2.0 volts in 0.1 volt increments.

Main power for the telemetry system was provided by 18 silver-zinc cells of 5 ampere-hour capacity. This provided a nominal 26 volt supply which was then transformed by DC-DC converters to the voltage levels required for the equipment. The standard telemetry package (Fig. 41a) was 15 inches in diameter, 4 inches high, and weighed 34 pounds with its batteries installed.

#### 4.2 Radar Beacon

Since accurate velocity and position data for the rocket was required throughout its entire trajectory, a radar beacon was provided by the Churchill Research Range. A beacon was necessary for continuous radar tracking because skin tracking of the rocket was only possible to an altitude of 200,000 feet. Range personnel had control of the beacon installation, check-out and operation.

### 4.3 Ionization Gauge Circuits

The primary part of the experiment involved the density measurements by the five cold cathode ionization gauges. A DC-DC converter was developed to provide a 4000 volt regulated supply from a 28 volt battery supply. The maximum current drawn from the high voltage supply was limited to 2 milliamperes by resistors in series with the ionization gauges. The amount of ripple on the 4 kilovolt supply was 20 volts rms. For reasons of reliability separate power supplies were constructed for each of the five gauges.

A DC amplifier was developed which converted a gauge current of 2.5 microamperes to a 5 volt output in its most sensitive gain configuration. Since the maximum gauge current was 2 milliamperes, a means of switching the amplifier gain was necessary. The gain was controlled by switching resistors into the circuit between the amplifier input and ground. An automatic voltage-sensing and switching circuit drove two relays which switched one of four gain control resistors into the circuit.

Rocket spin caused both DC and AC components to be present in the ionization gauge output. It was necessary that amplifier gain switching be performed on the basis of the peak value of the combined AC and DC signal. In this way the input waveform to the telemetry was not clipped. This range switching was performed by applying a peak follower to the amplifier output. The peak follower output was compared to an upper voltage level of 5 volts, and a lower voltage of nominally 0.5 volts since the gain factor between amplifier ranges was nominally 10. The outputs of the two level comparators were directed to logic circuitry. If the amplifier output was outside the range of the two voltage levels, different gain resistors were switched into the amplifier circuit in sequence until the value which put the amplifier output between 0.5 and 5 volts was found. The gain or range indication was provided to the telemetry in the form of 4 equally spaced voltage levels between 0 and 4.5 volts, with 0 volts indicating the most sensitive range. The ranges are defined as Range 1, Range 2, Range 3, and Range 4, with Range 1 having the highest gain.

An AC amplifier was designed to magnify the modulation of the DC amplifier output caused by the rocket spin. The AC amplifiers were necessary for two reasons. If no outgassing effect existed, then the AC component of the DC amplifier output became difficult to measure accurately when the voltage was close to the lower switching voltage. If the outgassing pressure was significant, then the ratio of the AC signal amplitude to the DC signal would become too small to permit accurate measurement of the AC component. For these reasons AC amplifiers were applied to the DC amplifier outputs of gauge numbers 2 and 5 (see Appendix B for the numbering system used for the cold cathode ionization gauges). It would have been desirable to put AC amplifiers on the outputs of gauges 3 and 4, which also had signal modulation, but the telemetry channels to permit these were not available. The same type of range switching circuitry was used for both the AC and DC amplifiers. The only difference was that the AC amplifier gains were switched by factors of 3 instead of 10 as with the DC amplifiers. The maximum AC amplifier gain factor was 70. A DC bias of 2.5 volts was applied to the AC signal before input to the telemetry in order to allow the maximum peak-to-peak AC signal to be transmitted.

#### 4.4 H.P. and M.P. Gauge Amplifiers

The outputs of the strain gauge pressure transducers, which have full range outputs of 250 millivolts, were amplified using Burr-Brown, type 1503 operational amplifiers. Gains employed varied between 620 and 20 depending on the gauge output. Range switching circuitry, the same as was built for the AC and DC amplifiers, provided for gain ratios of 3 between ranges. Each transducer was provided with a separate 30 volt mercury battery supply. Regulation was not necessary since the gauges had been ordered from the manufacturer with a built-in supply voltage regulator.

The thermocouple gauge signals were also amplified using the same operational amplifiers and gain switching circuitry. However, the gauge output varied between 1.5 millivolts at atmospheric pressure, and 10 millivolts at high vacuum. This required a maximum gain of 1100 in the most sensitive amplifier range. At these high gains, the amplifier temperature drift became significant. For this reason, a thermistor was mounted on the amplifier circuit board to monitor the temperature, and enable corrections to be made if necessary.

All of the circuits which were constructed for the experiment were tested over a temperature range from 50°F to 160°F to verify their performance. With the launch facilities available at the Churchill Research Range, there was little chance that the payload temperature would fall below 50°F, since the electronics dissipated over 150 watts of heat when it was operating. The effects of temperature on amplifier gain, switching voltage level stability, amplifier zero drift, and frequency response of both AC and DC amplifiers were recorded. This was done for each circuit in the payload and provided a basis for making temperature corrections to the data in the event that it should be found necessary.

#### 4.5 Timers and Firing Circuit

In order to activate the separation system, the bellows actuators had to be fired a certain time after lift-off. Two, acceleration actuated, mechanical timers were set for a time of 58 seconds. At this time the switching contacts in the timers closed the firing circuit for the bellows actuators. Power to fire the bellows actuators was obtained by tapping off 12 volts from the main UTIAS 28 volt battery supply. Each pair of actuators was connected to a separate firing circuit for reliability reasons. Resistors in the circuit limited the current to each actuator to 1 ampere. Even if a short circuit developed, the current drawn would not discharge the batteries within the flight time involved.

#### 4.6 Batteries

Silver-zinc cells were used to provide power for all of the equipment. The telemetry system had its own batteries and three battery supplies were assembled for the UTIAS experiment. Nineteen, 5 ampere-hour cells provided a nominal 28 volt supply for the high voltage power supplies and the thermocouple gauges. Twenty, 1 ampere-hour cells provided the  $\pm 14.6$  volts required for the amplifiers and the range switching circuits. The operational amplifiers required close matching of the  $\pm 14.6$  volt supplies. After charging,

an attempt was made to match the voltages within 0.1 volt by selecting the cells carefully when they were combined into a battery. Battery charging was performed by NRC personnel using the methods which they had found to give reliable performance (Ref. 53). After charging, the battery packs were wrapped in thin vinyl sheet to insulate them from the metal battery case. This minimized the possibility of discharging the cells in the event that the electrolyte should leak from them.

#### 4.7 Temperature Sensors

Component temperatures were necessary at a number of locations, both for reduction of the data, and also as a matter of engineering interest. Thermistors with a resistance of 10,000 ohm  $\pm$  1% at 25°C were employed for the temperature measurements. A 1200 ohm resistor in parallel with the thermistor tended to linearize the voltage output across the resistor-thermistor combination as the temperature varied over the region of interest. A typical thermistor calibration curve is seen in Fig. 40.

To aid in the data reduction, thermistors were located as follows:

- 1) Stagnation and cone surface pressure gauges
- 2) Ionization gauge volumes
- 3) Burr-Brown amplifier circuit board.

#### 4.8 Magnetometers

These units have been described in Section 3.2.10. The pulse outputs from the sun sensors were superimposed on the magnetometer outputs in order to conserve telemetry channels. The lateral magnetometer and the 45 degree sun sensor were combined, and the longitudinal (or Z-axis) magnetometer and the 65 degree sun sensor were combined.

#### 4.9 Miscellaneous Instrumentation

The payload contained instruments and circuits which did not provide primary information for data reduction, but rather monitored performance of instruments or provided information of engineering interest. In this category were two crossed, lateral accelerometers and a longitudinal accelerometer. The latter also proved to be useful in determining the rocket velocity at low altitude. A number of voltage monitors were built into the circuits to ensure that supply voltages remained at an acceptable value. These voltage monitors are indicated in Appendix B.

#### 4.10 Electronics Frame

The electrical equipment and circuit boards were mounted on frame constructed from aluminum sheet. Figures 41a, b, c, d, e, and f illustrate the type of construction and the mounting of equipment in the frame. The telemetry package was mounted on the extension body with the bulkhead on which it was constructed forming the aft limit of the pressurized electronics compartment (Fig. 9). The electronics frame was then mounted on top of the

telemetry package. Vertical panels from 0.091 inch thick aluminum sheet form compartments into which the various components can be fitted. Using circular end plates of 1/8 inch and 3/16 inch thick aluminum, this type of construction formed a very stiff structure. Since the electronics frame weighed 12 pounds, an adequate heat sink was also provided to absorb the heat dissipated by the electronics.

## 5. PRESSURE GAUGE CALIBRATION

### 5.1 Strain Gauge and Thermocouple Pressure Transducer Calibration

An attempt was made to calibrate the gauges using the electronic circuits and nose cone wiring in its final configuration. The transducers were assembled in the tip cone in their final configuration. Fitting the tip cone to the aft cone completed the electrical circuits as far as the bulkhead separating the conical section from the cylindrical section of the nose cone. Jumper wires then had to be attached to complete the connections between the bulkhead connector and the electronics frame, since the electronics was not placed inside the cylindrical section for reasons of convenience in handling. However, it was found that the use of the jumper wires did not affect the calibration. The pressure in each gauge volume was varied by the use of a vacuum manifold which could be fastened to the tip section of the cone. The impact and surface pressure gauges opened into this common manifold permitting each gauge volume to be evacuated to the same pressure. Employing a mechanical vacuum pump, it was possible to attain a pressure of  $5 \times 10^{-3}$  mm Hg in the manifold. This pressure was easily adjusted by leaking air into the pumping line through a needle valve. Depending on the pressure range involved, the pressure was measured with a McLeod gauge, a calibrated bourdon gauge, or a mercury manometer.

For a particular pressure setting in the manifold, the transducer signal, the amplifier output, and the amplifier gain (range indication) were recorded for each of the strain gauge and thermocouple pressure transducers. Electrical heating tapes were then wrapped around the nose cone and the calibrations repeated at temperatures of 114°F and 140°F. Over this temperature range the deviation from the 75°F calibration was found to be within 1% of the full scale output (Fig. 42). In the most sensitive amplifier ranges, the deviation appears to be very large for the strain gauge transducers because of the high amplifier gain employed. The thermocouple gauges indicated very little temperature sensitivity. The strain gauge transducers also exhibited a time dependent drift when first switched on, requiring an hour to stabilize completely. However, this amounted to less than 1/2% of full scale output, and could only cause significant error when the amplifier was in its most sensitive (highest gain) range.

### 5.2 Ionization Gauge Calibration

The amplifiers and range switching circuitry were designed for the measurement of pressures as low as  $10^{-7}$  mm Hg. However, the rocket apogee was only 96 miles instead of the 120 miles which had been anticipated at the time the circuits were designed. For this reason, an ultimate pressure of  $5 \times 10^{-7}$  mm Hg was considered adequate for calibration purposes.

A stainless steel calibration chamber was constructed with inside dimensions of 7 inches square by 18 inches high. This chamber was large enough to hold the complete gauge package and its wiring. The high voltage feedthrough which supplied power to the gauges was mounted on the end of the chamber in the same manner as it was in the nose cone (one side at high vacuum and the other side at atmospheric pressure). Pumping for the chamber was supplied by a 2 inch diffusion pump trapped with a liquid air trap. The pump and the trap could be isolated from the chamber by a water cooled baffle valve, which made rapid cycling of the system possible.

When the complete gauge package with its wires was placed in the chamber, the ultimate pressure attained was only  $10^{-5}$  mm Hg. Outgassing from the lengths of wire or from the silicone rubber poured into the gauge package was probably the reason for not being able to evacuate the chamber to a lower pressure. This meant that the gauges would have to be calibrated individually by pumping on each gauge volume in turn.

Although the gauge package was not calibrated inside the chamber, it was tested to ensure that a high voltage breakdown would not occur in either the gauge package or the feedthrough. The minimum pressure of  $10^{-5}$  mm Hg was maintained for more than a week, during which time the gauges were operated periodically. The pressure was also cycled to a value as high as 1 mm Hg to ensure that a high voltage breakdown would not occur at any of the possible operating conditions.

The actual calibration was carried out by pumping on each gauge volume in turn through the orifice in the surface of the gauge package. This was done by holding the gauge package in a fixture which allowed each gauge opening to be sealed over a hole in the calibration chamber. The fifth ionization gauge, in its mounting, was similarly attached to the chamber to permit it to be evacuated. It was possible to vary the pressure in the calibration chamber over a wide range by leaking air into it through a needle valve from a second chamber. A mechanical vacuum pump maintained a low pressure in the second chamber, whose pressure was also controlled by bleeding air into it through a needle valve. This arrangement was necessary because the needle valve on the calibration chamber permitted too high a leak rate into the chamber if air was bled in at atmospheric pressure. It was not possible to control the chamber pressure accurately in the  $10^{-7}$  to  $10^{-5}$  mm Hg pressure range unless the air was bled in at reduced pressure. The maximum pressure at which the second chamber was operated was 1 mm Hg. Dry air was provided for the calibration chamber by passing it through a small diameter copper tube immersed in liquid air before it was leaked into the chamber through the needle valve. Care was taken to ensure that the air was bled into the chamber far away from both the gauge being calibrated and the reference gauge being used for calibration.

Pressures in the calibration chamber were measured with a Bayard-Alpert type of ionization gauge, which was later calibrated against a McLeod gauge. The McLeod gauge was a Consolidated Vacuum Corporation type CM-110 which has high sensitivity to pressures as low as  $10^{-6}$  mm Hg. The stated accuracy for this gauge is  $\pm 4.4 \times 10^{-7}$  mm Hg at a pressure of  $10^{-5}$  mm Hg. After calibration had been completed the same ionization gauge was mounted in the nose cone to measure the nose cone pressure when it was evacuated.

After the McLeod gauge had been outgassed, the chamber pressure was measured, with the McLeod gauge and the calibration gauge, at two pressure levels with the following results:

Calibration Gauge Pressure $P_C$ (mm.Hg.)	McLeod Gauge Pressure $P_M$ (mm.Hg.)	$P_C/P_M$
$4.7 \times 10^{-5}$	$4.4 \times 10^{-5}$	1.29
$4.1 \times 10^{-4}$	$3.2 \times 10^{-4}$	1.30

The cold cathode ionization gauges were first evacuated to the ultimate pressure of the system. The high voltage supply for the gauge being calibrated was turned on, and the gauge allowed to operate for 5 minutes until it had stabilized. Readings of DC amplifier output, amplifier range, and corresponding calibration gauge pressure were recorded for a number of pressures, to a maximum value of  $10^{-3}$  mm Hg. The pressure was then reduced in steps to the ultimate pressure, with readings of pressure and gauge output again being recorded. Results of the calibration are illustrated in Fig. 43 for a typical gauge. The calibration revealed that gauge number 4 had two stable modes of operation. If the pressure was increased from  $10^{-6}$  mm, one calibration curve resulted; if the pressure was decreased from a value above  $10^{-3}$  mm, a different calibration curve resulted. This gauge calibration is shown in Fig. 44. It is believed that this double mode operation was the result of decreasing the magnetic field within the gauge by the shields put around the gauge magnets. The other four gauges did not exhibit this type of behaviour.

Three months elapsed between the time that the gauges were calibrated and the time that the rocket was fired. During this time the gauge package was wrapped in polyethylene sheet and crated to await shipment to the rocket range. This raised the question of whether the calibration might change during this time. Figure 45 compares calibrations for gauge number 5 obtained in May 1964 and the final calibration performed in December 1964. There is apparently no significant difference between the two calibrations. Since the gauges in the package were not operated after their final calibration, the internal surfaces could not become contaminated and change the calibration.

## 6. THE ROCKET LAUNCHING

### 6.1 Churchill Research Range

The launching of the University of Toronto rocket experiment in March, 1965 was one of a series of four firings coordinated by the National Research Council, Space Electronics Section, at the same time. The facilities of the Churchill Research Range were under the direction of the Office of Aerospace Research, United States Air Force. Pan American World Airways, Inc., operated and maintained the range under prime contract to the Office of Aerospace Research.

The launch site is 12 miles east of the base camp of Fort Churchill, Manitoba. Figures 46a and b indicate the size and location of the range and the facilities at the launch site. Launch complexes specifically designed for Nike Cajun, Aerobee, and Black Brant rockets are located at the launch site. A fourth complex, the Universal launcher, can be adapted for launching most solid propellant research rockets. Since this is a completely enclosed facility, most of the Black Brant rockets are fired from it, rather than from the outdoor Black Brant launcher.

The operations building houses central communications, range timing, primary telemetry, meteorology, a radar beacon laboratory, operations offices, a fire station, and a cafeteria. Space is also provided for Range users for nose cone assembly and general payload preparation (Ref. 54).

## 6.2 Payload Preparation and Rocket Launching

Assembly of the nose cone and payload was commenced on March 9. By March 12, the electronics and the gauges had been checked, and the nose cone (less the extension body and the electronics frame) was assembled to allow pumping to begin. The Range contractor provided a card which permitted the nose cone to be supported horizontally at a height of 5 feet. This allowed the pumping system to be attached to the nose cone, and hang freely beneath it. Figure 47 records the time variation of the nose cone pressure measured by the monitor ionization gauge. Leak rate tests on the nose cone were conducted by shutting the manual valve over the diffusion pump, and measuring the rate of pressure rise. On the day before the firing, the pressure attained in the nose cone was  $8.5 \times 10^{-5}$  mm. Hg. At this time, the rate of pressure rise, when the pumping line was closed was  $1.5 \times 10^{-6}$  mm Hg per second. This pressure was considered low enough to meet the requirements of the experiment. The leak rate was also sufficiently small to prevent the nose cone pressure from rising excessively when power was turned off to allow arming of the rocket.

When the pressure in the nose cone was below  $5 \times 10^{-4}$  mm. Hg. the ionization gauges were turned on, and the remaining checks on the operation of the gauges and associated circuitry were then completed.

On March 16, the nose cone and payload were prepared for transporting to the Universal launcher. The battery packs for the instruments and telemetry were installed, and the equipment operated briefly on internal battery power in order to verify power connections and operation of the instruments. The extension body and the electronics frame were then mated with the cylindrical section of the nose cone. Final electrical connections to the high voltage power supplies, and the bulkhead 50 pin connector, were made through the access door in the cylindrical section.

When the time came to move the payload from the operations building to the launcher, a portable generator, mounted on a truck, was available. This provided power for the pumping system, to enable it to keep operating, while the nose cone was moved. The nose cone cart was then towed slowly behind the vehicle to avoid breaking the vacuum seal between the nose cone and the pumping system (Fig. 48).

During the trip between the operations building and the launcher, the fan on the air cooled diffusion pump stopped. When this was discovered at the launcher, the diffusion pump was isolated from the nose cone with the baffle valve. The diffusion pump was then turned off until the trouble could be remedied. The pumping system could not be operated again until the rocket was mounted on the launcher, and the air blowers previously installed on the launcher were connected to the system. Approximately 2 hours elapsed before the nose cone was mated with the motor and the assembled rocket was put on the launcher rails. Only then could the blowers be connected. In addition, the power supply for the thermoelectric baffle had to be mounted on the launcher, and the previously installed mechanical backing pump connected to the diffusion pump. Only when all this had been done could evacuation of

the nose cone proceed. Because of the length of time the pumping system had been inoperative, it was decided to allow the pumping to continue overnight in order to reduce the pressure to an acceptable value.

On March 17, at 1200:00 CST, the count was picked up at T-180 minutes. The countdown proceeded smoothly through the horizontal checks, vehicle arming, and the launcher elevation (Fig. 49). During the vertical check, a hold was called when it was noted that the current drawn from the UTIAS 28 volt battery supply was much higher than recorded during the horizontal check. The countdown was resumed after it was decided that the current increase corresponded to a pressure increase in the nose cone, since the high voltage power supplies drew more current in that case. This pressure rise was verified by the telemetered data from ionization gauge number 4. This indicated that the  $-12^{\circ}\text{F}$  ambient temperature had cooled the diffusion pump sufficiently to virtually stop the pumping action. Since the mechanical backing pump was still operating, the nose cone pressure could not rise higher than 20 or 30 microns. This was still considered adequate to proceed with the launch. At T-90 seconds the valve in the nose cone was shut, the strap holding the pump to the nose cone released, and air let into the pumping line to break the suction. The heat shield surrounding the rocket was opened, carrying the pumping system clear of the vehicle. The rocket lifted off the launcher at 1513:29.5 CST. (Fig. 50). Nose cone separation and gauge package extension were observed at 1514:27.3 CST from the signals transmitted by the event oscillator inputs on the ionization gauge cable holder. Rocket impact occurred at 1519:46.8CST.

## 7. DATA REDUCTION AND DISCUSSION

Vehicle performance during the flight was excellent and telemetry signals were received for the full duration of the flight. During the flight, the information was recorded on magnetic tape for future playback, and certain channels of information were displayed on paper recorders for viewing as the flight progressed. The real time paper records merely provided an indication that the instruments were functioning and that the experiment was proceeding in a satisfactory manner. At a later time paper records were produced for all the channels of information recorded on magnetic tape. This work was done by the Space Electronics Section with their equipment in Ottawa.

### 7.1 Rocket Orientation Measurements

The pulses which the sun sensors superimposed on the magnetometer signals were easily observed on the paper telemetry records (Fig. 51). Using the pulses from the sun sensor slits parallel to the rocket axis, it was possible to obtain a very accurate record of spin rate vs time (Fig. 52). The angle between the rocket axis and the sun's direction was calculated using the pulses from the 45 degree sun sensor for almost the entire flight. The rocket motion was such that the sun stayed within the acceptance angle of this sensor for the ascent and most of the descent portions of the trajectory. Since the angles measured were small, the 45 degree sensor gave pulse separations twice as large as the 65 degree sensor. The time difference between the positive and negative pulses was measured from the paper telemetry records which had timing marks superimposed along each edge of the chart. By this method the time difference between pulses, and the time per spin cycle, could be deter-

ained within 0.001 seconds. Equation (7) enabled  $\theta$  to be determined and hence the value of  $\dot{\theta}$  could be obtained from Fig. 53. The error of 0.01 seconds in the time difference corresponded to a possible error in the calculated value of  $\dot{\theta}$  of approximately 1 degree. The variation of  $\theta$  with time between lift-off and impact is shown in Fig. 53. After the spin rate had stabilized at a value of 3.16 cps, the variation of  $\theta$  became sinusoidal. Figure 54 shows the variation of  $\theta$  after the spin rate had stabilized. It was found that a sine wave with a peak-to-peak amplitude of 10.4 degrees, and a period of 30 seconds, could be fitted to the calculated values of  $\theta$ .

The outputs from the Z-axis magnetometer and the lateral magnetometer are also illustrated in Fig. 51. Rocket spin caused the sinusoidal variation in the signal from the lateral magnetometer. The peak-to-peak amplitude of the signal represents twice the value of the magnetic field component perpendicular to the rocket spin axis. By referring to the calibration curves supplied by the magnetometer manufacturer, the value of the magnetic field component was determined. The output from the Z-axis magnetometer was nearly constant since it indicated the magnetic field component parallel to the rocket spin axis, whose orientation did not change greatly. These two magnetic field components could be used to calculate the tangent of the angle  $\Phi$ , which was the angle between the spin axis and the earth's magnetic field direction. Figure 54 also plots the calculated values of  $\Phi$  after the rocket spin rate had stabilized. It should have been possible to fit the same sine wave to these points as was fitted to the sun sensor points. The calculated values of  $\Phi$  had the same periodic variation, but they did not fit on a sine wave. The peak-to-peak amplitude was also 1.4 degrees less than for the sun sensor angles. This would indicate that the magnetic field direction was altered by the presence of the rocket. As a result the true values of  $\Phi$  should have been larger than those calculated.

At any time, the rocket axis must lie on the surface of a circular cone whose axis is the sun's direction, and whose semi-vertex angle is  $(90-\theta)$ . It must also lie on the surface of a circular cone whose axis is the earth's magnetic field direction, and whose semi-vertex angle is  $\Phi$ . Thus the solution for the orientation of the rocket axis in space involved the solution for the intersection of two cones with a common apex (Fig. 55). The solution was performed graphically by drawing the intersections of the two cones with a horizontal plane. The equations of the two cones in terms of the direction cosines of the axis and the angles  $(90-\theta)$  and  $\Phi$  are given by (Ref. 45).

$$\begin{aligned}
 & (\beta^2 + \gamma^2 - \alpha^2 \cot^2 \theta) x^2 + \left( \frac{\alpha^2 \beta^2 \gamma^2}{\beta^2 + \gamma^2} - \beta^2 \cot^2 \theta \right) y^2 + \left( \frac{\alpha^2 \gamma^2 + \beta^2}{\beta^2 + \gamma^2} - \gamma^2 \cot^2 \theta \right) z^2 \\
 & - 2\alpha\beta(1 + \cot^2 \theta)xy - 2\alpha\gamma(1 + \cot^2 \theta)xz - 2\beta\gamma \left( \frac{1 - \alpha^2}{\beta^2 + \gamma^2} + \cot^2 \theta \right) yz = 0
 \end{aligned}
 \tag{7.1}$$

where  $(\alpha, \beta, \gamma)$  are direction cosines of the sun vector, and

$$(m^2 + n^2 - l^2 \tan^2 \Phi) x^2 + \left( \frac{l^2 m^2 + n^2}{m^2 + n^2} - n^2 \tan^2 \Phi \right) y^2 + \left( \frac{l^2 n^2 + m^2}{m^2 + n^2} - m^2 \tan^2 \Phi \right) z^2$$

$$-2lm(1 + \tan^2 \Phi)xy - 2ln(1 + \tan^2 \Phi)xz - 2mn \left( \frac{1 - l^2}{m^2 + n^2} + \tan^2 \Phi \right) yz = 0 \quad (7.2)$$

where  $(l, m, n)$  are direction cosines of the earth's magnetic field.

The intersection of the cones with the horizontal plane  $z = 1$  results in

$$(\beta^2 + \gamma^2 - \alpha^2 \cot^2 \theta) x^2 + \left( \frac{\alpha^2 \beta^2 + \gamma^2}{\beta^2 + \gamma^2} - \beta^2 \cot^2 \theta \right) y^2 - 2\alpha\beta(1 + \cot^2 \theta)xy$$

$$-2\alpha\gamma(1 + \cot^2 \theta)x - 2\beta\gamma \left( \frac{1 - \alpha^2}{\beta^2 + \gamma^2} + \cot^2 \theta \right) y + \left( \frac{\alpha^2 \gamma^2 + \beta^2}{\beta^2 + \gamma^2} - \gamma^2 \cot^2 \theta \right) = 0 \quad (7.3)$$

with a similar expression from Eq. 7.2 being

$$(m^2 + n^2 - l^2 \tan^2 \Phi) x^2 + \left( \frac{l^2 m^2 + n^2}{m^2 + n^2} - m^2 \tan^2 \Phi \right) y^2 - 2lm(1 + \tan^2 \Phi) xy$$

$$-2ln(1 + \tan^2 \Phi) x - 2mn \left( \frac{1 - l^2}{m^2 + n^2} + \tan^2 \Phi \right) y$$

$$+ \left( \frac{l^2 n^2 + m^2}{m^2 + n^2} - n^2 \tan^2 \Phi \right) = 0 \quad (7.4)$$

Equations 7.3 and 7.4 are plotted in Fig. 56 for a range of values of  $\theta$  and  $\Phi$ . The direction cosines for the sun's direction were calculated for a time near rocket apogee and hence represent an average value for the  $3\frac{1}{2}$  minutes which the ionization gauges were operating (Ref. 55 and 56). This results in a maximum angular error of less than  $1/3$  degree. The magnetic field direction was obtained from measurements made by the Defence Research Northern Laboratories at Fort Churchill. No attempt was made to correct for the variation in the field direction over the short flight path involved. For the case of the sun angle, the intersection of the cone with the horizontal plane gave rise to a family of hyperbolae; in the case of the magnetic field angle, the intersection produced a family of ellipses.

It was found that if the angles  $\theta$  and  $\Phi$  were used as calculated, the two curves did not intersect in all cases. Since the sun sensor data was believed to be reliable, an attempt was made to apply logical corrections to the magnetic field data. It can be shown that the correction to the measured value of  $\Phi$  due to distortion of the uniform magnetic field by the steel motor casing is approximately proportional to the angle itself. Consider that the external field around the motor is the result of superimposing magnetic fields perpendicular and parallel to the rocket axis (Fig. 57). As the point being considered approaches the motor along the axis, the perpendicular field component ( $B_{\perp}$ ) decreases, and the parallel component ( $B_{\parallel}$ ) increases (Ref. 57). For small values of  $\Phi_0$  the change in the angle caused by the motor is approximately given by

$$\Delta\Phi = \frac{\Delta B_{\perp}}{B_0}$$

where  $\Phi_0$  = the undistorted field direction  
 $\Delta\Phi$  = the change in the angle  
 and  $\Delta B_{\perp}$  = the change in the perpendicular field component  
 $B_0$  = the magnitude of the undistorted field.

Since  $\Delta B_{\perp}$  is proportional to  $B_0 \sin\Phi_0$ , it is also approximately proportional to  $\Phi_0$  if  $\Phi_0$  is small. Therefore it can be said that  $\Delta\Phi_0$  is proportional to  $\Phi_0$  if  $\Phi_0$  is small.

The first step in making the correction was to fit the sine wave obtained from the sun sensor data to the  $\Phi$  vs time plot as in Fig. 54, keeping the minimum value of  $\Phi$  the same. Then the values of  $\Phi$  were increased by a constant, determined by the difference between the maximum calculated value of  $\Phi$  and the maximum value of the sine wave. As a result of this,  $\Phi_{\min}$  was increased by 1.4 degrees and  $\Phi_{\max}$  was increased by 2.8 degrees. With these corrections, it was possible to obtain a solution for the rocket axis orientation at all times. The projection of the solution in the x-y plane, resembled an elongated ellipse (Fig. 56).

In Fig. 53 it is apparent that the direction of the rocket axis began to deviate from its essentially fixed orientation in space after 30 seconds. This would indicate that the rocket fins began to lose their stabilizing influence but that the aerodynamic forces were still of sufficient strength to cause the rocket axis orientation to change. After 60 seconds the variation of  $\theta$  had become extremely regular indicating that all aerodynamic forces were now negligible. Under these conditions the solution of the equation of motion for the force-free motion of a rigid body with an axis of symmetry is a right circular cone (Ref. 58). The sinusoidal variation of  $\theta$  with time indicated that the rocket axis was generating a right circular cone with a vertex angle of 10.4 degrees. With this information, an ellipse with the proper eccentricity was fitted to the points obtained from the graphical solution. In spite of the corrections, the final solution was still considered to give the true orientation of the rocket axis to within 3 degrees in the worst case.

It can be seen that in general there will be two mathematically possible solutions for the intersection of the two cones. One of these must be rejected on physical grounds. Figure 58 shows the angular orientation of the sun sensors and the lateral magnetometers in the nose cone. With this information and the spin rate, it is possible to calculate the time difference between the positive sun sensor pulse and a maximum or minimum value of lateral field component for corresponding points on the two possible solutions. This time difference can be compared with the observed value from the telemetry records to reject one of the mathematical solutions. Once the correct solution has been determined, the intersection of the rocket axis vector with the  $z = 1$  plane can be determined as function of time. If the intercepts are given by the coordinates  $(x_R, y_R, 1)$  then the direction cosines (a,b,c) are

$$\left( \frac{x_R}{\sqrt{x_R^2 + y_R^2 + 1}}, \frac{y_R}{\sqrt{x_R^2 + y_R^2 + 1}}, \frac{1}{\sqrt{x_R^2 + y_R^2 + 1}} \right)$$

The Range supplied the radar information in the form of analogue records from large plotting boards. This information was plotted in the form of height vs range (Fig. 59), and the coordinates of the rocket projected on a horizontal plane passing through the launcher. With this information the magnitude and direction of the rocket velocity could be calculated as a function of time.

The Space Electronics Section of the National Research Council performed the initial reduction of the radar plots. Range and height were read from the radar records at intervals of one second for most of the ascent and descent portions of the trajectory, and at 5 second intervals near apogee. Average vertical and horizontal velocity components could then be calculated over short time intervals.

The plotting board data did not provide sufficient accuracy for the powered portion of the flight since the velocity was changing rapidly. An accelerometer which measured acceleration components parallel to the rocket axis enabled the velocity to be determined. This accelerometer had a range of 20g in the forward direction and 3g in the rearward direction. By integrating the acceleration record with respect to time, the resultant velocity in the direction of the rocket axis was obtained. From the radar plot of height vs range, the angle of elevation of the rocket axis was measured and used to compute the vertical component of velocity. The velocity  $V_R$  is plotted from both the radar records and the accelerometer calculations for comparison (Fig. 60). A second check on the radar data was made by computing the vertical velocity  $V_V$  under conditions of free fall from apogee with no air drag. The variation of the acceleration of gravity was taken into account in the calculation. These values are also plotted with the values obtained from radar for comparison (Fig. 61). The velocities calculated from the accelerometer records agreed very well with the values from radar, when these became available 10 seconds after lift-off. The vertical velocity components obtained from radar data agreed with the calculated values above 150,000 feet, indicating negligible air drag above this altitude.

The horizontal velocity component was determined by calculating the average velocity over a 50 second time interval. With this long time interval, the error in the range measurements was insignificant. By using this method it was possible to observe a slow variation with time in the horizontal velocity component  $V_H$  (Fig. 62).

Figure 63 shows the rocket velocity vector direction in the coordinate system used for the calculations, where

$$\tan \theta_R = \frac{V_H}{V_V}$$

The azimuth angle,  $\phi_R$ , was measured from the radar plot and found to be  $3^{\circ}48'$ . The direction cosines (i, j, k) of the velocity vector are  $(-0.06627 \sin \theta_R, 0.99780 \sin \theta_R, \cos \theta_R)$ .

### 7.3 Low Altitude Properties

Analysis of the telemetered data from the stagnation and surface pressure gauges, indicated that the gauge outputs were shifted from the original calibrations. In the case of the strain gauge transducers, the gauge output was compared at atmospheric pressure at ground level, and also at the low pressures experienced at high altitude. These two readings give an indication of the deviation from the original calibration. The ground level pressure at launch time was 769.7 mm Hg and the air temperature was  $-12^{\circ}\text{F}$ . By dividing the difference in readings by the appropriate amplifier gain, the deviation can be compared to the nominal full scale output of 250 millivolts.

Gauge	Deviation	
	Atmos. Press.	Vacuum
H.P. 1 (Impact Pressure)	5.48 mv	2.42 mv
H.P. 2 (Surface Pressure)	8.57 mv	1.64 mv

Figures 64a and b show the deviation for H.P. 2 in range 2 and range 4. An attempt was made to compensate for the deviation by introducing a linearly varying time dependent shift to the calibration curves based on the observed deviations. During laboratory calibration, the gauges were found to be highly repeatable, with any deviations being well within the 1% of full scale output stated in the specifications. The calibration change observed during the flight was of the order of 3%, and thus was much higher than the specified accuracy. This suggested that it might be caused by the amplifiers. Since the deviation decreased greatly over a period of 53 seconds, this suggested that employing a much longer warm-up time for the gauges and amplifiers might have greatly reduced or eliminated the observed calibration change.

In the case of the thermocouple gauges it was only possible to obtain a high pressure reading to compare with the calibration. The calibration at high vacuum could not be compared because the gauge signals were no longer available when the tip section of the nose cone was ejected. For this reason, a constant displacement was applied to the calibration to correct for the observed deviation at atmospheric pressure (Fig. 65).

When the corrections to the calibration had been made, the amplifier outputs were converted to values of impact and surface pressure for use in computing density and temperature. The initial calculations employed Eq. 2.6 and values of  $p_1$  from Ref. 29 to enable the ambient density to be determined. In order to ascertain whether a correction to the measured impact pressure was necessary at higher altitudes, the Reynolds number was computed using viscosity data from Ref. 29 and the computed ambient density. Using the diameter of the flat tip of the impact probe as the reference length, the Reynolds number at 240,000 feet was 67.8 and 100 at 220,000 feet. The experimental data in Ref. 30 indicates that the measured impact pressure depends on both Reynolds number and Mach number. For Mach numbers in the range 5.4 to 5.7 the correction to the impact pressure is only of the order of 2% for Reynolds numbers as low as 60. It appears that viscous effects were negligible and hence no correction for them was made. Figure 66 shows the density profile calculated from the flight data.

Knowing the impact pressure  $p_s$  and the surface pressure  $p_s$ , the flight Mach number, and hence the static temperature, could be determined from Fig. 2. Before this could be done it was necessary to examine the effect of boundary layer growth on the cone since this would cause an increase in the pressure over the value computed assuming no boundary layer. Talbot, Foga, and Sherman (Ref. 28) correlated the available experimental data in terms of the parameter  $M_c \sqrt{C}/Re_c$  (Fig. 3). This experimental data was used to estimate the correction to the measured surface pressure to reduce it to the value if there were no boundary layer growth on the cone. In order to calculate  $M_c \sqrt{C}/Re_c$  it was necessary to assume an atmospheric temperature profile to calculate the flight Mach number. This was chosen to be that given by the U.S. Standard Atmosphere (Ref. 29). By interpolation in Kopal's tables of the flow around cones (Ref. 33) the Mach number  $M_c$ , density  $\rho_c$ , and temperature  $T_c$  (hence viscosity  $\mu_c$ ) were calculated for altitudes above 150,000 feet. The length on which the  $Re_c$  was based was 19 inches, the distance of the surface pressure orifice from the tip of the cone. Using the previously computed values of  $p_s$  the parameter  $M_c \sqrt{C}/Re_c$  was calculated as a function of altitude and the corresponding corrections to  $p_s$  have the following values:

Altitude (feet)	$p_s/p_c$
150,000	1.03
180,000	1.05
210,000	1.07
240,000	1.11

After making the appropriate corrections to  $p_s$ , the flight Mach number and free stream temperature were calculated. The atmospheric temperature profile determined by this method is illustrated in Fig. 57, which also indicates balloon measurements made before the flight and previous rocket grenade measurements made under similar conditions (Ref. 14). Figure 68 illustrates the atmospheric pressure profile obtained by using the equation of state.

If one accepts the grenade and balloon measurements of temperature as being reasonably accurate, then it is apparent that the temperature computed from the measured pressures is considerably lower than it should be. It is believed that the major source of this error can be traced to the apparent shift in the pressure calibration for all of the gauges. Up to a height of 40 km the temperature data appears to agree within 10 to 15%. Over this altitude range the temperature was calculated using the data from the strain gauge transducers. Since it was possible to obtain an in-flight calibration check at both high and low pressure, the method of correcting the calibration between these extremes is believed to be accurate to within 10 to 15%. Above 40 km, the temperature was obtained from the thermocouple gauges. In this case only the single calibration check at high pressure was available. As a result the calibration curves could not be accurately corrected at a later time in the flight when the pressure became very low. If the shift were really due to insufficient warmup time for the electronics then one would expect that the deviation from the original calibration would decrease as the flight progressed. The outputs from the amplifiers on the strain gauge transducers verify this type of time dependent correction. As a result the corrected calibration should possibly have approached the original calibration as the flight progressed. However unless the magnitude of the correction is known at very low pressure there is no basis for making a better approximation to the true calibration curve.

Since the density is nearly proportional to  $P$ , and the impact pressure transducers showed the least calibration shift, it can be said that the density profile is more accurate than either the temperature or pressure profiles. The percentage error in the density is almost the same as the error in the measured impact pressure. This error is greatest at altitudes around 46 km where the thermocouple gauge is relatively insensitive to the pressure changes. In this range the error could possibly be 50%. However over most of the trajectory the error should not exceed 15%. The ambient temperature measurements and also the ambient pressure measurements are more sensitive to errors in the measured pressures. In their case, an error of 10% in the value of  $P/p_s$  at  $M_1 = 5$  results in an error of almost 15% in  $T_1$  and  $p_1$ . Since the calibration shift for the surface pressure transducers was larger than for the impact pressure transducers one would expect the possible error in  $T_1$  and  $p_1$  to be much larger. The temperature profile appears to bear this out. At 75 km the error in  $T_1$  could be as much as 100°K, while the error below 40 km appears to be in the range between 20° and 30°K.

## 7.4 Upper Atmosphere Properties

### 7.4.1 Upper Atmosphere Wind

After the orientation of the rocket axis (Section 7.1) and the direction and magnitude of the rocket velocity with respect to the ground (Section 7.2) had been determined, it was possible to examine the telemetered signals from the ionization gauges for evidence of upper atmosphere winds. Figure 69 illustrates the modulated signal from the ionization gauges. In order to determine whether significant winds were present, it was first necessary to compute the time at which a maximum gauge signal would have been observed if no winds were present. During a spin cycle, the zero-time reference was chosen to be the time at which the 45° sun sensor produced a pulse from its central slit. If there were no wind then the gauges would produce their maximum or minimum signal then the rocket velocity vector, the rocket axis orientation, and the normal to the gauge orifice were all coplanar. Therefore, it was necessary to calculate the angle between the planes formed by the rocket axis and the sun's direction, and the rocket axis and the velocity vector. The angle between the two planes is given by

$$\cos \Delta\phi_{S,V} = \frac{\begin{vmatrix} b & c \\ j & k \end{vmatrix} \cdot \begin{vmatrix} b & c \\ \beta & \gamma \end{vmatrix} + \begin{vmatrix} c & a \\ k & i \end{vmatrix} \cdot \begin{vmatrix} c & a \\ \gamma & \alpha \end{vmatrix} + \begin{vmatrix} a & b \\ i & j \end{vmatrix} \cdot \begin{vmatrix} a & b \\ \alpha & \beta \end{vmatrix}}{\sqrt{\left(\begin{vmatrix} b & c \\ j & k \end{vmatrix}\right)^2 + \left(\begin{vmatrix} c & a \\ k & i \end{vmatrix}\right)^2 + \left(\begin{vmatrix} a & b \\ i & j \end{vmatrix}\right)^2} \cdot \sqrt{\left(\begin{vmatrix} b & c \\ \beta & \gamma \end{vmatrix}\right)^2 + \left(\begin{vmatrix} c & a \\ \gamma & \alpha \end{vmatrix}\right)^2 + \left(\begin{vmatrix} a & b \\ \alpha & \beta \end{vmatrix}\right)^2}}$$

where  $\Delta\phi_{S,V}$  is the angle between the planes defined by the rocket axis and the sun vector, and the rocket axis and the rocket velocity vector,

(a,b,c) are the direction cosines of the rocket axis  
 (α,β,γ) are the direction cosines of the sun's direction  
 and (i,j,k) are the direction cosines of the rocket velocity with respect to the ground.

From previous measurements of the orientation of the gauge package in the nose cone, the position of the gauges with respect to the sun sensor was determined and is shown in Fig. 58. Having this information and the rocket spin rate, it was possible to calculate the time of maximum gauge signal, assuming there were no atmospheric winds. If the maximum gauge signal did not occur at this time, then the phase shift must have been due to atmospheric wind or phase shift caused by the electronics. Since the DC amplifiers caused a phase shift of  $11^\circ$  in the gain ranges employed, this correction was applied to obtain the true phase shift due to wind. The computations were carried out for a series of altitudes between 35,000 feet and 498,000 feet using ascent and descent data.

After the angular phase shift caused by wind had been calculated, the graphical method described by Ainsworth, Fox and LaGow (Ref. 10) was used to obtain the wind direction and magnitude. Figure 70 illustrates the method. It was necessary to calculate the direction and magnitude of the rocket velocity component perpendicular to the rocket axis  $V_y$ , at the same altitude during ascent and descent. It became apparent during the calculations that sizable errors in the wind vector were possible depending on the angle between the rocket axis and the rocket velocity vector. When the angle was small, then the uncertainty in the value of (a,b,c) was magnified and resulted in considerable possible error in the calculated phase shift. At best, the measured phase shift was only considered to be accurate to within  $5^\circ$ . To obtain accurate wind measurements, rocket attitude measurements to better than 1 degree would be necessary. In addition, the angle between the rocket axis and the velocity vector should be larger as it would be near apogee, or if the precession cone had a larger vertex angle. Except for a small portion of the trajectory, the phase measurements all indicated that the wind vector was from a northerly direction. However at an altitude of 375,000 feet, during ascent, the phase measurements indicated a strong wind from a southerly direction. During descent, at the same altitude, the phase shift was indicative of a relatively low wind velocity from the north. However, this type of atmospheric wind pattern is possible. Greenhow and Neufeld (Ref. 46), by observing meteor trails in the region from 80 to 100 km, found wind eddies having vertical scales of 7 km and a horizontal size of 150 km. The observed wind change had a vertical scale of roughly 12 km.

Since there was considerable doubt concerning the accuracy of the wind velocities determined by the graphical method it was decided to reduce the ionization gauge data under the assumption that the wind velocity was zero. Using Eqs. 2.21 and 2.22 it was then possible to estimate the error caused by assuming zero wind velocity.

#### 7.4.2 Upper Atmosphere Density

Reduction of the telemetered data from the two gauges oriented with  $\beta = 90^\circ$  provided the atmospheric density and the magnitude of the outgassing effect observed by pre-evacuated and unprepared gauges.

In addition to the gauge signal (Fig. 69), the thermistor voltages and the amplifier range indicator voltages were measured. The corresponding ionization gauge temperatures were calculated and are displayed in Fig. 71. A typical DC amplifier range indication is plotted in Fig. 72. Due to the presence of the outgassing cloud, the DC amplifiers operated in only their two low gain ranges during the flight. In the case of the unpre-

pared gauge in the cylindrical section, the gauge pressure never became low enough to permit the amplifier to switch out of its least sensitive range.

In the case of ionization gauge 4 (in the gauge package), the peak-to-peak amplifier signal was read from the telemetry records and a corresponding value of gauge density variation obtained from the relevant calibration curve. The angle of attack  $\alpha$  in Eq.(2.17) was given by

$$\alpha = \cos^{-1} (a.i + b.j + c.k) \quad (7.2)$$

Since the wind velocity was assumed to be zero, the value of V in Eq. 2.17 is simply given by  $V_R$  (the rocket velocity determined by radar),

$$V_R = \sqrt{V_V^2 + V_H^2} \quad (7.3)$$

With this information it was possible to compute a value of  $\rho_1$  from Eq. 2.17, i.e.

$$\rho_1 = \frac{\Delta\rho_2 \sqrt{R_2 T_2}}{\sqrt{2\pi} V \sin \alpha}$$

It was also necessary to assume a value of  $R_2$  and this was taken to be the value for dry air.

At approximately 100 km, it was necessary to examine the atmospheric mean free path to determine whether the gauge package was truly in free molecule flow. Due to the levelling out of the gauge output at pressures above  $10^{-3}$  mm Hg, it was not possible to make accurate determinations of  $\Delta\rho_2$  below 102 km. At this altitude the atmospheric properties do not generally deviate greatly from the standard atmosphere values. The following are values of mean free path taken from the standard atmosphere tables:

<u>Altitude (km)</u>	<u>Mean Free Path (cm)</u>
102	23.2
107	52.2
112	111.7
117	223.9

The Knudsen number for the gauges in the package was based on a mean value of the cross section dimensions of the package. This mean dimension was taken to be 9.5 cm. In the case of gauge 5 which was located in the cylindrical section, the nose cone diameter of 43.7 cm was taken as the representative length. The Knudsen numbers based on these lengths are given below:

<u>Altitude (km)</u>	<u>Kn (gauge 4)</u>	<u>Kn (gauge 5)</u>
102	2.44	.53
107	5.50	1.20
112	11.75	2.56
117	23.6	5.13

Enkenhus (Ref. 47) gives the ratio of measured impact pressure to free stream static pressure as a function of Knudsen number for a range of subsonic and

supersonic Mach numbers. Over the altitude range being considered the Mach number of the flow perpendicular to the rocket axis ranged between 0.9 and 1.5. It is only necessary to consider the correction to the maximum pressure since the correction when the gauge is measuring the minimum pressure is only of secondary importance. Using Enkenhus' experimental results as a guide, the following correction factors were applied to the measured values of  $\Delta p_2$ :

<u>Altitude (km)</u>	<u>Gauge 4 Correction</u>	<u>Gauge 5 Correction</u>
102	1.10	1.39
107	1.03	1.21
112	1.00	1.10
117	1.00	1.03

Except for the case of gauge 5 at the lower altitudes, the corrections are not great and rapidly become unimportant.

Applying the appropriate corrections, the gauge 4 readings were reduced and the calculated values of  $\rho_1$  are indicated in Fig. 73.

For a gauge with this orientation there are two positions during a spin cycle where there will be no velocity component directed into the gauge. These two positions are indicated on Fig. 69. The relation between  $\rho_1$  and the measured quantities at this time is

$$\frac{\rho_2 \sqrt{R_2 T_2}}{\rho_1 \sqrt{R_1 T_1}} = 1$$

By measuring the value of  $\rho_2$  at this position and using the previously calculated value of  $\rho_1$ , a value of  $R_1 T_1$  can be obtained. If there were no outgassing of the gauges on the rocket, this value of  $R_1 T_1$  would be the true value for the atmosphere. If outgassing exists then it gives a measure of the outgassing, since it is an indication of the ambient conditions required to produce the observed gauge reading. An effective ambient pressure can be calculated from

$$(p_1)_{\text{eff.}} = \rho_1 (R_1 T_1)_{\text{eff.}}$$

The values of  $(p_1)_{\text{eff.}}$  calculated during rocket ascent and descent are plotted in Fig. 74.

The signals from the DC amplifier on gauge 5 were treated in the same way as those from gauge 4, with values of  $\rho_1$  and  $(p_1)_{\text{eff.}}$  being calculated during ascent and descent. For gauge 5, the DC signal level remained relatively high causing the amplifier to remain in its lowest gain range during the whole flight. The signal slowly dropped to a value close to the lower amplifier switching voltage and remained there for most of the flight. As a result, the measurement of the AC component of the signal from the DC amplifier was impossible for a large part of the time due to the low ratio of AC to DC in the amplifier output. However, this gauge was equipped with an AC amplifier on the output of the DC amplifier. As a result, the AC component of the signal could be measured accurately, even though it was barely observable on the DC amplifier signal. Figure 75 shows the form of the AC amplifier signal on gauge 5. The AC amplifier record was not continuous since it was

obtained by using the commutator to sample the signal at a rate of 30 times per second. As the record shows this sampling rate was adequate to accurately define the waveform since only the peak-to-peak amplitude was required. To calculate the gauge volume density variation, one requires the AC signal amplitude, the AC amplifier voltage gain, and the slope of the density vs. voltage calibration curve for the ionization gauge at the density value indicated by the DC amplifier. If these quantities are known, then

$$\Delta\rho_2 = \frac{\text{AC signal voltage (peak-to-peak)}}{\text{AC amplifier voltage gain}} \times \left( \frac{d\rho_2}{dv} \right)_5$$

where  $(d\rho_2/dv)_5$  is the slope of the calibration curve for gauge 5.

After applying the appropriate Knudsen number corrections to  $\rho_2$ , the density  $\rho_1$  was calculated at regular intervals during ascent and descent of the rocket (Fig. 73).

A question which may arise is whether one is justified in applying a pressure calibration which was obtained under static conditions to a case in which the gauge conditions are changing at the spin rate. Previous experimenters (Ref. 25) have subjected similar gauges to periodic pressure changes and found that the gauge signal varied in the manner predicted by the static calibration curve. Using the DC amplifier readings for gauge 5, an effective pressure was calculated for the gauge. The values are plotted in Fig. 74 along with the calculated values of  $(p_1)_{\text{eff}}$  for gauge 4. This enables a comparison to be made to see how effective the experiment was in reducing outgassing. It is evident from the values from gauge 4 that some outgassing was still present. However, it was decreasing rapidly in the case of gauge 4, while it remained almost constant for gauge 5. The ratio of  $(p_1)_{\text{eff},5}$  to  $(p_1)_{\text{eff},4}$  reached a value of 5 during the descent portion of the flight. Pre-evacuation of the gauges did reduce the outgassing level observed by them.

Examination of the density profile in Fig. 73 indicates agreement between the ascent and descent data to within 10% in most cases and 20% in the worst case. This is in the range that one might expect considering the possible sources of error. During calibration the gauges indicated a scatter of  $\pm 5\%$ . The specified accuracy for the telemetry system was  $\pm 2\%$ . Then if one considers that the orientation accuracy was between 1 and 3 degrees, then the observed agreement is good. There is no systematic difference between ascent and descent calculated density for gauges 4 or 5. This would indicate that any winds which may have been present were not sufficient to over-ride the measurement errors which were present. Calculations done to consider the magnitude of the wind effect, concluded that winds much higher than 300 feet per second would have been necessary to cause an appreciable difference between the ascent and descent data, especially if they were from the north as the phase information indicated.

The density profile is unusual in that it tends to indicate a minimum in the temperature profile in the atmosphere at approximately 140 km. Standard atmosphere tables do not indicate an inversion at such a low altitude although they do indicate a decrease in the temperature gradient. The existence of a temperature minimum in the atmosphere between 200 and 250 km has been noted by a number of authors (Refs. 59-64) from studying atmospheric density determined from satellite drag data. Since most of their published data was taken during a period of high solar activity this may account for

the minimum temperature occurring at a higher altitude. It is difficult to compare results since most previous rocket data was also obtained during the IGY, and the satellite data for periods of minimum solar activity is not available at low enough altitudes. The exact cause of the minimum temperature is not known, but it has been hypothesized that the concentration of molecular species such as  $O_2$  and  $NO$  may be high enough to radiate sufficient energy and cause a local temperature minimum (Ref. 59,61).

### 7.4.3 Atmospheric Molecular Scale Temperature

It was shown in Sections 2.2.2b and 2.2.2c that in practice, solutions for  $R_1T_1$  could be attained only for certain angles of attack of the rocket. On calculating the angle of attack it is apparent that gauge 3 (pointing rearward) is only useful during ascent and gauge 2 (pointing forward) is only useful during descent.

Equations 2.31 to 2.33 have the general form

$$\frac{\Delta p_2 \sqrt{R_2 T_2}}{\rho_1} = \sqrt{R_1 T_1} F(S, \alpha)$$

After first computing  $\Delta p_2 \sqrt{R_2 T_2} / \rho_1$  from the gauge outputs and other known data, the value of  $F(S, \alpha)$  was then determined for a range of values of  $S$  at the proper value  $\alpha$ . Since  $S = V / \sqrt{2R_1 T_1}$ , the corresponding values of  $\sqrt{R_1 T_1}$  were calculated and a plot of  $\sqrt{R_1 T_1} \cdot F(S, \alpha)$  vs  $S$  was made. The value of  $S$  for which  $\sqrt{R_1 T_1} \cdot F(S, \alpha)$  was equal to  $\Delta p_2 \sqrt{R_2 T_2} / \rho_1$  was the one which enables the true value of  $R_1 T_1$  to be calculated.

The preceding method was used to determine  $R_1 T_1$  during rocket descent using gauge 2. Since this gauge signal was amplified with both AC and DC amplifiers, a useful signal amplitude was obtained throughout the flight. This gauge signal was treated in the same way as described in the analysis of gauges 4 and 5 to determine the value of  $\Delta p_2$  at regular intervals. The quantities  $V$ ,  $\alpha$  and  $\rho_1$  were those calculated previously for gauges 4 and 5. Values of  $R_1 T_1$  were calculated from both the AC and DC amplifier signals but the AC amplifier permitted more accurate determination of  $\Delta p_2$ . The quantity  $R_1 T_1$  was put in the form of a temperature by dividing by the gas constant for dry air  $R_0$ , thus

$$T_M = \frac{R_1 T_1}{R_0} = \text{molecular scale temperature.}$$

The DC amplifier output from gauge 3 permitted values of  $R_1 T_1$  to be calculated for only a limited number of points during the rocket ascent. For much of the time, the ratio of AC to DC signal was so small that  $\Delta p_2$  could not be calculated. No correction to the readings was applied at lower altitude to compensate for near-free-molecule flow effects. Since the ratio of 2 gauge readings was involved in  $\Delta p_2 / \rho_1$ , the use of uncorrected readings in determining  $\Delta p_2$  and  $\rho_1$  should cause little error as the correction for either value was only 10% in the worst case. The calculated values of  $T_M$  are plotted in Fig. 76.

There was a considerable scatter in the calculated value of  $T_M$  near apogee due to the value of  $S$  becoming small, and the function  $\sqrt{R_1 T_1} \cdot F(S, \alpha)$

becoming relatively insensitive to changes in S for the angles of attack occurring near apogee. Figure 77 illustrates the solution for one of the points close to apogee and indicates how errors in the gauge readings can be greatly magnified. If one considers a  $\pm 10\%$  error in  $\Delta\rho_2\sqrt{R_2T_2}/\rho_1$ , then the corresponding error in  $R_1T_1$  is 32% and 37%. At lower altitudes where the speed ratio is greater the value of  $\Delta\rho_2\sqrt{R_2T_2}/\rho_1$  is more sensitive to changes in S, and the errors are comparable. In the second example illustrated in Fig. 78, an error of  $\pm 10\%$  in  $\Delta\rho_2\sqrt{R_2T_2}/\rho_1$  results in corresponding errors of 8% and 11% in  $R_1T_1$ . If one wishes to make accurate determinations of  $R_1T_1$  at higher altitudes, then it is necessary to have very accurate gauge calibrations and orientation measurements. The effects of wind would also be more important than in the case of the density determinations. Thus it is important that the orientation measurements be accurate enough to allow the wind velocities to be measured.

Having the values of  $\rho_1$  and  $R_1T_1$ , the ambient pressure  $p_1$  was calculated and is plotted in Fig. 74 for comparison with the effective outgassing pressures for the gauges. This illustrates once more that, although the outgassing was reduced by pre-evacuating the gauges, it was not eliminated.

For comparison purposes and to check the self-consistency of the measurements, Eq. 2.46 was used to calculate the density profile using the calculated temperatures. It was found that the temperatures measured using gauge 2 were too small at the lower altitudes. In order to determine the amount of the error, a temperature profile was fitted to the density profile also using the hydrostatic equation, and this is also plotted in Fig. 76. It is believed that the discrepancy in the temperatures determined using gauge 2 were due to a sudden jump in the gauge calibration. This was observed to have occurred during ascent and resulted in a decrease of approximately 25% in the gauge signal used to calculate  $\Delta\rho_2$ . This could explain the large difference and again points out the need for accurate, repeatable gauges in making the temperature measurements.

## 8. RECOMMENDATIONS

Although the experiment achieved its objectives, certain aspects of it should be improved to yield better information.

(1) One problem which arose concerned the pumping system. The cold air temperature apparently cooled the diffusion pump sufficiently to cause the pumping action to be greatly reduced. As a result the pressure in the nose cone rose above  $10^{-3}$  mm. For winter firings the pumping system could be modified in two ways. The complete pumping system could be enclosed in a thin polyethylene envelope so that the warm air being pumped through the heat shield would also warm the diffusion pump. A second solution would be to wrap insulation around the diffusion pump before it was exposed to the cold weather and also to control the power input to the diffusion pump heaters. For summer firings the pumping system could be used as it was. The possibility should also be considered of installing an auxiliary pump in the nose cone to maintain a low pressure in the cone during the flight. An ion pump or a zeolite pump with a speed of 20 litres per second would probably be sufficient for this purpose. With this auxiliary system, the diffusion pump system could be detached while the launcher was horizontal, thus eliminating the possibility of its failing to release properly when the launcher was vertical.

(2) Determination of the rocket axis orientation was complicated by the distortion of the earth's magnetic field by the presence of the rocket. While the correction applied to the data to account for the field distortion is not large, it still means that the orientation is not known accurately enough to yield accurate wind information. If the magnetic field and the sun's direction must be used as references, then the position of the sun could be selected to make the mathematical solution for orientation less sensitive to errors in the data. By choosing a sun azimuth angle  $90^\circ$  greater or less than the magnetic field azimuth, the intersection of the two families of curves (Fig. 56) would be almost orthogonal. For this experiment the two sets of curves were almost tangent for some of the intersection points, making the solution very sensitive to small angular errors. A primary reason for firing the rocket eastward with the sun low in the west was to make the sun's direction close to perpendicular to the rocket axis. This would allow the sun sensors to observe the sun even if the precession cone of the rocket axis became large. There are a number of factors which complicate the selection of a firing time. The intersecting curves in the graphical solution depend on the precession cone angle, which cannot be accurately predicted. Since the sun's positions at sunrise and sunset limit the choice of a firing time, it may not always be possible to time the firing for a more accurate graphical solution. As a result, the firing time chosen will usually be a compromise reached by attaching varying importance to the complicating factors.

(3) The experiment indicates the feasibility of measuring  $R_1 T_1$  or the molecular scale temperature with gauges oriented in the way that gauges 2 and 3 were positioned. It is also obvious that AC amplifiers as well as DC amplifiers should be provided for all gauges which have an AC component in their signal. In this way solutions could be attained during ascent and descent for comparison. The orientation of the gauges at angles of  $45^\circ$  and  $135^\circ$  makes solutions for  $R_1 T_1$  possible over a large part of the trajectory but not near apogee. Since this is due to the angle of attack being in an insensitive range, it may be possible to produce a more suitable range of angles by increasing the angle of the precession cone. The UTIAS rocket experienced only a small coning motion compared to the much larger coning which the Black Brant rockets usually experienced. Since the rockets are usually fired with spin rates below 1 cps, it may be possible to increase the coning by using a spin rate below 3 cycles per second, although stability problems may be encountered at low altitude.

(4) The use of cold cathode ionization gauges had both advantages and disadvantages. These gauges were extremely rugged and gave higher current output than hot cathode ionization gauges. Although the hot cathode gauges may be more accurate and give better repeatability in making pressure measurements, they present greater electrical and mechanical problems if they are used. From the density data obtained with gauges 4 and 5, it is seen that the results from the different gauges agree within 10 to 20%. This agreement is more remarkable if one considers that gauge 4 was operating in one stable mode during ascent and another during descent. In addition gauge 5 was operating at a much higher background pressure level. Calibration data indicates that if the internal gauge surfaces are kept free of contamination, the calibration remains unchanged for long periods of time.

One of the major disadvantages of the cold cathode ionization gauge is the presence of instabilities in the glow discharge. This can be tolerated if it is discovered during the gauge calibration, as gauge 4 demon-

strated. However, small instabilities can occur which may not be evident during the gauge calibration. If cold cathode gauges were to be used again, then a study of the effects of voltage and magnetic field should be carried out to try to eliminate the instabilities in the discharge.

(5) While the method of pre-evacuating the gauges does reduce the outgassing level considerably, much improvement is still possible. Perhaps the best way of reducing the outgassing significantly would be to completely separate the nose cone or the gauges from the motor. A second alternative would be to enclose all the equipment in a package which was contained within the nose cone. If the complete package were pre-evacuated and then ejected from the nose cone, then all the surfaces would also be outgassed. However, this could entail considerable effort in miniaturizing the equipment if a number of gauges were required.

## 9. CONCLUSIONS

The data obtained from the ionization gauges indicated that the method of pre-evacuation of the gauges was successful in reducing the background density around the gauges. Comparison of the effective pressure measured by gauges 4 and 5, shows a reduction by a factor of 5 in the effective pressure of the gas cloud. With some minor modifications to the pumping system, an even greater reduction could probably be achieved.

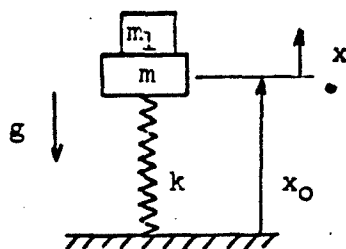
Above 100 km, the density profiles measured during ascent and descent show good agreement. While the phase measurements indicate the presence of winds, these were not of sufficient velocity to affect the density measurements appreciably. The measured density indicates the presence of a local temperature maximum at approximately 140 km. The experimental errors do not appear to be sufficiently large to account for all of this apparent inversion. The temperature profile calculated on the basis of the density profile exhibits this inversion, although it is not of large magnitude.

The experiment demonstrated the feasibility of measuring the quantity  $R_1 T_1$  under conditions of free molecule flow with suitably oriented gauges. It was also apparent that accurate, repeatable gauges are a necessity, and rocket attitude measurements must be accurate to within  $1^\circ$  or better if the wind velocity was to be determined. The accuracy of the measurements near apogee was not sufficient to verify the slight temperature inversion indicated by the density profile.

## APPENDIX A

### Analysis of the Action of the Extension and Braking System

A simple analysis of the extension and braking system described in Section 3.2.5 was carried out assuming a constant friction force (Ref. 65). The system can be represented by the following spring-mass system:



The following symbols describe the system:

$m_1$  = mass of the tip section which is separated and ejected

$m$  = mass of the gauge package, tubes, etc, which remains with the rocket

$g$  = acceleration of gravity

$F$  = retarding friction force whose direction is opposite to the motion

$x_0$  = reference position of the system with no external forces acting on it

$x$  = displacement of the masses from the reference position

$k$  = spring constant of the coil spring.

When the spring is compressed and then released, the following equation of motion applies:

$$M\ddot{x} + kx + k \left( \frac{Mg + F}{k} \right) = 0 \quad \text{for } \dot{x} > 0 \quad (\text{A.1})$$

where  $M = m + m_1$ .

This has the solution

$$x = -a + (a - d) \cos \omega t \quad (\text{A.2})$$

$$\dot{x} = (d-a)\omega \sin \omega t \quad (\text{A.3})$$

where

$$a = (Mg + F)/k$$

$x = -d$  = the initial compression of the spring

$$\omega = \sqrt{k/M}$$

and

$t$  = time from the release of the compressed spring.

This solution describes the motion up until the time when the nose cone and the gauge package separate. After this time the gauge package is decelerated by the spring. The equation of motion for the gauge package after separation is

$$m\ddot{x} + kx + k(mg + F)/k = 0 \quad (\text{A.4})$$

The general solution of this is

$$x = -a_1 + B \sin(\omega_1 t - \eta) \quad (\text{A.5})$$

$$\dot{x} = B\omega_1 \cos(\omega_1 t - \eta) \quad (\text{A.6})$$

where

$B$  and  $\eta$  are arbitrary constants

$$a_1 = (mg + F)/k$$

and

$$\omega_1 = \sqrt{k/m}.$$

Determination of  $B$  and  $\eta$  requires the time of separation,  $t_1$ , and the velocity at separation,  $V_s$ , to be calculated from Eqs. A.2 and A.3. The position when separation occurs is  $x = -a_1$ . The time and velocity at separation are given by

$$\sin\omega_1 t_1 = \frac{\sqrt{(a-d)^2 + (a-a_1)^2}}{-(a-d)} \quad (\text{A.7})$$

and

$$V_s = \omega \sqrt{(a-d)^2 + (a-a_1)^2} \quad (\text{A.8})$$

Using these as boundary conditions for Eqs. A.5 and A.6, the position of the gauge package after separation is

$$x = -a_1 + \frac{\omega}{\omega_1} \sqrt{(a-d)^2 + (a-a_1)^2} \sin(\omega_1 t') \quad (\text{A.9})$$

where  $t' = t - t_1$ .

From Eq. A.9 the maximum extension of the gauge package is given by

$$x = -a_1 + \sqrt{\frac{m}{M}} \cdot \sqrt{(d-a)^2 + (a-a_1)^2} \quad (\text{A.10})$$

The equation of motion of the package after the point of maximum extension is

$$m \ddot{x} + kx + k \left( \frac{mg - F}{k} \right) = 0 \quad (\text{A.11})$$

It is desirable that the acceleration on the return stroke be zero at the point of maximum extension. From Eqs. A.10 and A.11 this requirement results in the following relation between  $d$  and  $F$ :

$$\frac{2F}{k} = \sqrt{\frac{m}{M}} \cdot \sqrt{(d-a)^2 + (a-a_1)^2} \quad (\text{A.12})$$

Equation A.12 permits the relation between  $d$  and  $F$  to be determined and hence the extension given in Eq. A.10 can be calculated as a function of  $d$ .

## APPENDIX B

### Telemetry Channel Allocations for the Experiment

a) Subcarrier Oscillators:

The main telemetry channels for the experiment were allocated as shown in the following table:

<u>Channel Frequency</u>	<u>Function</u>
400 cps	Gauge Package Extension (Event Oscillator)
560 cps	Gauge Package Extension (Event Oscillator)
730 cps	Gauge Package Extension (Event Oscillator)
3.9 kc	HP1 (Stagnation Pressure), DC amplifier output
5.4 kc	* CCG1 ( $\beta = 0^\circ$ ) DC amplifier output HP2 (Cone Surface Pressure) DC amplifier output
7.35 kc	* CCG2 ( $\beta = 45^\circ$ ) DC amplifier output M.P.1 (Stagnation Pressure) DC amplifier output
10.5 kc	* CCG3 ( $\beta = 135^\circ$ ) DC amplifier output MP2 (Cone Surface Pressure) DC amplifier output
14.5 kc	* CCG4 ( $\beta = 90^\circ$ ) DC amplifier output
22.0 kc	CCG5 ( $\beta = 90^\circ$ ) DC amplifier output
30.0 kc	CCG4 ( $\beta = 90^\circ$ ) DC amplifier output
40.0 kc	45° sun sensor/lateral magnetometer
52.5 kc	65° sun sensor/Z-axis magnetometer
70.0 kc	Z-axis linear accelerometer, + 20g to -3g Commutator, 30 channels at 10 cps

\* The SCO inputs were transferred from the stagnation and cone surface pressure gauges to the cold cathode ionization gauges when the nose cone was ejected. CCG1 to 4 are located in the gauge package.

The event oscillators do not provide quantitative information but merely given an on-off indication. Their method of connection was described in Section 3.2.7.

b) Commutator

<u>Channel</u>	<u>Function</u>
1	0 volt calibration pulse
2	5 volt calibration pulse
3	Lateral accelerometer 1
	* CCG2 AC amplifier output
4	Lateral accelerometer 2
	* CCG5 AC amplifier output
5	HP2, DC amplifier range
6	HPL, DC amplifier range
7	Nose Cone thermistor
8	CCG4, DC amplifier range
9	CCG5, DC amplifier range
10	CCG1, DC amplifier range
11	CCG2, DC amplifier range
12	CCG3, DC amplifier range
13	CCG2, AC amplifier output
14	CCG5, AC amplifier output
15	Nose cone thermistor 2
16	CCG1, thermistor
17	CCG2, thermistor
18	CCG3, thermistor
19	CCG4, thermistor
20	CCG5, thermistor
21	Subcommutator channel indicator
22	CCG2, AC amplifier range
23	CCG2, AC amplifier output
24	CCG5, AC amplifier output
25	CCG5, AC amplifier range
26	Subcommutator output
27	Timer and separation mechanism firing indicator
28	Separation mechanism thermistor
29	Master
30	Master

\* The inputs to channels 3 and 4 were switched from the lateral accelerometers to the AC amplifier outputs when the nose cone was ejected. The three channels allocated to sample each AC amplifier were spaced to sample the AC signal at equal time intervals. This sampling rate of 30 times per second was fast enough to adequately define the 3 cps waveform.

Nose cone thermistors 1 and 2 measured the temperatures of the stagnation and surface pressure gauges respectively.

The timer and firing indication was provided by voltage signals of different magnitudes, corresponding to various possible states of the firing system.

<u>Channel</u>	<u>Function</u>
1	MP2, DC amplifier range
2	Nose cone thermistor 1
3	Nose cone thermistor 2
4	Amplifier board thermistor
5	Electronics frame thermistor
6	Telemetry 26 volt monitor
7	UTIAS Internal power, 28 volt monitor
8	UTIAS Internal power, + 14.6 volt monitor
9	UTIAS Internal power, -14.6 volt monitor
10	Beacon -6.5 volt monitor
11	CCG1, High voltage supply monitor
12	CCG2, High voltage supply monitor
13	CCG3, High voltage supply monitor
14	CCG4, High voltage supply monitor
15	CCG5, High voltage supply monitor
16	Telemetry 250 volt monitor
17	Battery box thermistor
18	H.P.1, DC amplifier range
19	H.P.2, DC amplifier range
20	MPI, DC amplifier range

**BLANK PAGE**

## REFERENCES

1. Newell, H.E., Jr. High Altitude Rocket Research, Academic Press, Inc., New York, 1953.
2. Boyd, R.L.F.  
Seaton, M.J. (Editors) Rocket Exploration of the Upper Atmosphere, Pergamon Press Ltd., London, 1954.
3. Kondrat'yev, K. Ya.  
Filipovich, O.P. The Thermal State of Upper Atmospheric Layers, NASA TT F-103, October 1962.
4. Kaplan, J.  
Schilling, G.F.  
Kallman, H.K. Methods and Results of Upper Atmosphere Research, Geophysical Research Papers, No. 43 Air Force Cambridge Research Center, Report AFCRC-TR-224, November, 1955.
5. Newell, H.E., Jr. Physics of the Upper Atmosphere, Academic Press, New York and London, 1960.
6. Garstens, M.A.  
Newell, H.E., Jr.  
Siry, J.W. (Editors) Upper Atmosphere Research Report No. 1, Naval Research Laboratory Report No. R-2955, October 1946.
7. Newell, H.E., Jr.  
Siry, J.W. (Editors) Upper Atmosphere Research Report No. IV Naval Research Laboratory Report R-3171, October 1947.
8. LaGow, H.E.           Artic Upper-Atmosphere Pressure and Density Measure-  
Ainsworth, J.           ments with Rockets, Journal of Geophysical  
Research, Volume 61, No. 1, March, 1956.
9. Havens, R.J.  
Koll, R.T.  
LaGow, H.E. The Pressure, Density and Temperature of the Earth's Atmosphere to 160 Kilometers, Journal of Geophysical Research, Vol. 57, No. 1, March, 1952.
10. Ainsworth, J.E.  
Fox, D.F.  
LaGow, H.E. Upper Atmosphere Structure Measurements Made With the Pilot-Static Tube, Journal of Geophysical Research, Volume 66, No. 10, Oct. 1961.
11. Peterson, J.W.  
McWatters, K.D. The Measurement of Upper-Air Density and Temperature by Two Radar-Tracked Falling Spheres, NASA CR-29, April, 1964.
12. Faire, A.C.  
Champion, K.S.W. Falling Sphere Measurements of Atmospheric Density, Temperature and Pressure Up to 115 km. Space Research V, North Holland Publishing Co., Amsterdam, 1965.
13. Broglio, L. First Density Experiment with San Marco Instrumentation, Space Research V, North Holland Publishing Co., Amsterdam, 1965.

14. Smith, W.,  
Katchen, L.  
Sacher, P.  
Sartz, P. and  
Theon, J.                      Temperature, Pressure, Density, and Wind  
Measurements with the Rocket Grenade Experi-  
ment, 1960-1963, NASA TR R-211, October, 1964.
  
15. Stroud, W.G.  
Nordberg, W.  
Bandeem, W.R.  
Bartman, F.L.  
Titus, P.                      Rocket Grenade Measurements of Temperatures  
and Winds in the Mesosphere over Churchill,  
Canada, Presented at the IAS 28th Annual  
Meeting, New York, New York, January 25-27,  
1960, IAS Paper No. 60-47.
  
16. Stroud, W.G.  
Nordberg, W.  
Bandeem, W.R.  
Bartman, F.L.  
Titus, P.                      Rocket Grenade Measurements of Temperature  
and Winds in the Mesosphere Over Churchill,  
Canada, Space Research I, North Holland Pub-  
lishing Co., Amsterdam, 1960.
  
17. Groves, G.V.                      Meteorological and Atmospheric Structure  
Studies with Grenades, Space Research IV,  
North Holland Pub. Co., Amsterdam, 1964.
  
18. King-Hele, D.G.  
Rees, J.M.                      Scale Height in the Upper Atmosphere Derived  
From Changes in Satellite Orbits, Proceedings  
of the Royal Society (London), Vol. 270 A, 1962.
  
19. Izakov, M.N.                      Some Problems of Investigating the Structure  
of the Upper Atmosphere and Constructing its  
Model, Space Research V, North Holland Pub.,  
Co., Amsterdam, 1965.
  
20. Martin, H.A.  
Neveling, W.  
Priester, W.  
Roemer, M.                      Model of the Upper Atmosphere From 130 Through  
1600 km, Derived from Satellite Orbits, Space  
Research II, North Holland Publishing Co,  
Amsterdam, 1961.
  
21. Poloskov, S.M.                      Upper Atmosphere Structure Parameters Accord-  
ing to Data Obtained from USSR Rockets and  
Satellites During IGY. Space Research I,  
North Holland Publishing Company, Amsterdam, 1960.
  
22. Roemer, M.                      Exospheric Densities Deduced From Satellite  
Drag Data, Space Research IV, North Holland  
Pub. Co., Amsterdam, 1964.
  
23. Horowitz, R.  
LaGow, H.E.                      Summer-Day Auroral-Zone Atmospheric Structure  
Measurements from 100 to 210 Kilometers,  
Journal of Geophysical Research, Vol. 63, No.4,  
December 1958.
  
24. LaGow, H.E.  
Horowitz, R.  
Ainsowrth, J.                      Rocket Measurements of the Arctic Upper Atmos-  
phere, Annales de Geophysique, Tome 14, Fas-  
cicule 2, Avril-Juin, 1958.

25. Horowitz, R.  
LaGow, H.E. Upper Air Pressure and Density Measurements From 90 to 220 km with the Viking 7 Rocket, Journal of Geophysical Research, Vol. 62, No.1 March, 1957.
26. Pfister, W.  
Ulwick, J.C. Effects of Rocket Outgassing on RF Experiments, Radio Science, Journal of Research NBS/UNNC-URSI, Volume 69D, No. 9, September, 1965.
27. Tausch, D.R.  
Carignan, G.R.  
Niemann, H.B.  
Nagy, A.F. The Thermosphere Probe Experiment, The University of Michigan, ORA Report 07065-1-S, Ann Arbor, March, 1965.
28. Equations, Tables and Charts for Compressible Flow, NACA Report 1135, 1953.
29. U.S. Standard Atmosphere, 1962, U.S. Government Printing Office, Washington, Dec. 1962.
30. Matthews, M.L. An Experimental Investigation of Viscous Effects on Static and Impact Pressure Probes in Hypersonic Flow, Guggenheim Aeronautical Laboratory, California Institute of Technology, Hypersonic Research Project, Memorandum No. 44, June, 1958.
31. Chambré, P.L. The Theory of the Impact Tube in a Viscous Compressible Gas, University of California, Institute of Engineering Research, Report No. HE-150-50, Nov. 1, 1948.
32. Schaaf, S.A.  
Talbot, L. Handbook of Supersonic Aerodynamics, Volume 5, Section 16, Mechanics of Rarefied Gases, U.S. Government Printing Office, Washington, D.C. Feb. 1959.
33. Staff of the Computing Center, Center of Analysis, Massachusetts Institute of Technology. Tables of Supersonic Flow Around Cones, Technical Report No. 1, 1947.
34. Lin, T.C.  
Schaaf, S.A.  
Sherman, F.S. Boundary Layer Effect on the Surface Pressure of an Infinite Cone in Supersonic Flow. University of California, Institute of Engineering Research, Report No. HE-150-80, March 5, 1951.
35. Talbot, L.  
Koga, T.  
Sherman, P.M. Hypersonic Viscous Flow Over Slender Cones, NASA TN 4327, September, 1958.
36. Talbot, L. Viscosity Corrections to Cone Probes in Rarefied Supersonic Flow at a Nominal Mach Number of 4, University of California, Institute of Engineering Research, Report No. HE-150-113, June 1, 1953.

37. Probst, R.F.  
Kemp, N.H. Viscous Aerodynamic Characteristics in Hyper-sonic Rarefied Gas Flow, Journal of the Aero/Space Sciences, Vol. 27, No. 3, March 1960.
38. Patterson, G.N. Molecular Flow of Gases, John Wiley and Sons, Inc., New York, 1956.
39. Patterson, G.N. Theory of Free-Molecular Orifice-Type Probes in Isentropic and Non-Isentropic Flow, UTIA Report No. 41 (Revised) May 1959.
40. Tsien, H.S. Superaerodynamics, Mechanics of Rarefied Gases, J. of Aeronautical Sciences, Vol. 13 No. 12 December, 1946.
41. Liu, V.C. On Pitot Pressure in an Almost-Free Molecule Flow: A Physical Theory for Rarefied Gas Flow, Journal of the Aero/Space Sciences, Vol. 25, No. 12, Dec, 1958.
42. Mikhnevich, V.V. Atmospheric Density at Heights of 100 to 350 km, Space Research V, North Holland Publishing Co., Amsterdam, 1965.
43. Ivanovsky, A.I.  
Repnev, A.I. Interaction of Instruments for Measuring Structural Parameters of Atmosphere with the Rarefied-Gas Flow, Space Research V, North-Holland Publishing Company, Amsterdam, 1965.
44. Manring, E.  
Bedinger, J. Winds in the Atmosphere From 80 to 230 km, Space Research I, North Holland Publishing Co., Amsterdam, 1960.
45. Nowlan, F.S. Analytic Geometry, McGraw Hill Book Company, Inc., New York, 1946.
46. Greenhow, J.S.  
Neufeld, E.L. Measurements of Turbulence in the Upper Atmosphere, Proceedings of the Physical Society of London, Vol. 74, Part 1, 1959.
47. Enkenhus, K.R. Pressure Probes at Very Low Density, University of Toronto, Institute of Aerophysics, Report No. 43, Jan. 1957.
48. Dushman, S. Scientific Foundations of Vacuum Technique, John Wiley and Sons, Inc., New York, 1962.
49. Davis, W.T. Lag in Pressure Systems at Extremely Low Pressures, NACA TN 4334, Sept. 1958.
50. Tiffany, A. A Simple and Rapid Method of Evaluating the Response Time of Pressure Measuring Systems, Aircraft Research Association Limited, Wind Tunnel Note No. 16, July 1957.

51. Sinclair, A.R.  
Robins, W. A Method for the Determination of the Time Lag in Pressure Measuring Systems Incorporating Capillaries, NACA TN 2793, September 1952.
- 52 . Metal Finishing, Guidebook-Directory, 29th Edition, Metals and Plastics Publications, Inc., Westwood, N.J., 1961.
53. Cairns, F.V.  
Cox, L.G.  
Craven, J.H.  
Jones, S.G.  
O'Hara, D.  
Pulfer, J.K.  
Steele, K.A. January 1964 Sounding Rocket Launchings at Churchill Research Range, Rockets AA-II-25, AA-II-41, AD-II-42, National Research Council, Radio and Electrical Engineering Division, Report ERB-679, Ottawa, June, 1964.
54. USAF Office of Aerospace Research. Churchill Research Range, Fort Churchill, Manitoba, Range Users Hand Book.
55. U.S. Navy Hydrographic Office. American Practical Navigator, Bowditch. U.S. Government Printing Office, Washington, 1962.
56. U.S. Naval Observatory The Nautical Almanac for the Year 1965. U.S. Government Printing Office, Washington, 1963.
57. Panofsky, W.H.K.  
Phillips, M. Classical Electricity and Magnetism, Addison-Wesley Publishing Company, Inc., Reading, Mass, 1955.
58. Synge, J.L.  
Griffith, B.A. Principles of Mechanics, McGraw Hill Book Company, Inc., New York, 1949.
59. Paetzold, H.K. Solar Activity Effects in the Upper Atmosphere Deduced From Satellite Observations, Space Research III, North Holland Publishing Co., Amsterdam, 1962.
60. Paetzold, H.K.  
Zschörner, H. The Structure of the Upper Atmosphere and its Variations After Satellite Observations, Space Research II, North Holland Publishing Company, Amsterdam, 1961.
61. Kallman-Bijl, H.K.  
Sibley, W.L. Diurnal Variation of Temperature and Particle Density Between 100 km and Approximately 500 km, Space Research IV, North Holland Publishing Company, Amsterdam, 1964.
62. King-Hele, D.G.  
Walker, D.M.C. Upper-Atmosphere Density During the Years 1957 to 1961, Determined From Satellite Orbits, Space Research II, North Holland Publishing Company, Amsterdam, 1961.

63. Priester, W.  
Martin, H.A. Earth Satellite Observations and the Upper  
Atmosphere, Nature, Vol. 188, No. 4746,  
October 15, 1960.
64. King-Hele, D.G. Properties of the Atmosphere Revealed by  
Satellite Orbits, Progress in the Astronautical  
Sciences, Vol. 1, North Holland Publishing  
Company, Amsterdam, 1962.
65. Myklestad, N.O. Fundamentals of Vibration Analysis, McGraw  
Hill Book Company, Inc., New York, 1956.

TABLE I

$M_1$	$p/p_1$	$0.92 \frac{\rho_1 v^2}{p_1}$	$0.92 \frac{\rho_1 v^2}{p_1} + 0.46$
1	1.89	1.29	1.75
1.5	3.41	2.90	3.36
2	5.64	5.15	5.61
3	12.06	11.59	12.05
4	21.06	20.6	21.06

**BLANK PAGE**

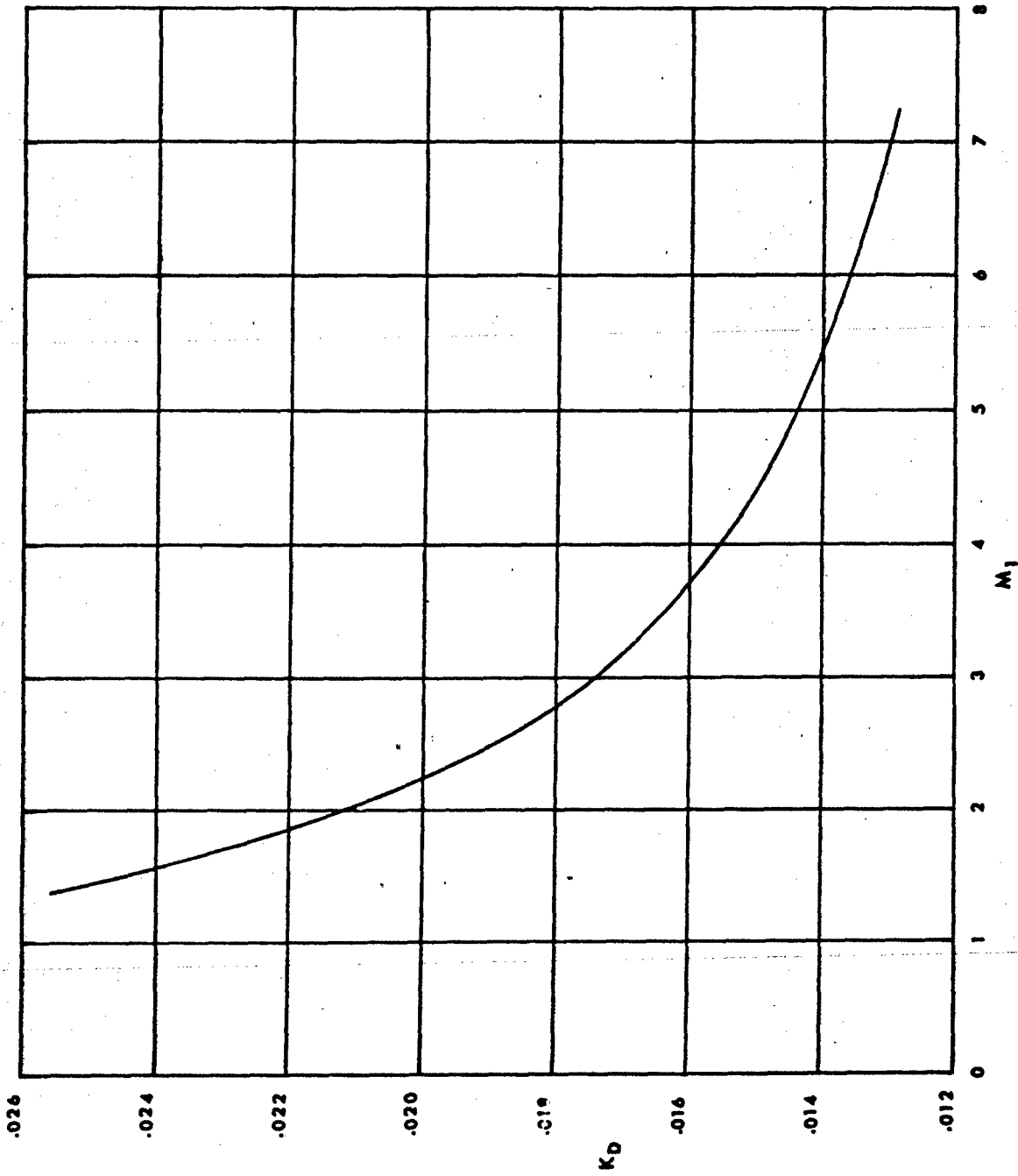


FIG. 1 SURFACE PRESSURE COEFFICIENT  $K_D$  FOR A CONE WITH A SEMI-VERTEX ANGLE OF  $5^\circ 42'$  AS A FUNCTION OF FREE STREAM MACH NUMBER  $M_1$

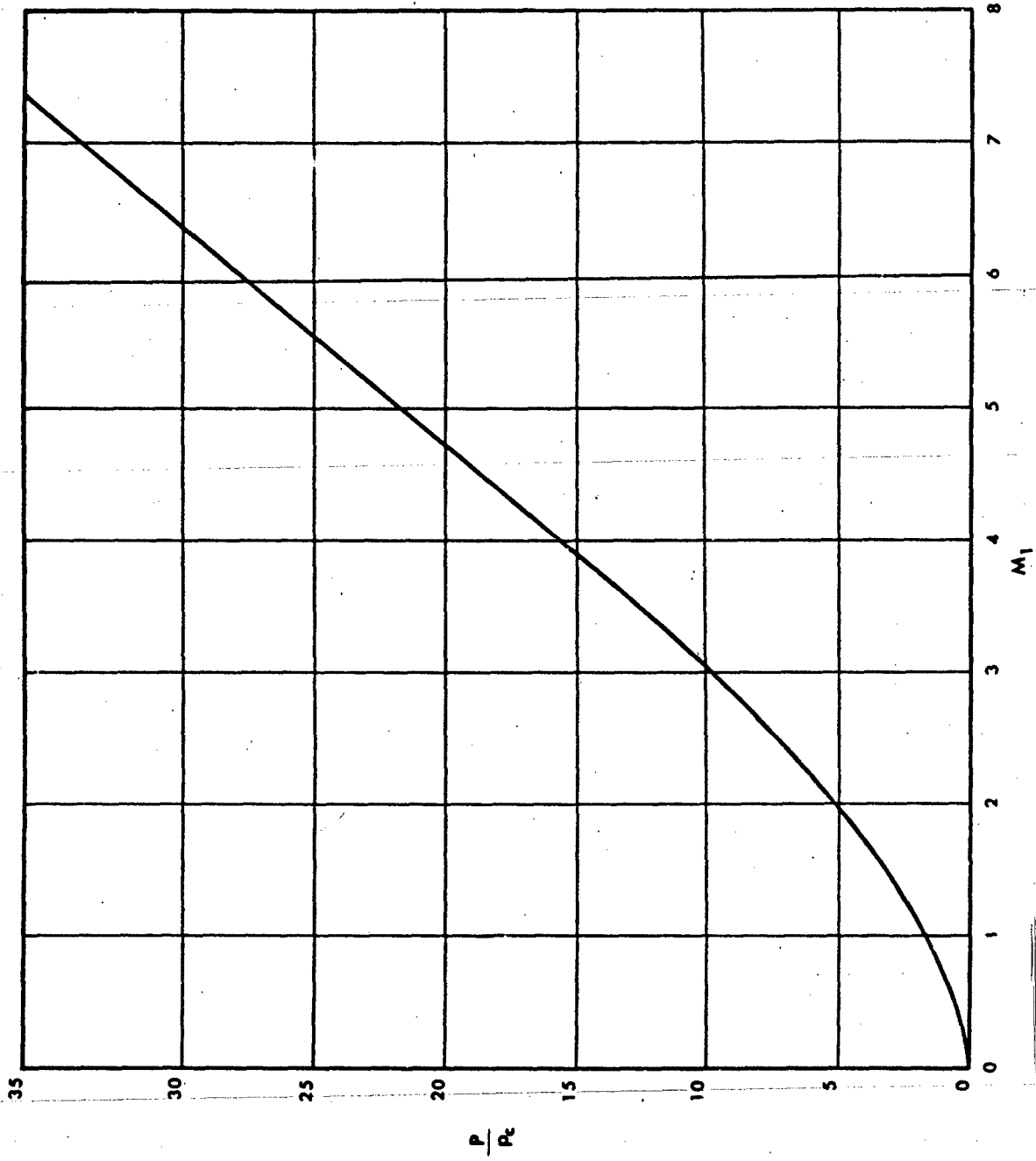


FIG. 2 RATIO OF STAGNATION PRESSURE TO NOSE CONE SURFACE PRESSURE AS A FUNCTION OF FREE STREAM MACH NUMBER

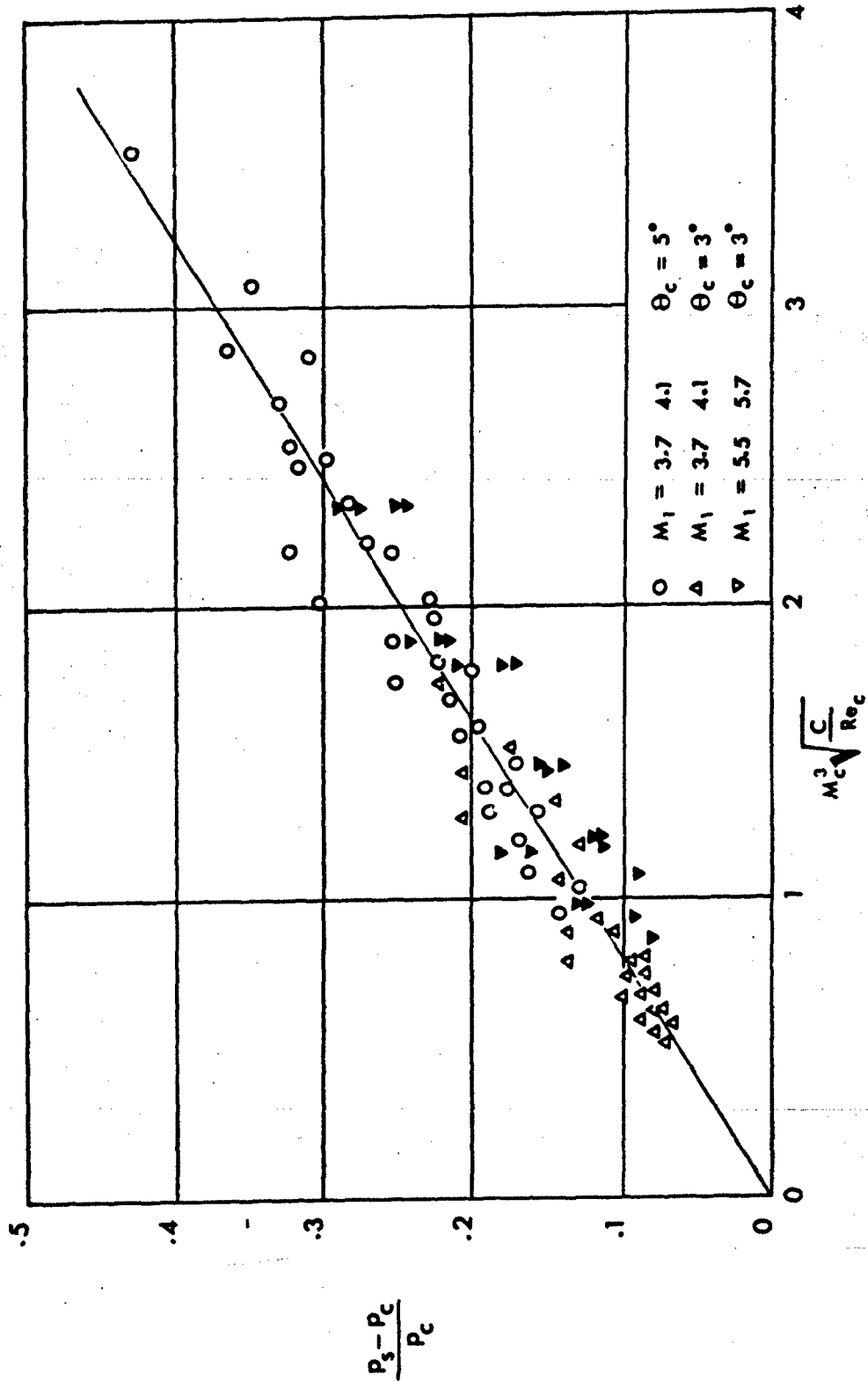


FIG. 3 CORRECTIONS TO THE MEASURED SURFACE PRESSURE CAUSED BY BOUNDARY LAYER GROWTH

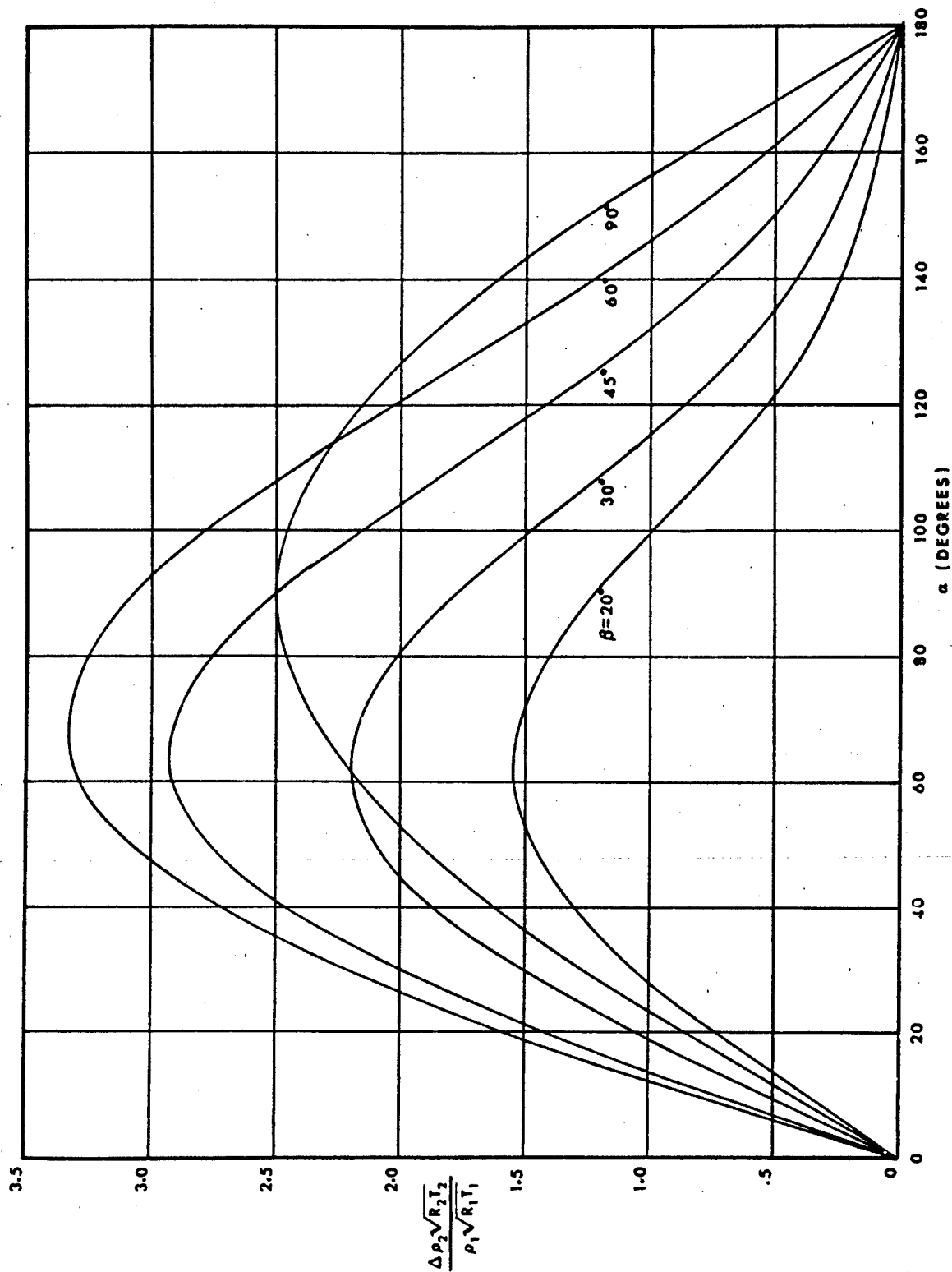


FIG. 4  $\frac{\Delta p_2 \sqrt{R_2 T_2}}{\rho_1 \sqrt{R_1 T_1}}$  AS A FUNCTION OF  $\alpha$  FOR  $\beta = 20^\circ, 30^\circ, 45^\circ, 60^\circ$  and  $90^\circ$  and  $S = 1$

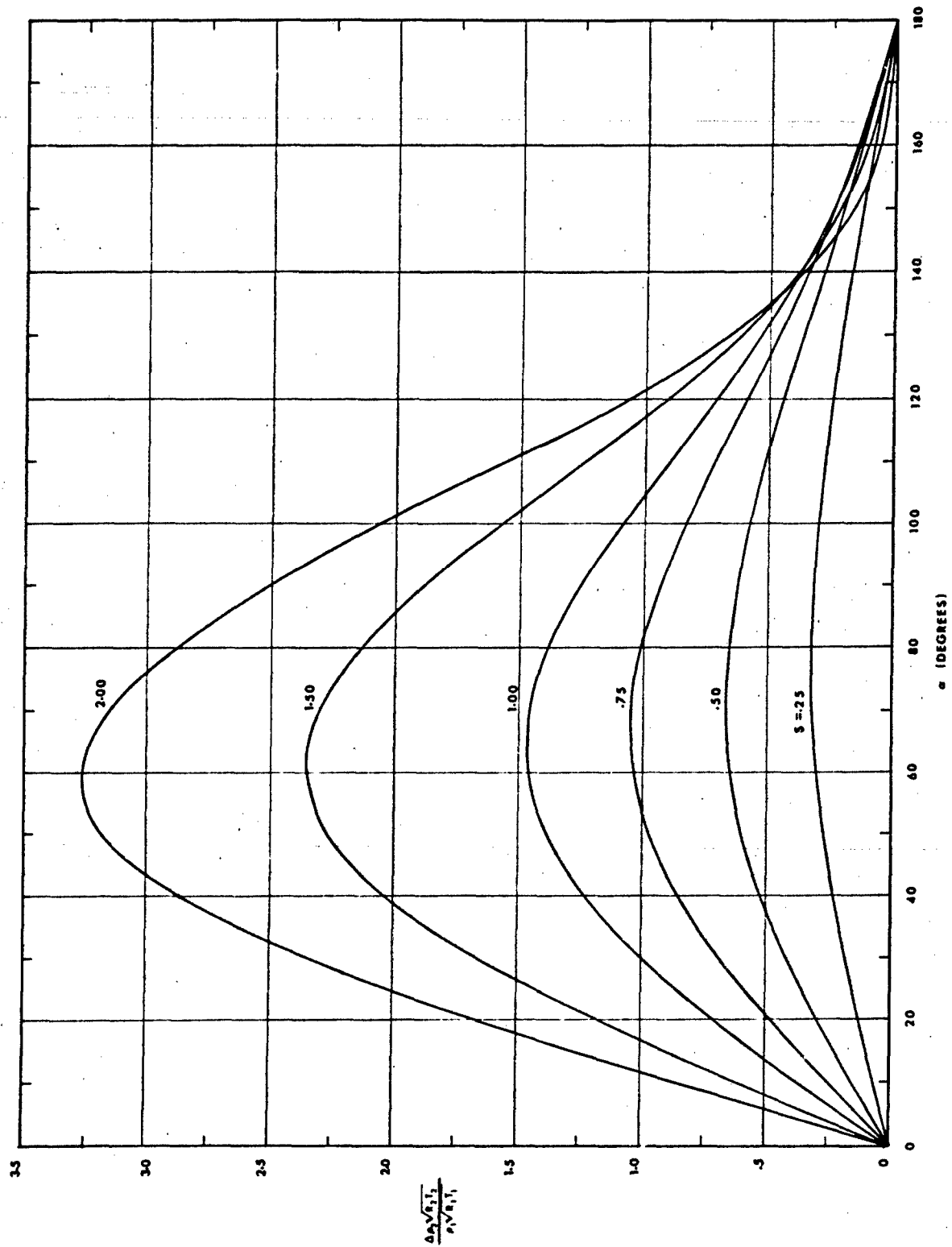


FIG. 5  $\frac{\Delta p \sqrt{R_2 T}}{\rho_1 \sqrt{R_1 T}}$  AS A FUNCTION OF  $\alpha$  FOR  $\beta = 45^\circ$  and  $S = .25, .50, .75, 1.00, 1.50$  and  $2.00$

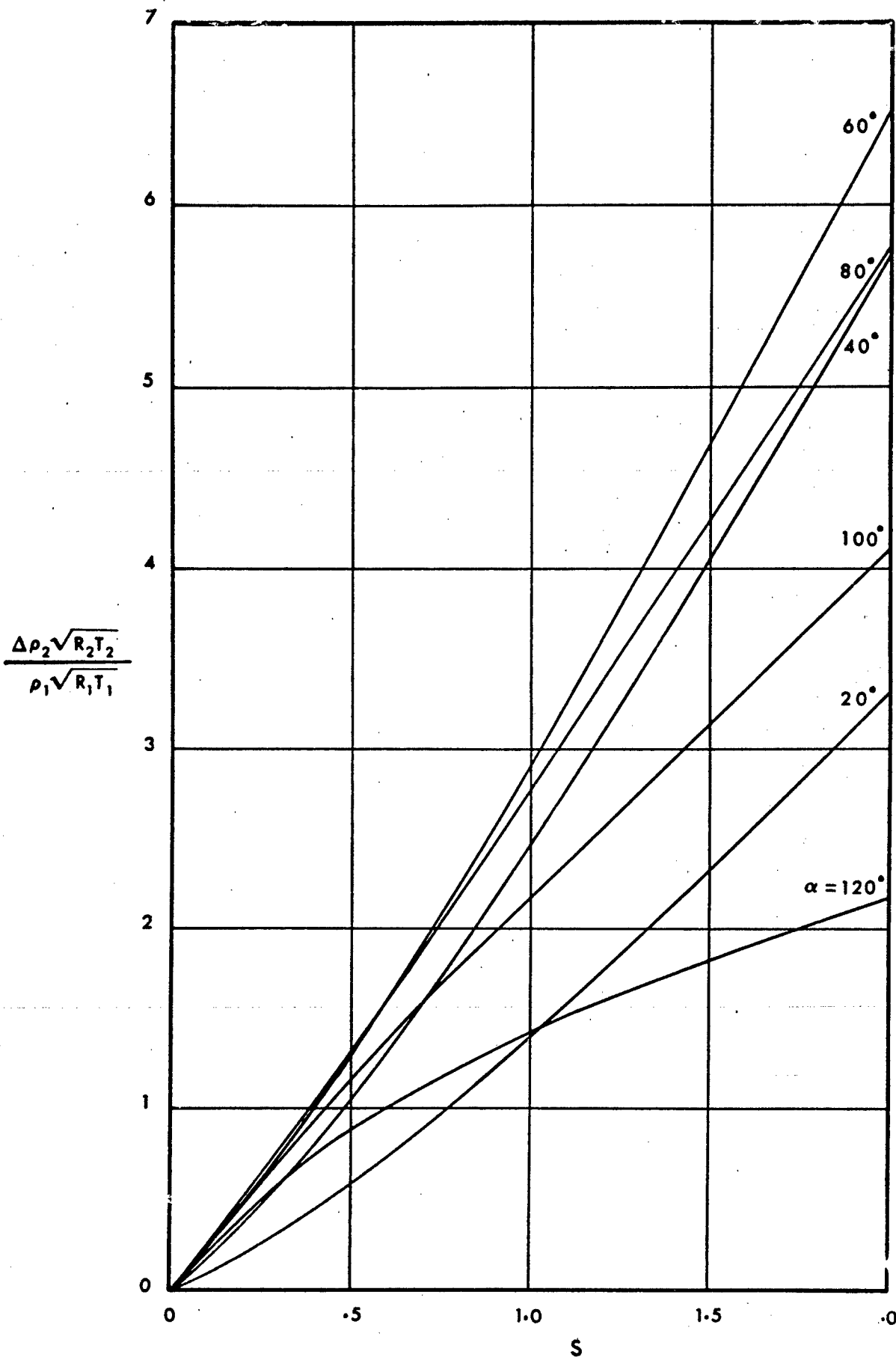


FIG. 6a  $\frac{\Delta \rho_2 \sqrt{R_2 T_2}}{\rho_1 \sqrt{R_1 T_1}}$  AS A FUNCTION OF  $S$  FOR  $\alpha = 0^\circ$  TO  $120^\circ$

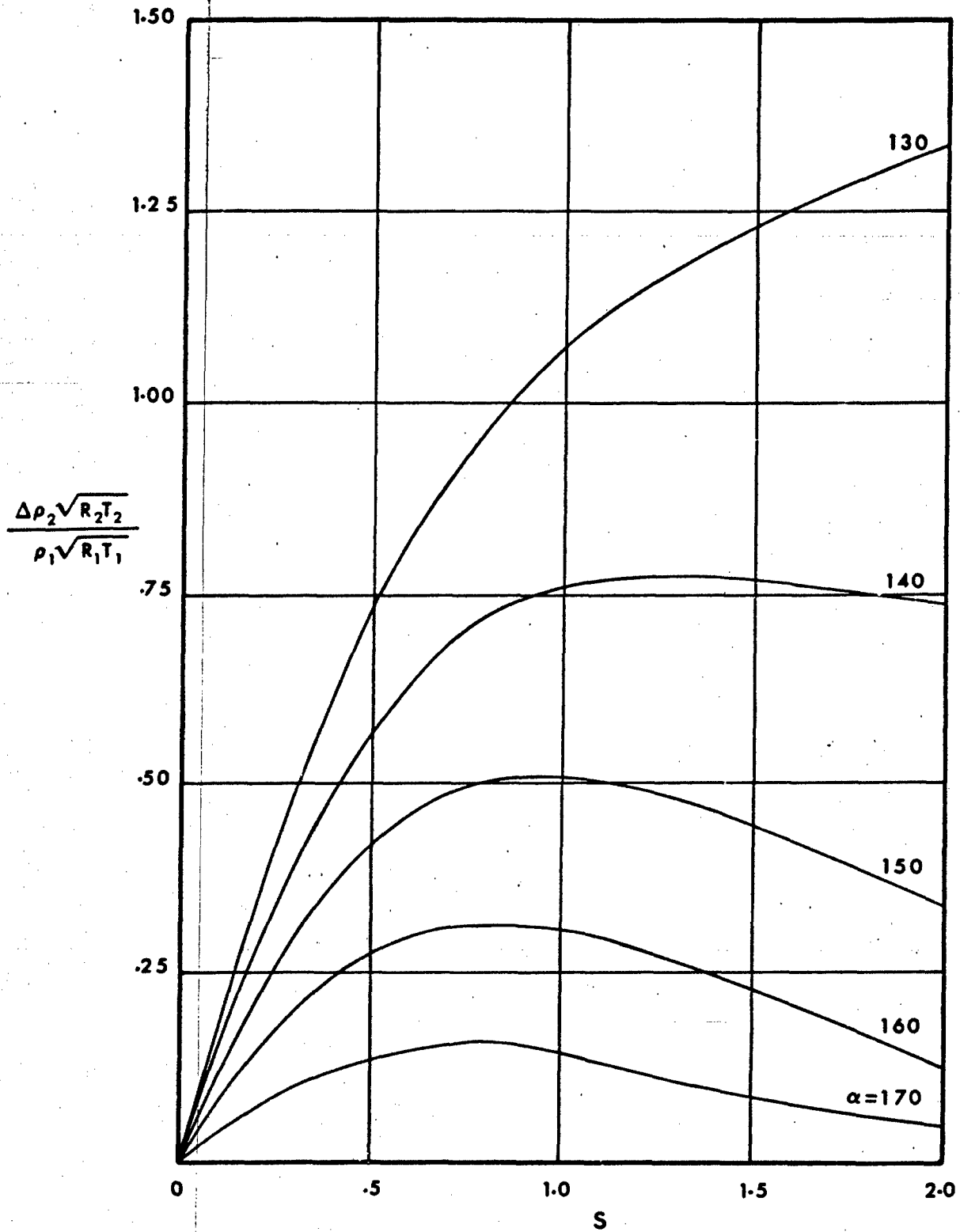
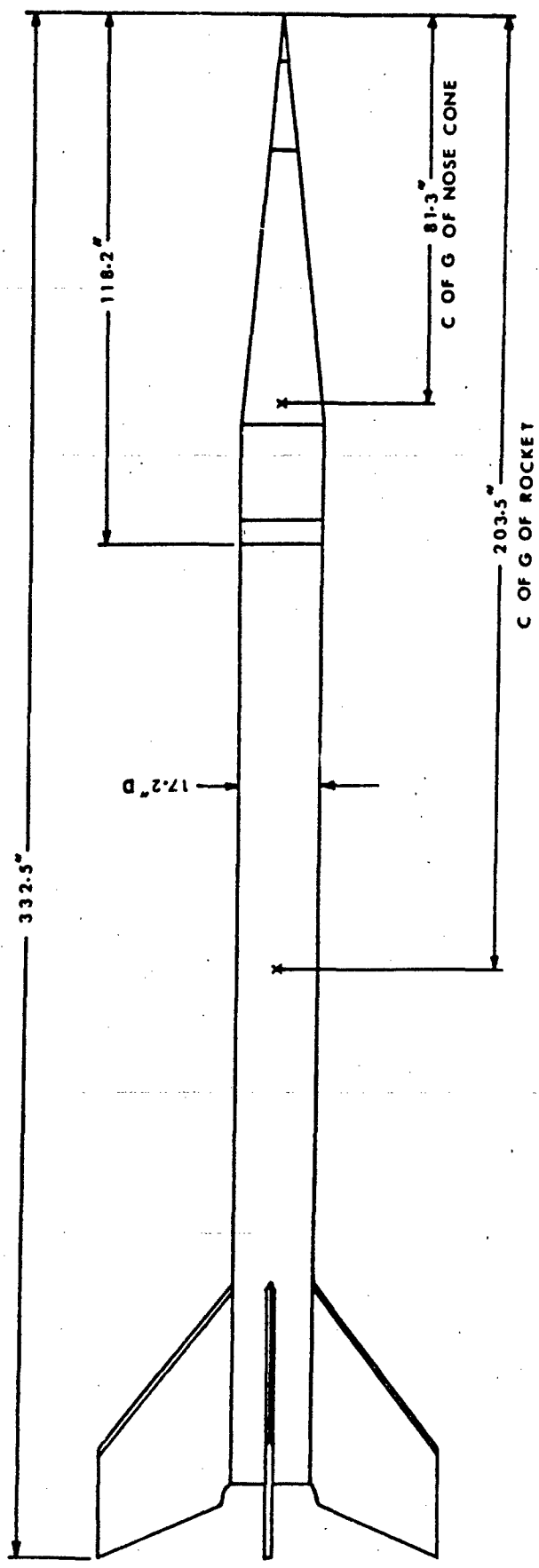


FIG. 6b  $\frac{\Delta p_2 \sqrt{R_2 T_2}}{\rho_1 \sqrt{R_1 T_1}}$  AS A FUNCTION OF  $S$  FOR  $\alpha = 130^\circ$  TO  $180^\circ$



WEIGHT  
 NOSE CONE + INSTRUMENTS 315 LBS.  
 MOTOR + FINS 2420 LBS.

FIG. 7 BLACK BRANT IIA VEHICLE CONFIGURATION

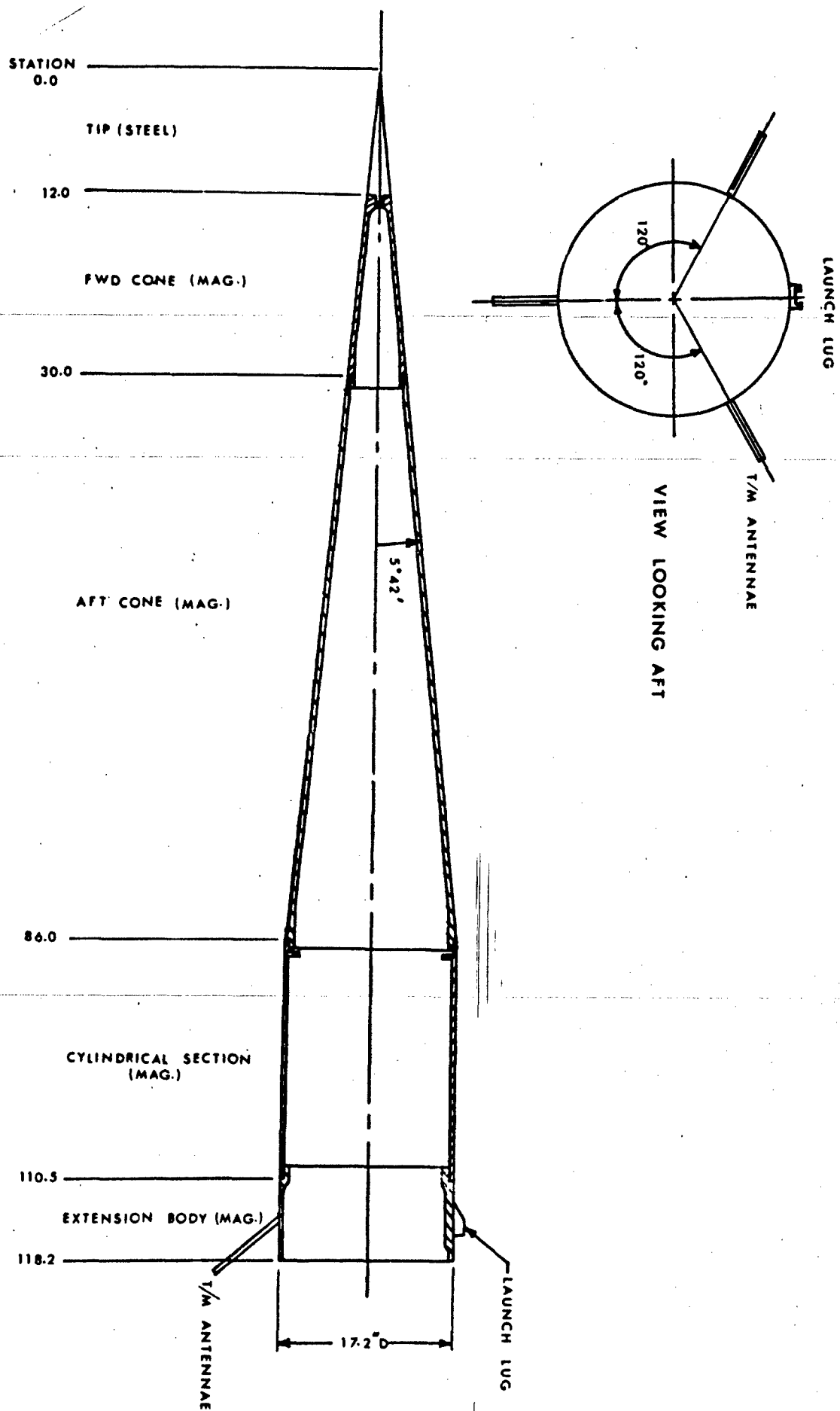


FIG. 8 BLACK BRANT IIA NOSE CONE (UNMODIFIED)

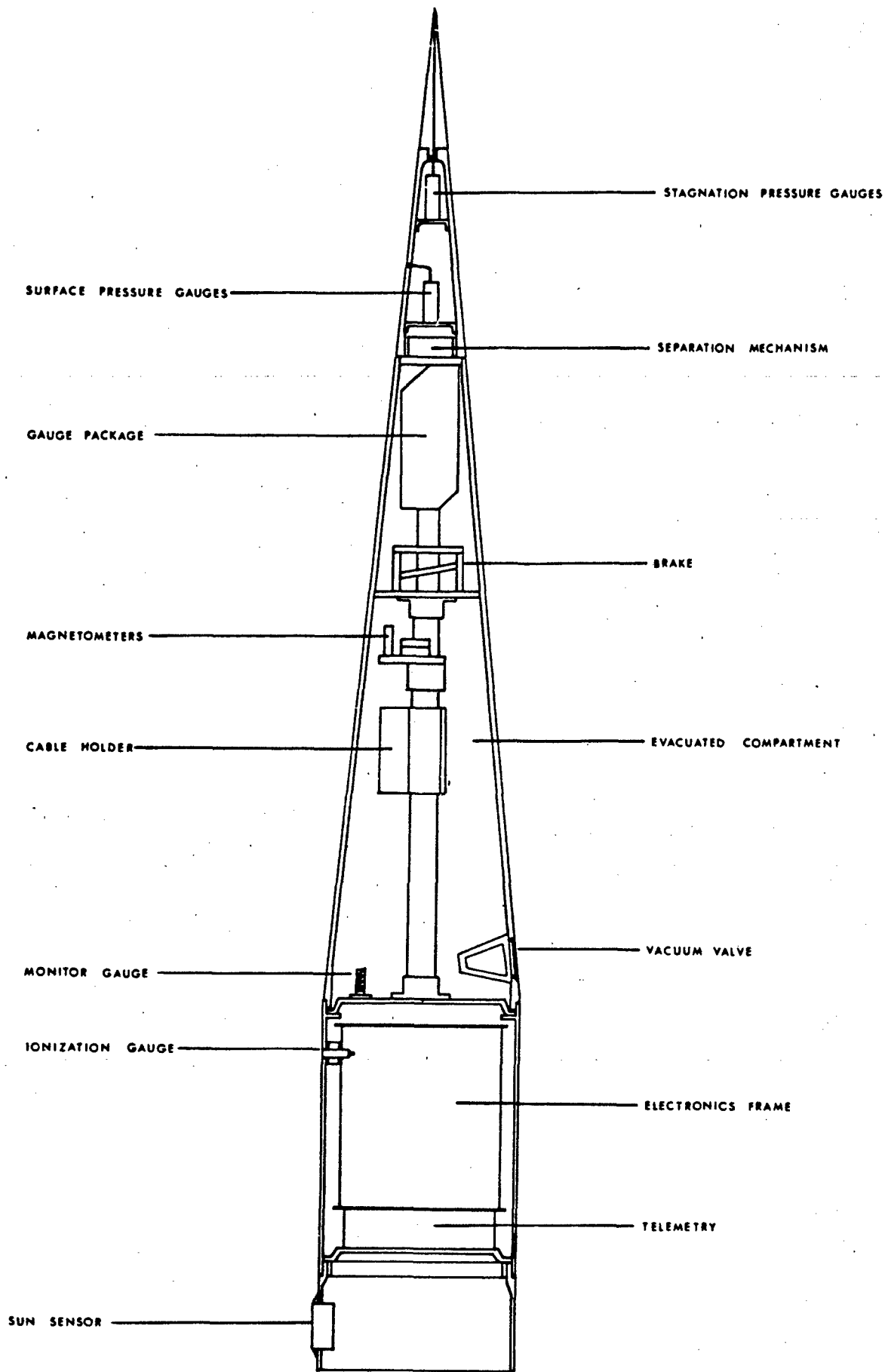
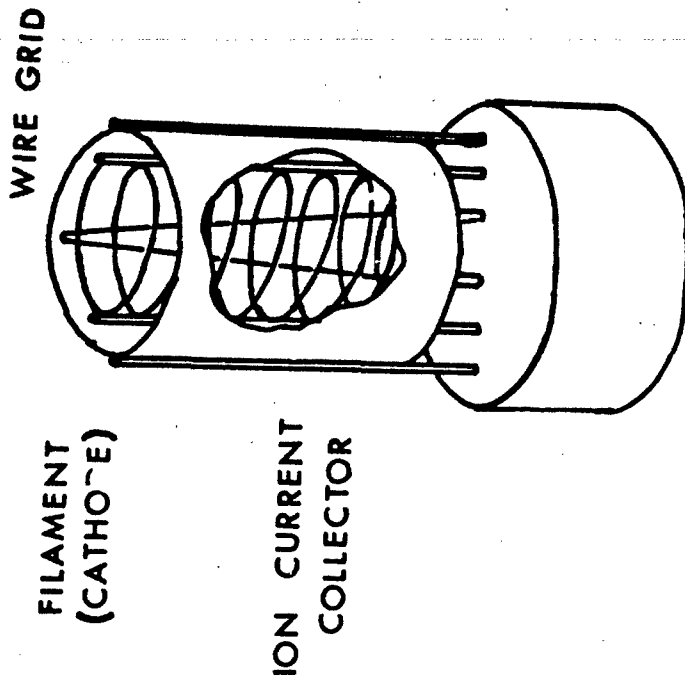
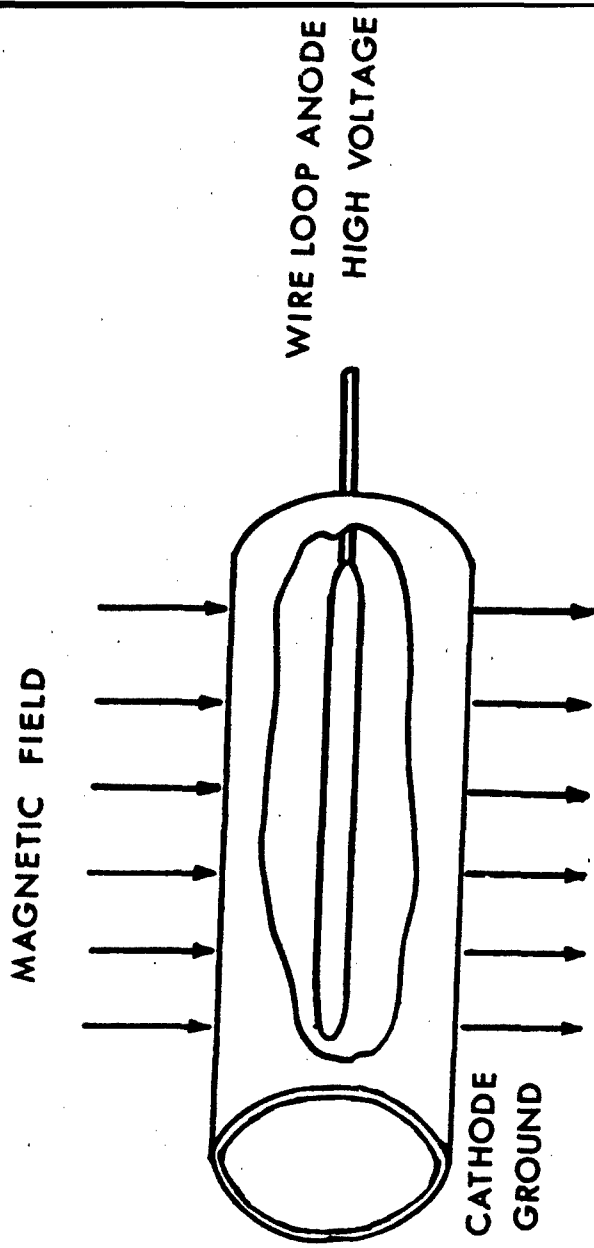


FIG. 9 SCHEMATIC VIEW OF NOSE CONE INSTRUMENTATION



HOT CATHODE IONIZATION GAUGE



COLD CATHODE IONIZATION GAUGE

FIG. 10 ELECTRODE STRUCTURES OF HOT CATHODE AND COLD CATHODE IONIZATION GAUGES

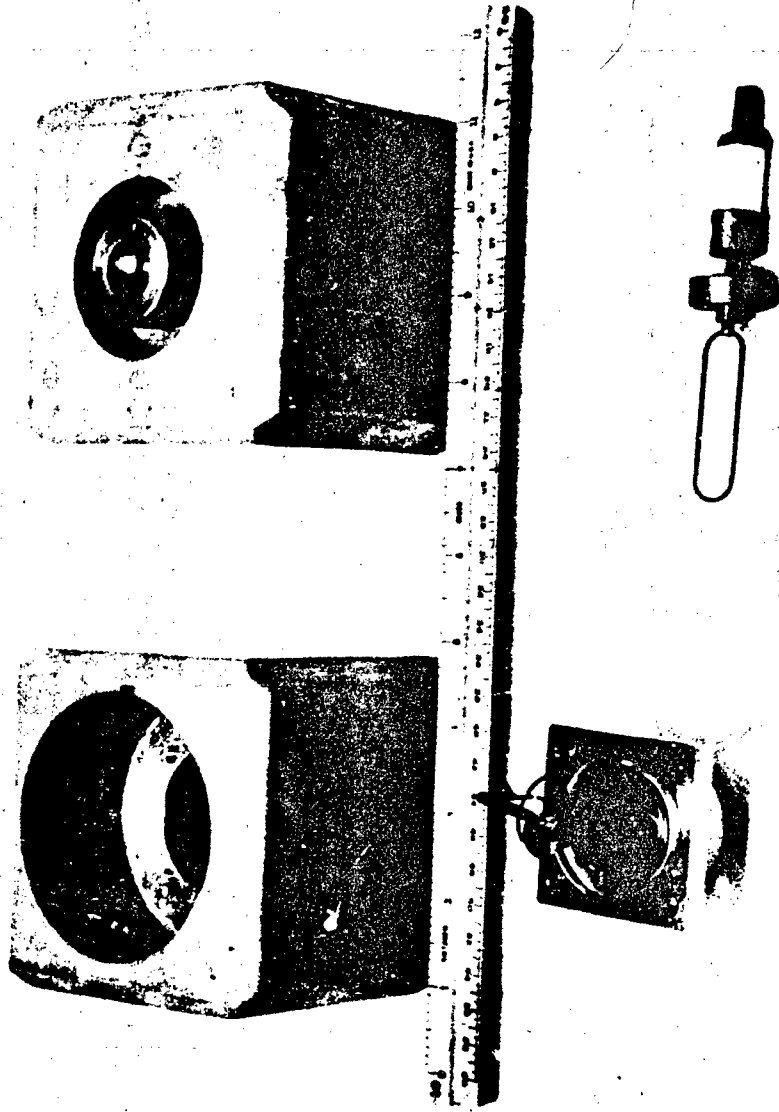


FIG. 11 HOT AND COLD CATHODE IONIZATION GAUGES AFTER VIBRATION TESTING SHOWING ELECTRODE FAILURE.

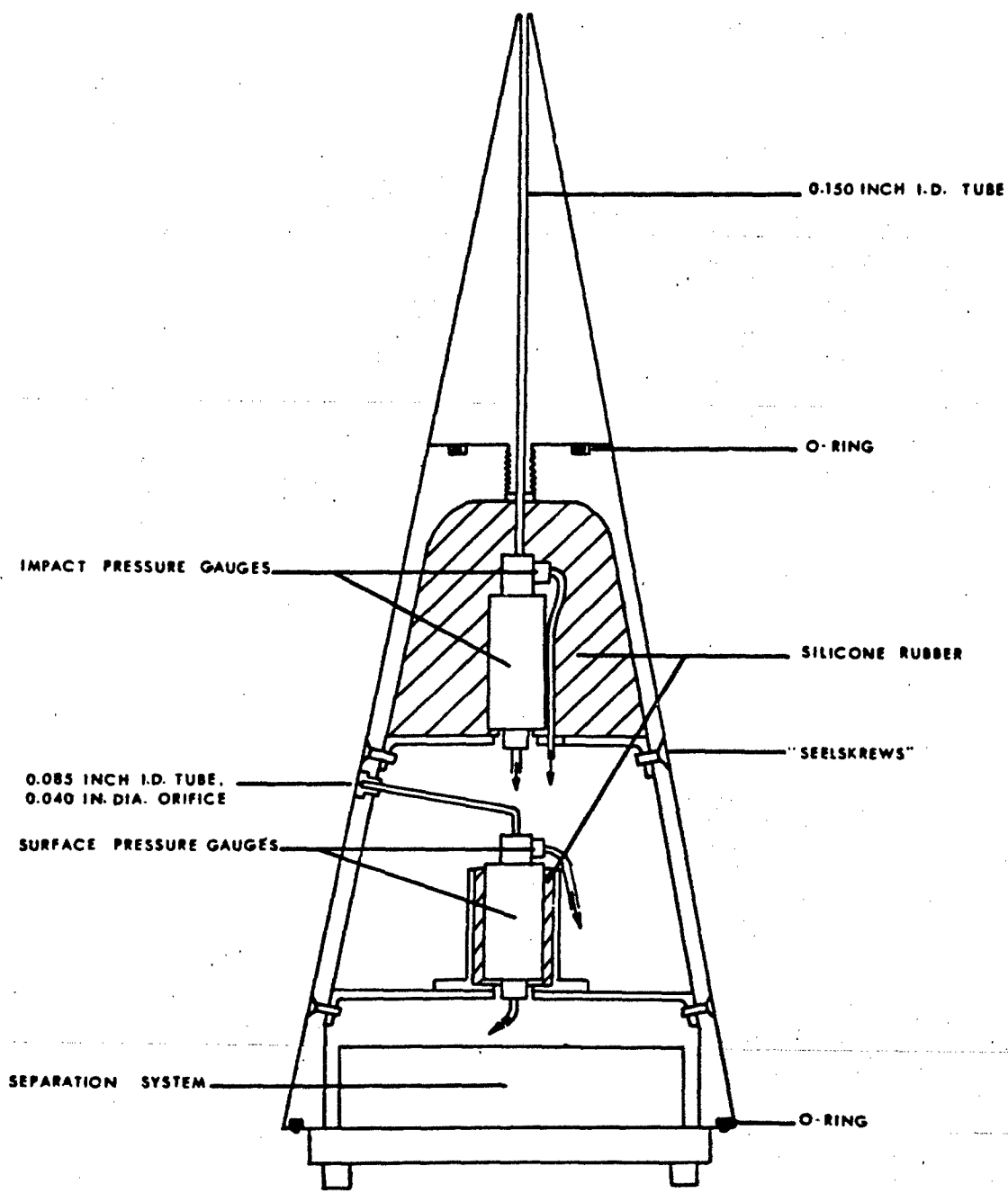


FIG. 12 MOUNTING OF STRAIN GAUGE AND THERMOCOUPLE PRESSURE TRANSDUCERS IN THE NOSE CONE

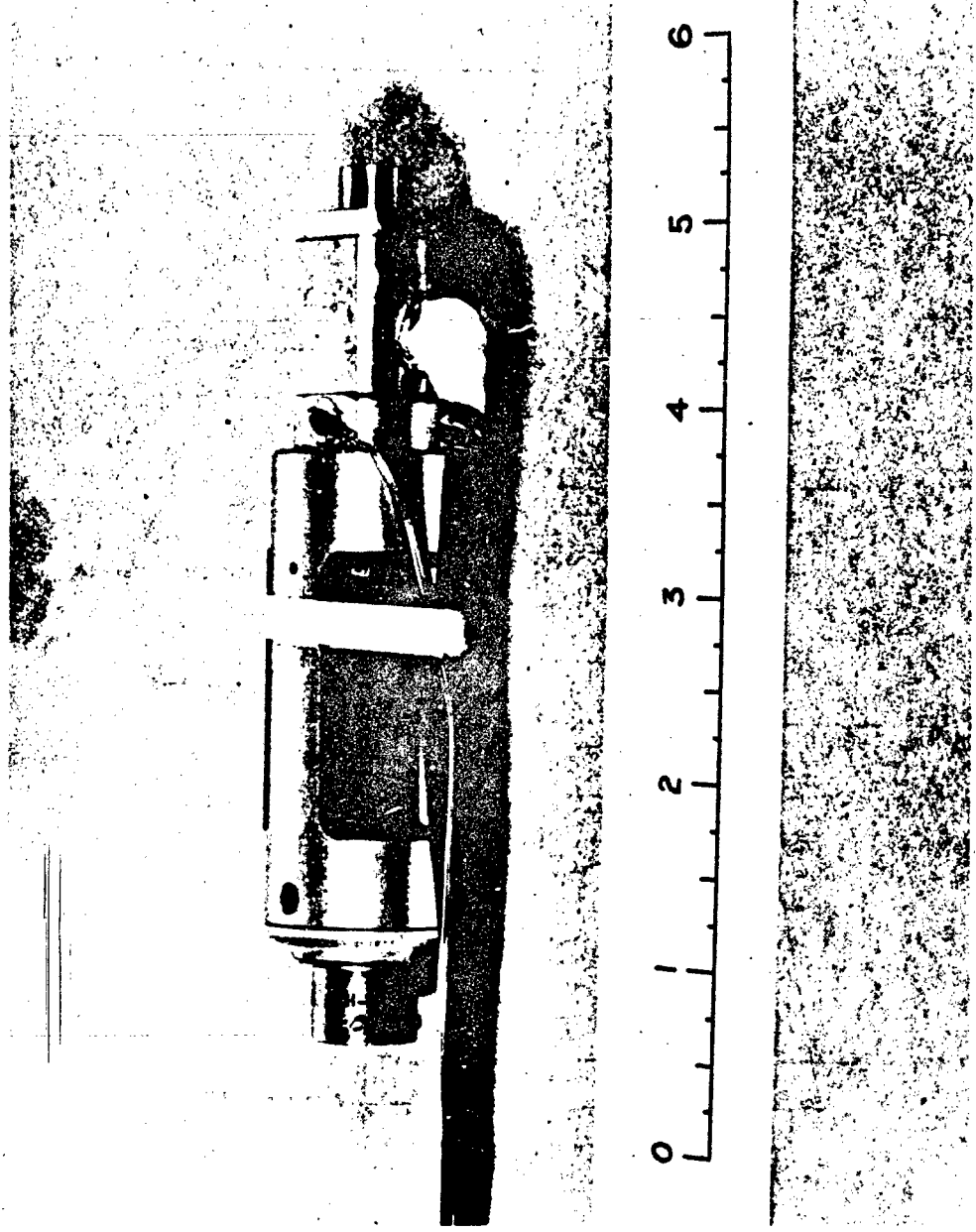


FIG. 13 STRAIN GAUGE AND THERMOCOUPLE PRESSURE TRANSDUCERS CONNECTED TO A COMMON PRESSURE MANIFOLD



FIG. 14 SURFACE PRESSURE TRANSDUCERS MOUNTED ON THE SHELF WHICH SUPPORTED THEM IN THE NOSE CONE

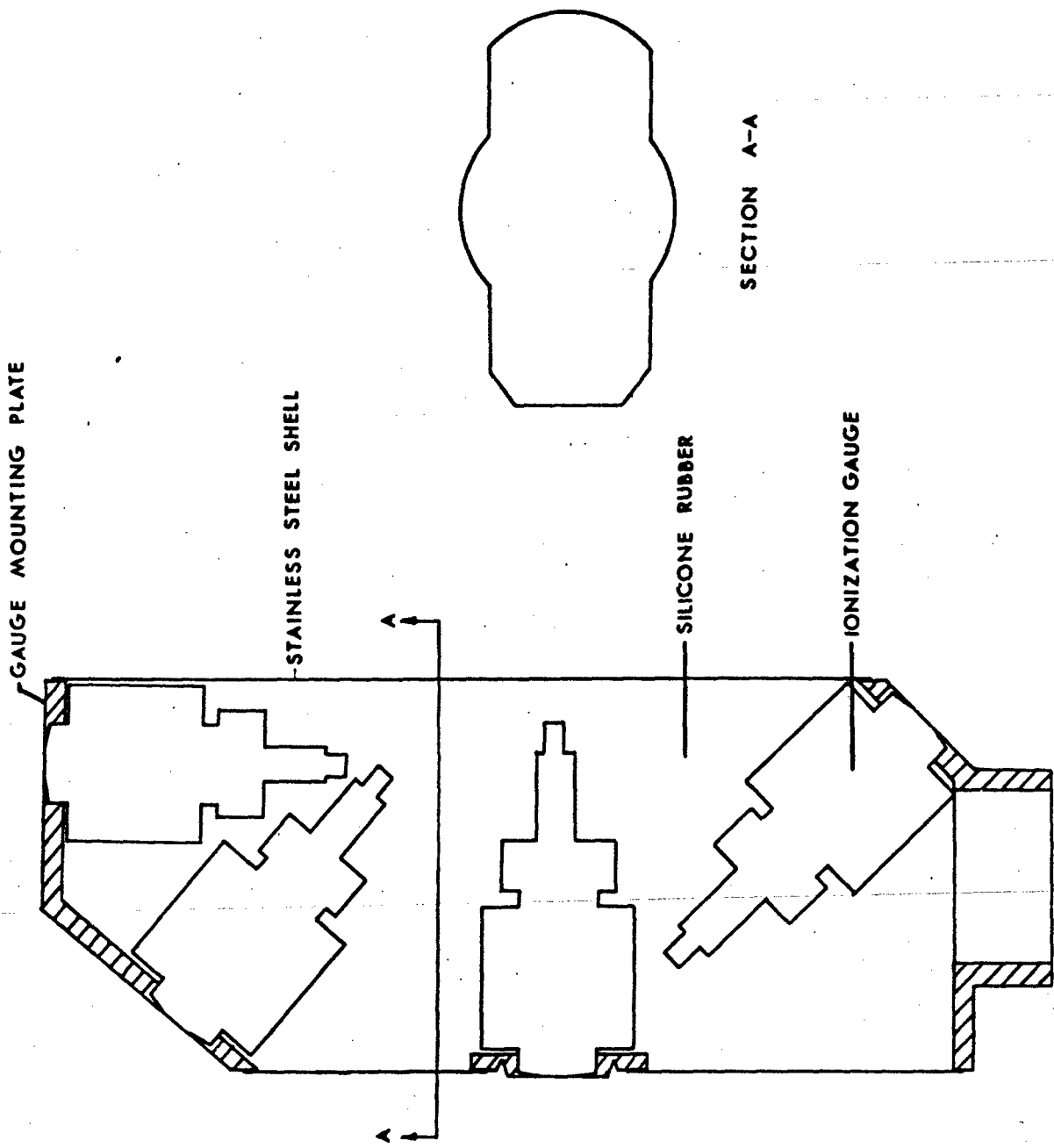


FIG. 15 GAUGE PACKAGE CONFIGURATION

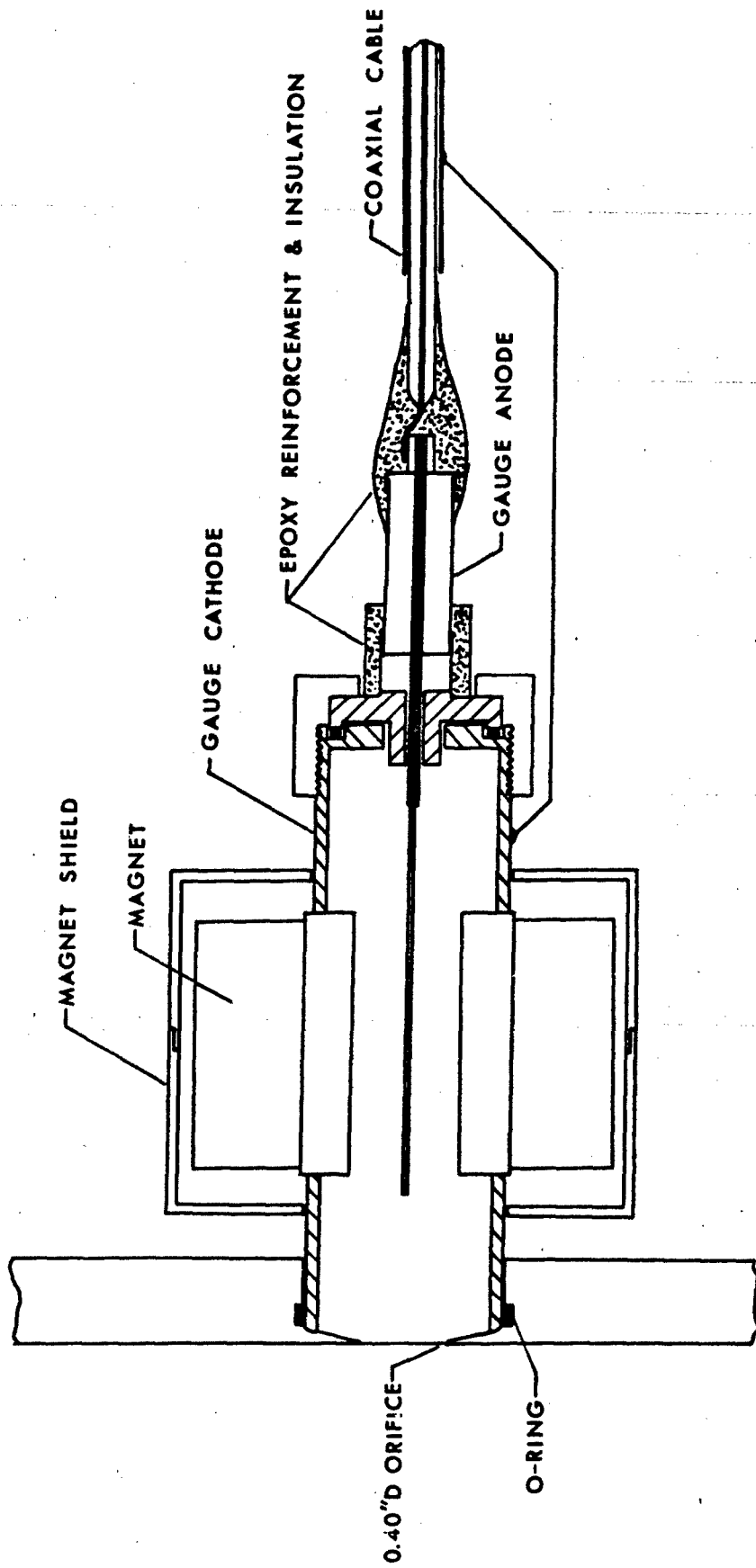


FIG. 16 DETAILS OF COLD CATHODE IONIZATION GAUGE MOUNTING AND ELECTRICAL INSULATION

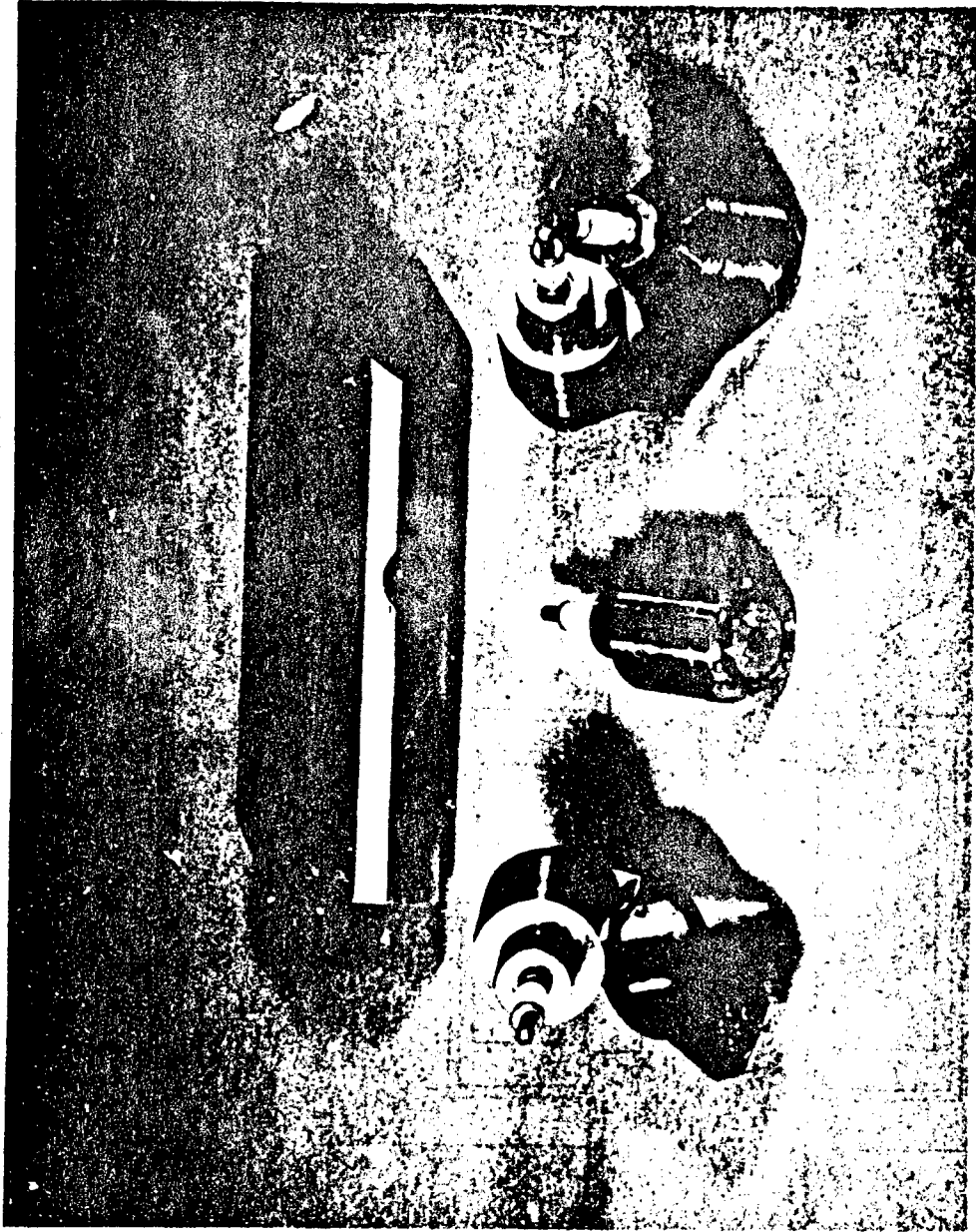


FIG. 17 IONIZATION GAUGES BEFORE FINAL ASSEMBLY IN THE GAUGE PACKAGE SHELL

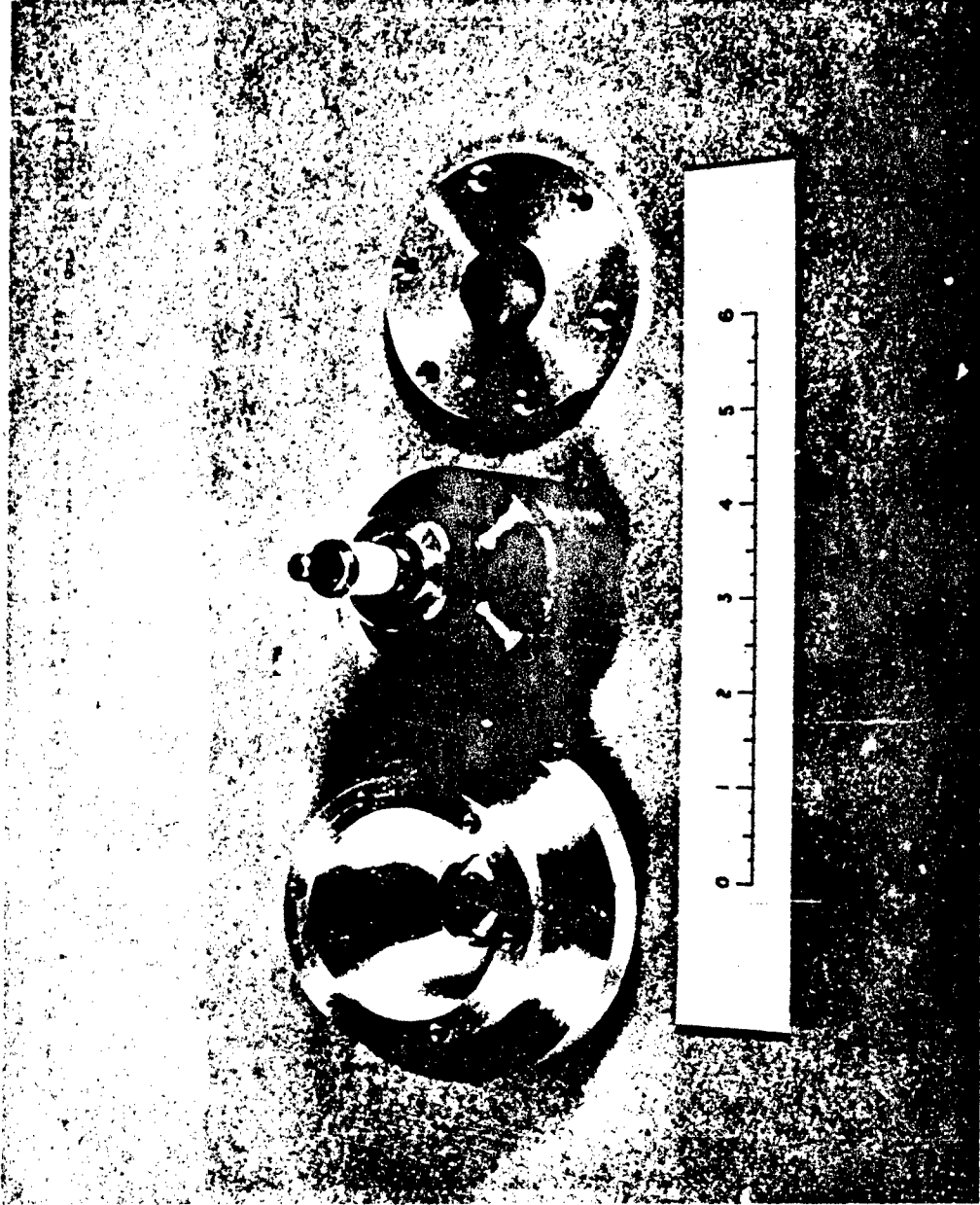


FIG. 18a IONIZATION GAUGE AND MOUNTING FOR THE FIFTH GAUGE INSTALLED IN THE CYLINDRICAL SECTION

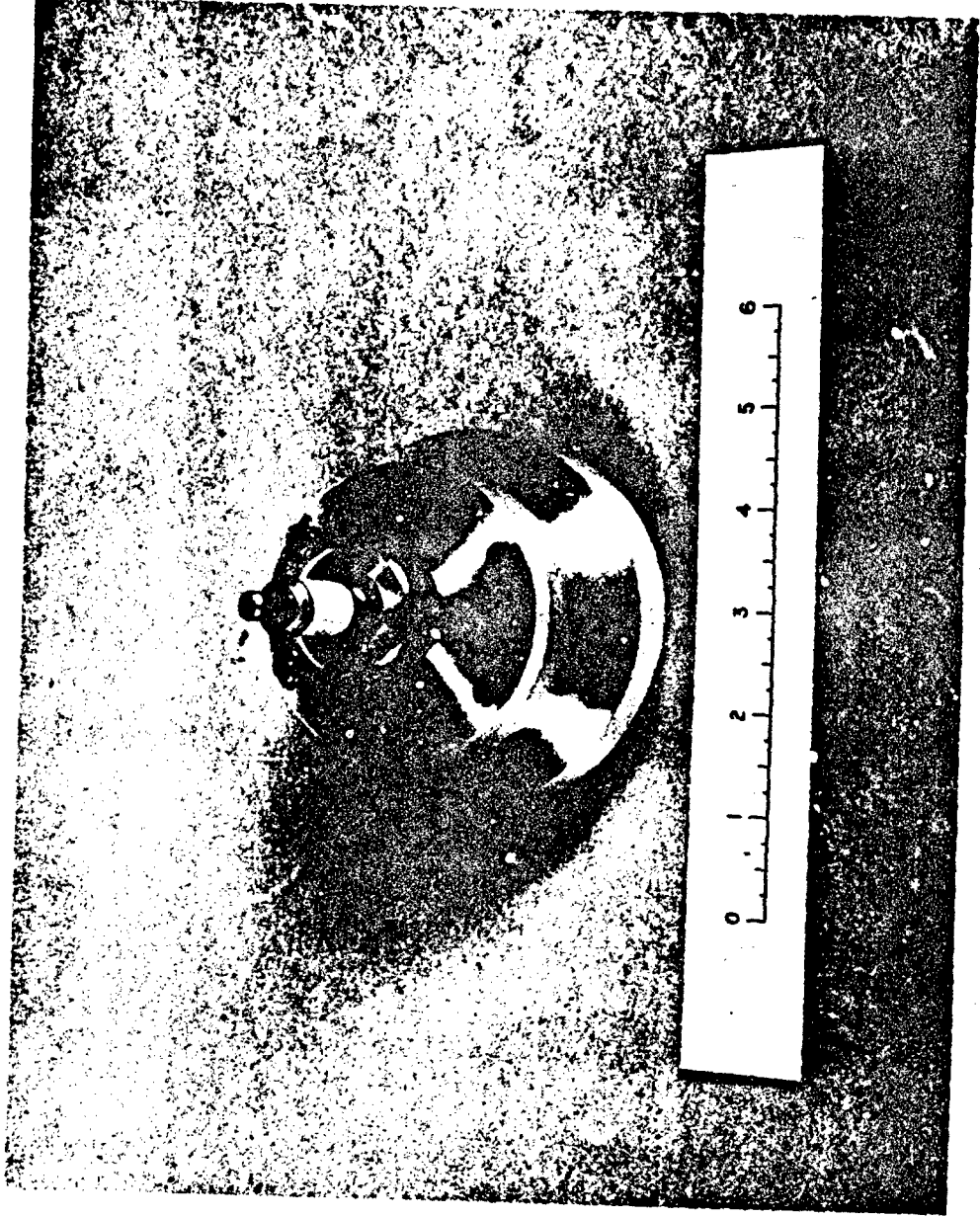


FIG. 18b ASSEMBLY OF FIFTH IONIZATION GAUGE IN ITS MOUNTING

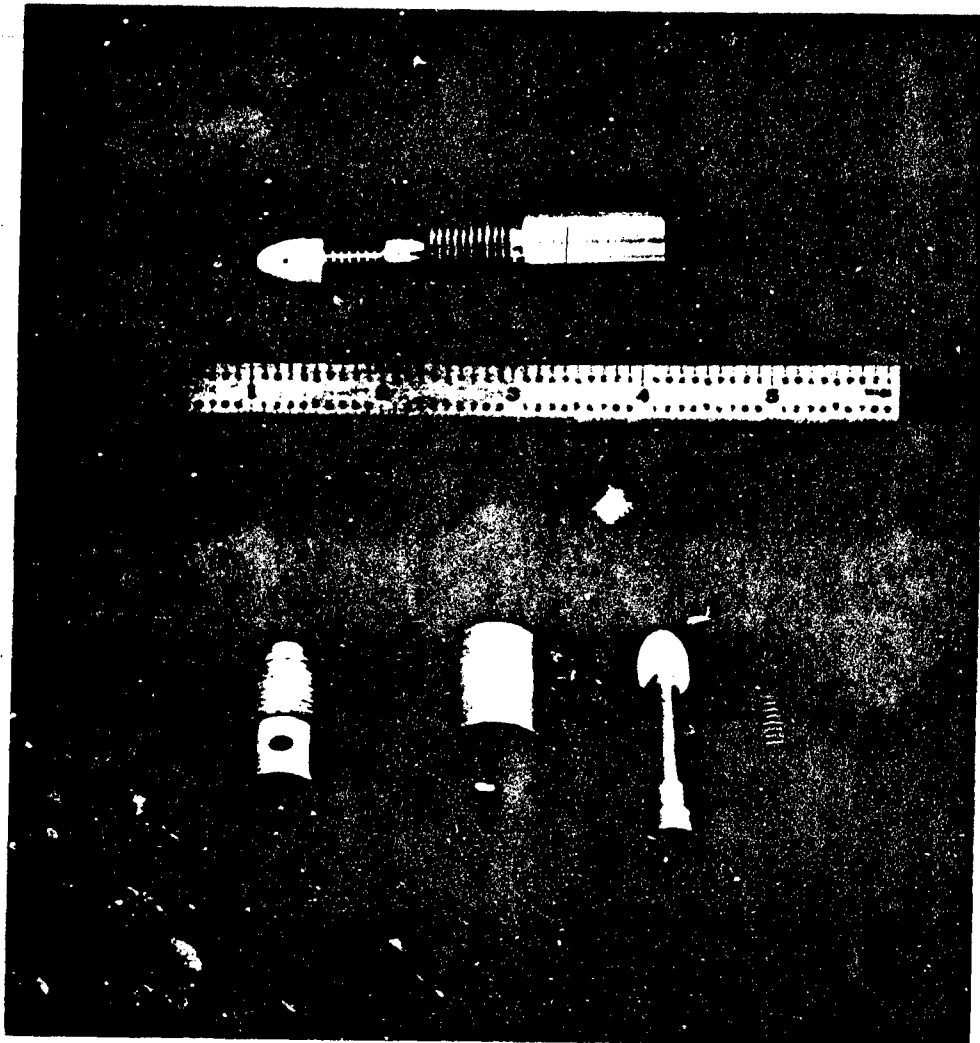


FIG. 19      DETAILS AND ASSEMBLY OF A BALL-AND-RACE FASTENER



FIG. 20a SEPARATION MECHANISM DETAILS, CAM AND BASE PLATE WITH BELLOWS ACTUATORS IN THEIR GUIDES

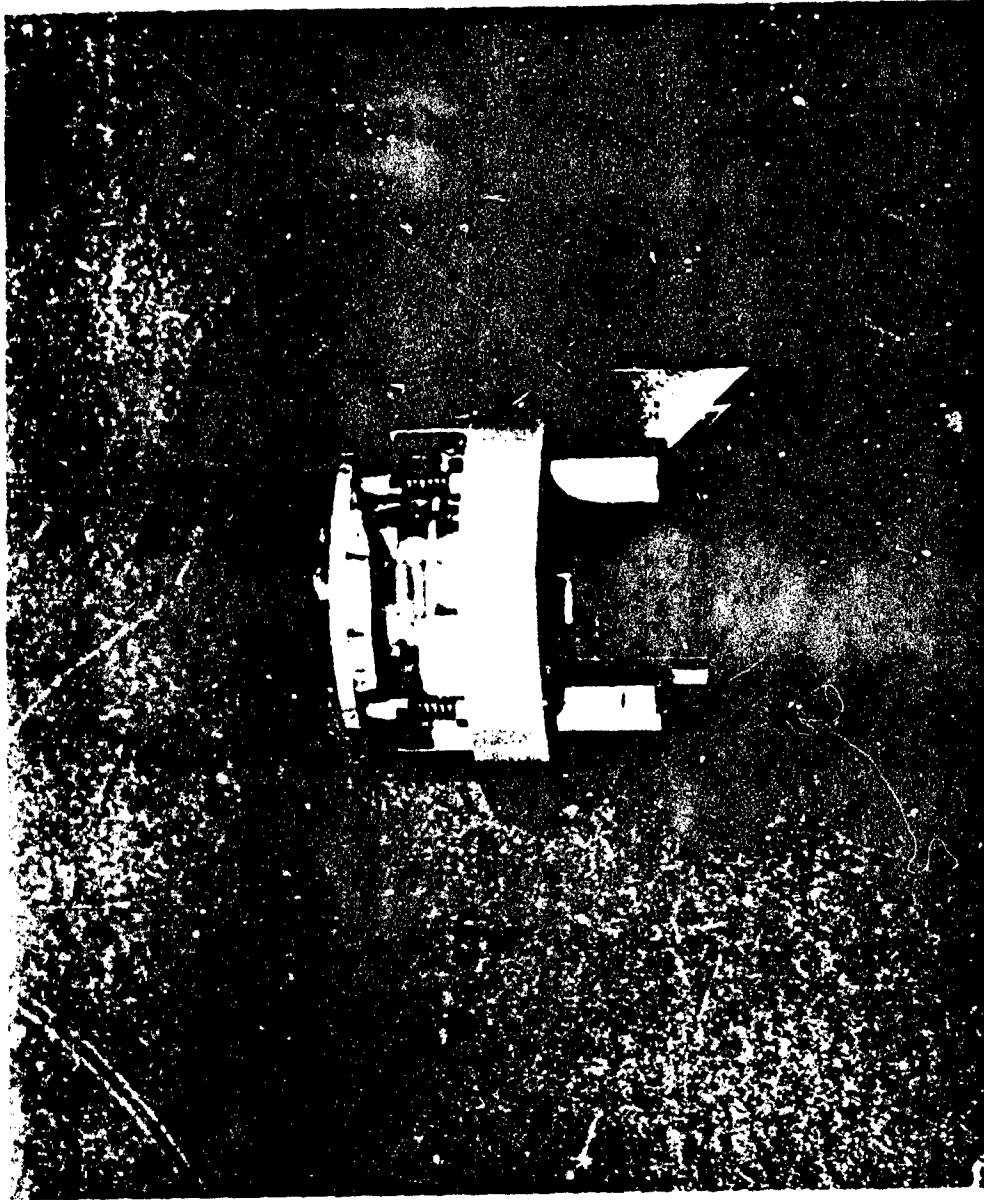


FIG. 20b ASSEMBLED SEPARATION MECHANISM

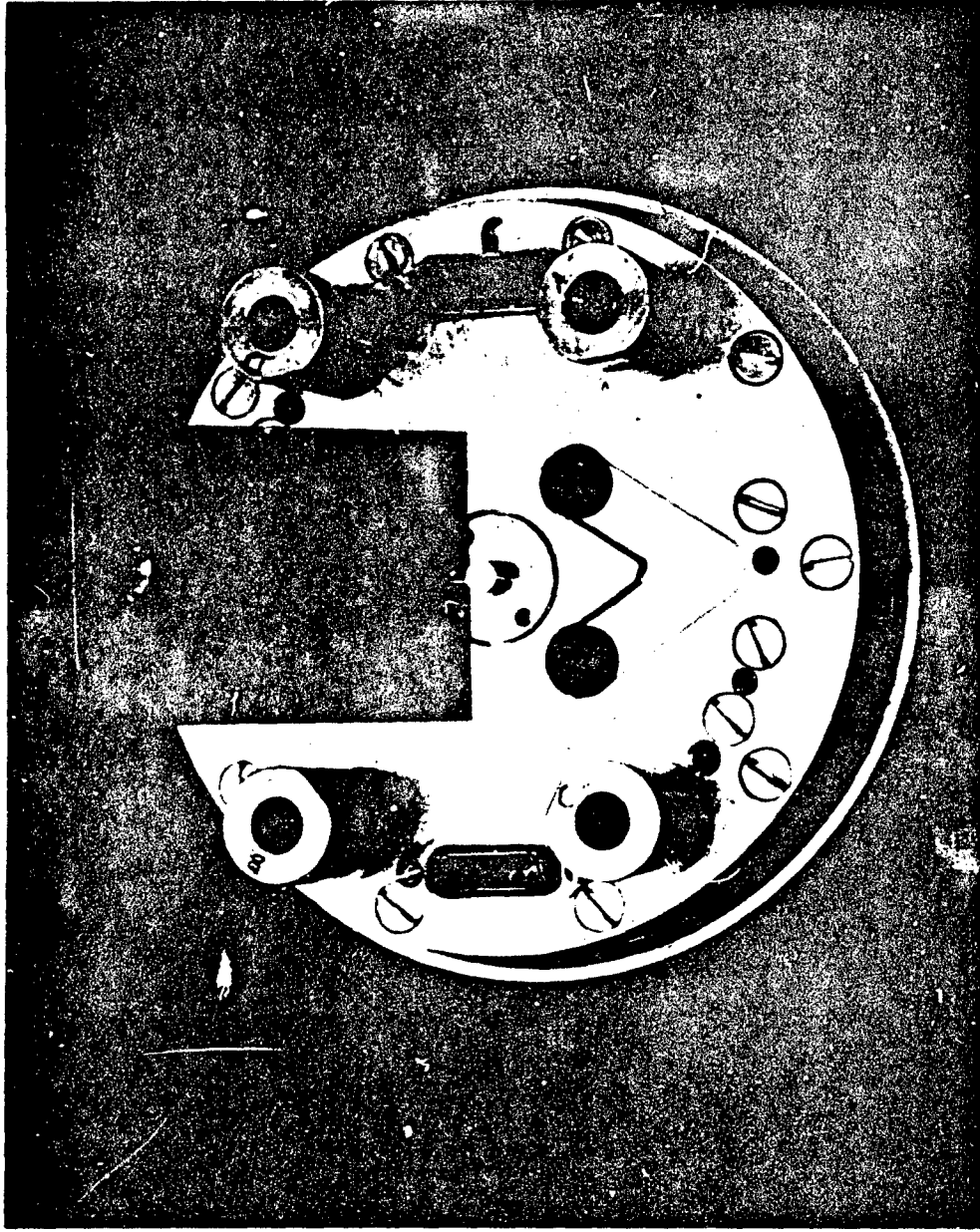


FIG. 20c BASE OF THE SEPARATION MECHANISM

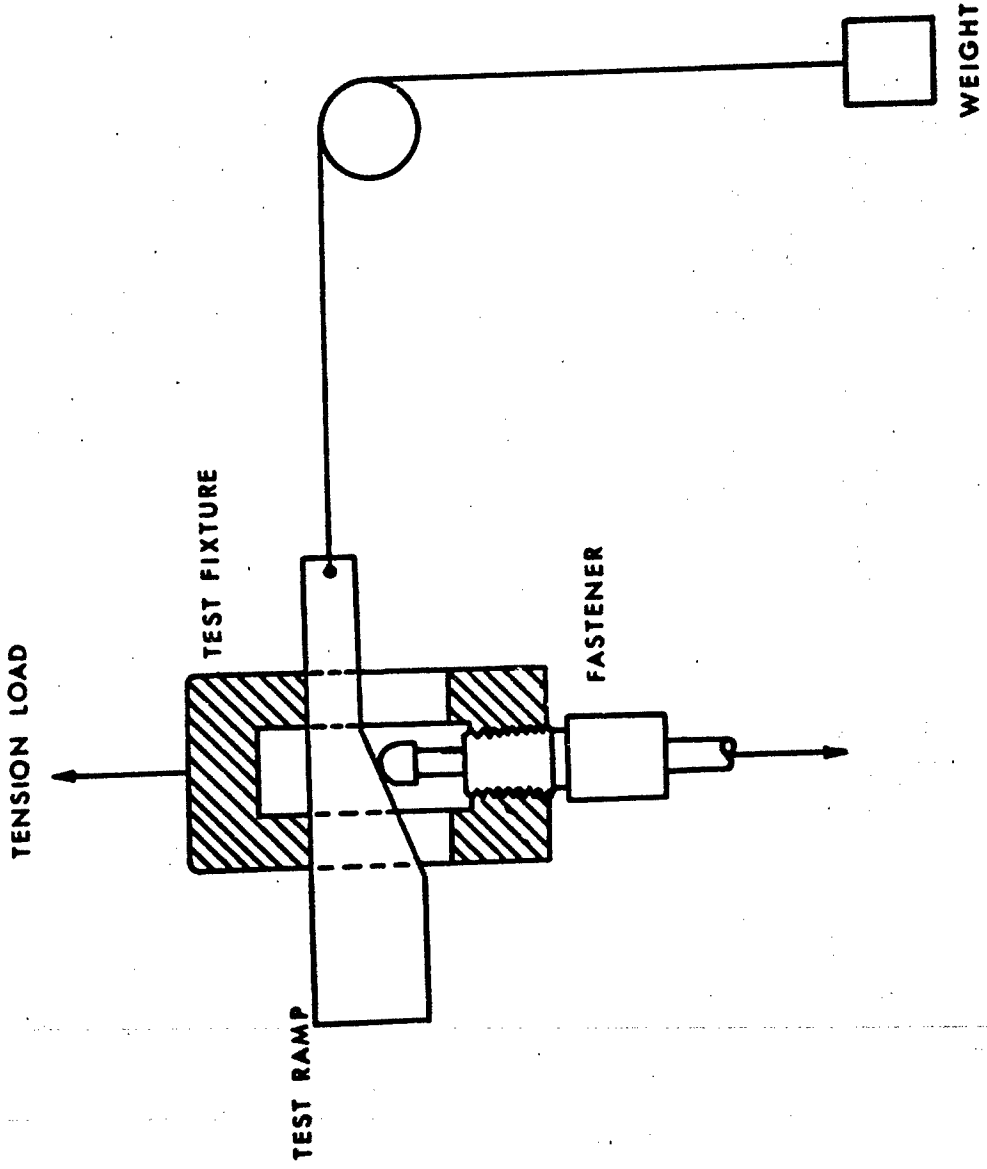


FIG. 21 TEST FIXTURE FOR BALL-AND-RACE FASTENERS

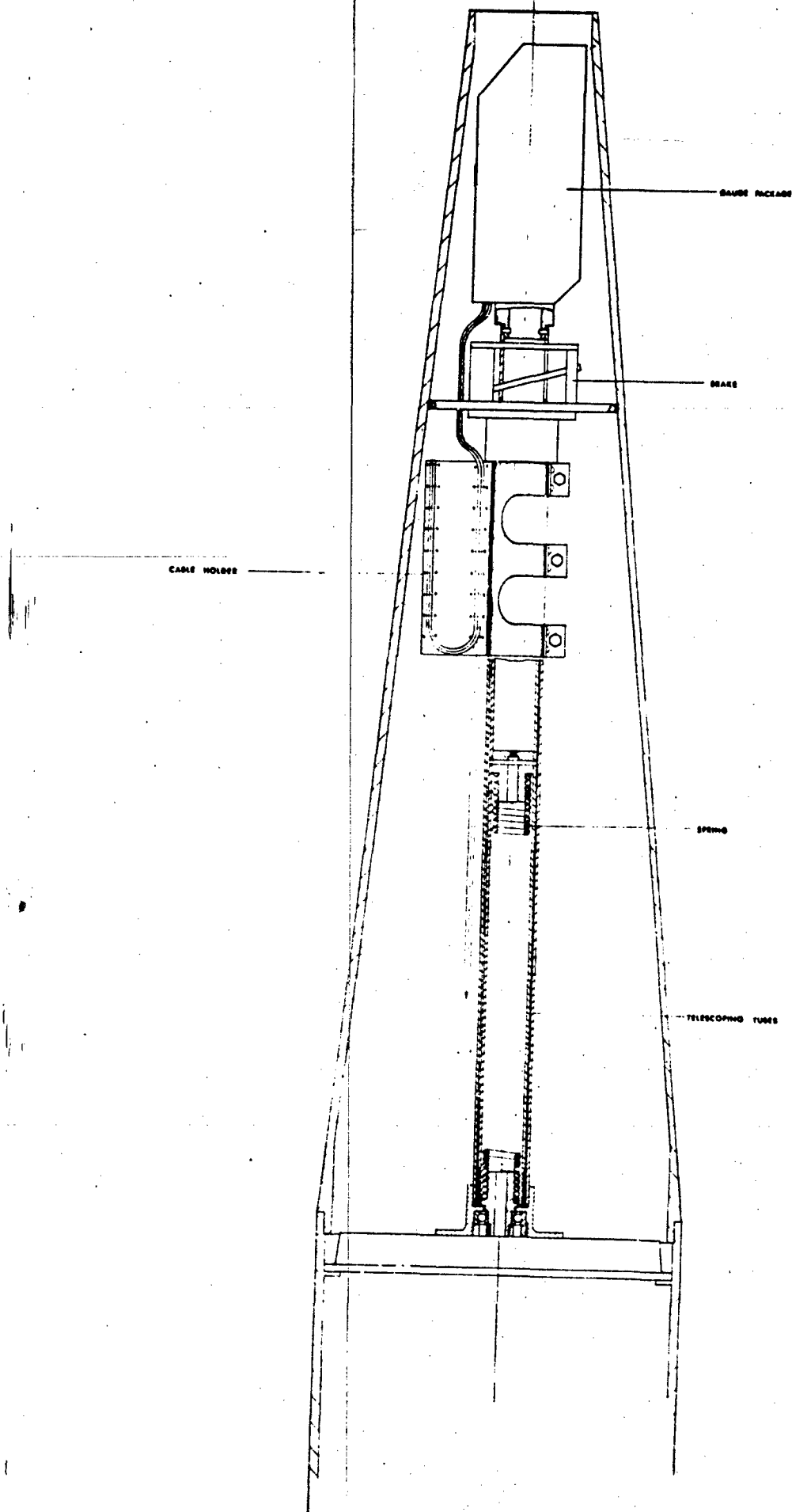


FIG. 22a ASSEMBLY DRAWING OF THE EXTENSION AND BRAKING SYSTEM

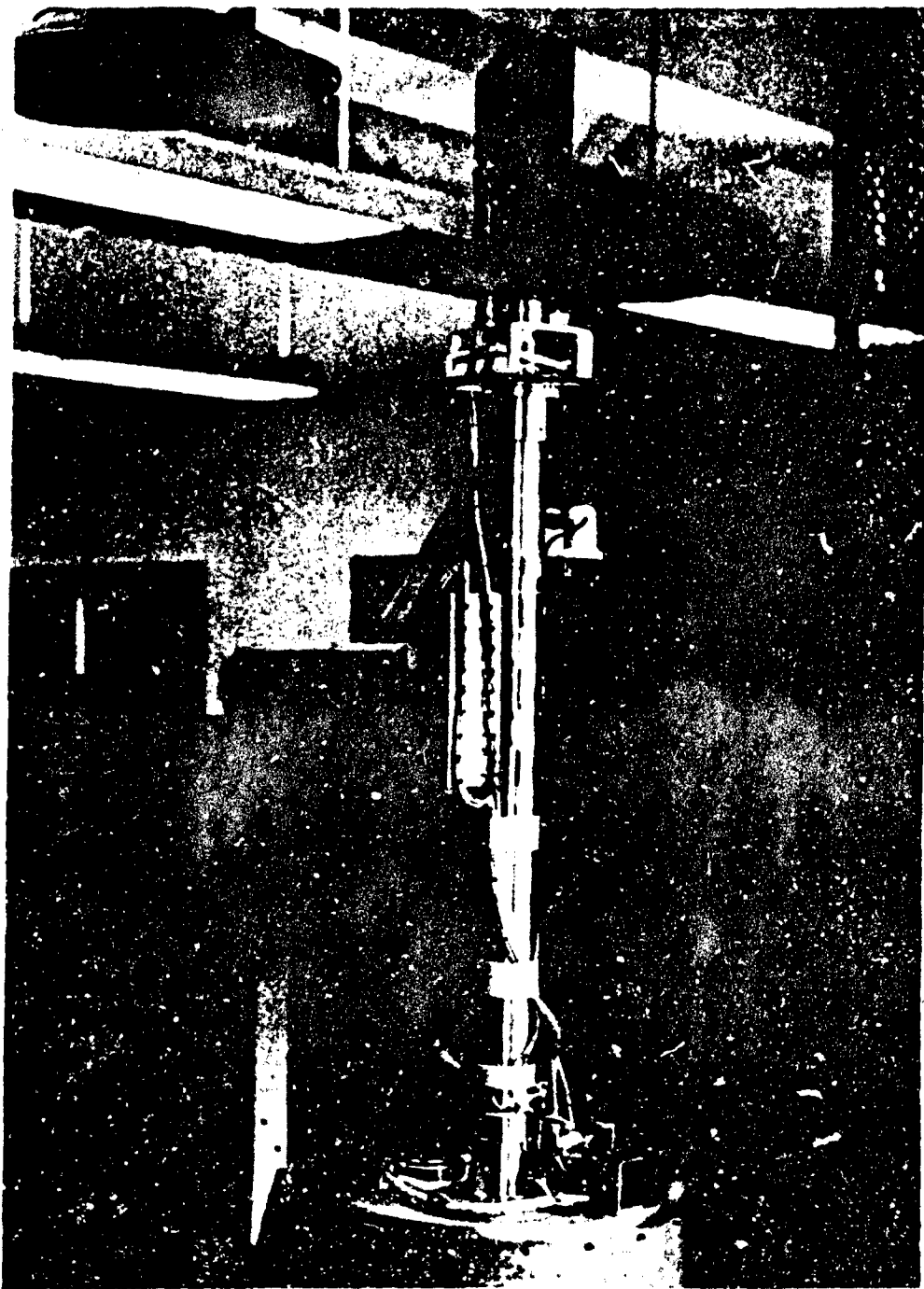


FIG. 22b ASSEMBLED EXTENSION AND BRAKING SYSTEM BEFORE NOSE CONE ASSEMBLY

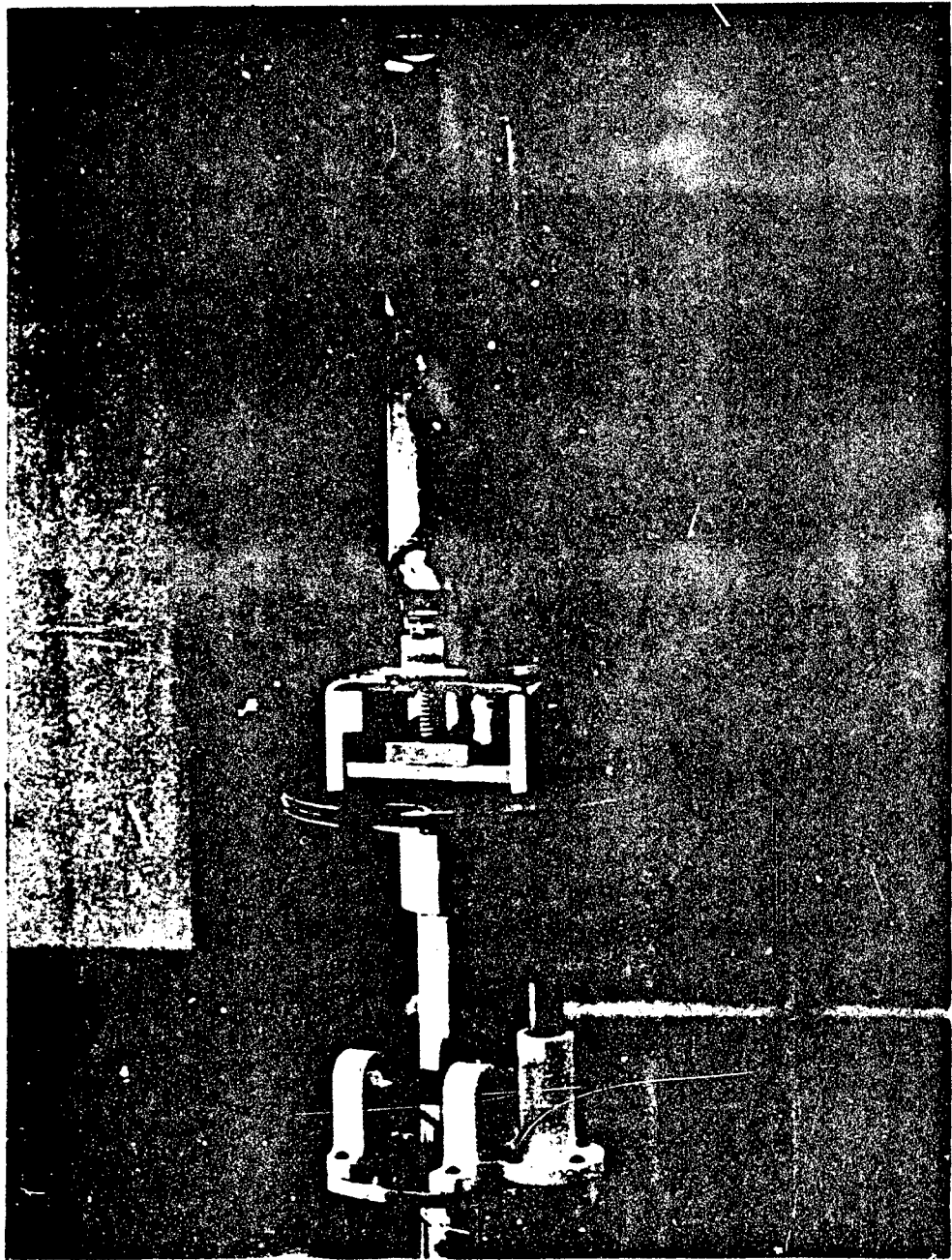


FIG. 23      DETAILS OF THE BRAKING SYSTEM, GAUGE PACKAGE AND MAGNETOMETER MOUNTING

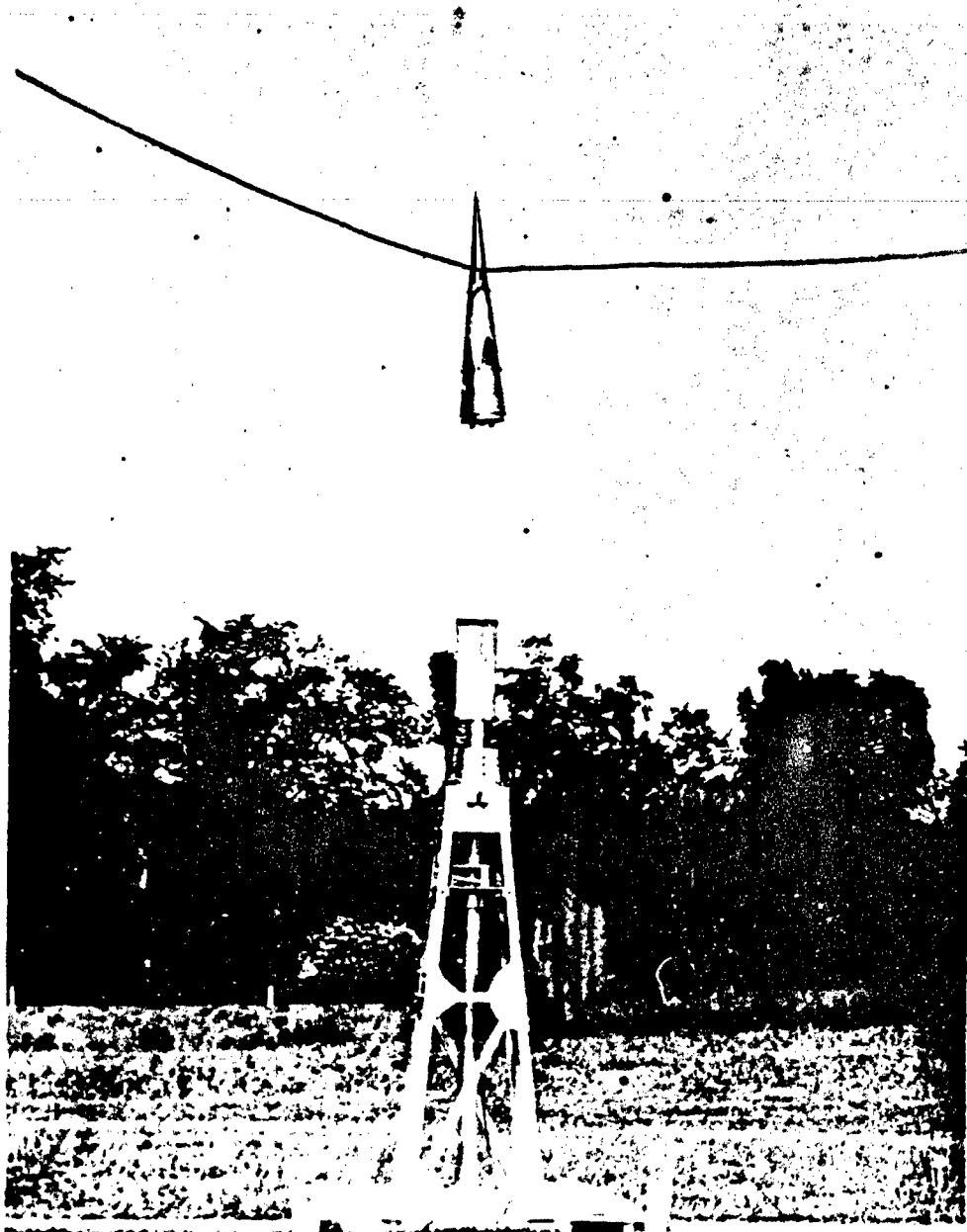


FIG. 24a TESTING OF COMPONENTS OF THE SEPARATION, EXTENSION, AND BRAKING SYSTEMS

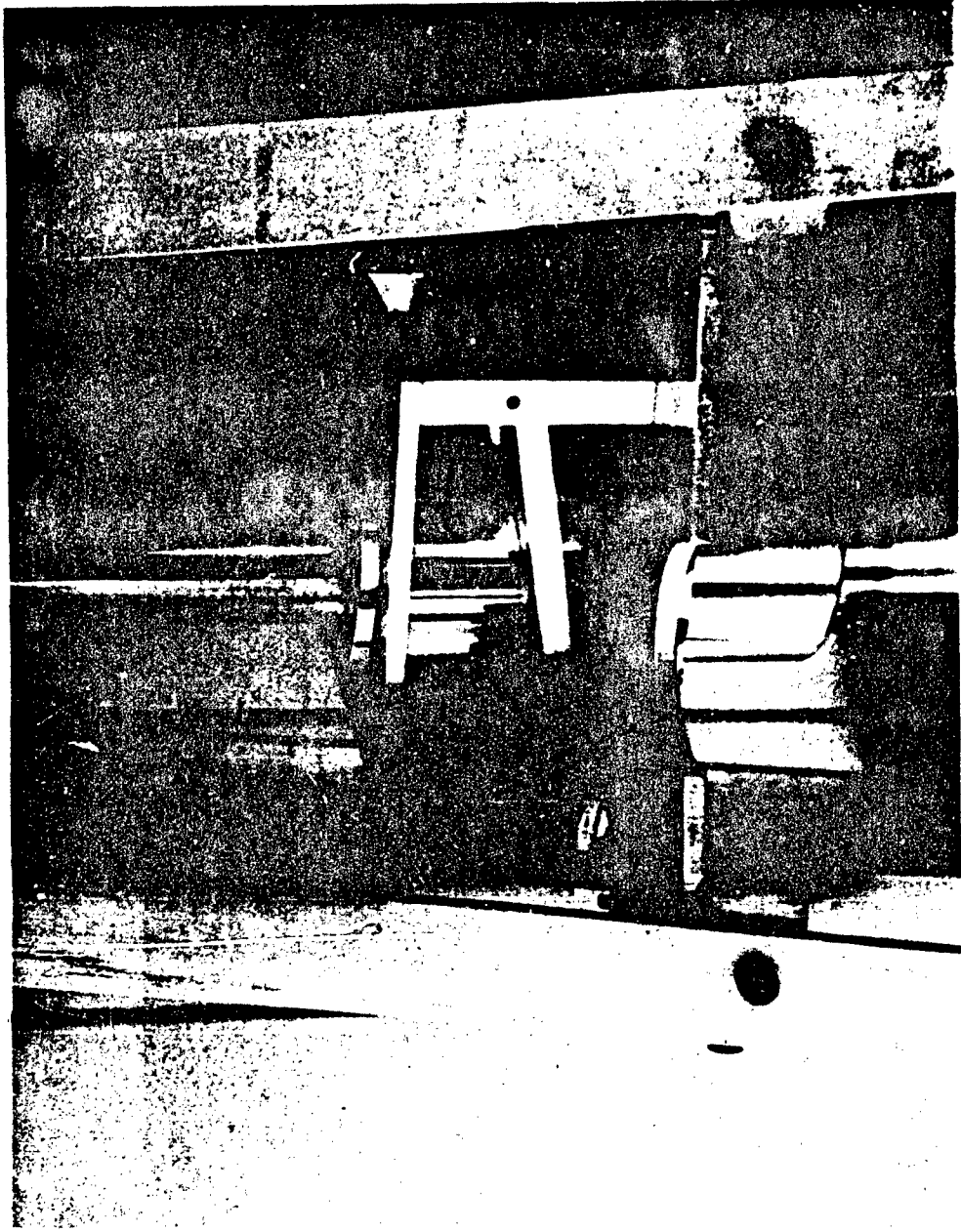


FIG. 24b BRAKING SYSTEM MOUNTED IN THE TEST FRAME

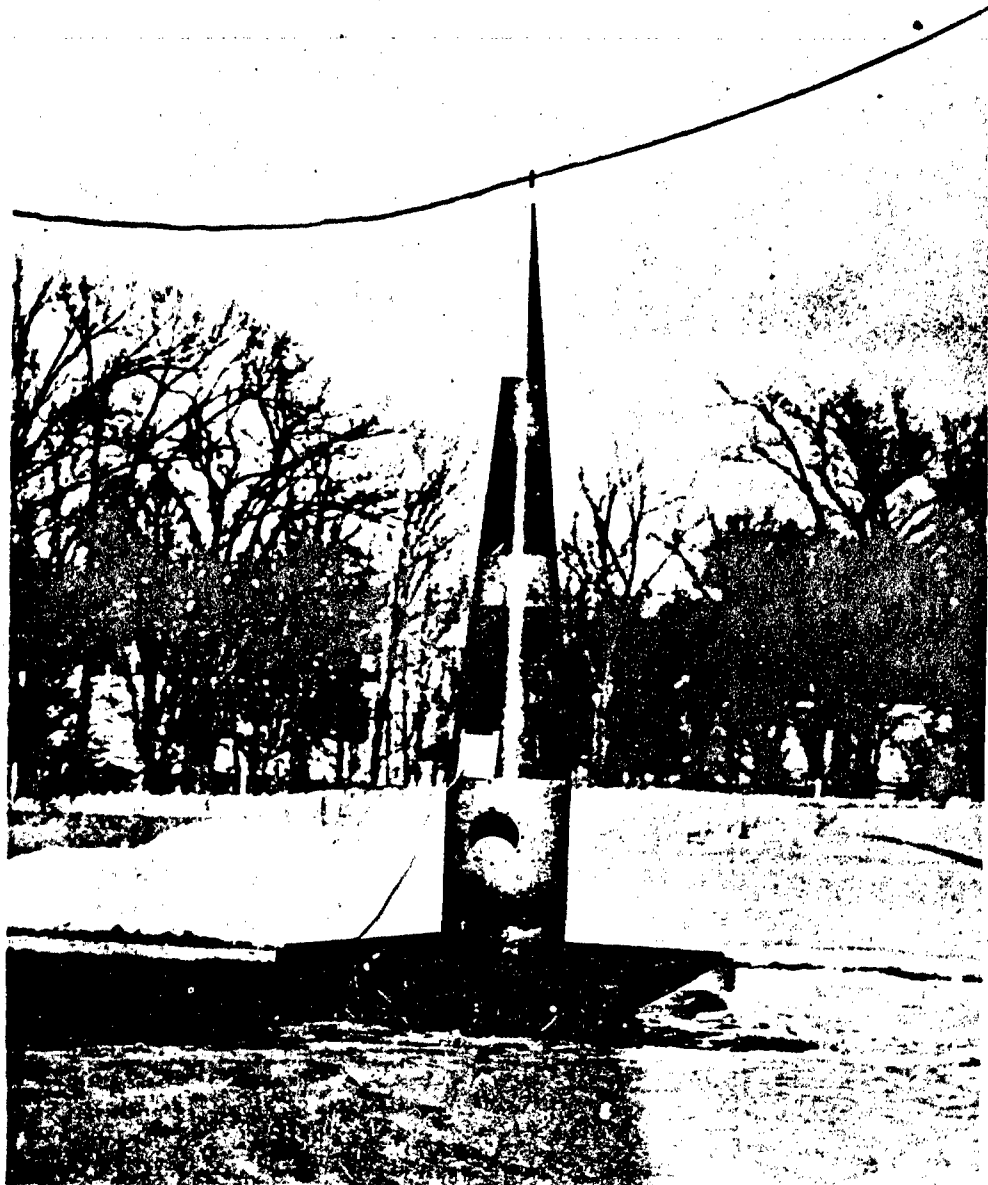


FIG. 25a FINAL TESTS OF SEPARATION SYSTEM MOUNTED IN THE NOSE CONE  
(BEFORE SEPARATION).

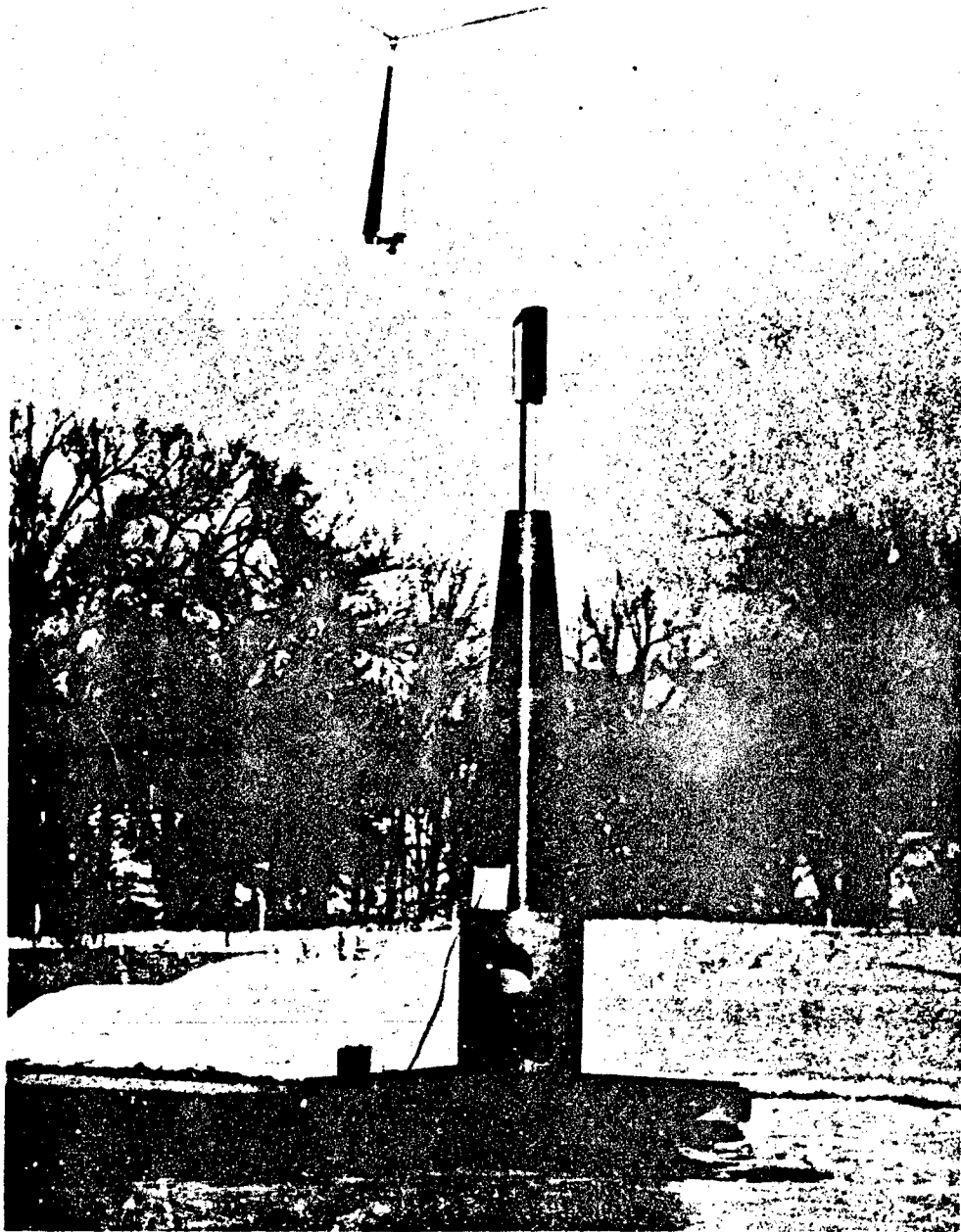


FIG. 25b FINAL TESTS OF SEPARATION SYSTEM MOUNTED IN THE NOSE CONE  
(AFTER SEPARATION)

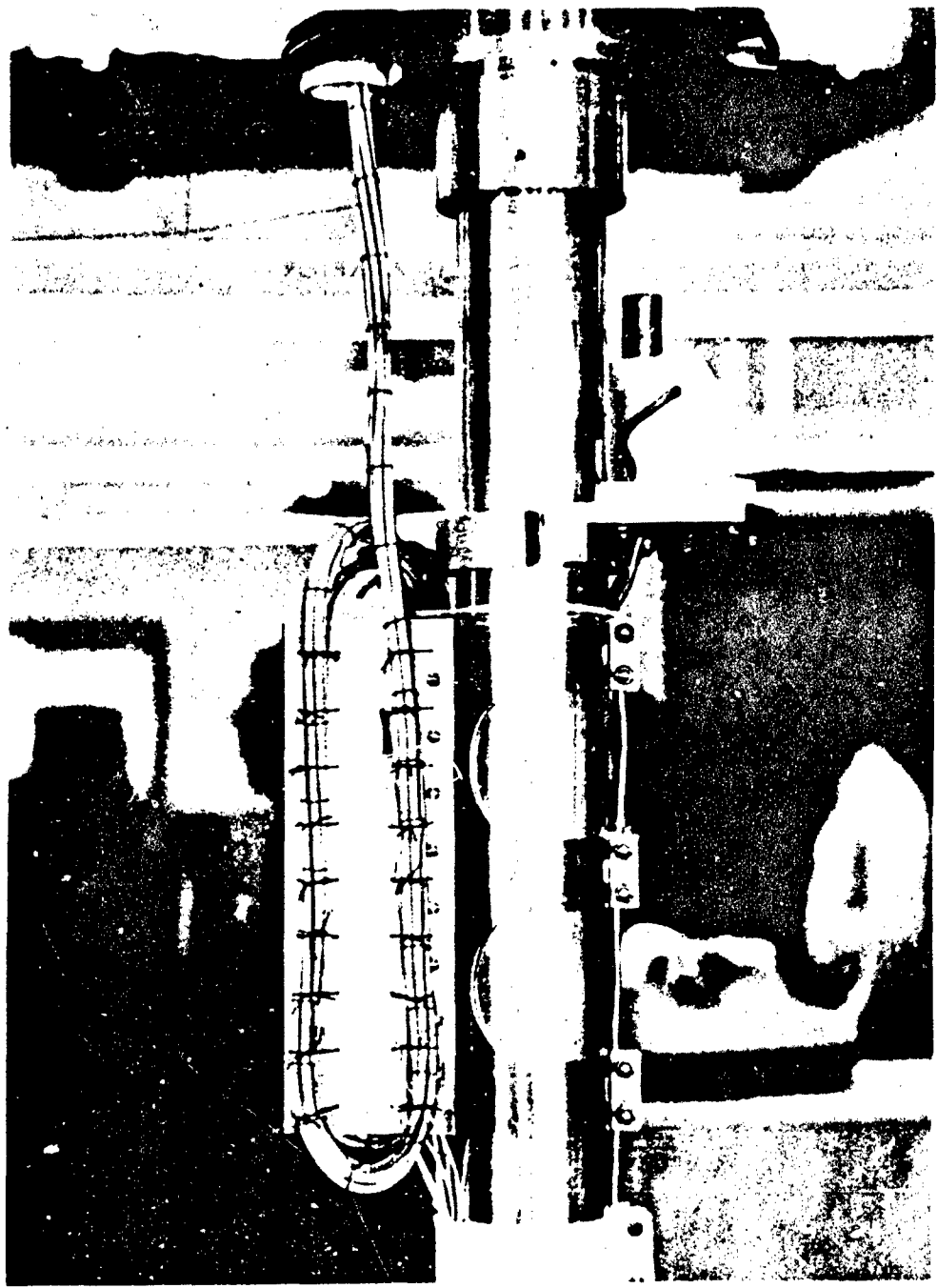


FIG. 26 CABLE HOLDER

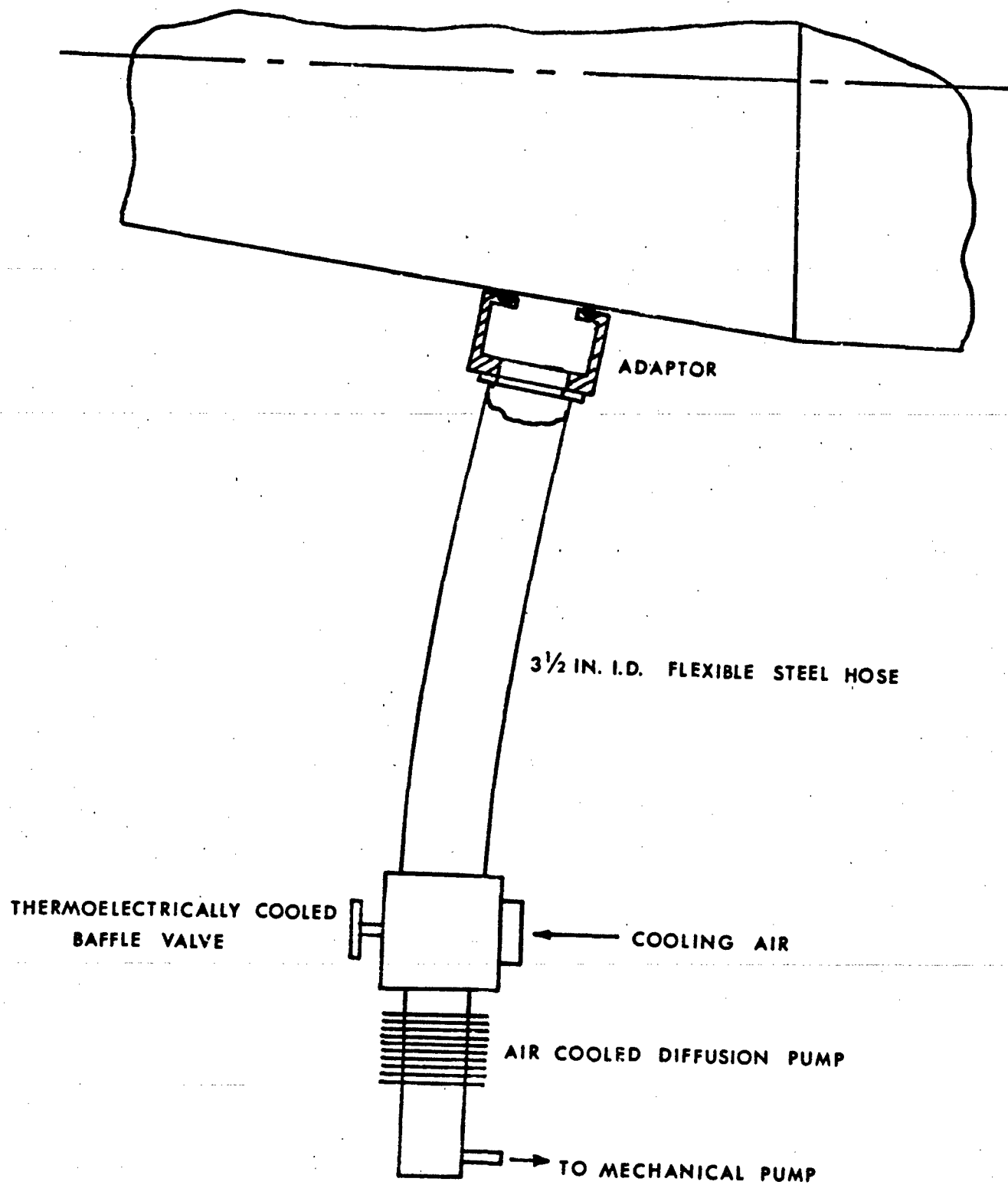


FIG. 27a SCHEMATIC VIEW OF THE PORTABLE HIGH VACUUM PUMPING SYSTEM

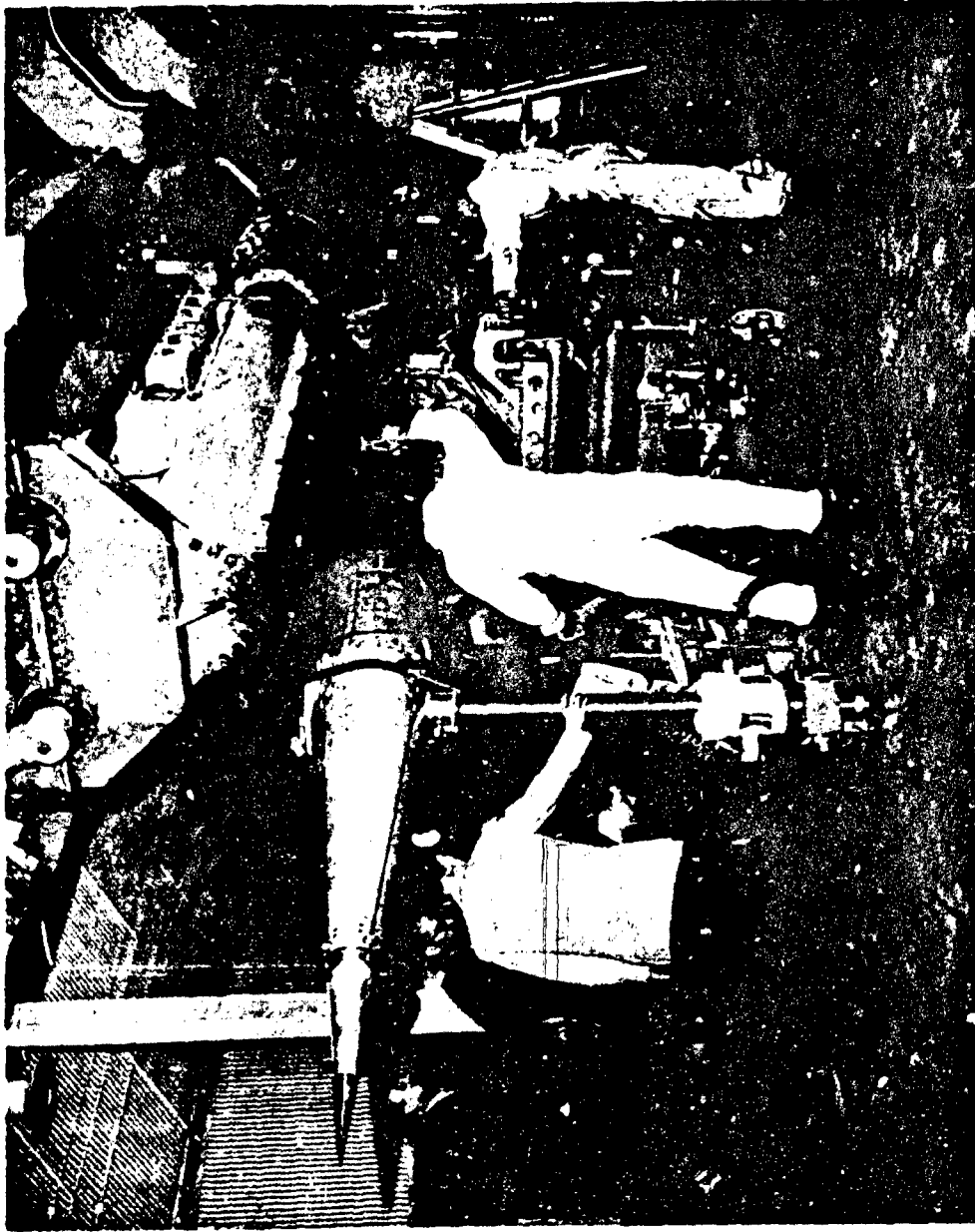


FIG. 27b PUMPING SYSTEM ATTACHED TO THE NOSE CONE



FIG. 28 SYSTEM FOR QUICK RELEASE OF THE PUMPING SYSTEM FROM THE NOSE CONE

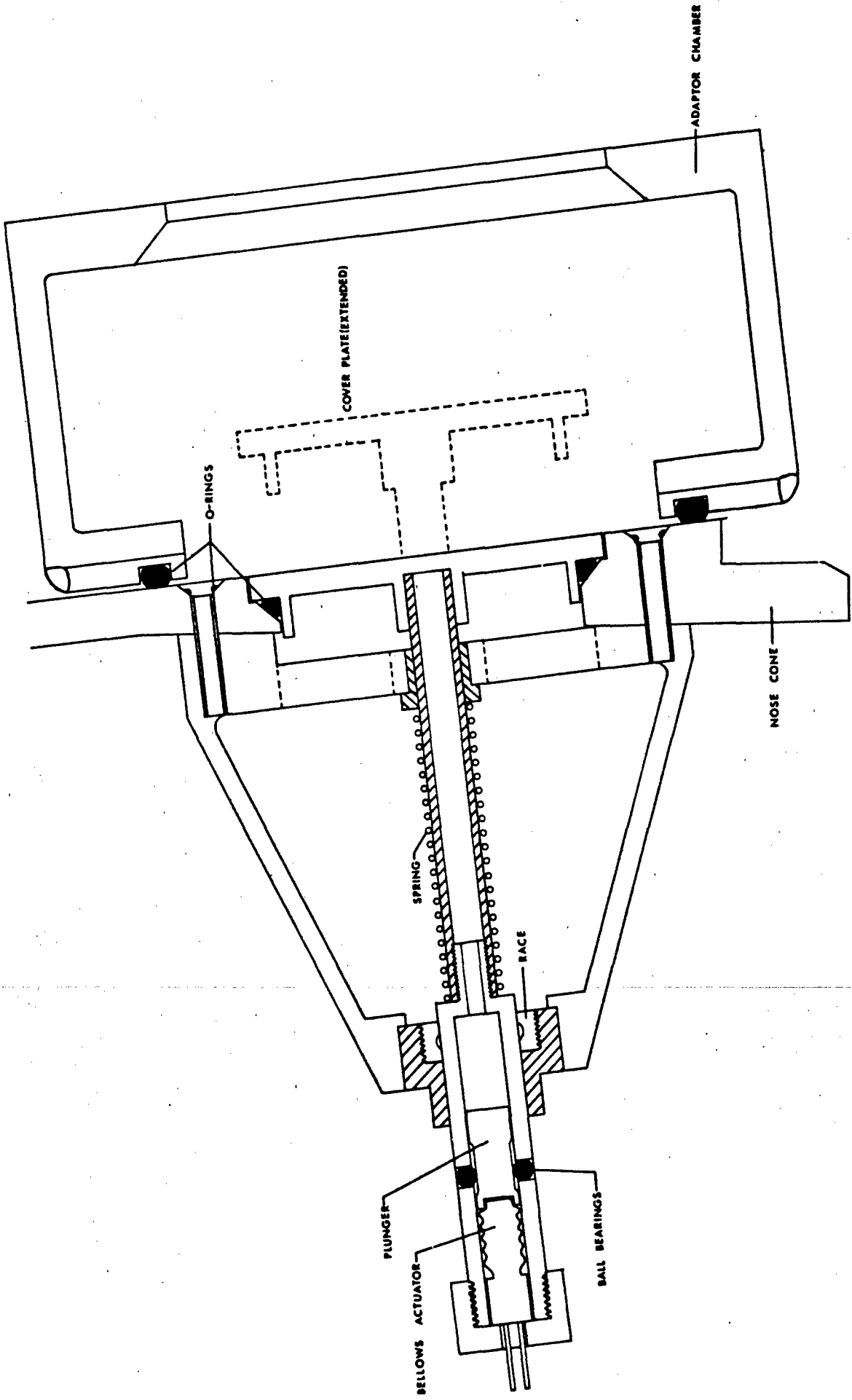


FIG. 29a ASSEMBLY DRAWING OF THE CLOSURE VALVE IN THE NOSE CONE

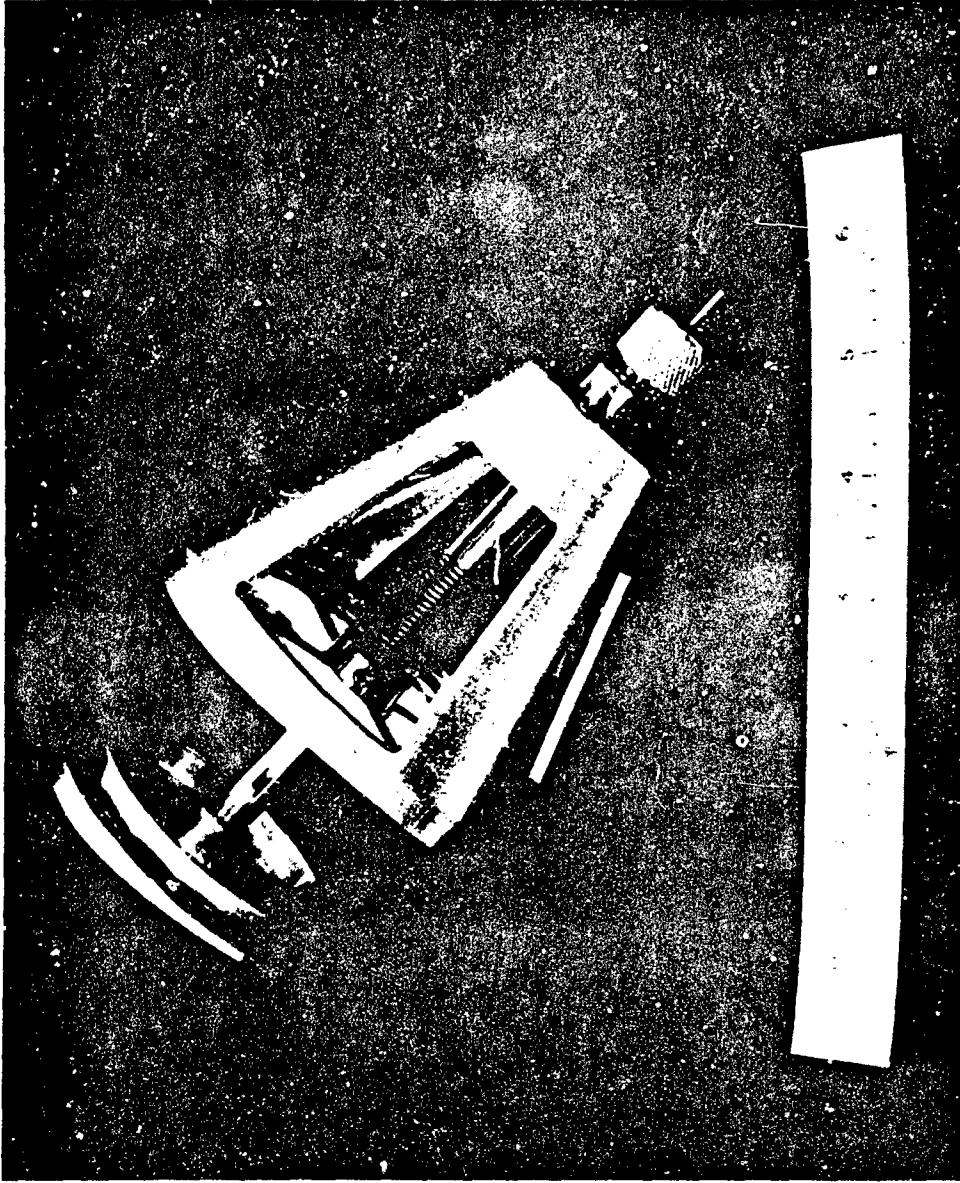


FIG. 29b CLOSURE VALVE BEFORE MOUNTING IN THE NOSE CONE



FIG. 29c CLOSURE VALVE BEFORE MOUNTING IN THE NOSE CONE

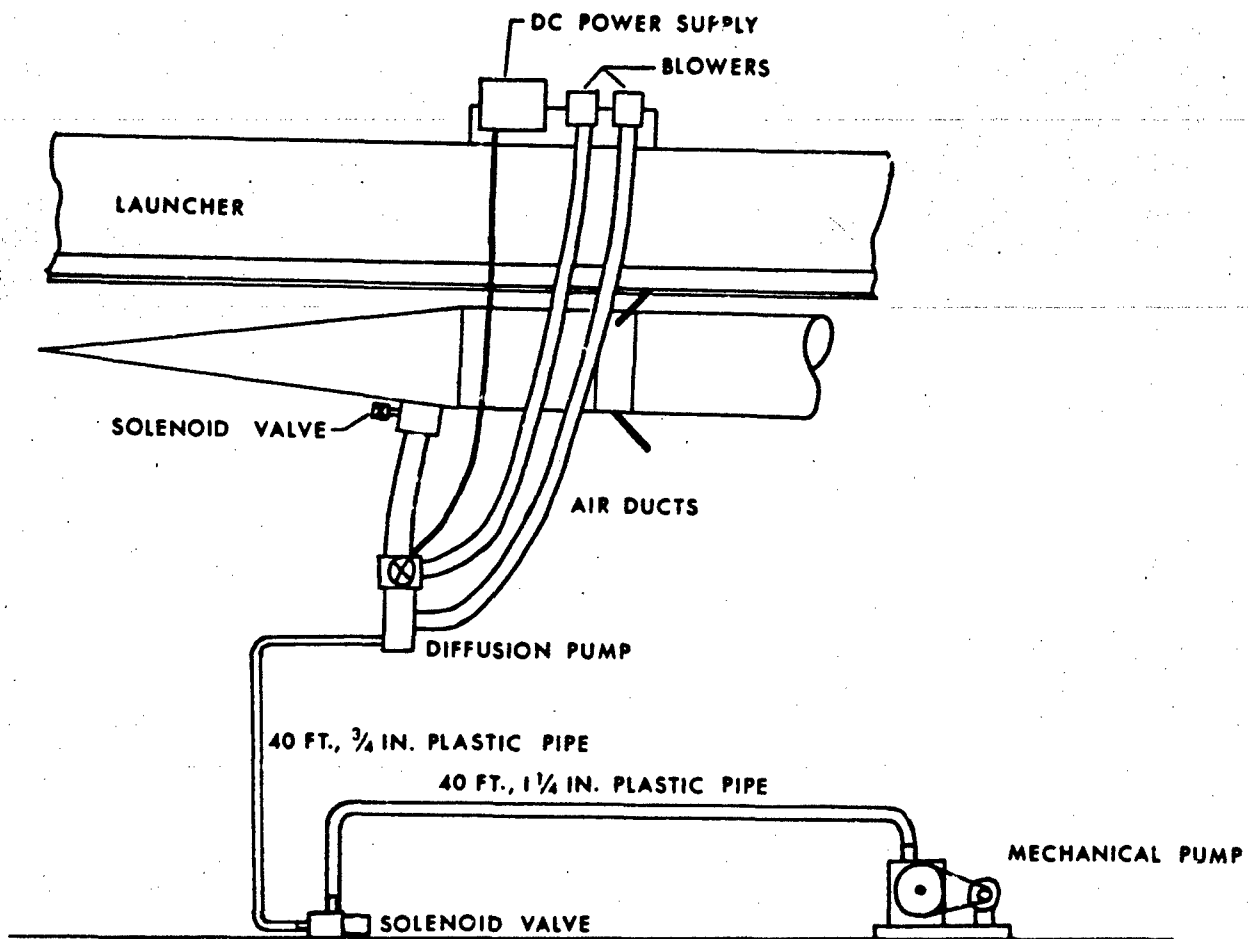


FIG. 30 SCHEMATIC LAYOUT OF THE AUXILIARY PUMPING SYSTEM EQUIPMENT AT THE LAUNCHER

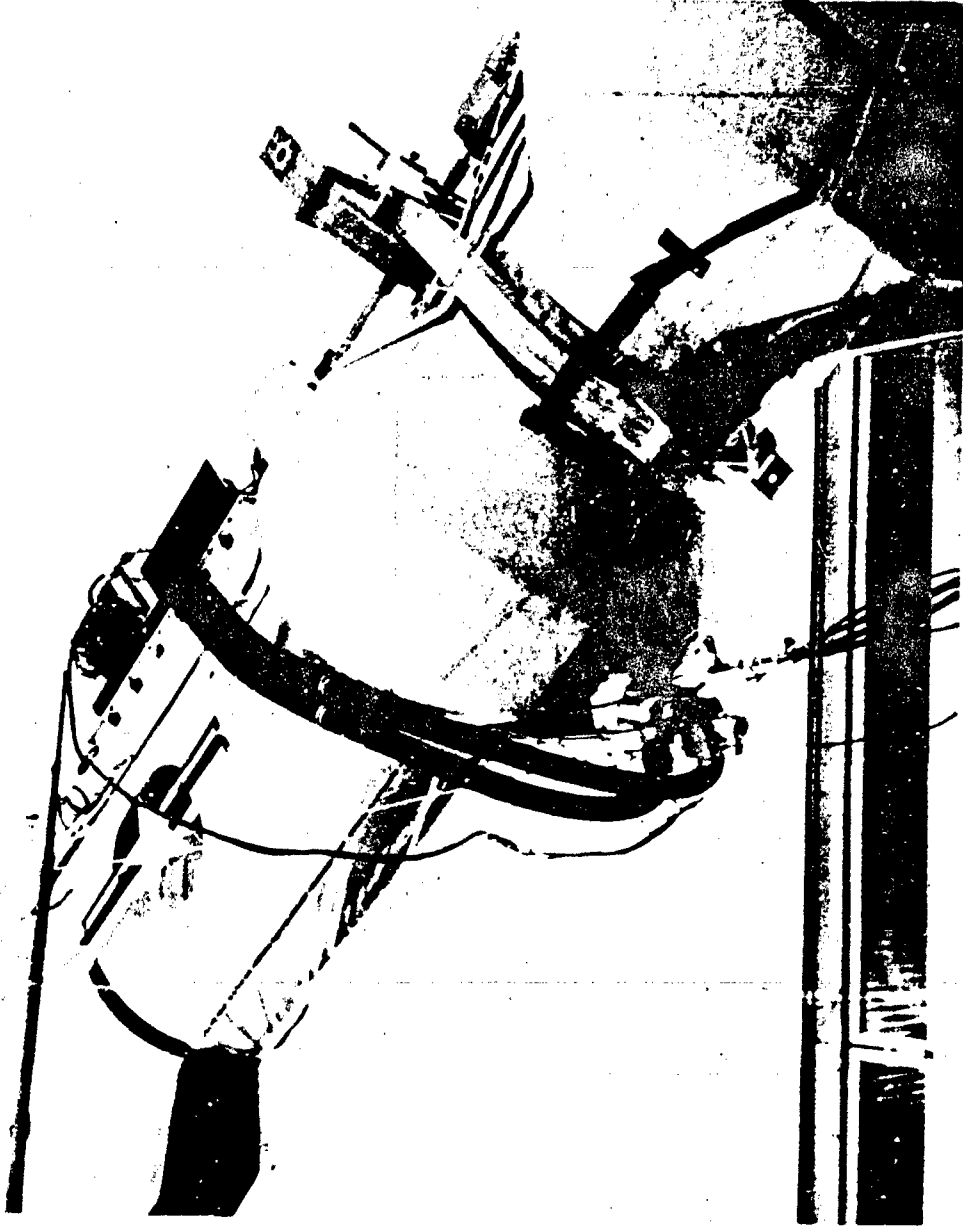


FIG. 31 PUMPING SYSTEM MOUNTED ON THE LAUNCHER

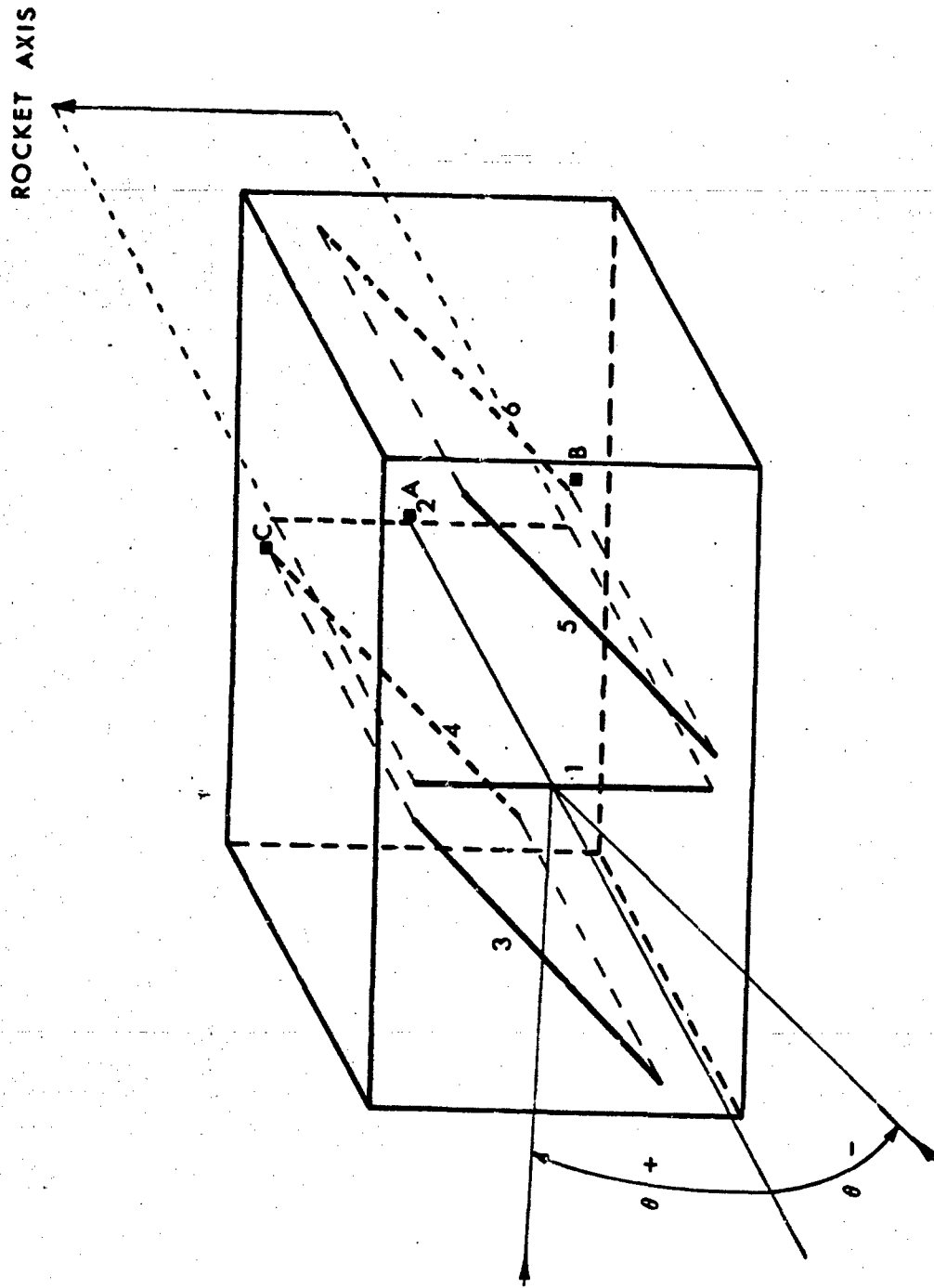


FIG. 32 SCHEMATIC LAYOUT OF THE SLIT PATTERN FOR THE SUN SENSORS

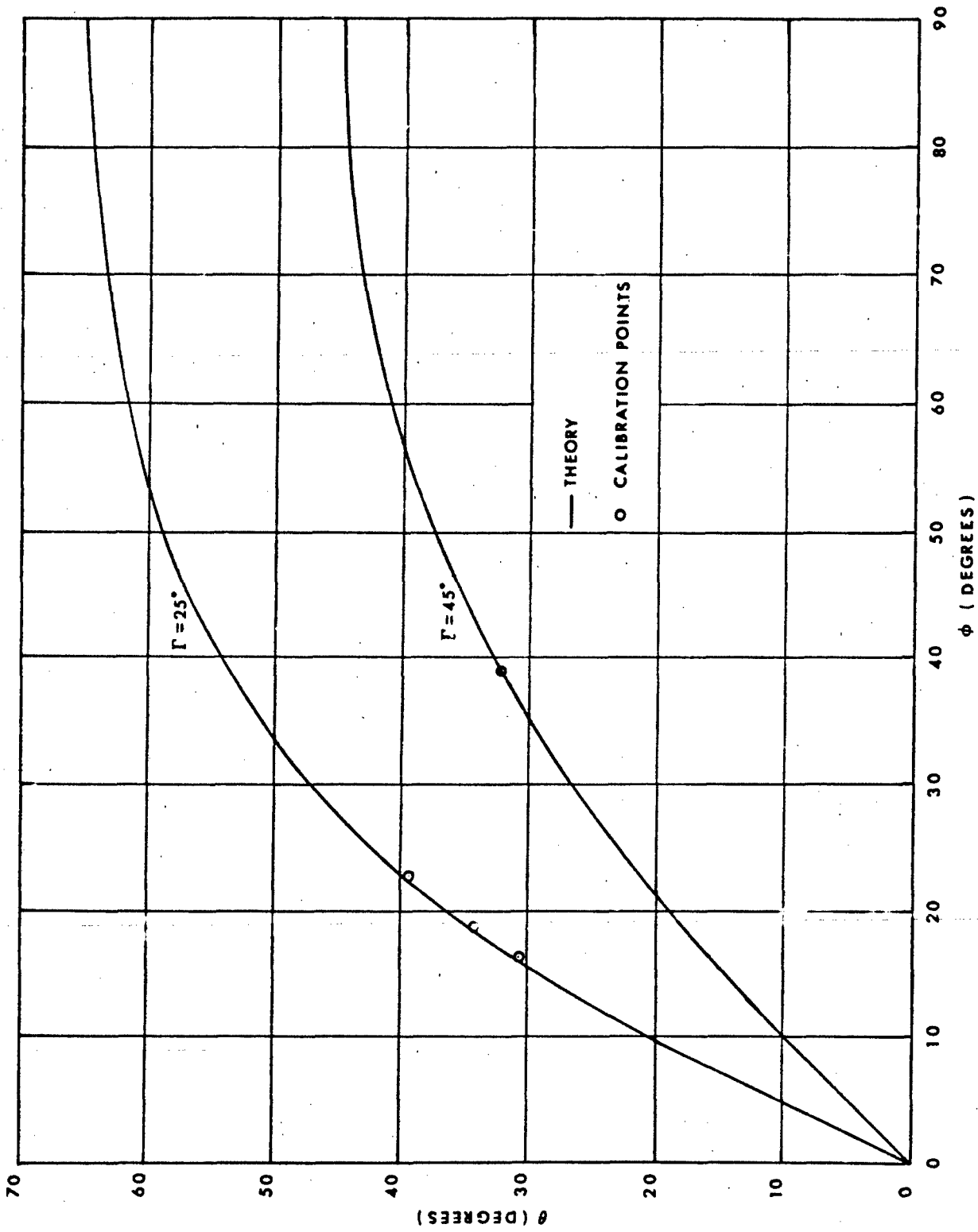


FIG. 33 THEORETICAL CALIBRATION FOR THE  $45^\circ$  AND  $65^\circ$  SUN SENSORS

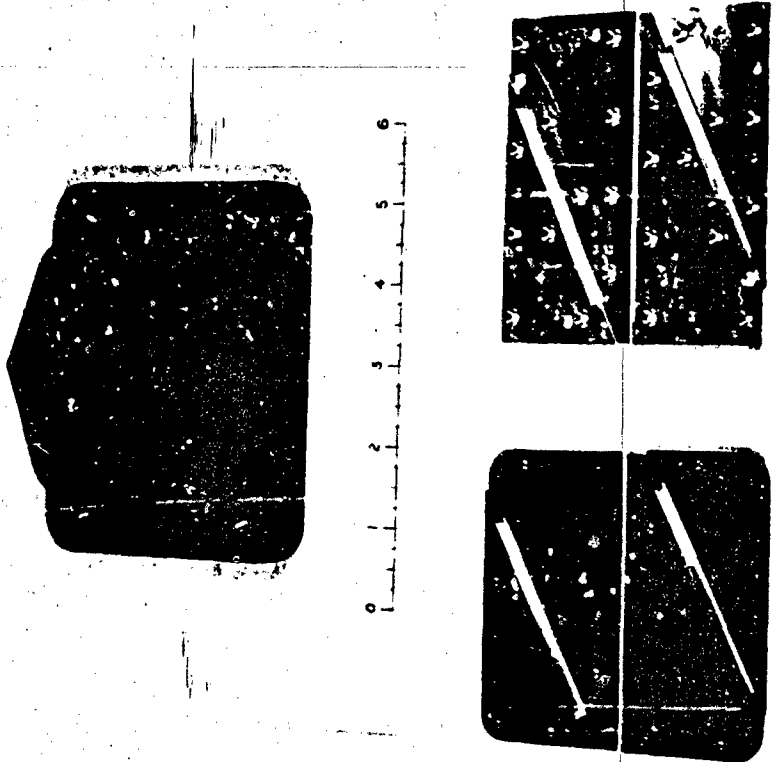


FIG. 34 MOUNTING BLOCK AND SLIT PLATES FOR THE 65° SUN SENSOR

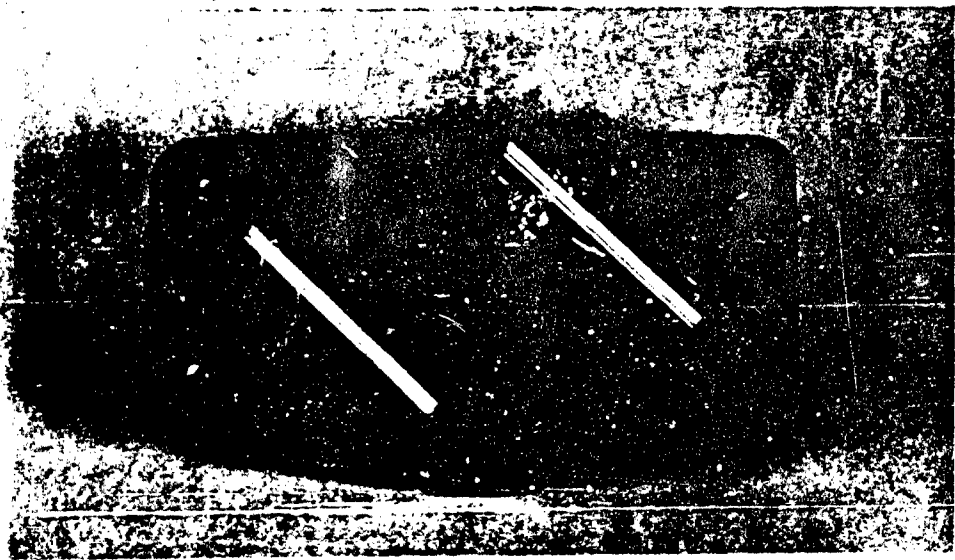
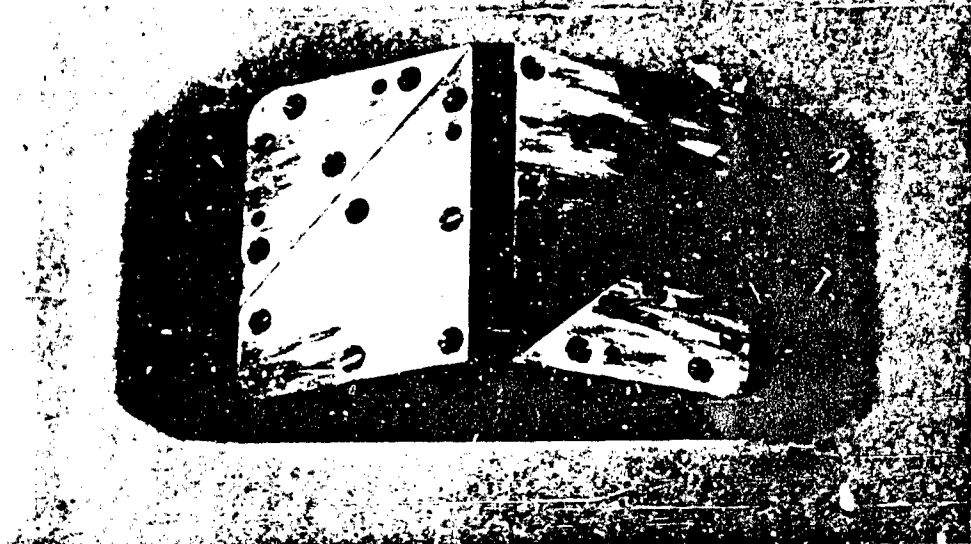


FIG. 35 ASSEMBLED 45° SUN SENSOR

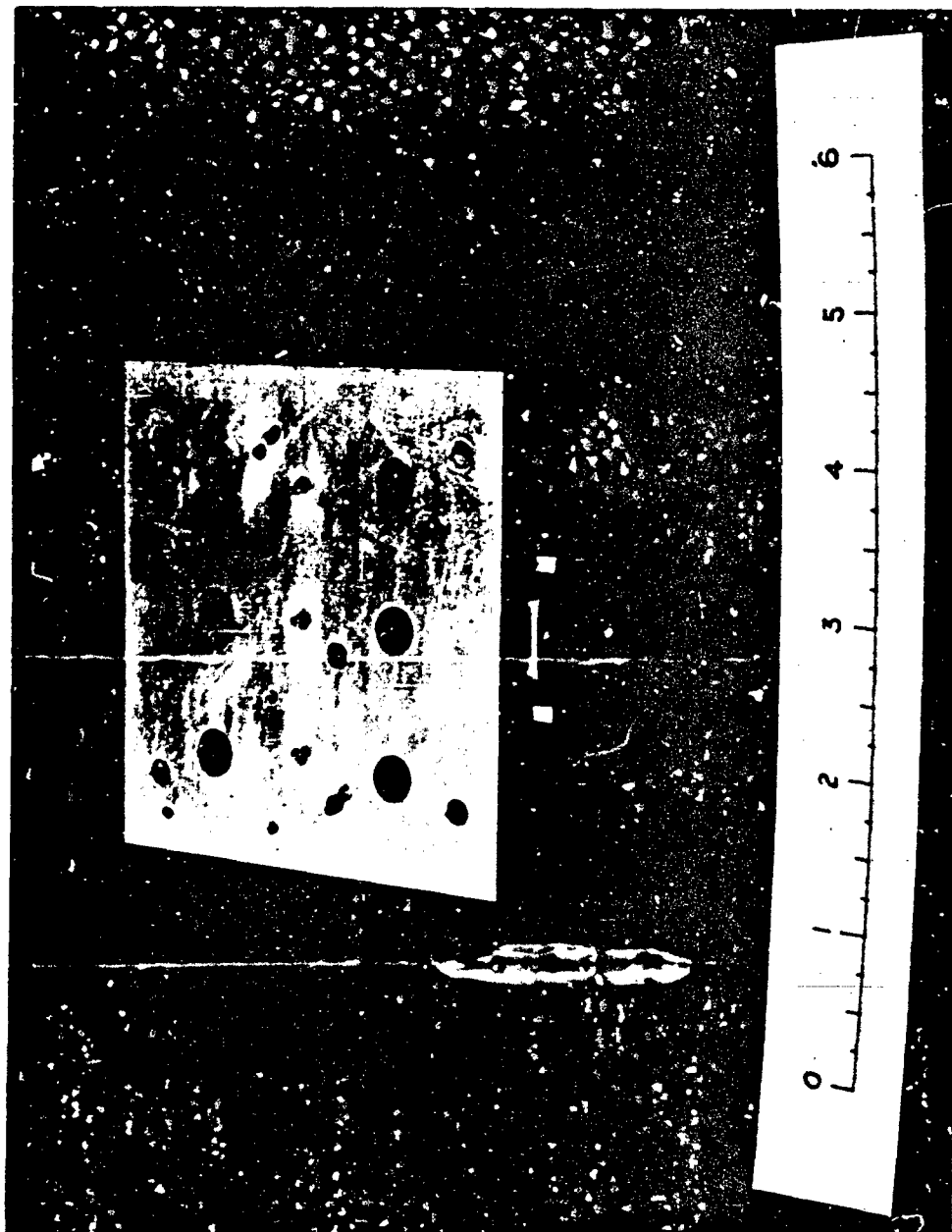
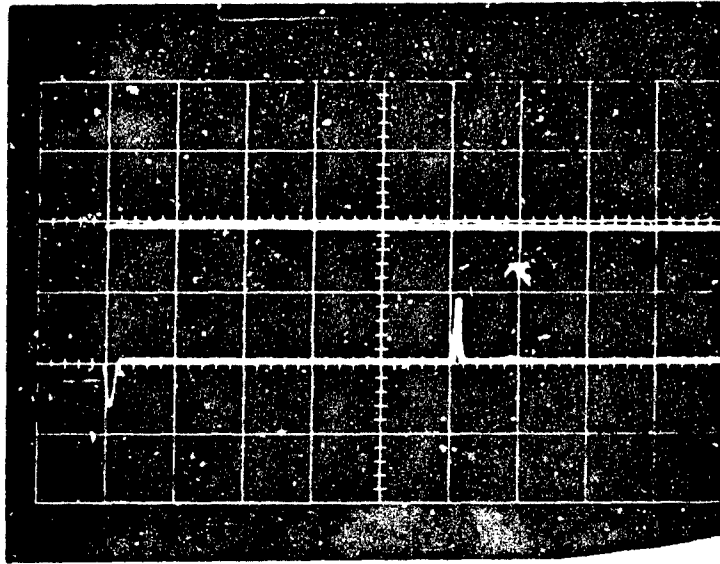


FIG. 36 MOUNTING PLATE FOR THE PHOTO-DIODES



TIME BASE      10 MS/CM

VERTICAL SCALE    5 VOLTS/CM

FIG. 37    OSCILLOSCOPE TRACE OF THE PULSE OUTPUTS FROM THE SUN SENSOR

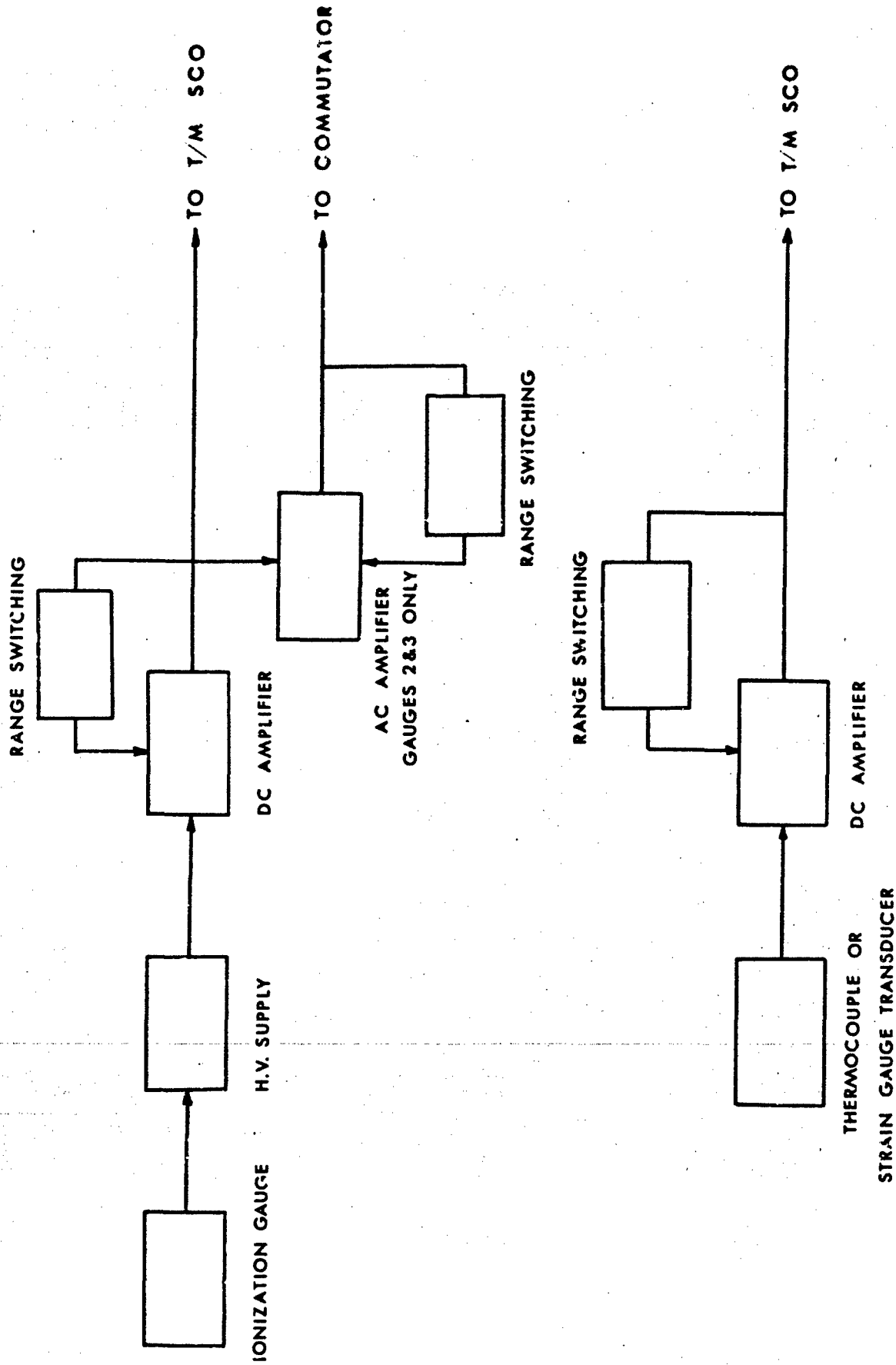


FIG. 38 BLOCK DIAGRAM OF THE ROCKET ELECTRICAL SYSTEM

AE-II-24

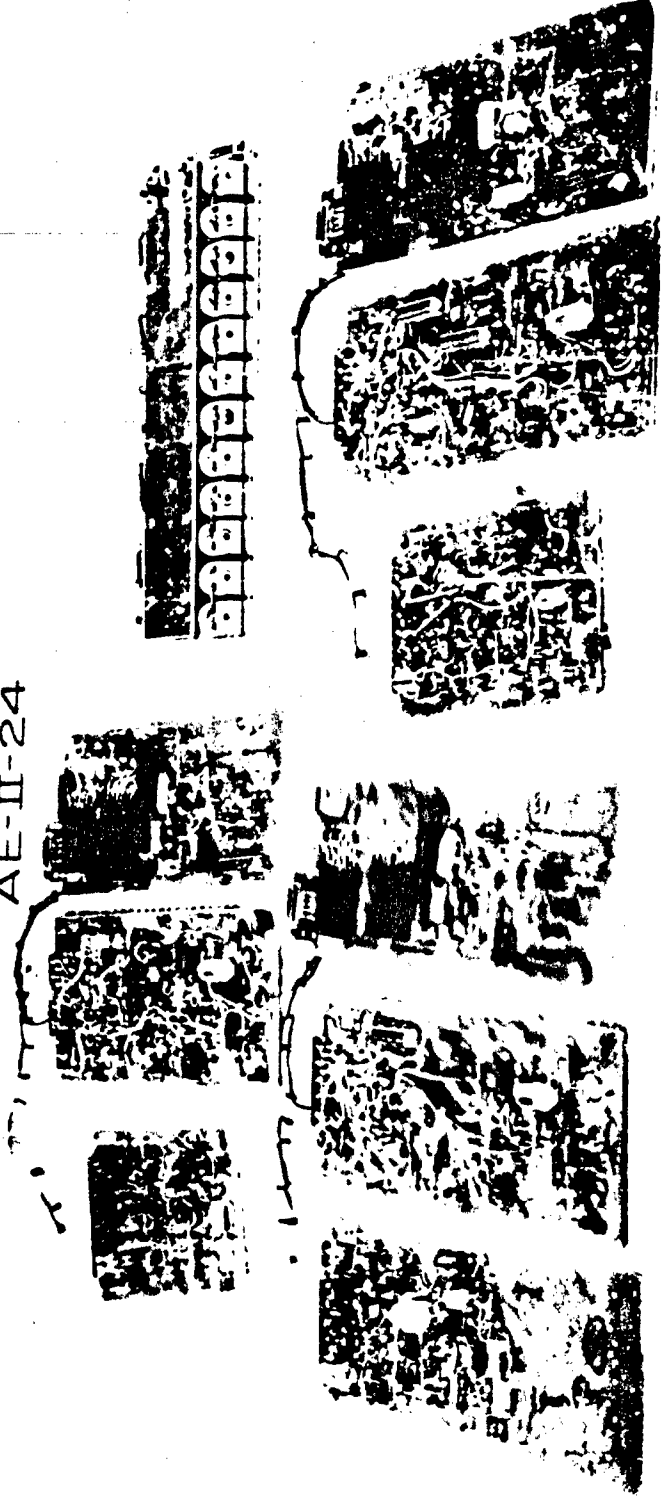


FIG. 39 TYPICAL CIRCUITS CONSTRUCTED FOR THE EXPERIMENT

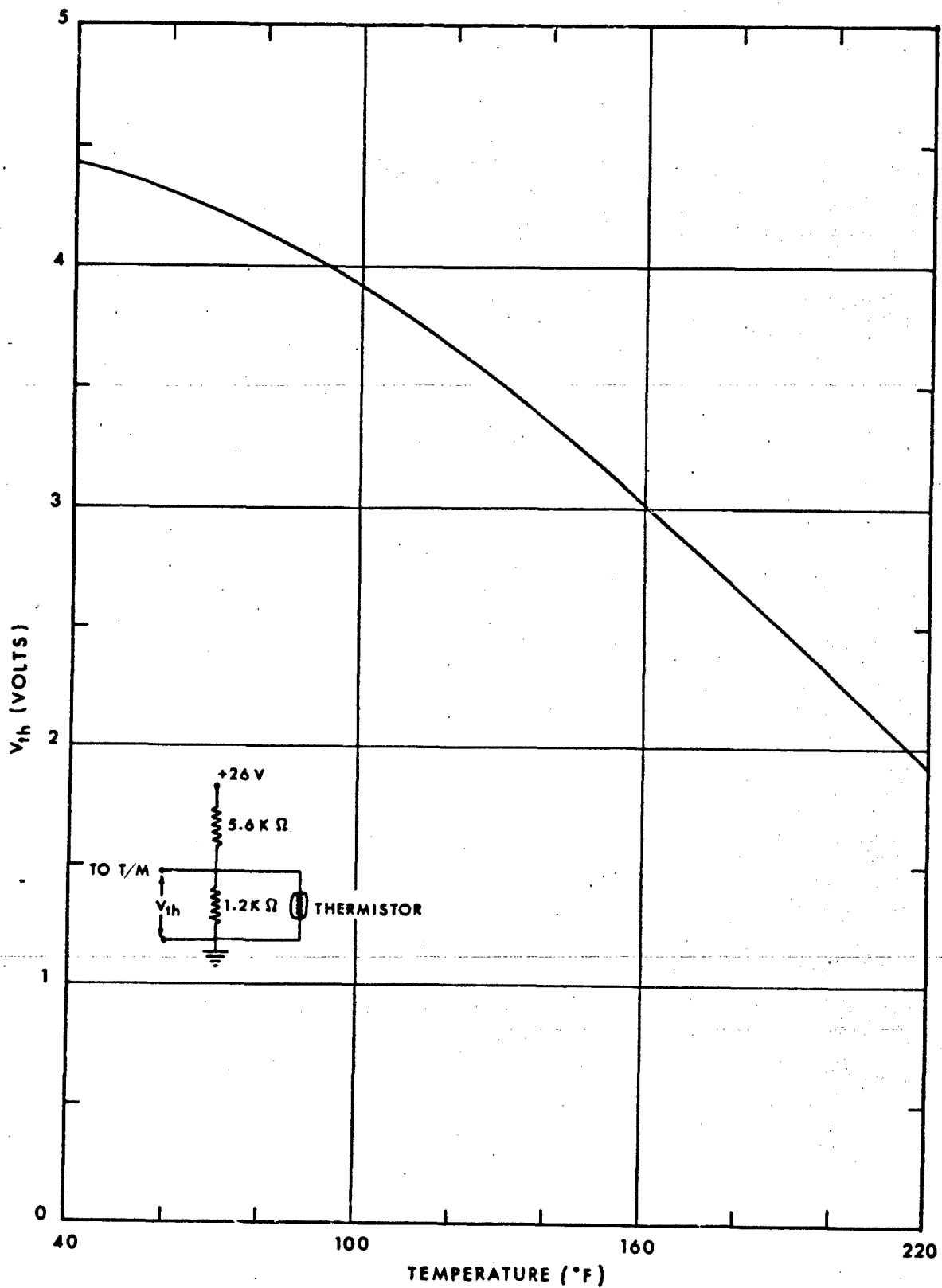
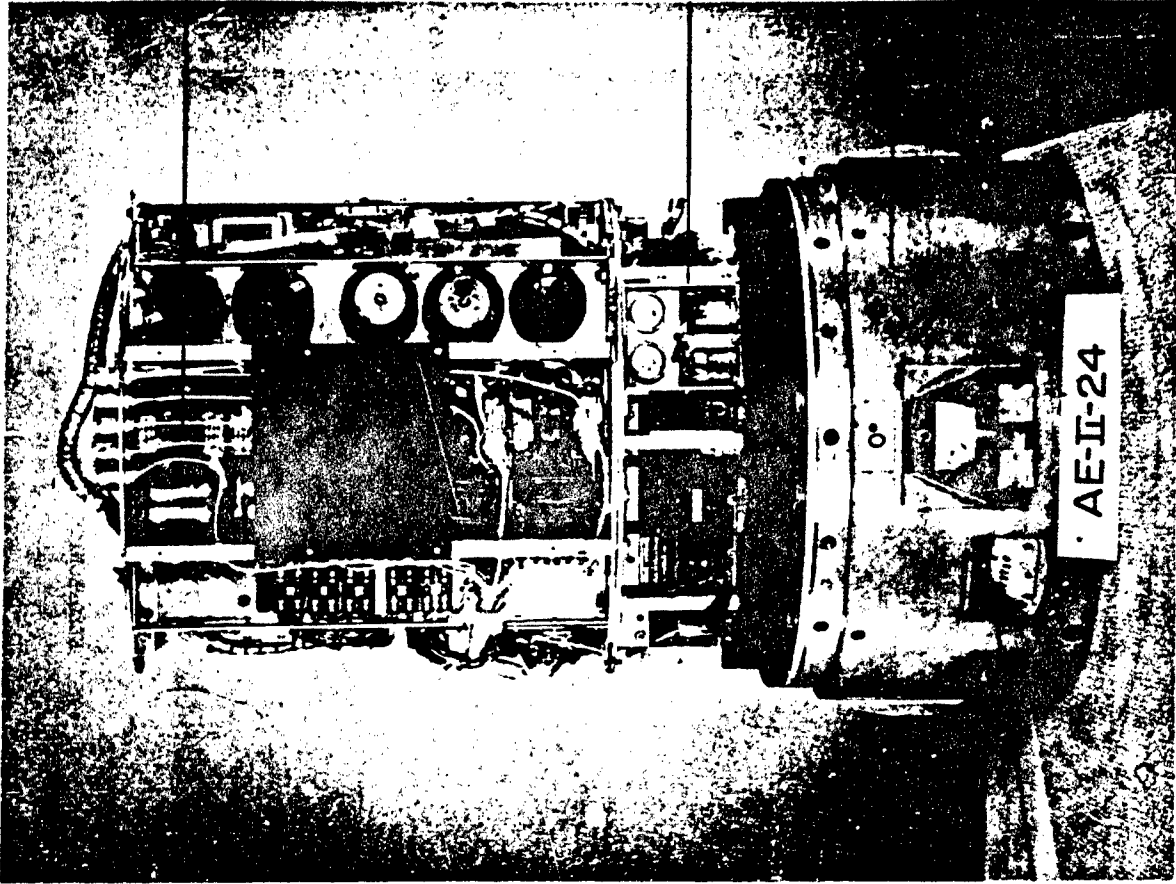


FIG. 40 THERMISTOR CIRCUIT AND TYPICAL TEMPERATURE CALIBRATION



HIGH VOLTAGE  
POWER SUPPLIES

TELEMETRY

EXTENSION BODY

TELEMETRY ANTENNA  
LOCATION

RADAR BEACON  
ANTENNA

UMBILICAL PLUG

FIG. 41a ELECTRONICS FRAME (0° ROLL POSITION)

SUBCOMMUTATOR

COMMUTATOR

45° SUN SENSOR

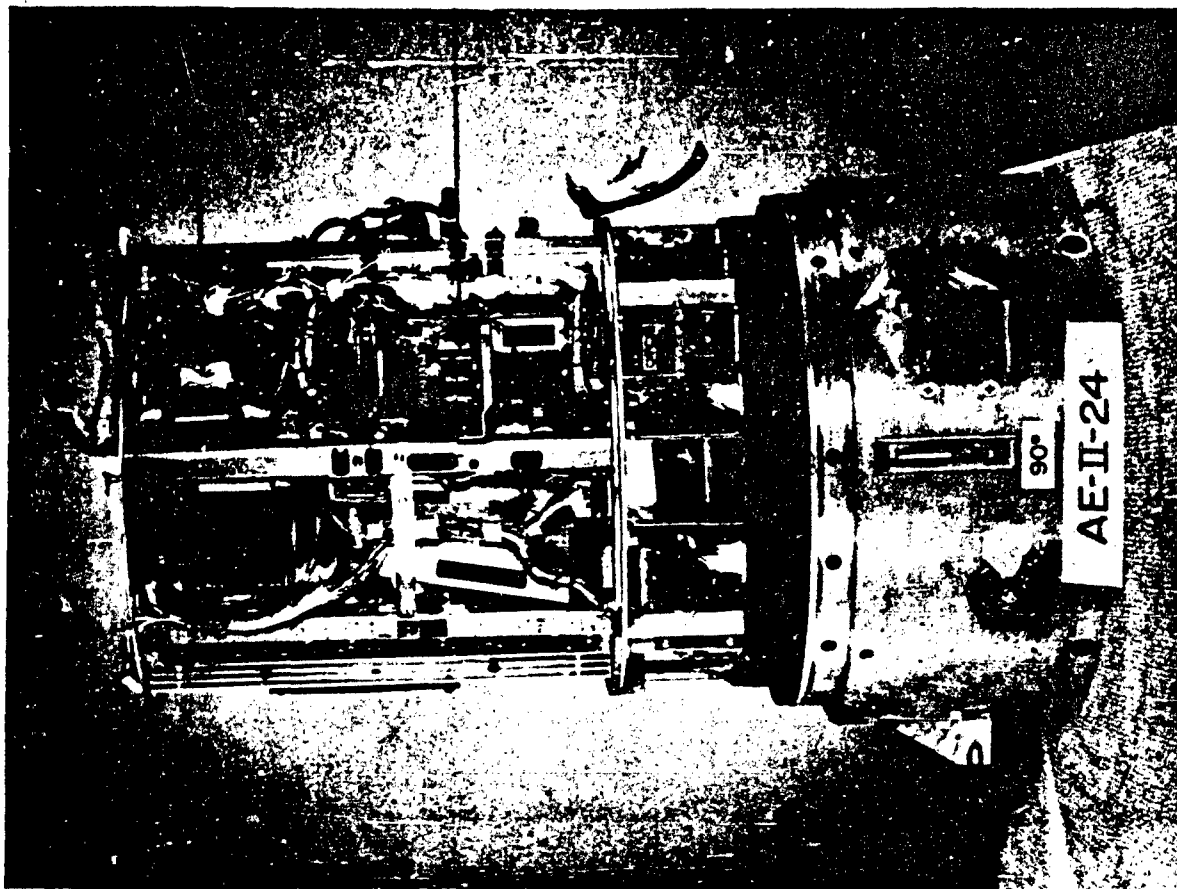


FIG. 41b ELECTRONICS FRAME (90° ROLL POSITION)

MAGNETOMETER  
ELECTRONICS

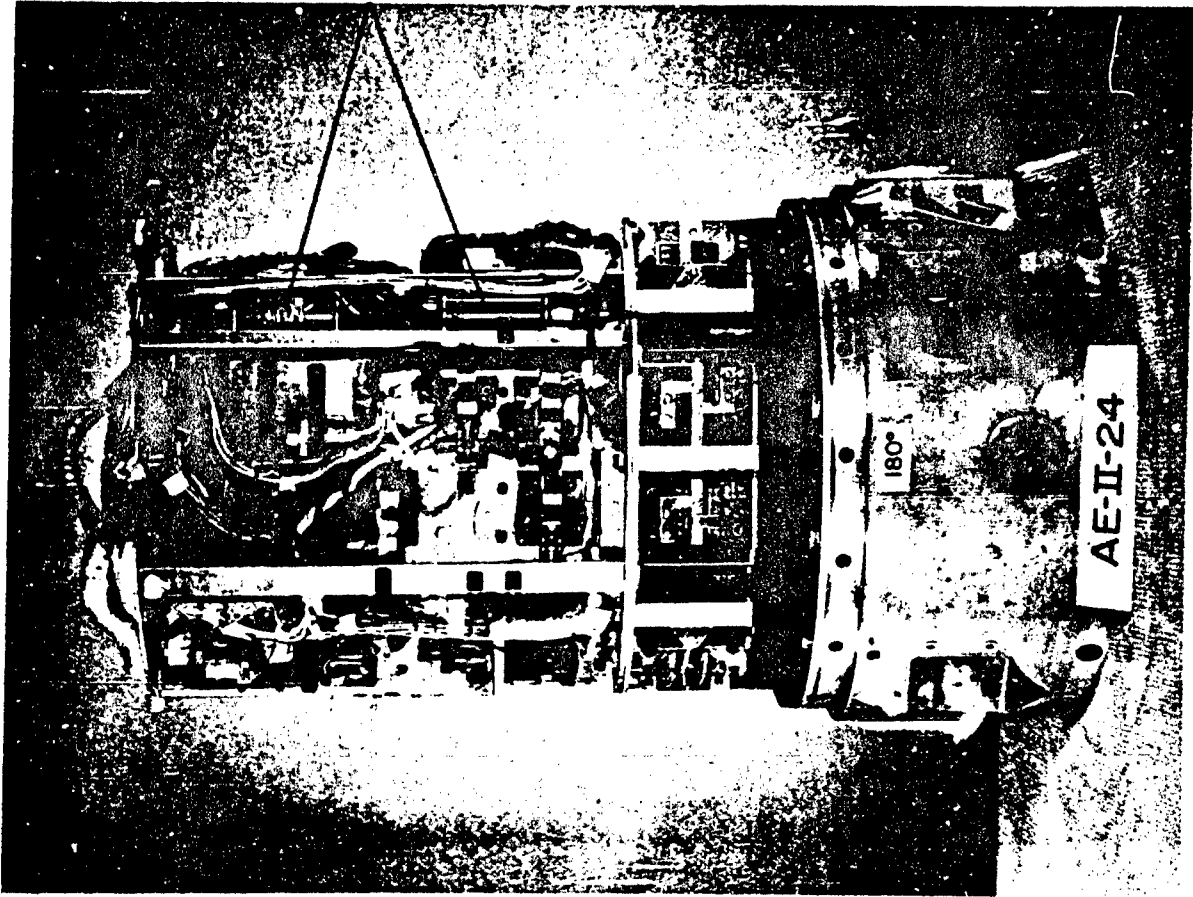
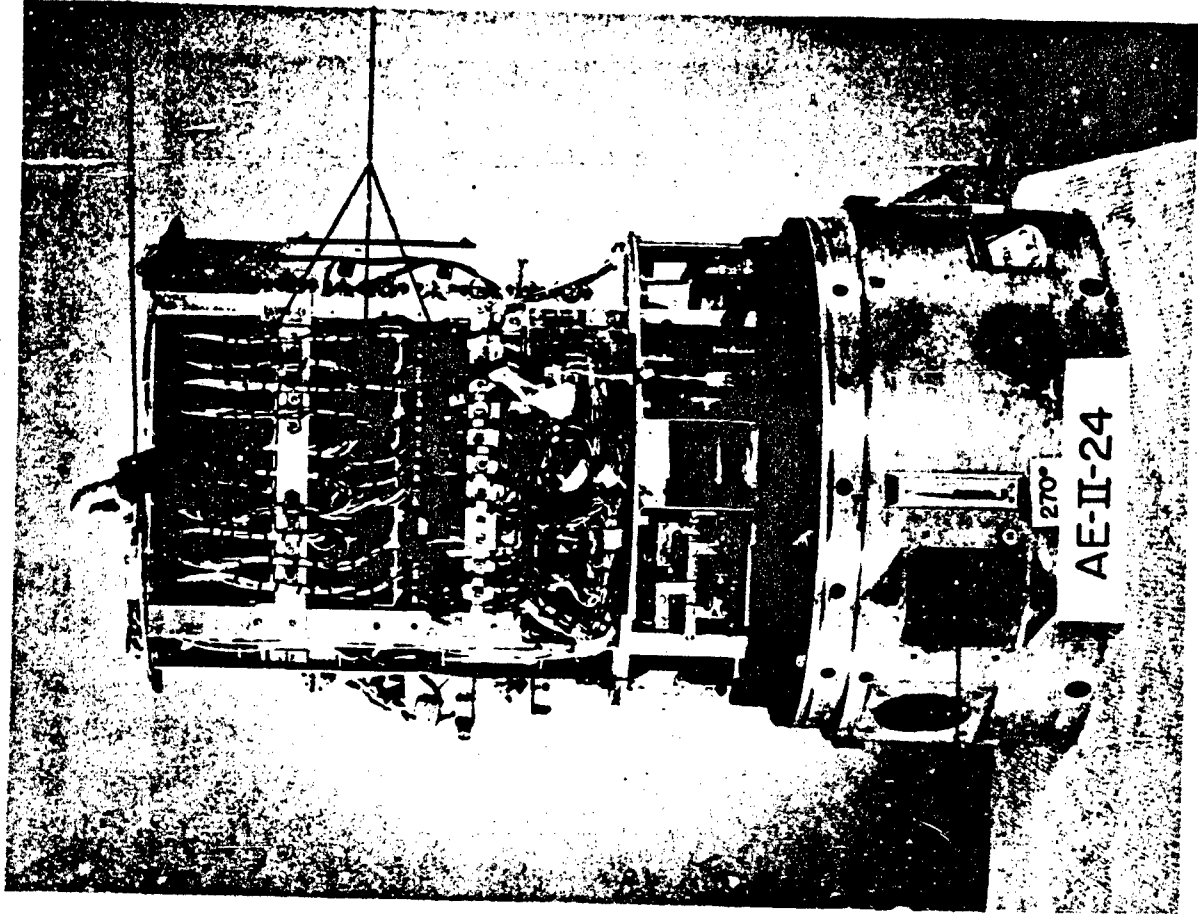


FIG. 41c ELECTRONICS FRAME (180° ROLL POSITION)



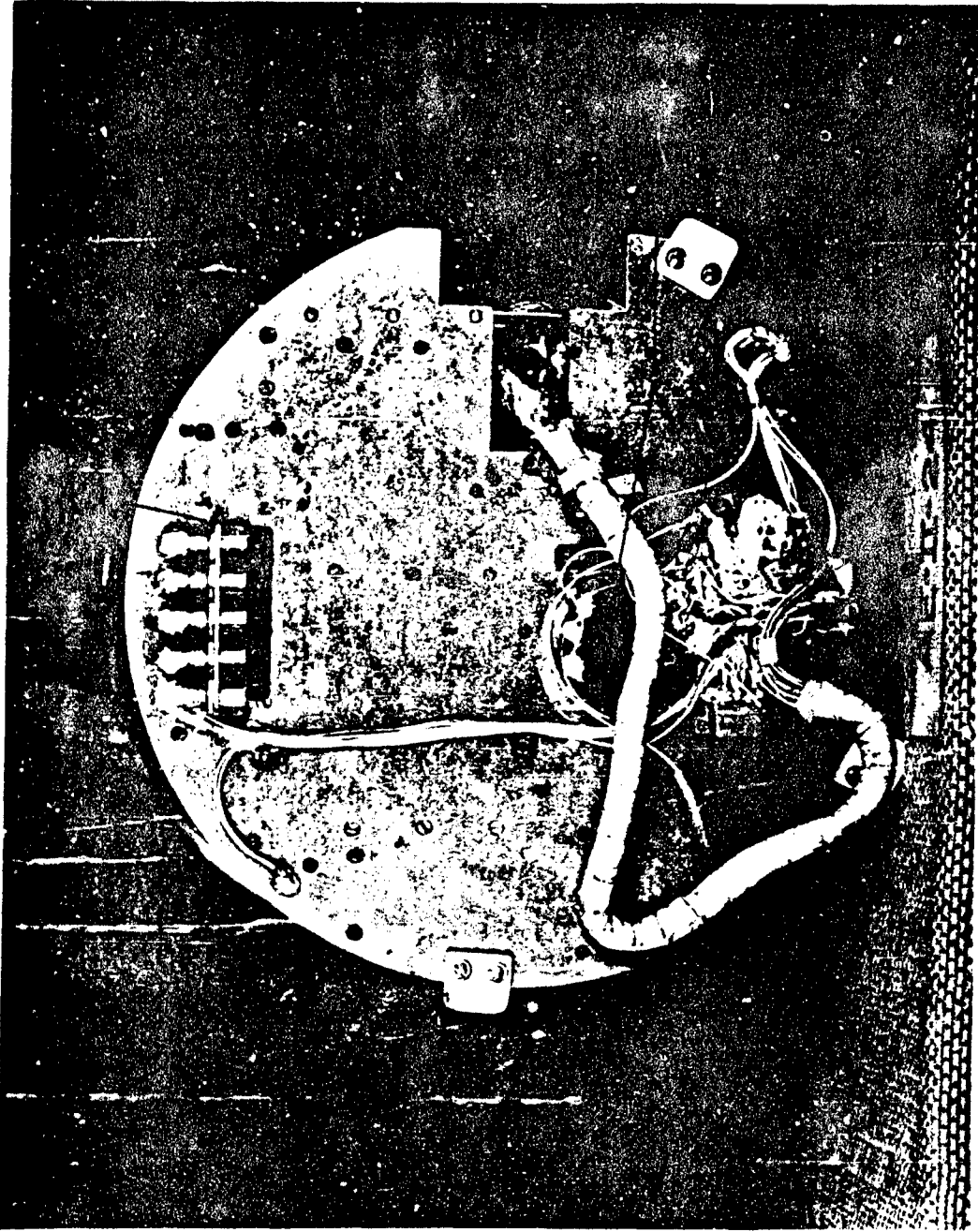
BULKHEAD CONNECTOR

CIRCUIT BOARDS

65° SUN SENSOR

FIG. 41d ELECTRONICS FRAME (270° ROLL POSITION)

HIGH VOLTAGE CONNECTORS



THERMOCOUPLE GAUGE  
POWER SUPPLIES

FIG. 41e TOP OF THE ELECTRONICS FRAME

COAXIAL CABLE  
TO ANTENNAE



FIG. 41f VIEW LOOKING FORWARD INTO THE EXTENSION BODY .

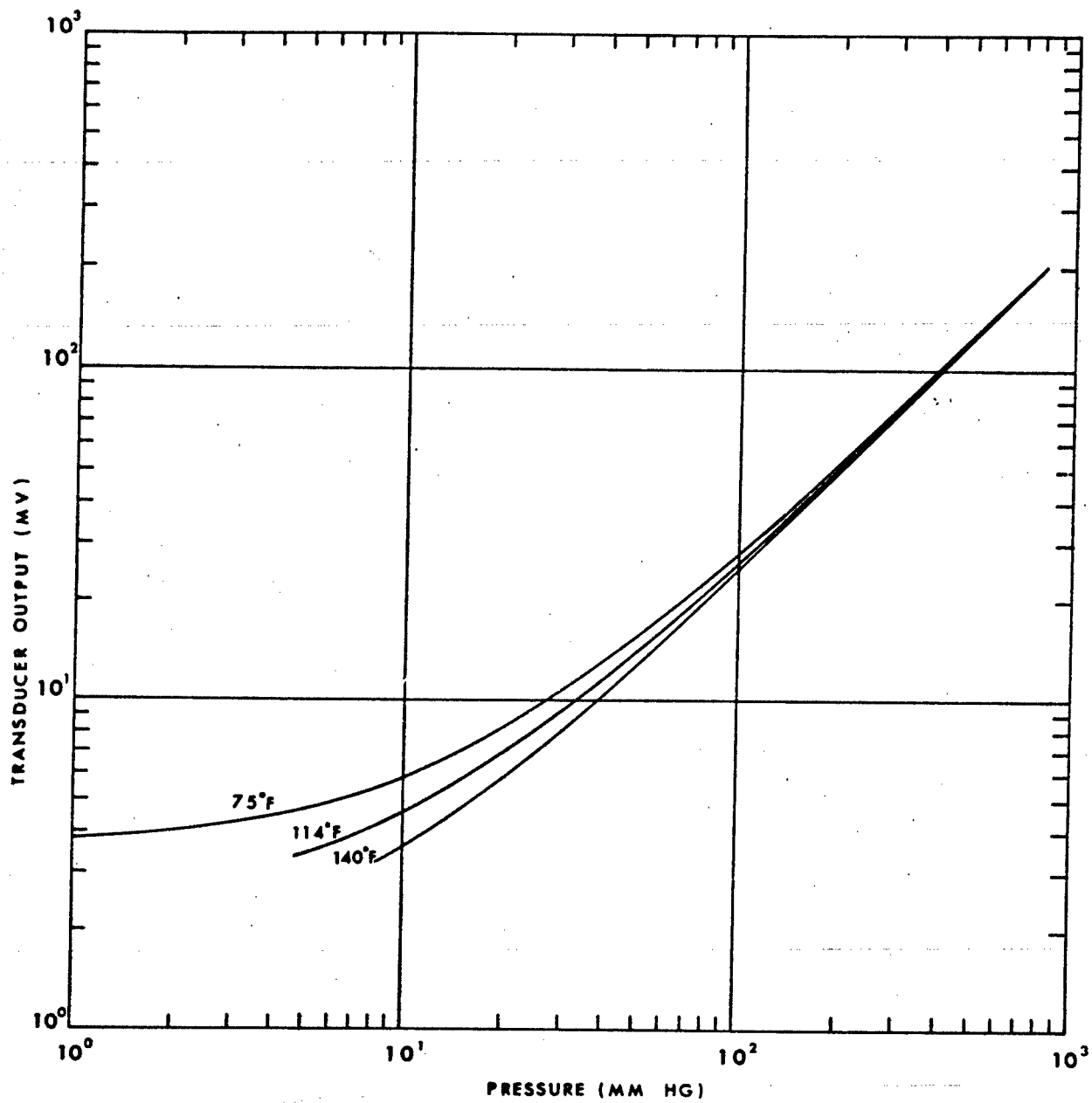


FIG. 42 TEMPERATURE DEPENDENCE OF THE CALIBRATION FOR THE STRAIN GAUGE PRESSURE TRANSDUCER (H.P.2)

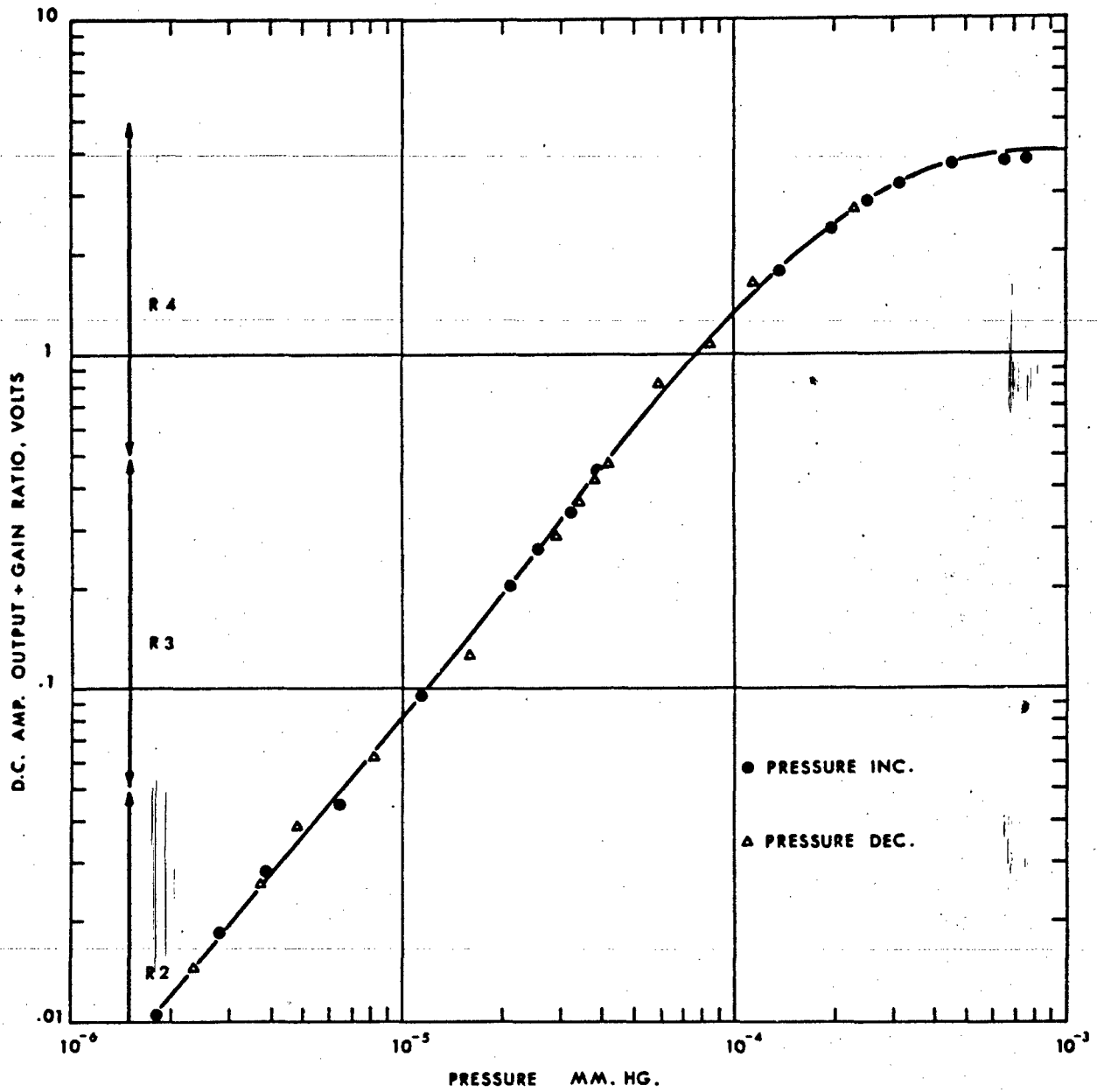


FIG. 43 TYPICAL IONIZATION GAUGE CALIBRATION

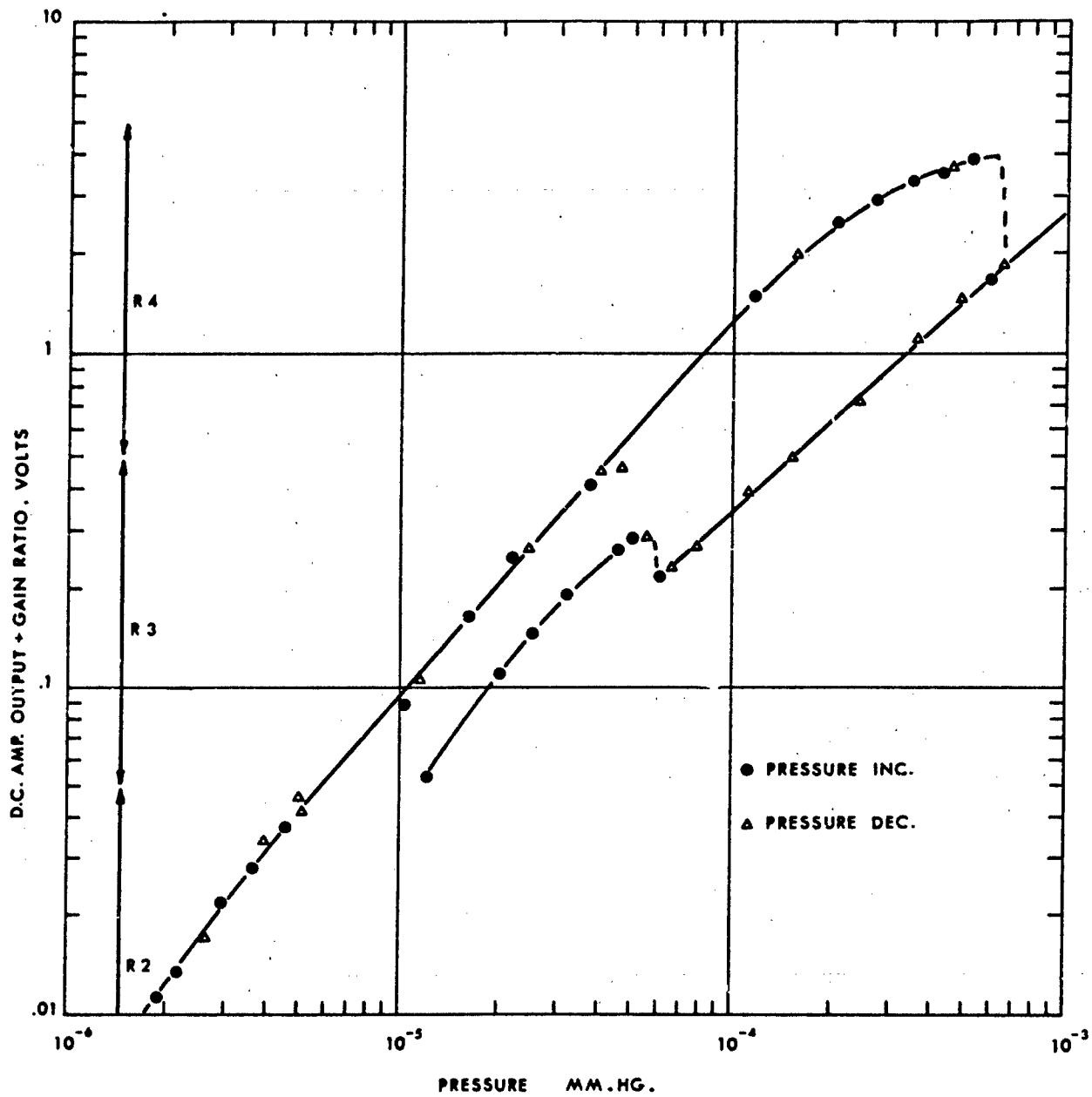


FIG. 44 CALIBRATION FOR IONIZATION GAUGE 4 INDICATING THE 2 STABLE OPERATING MODES

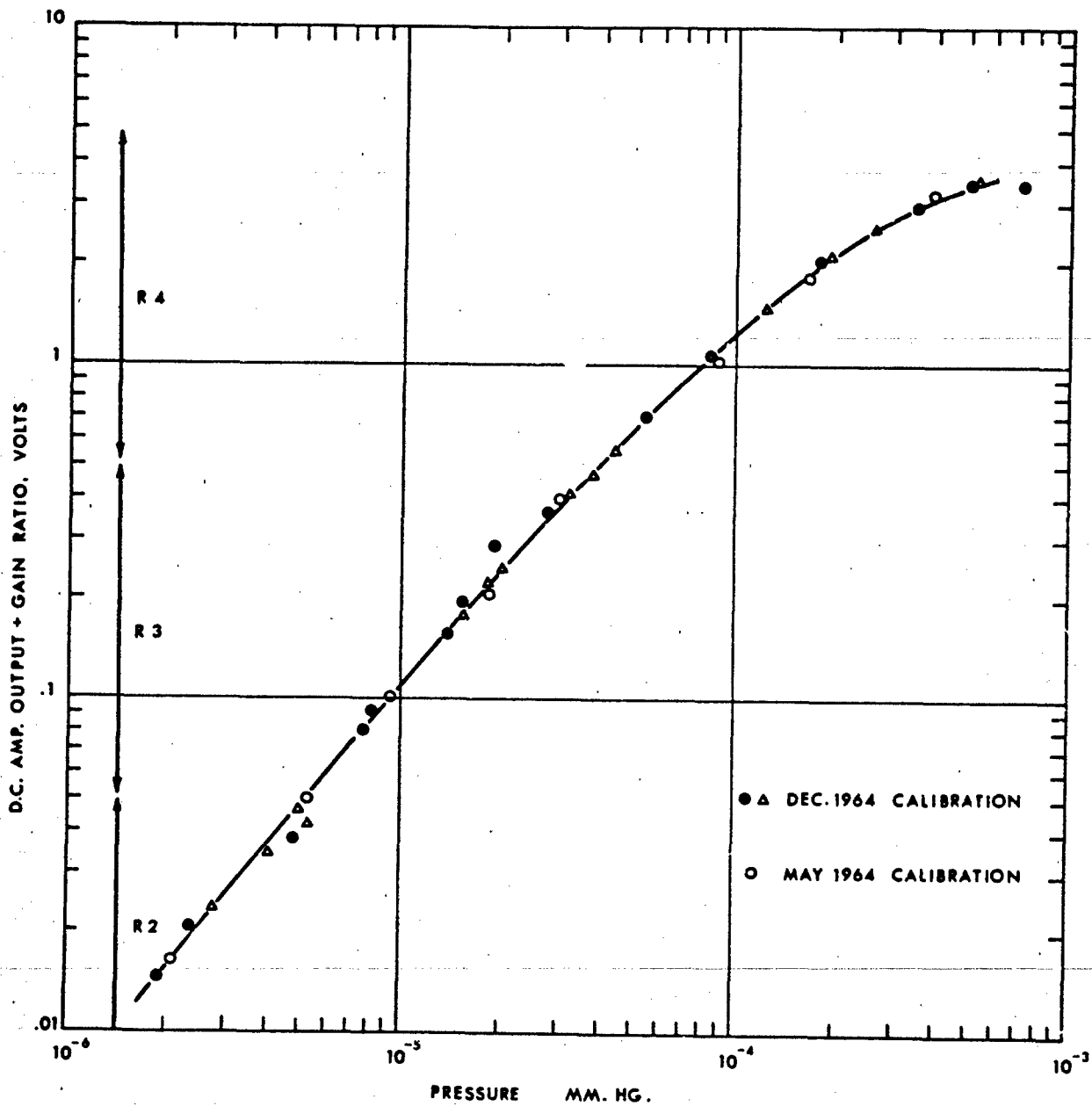


FIG. 45 CALIBRATION OF IONIZATION GAUGE 5 INDICATING REPEATABILITY OF THE CALIBRATION.



FIG. 46a LOCATION AND SIZE OF THE CHURCHILL RESEARCH RANGE

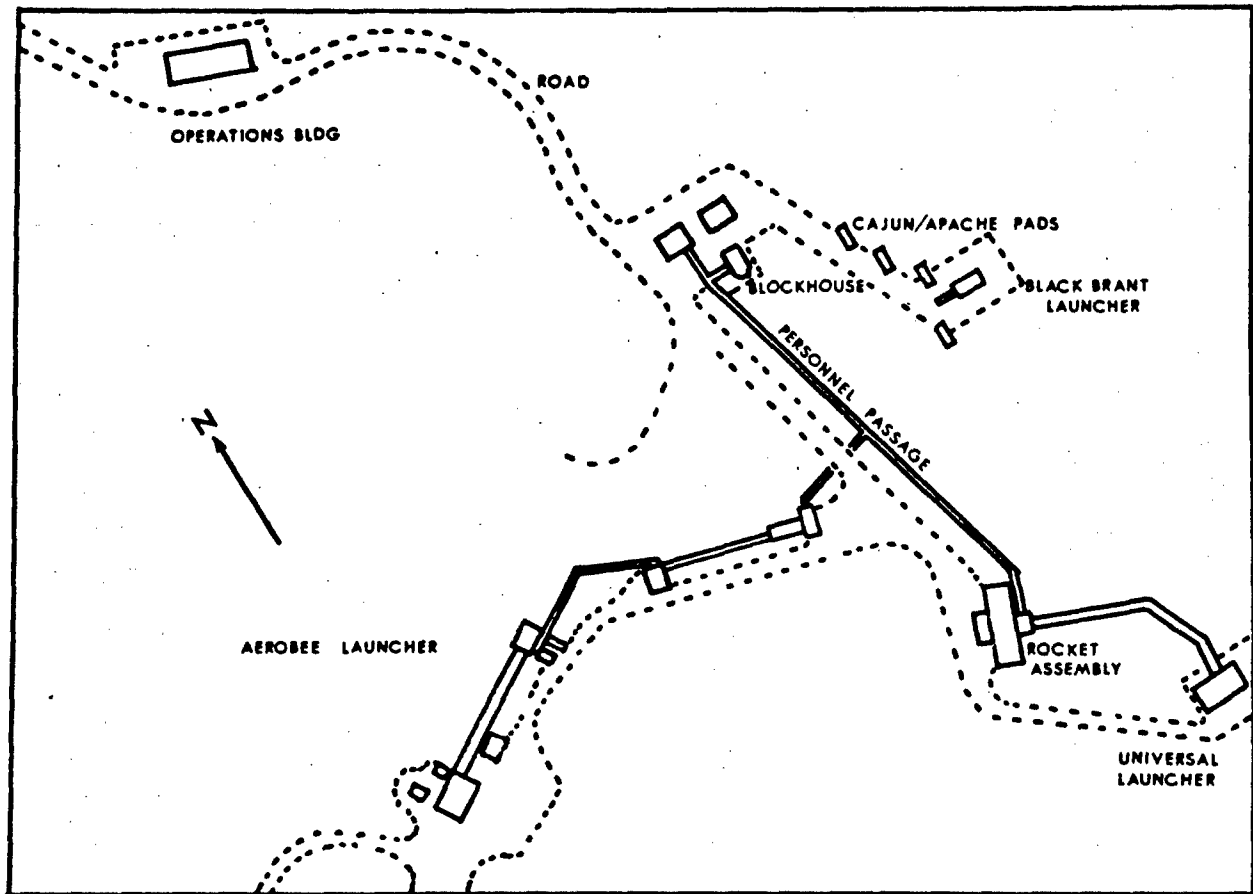


FIG. 46b FACILITIES AVAILABLE AT THE LAUNCH SITE

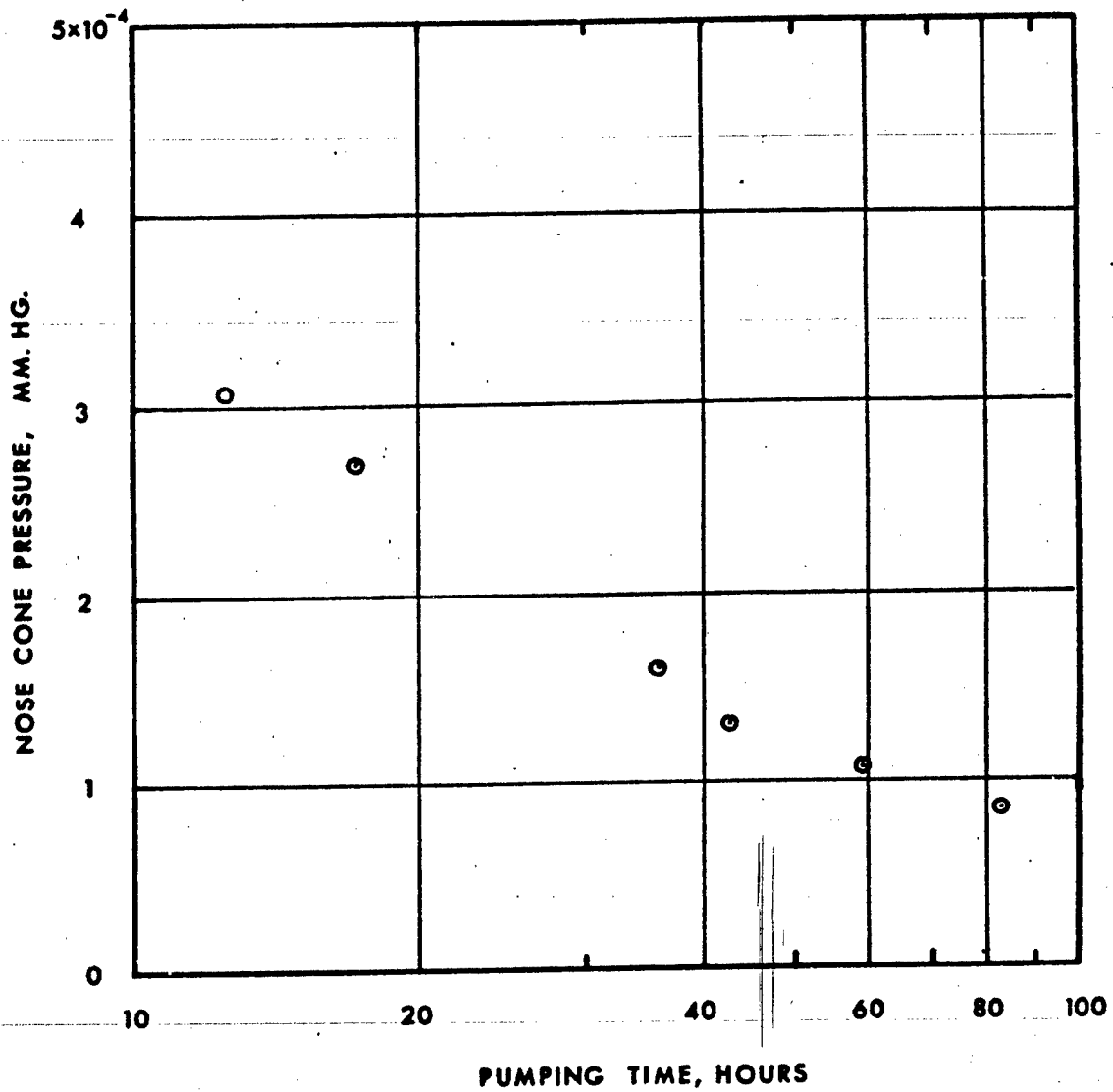


FIG. 47 PRESSURE HISTORY OF THE NOSE CONE DURING THE PRE-FLIGHT PREPARATION

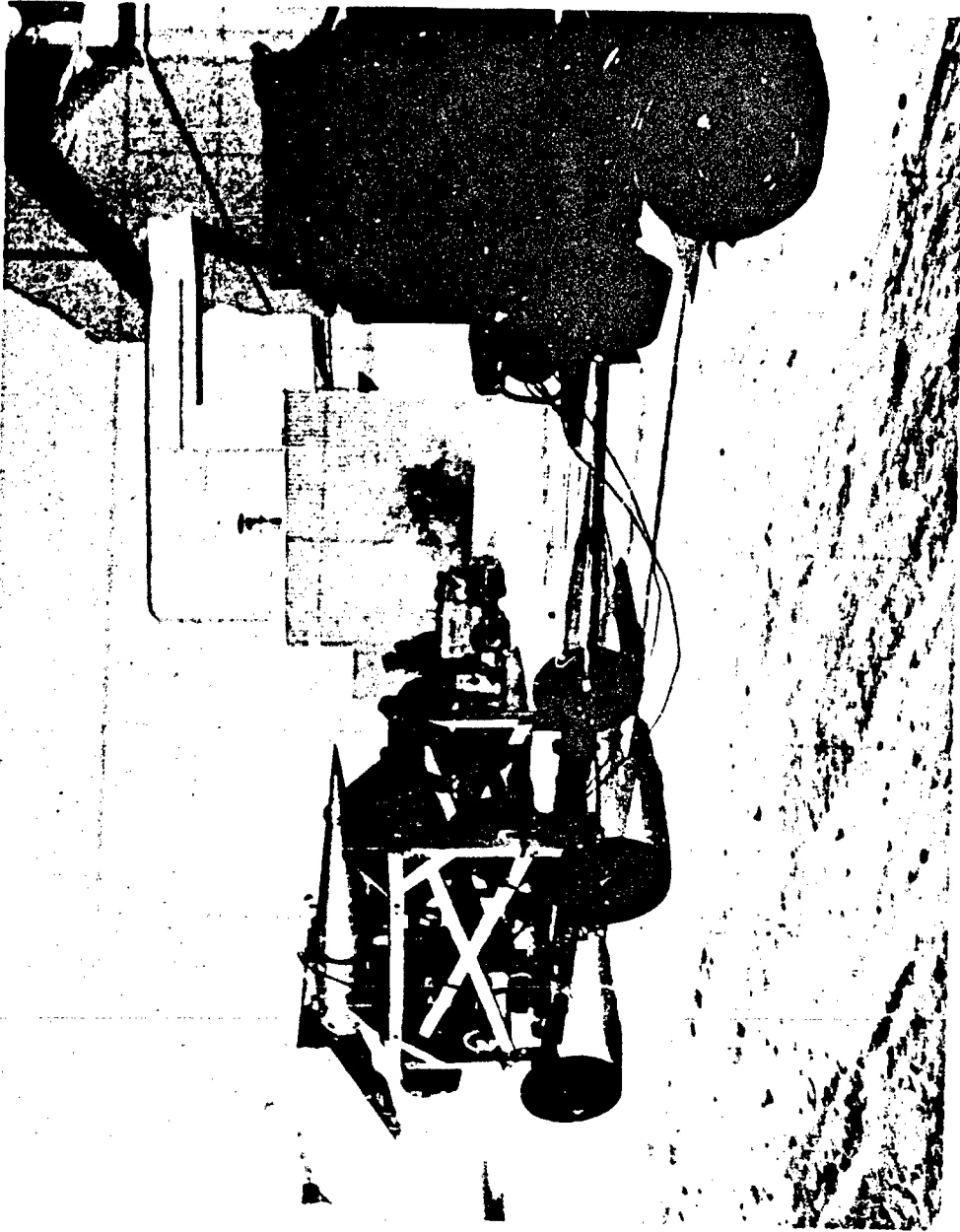


FIG. 46 TRANSPORTING THE NOSE CONE AND PUMPING SYSTEM TO THE LAUNCHER

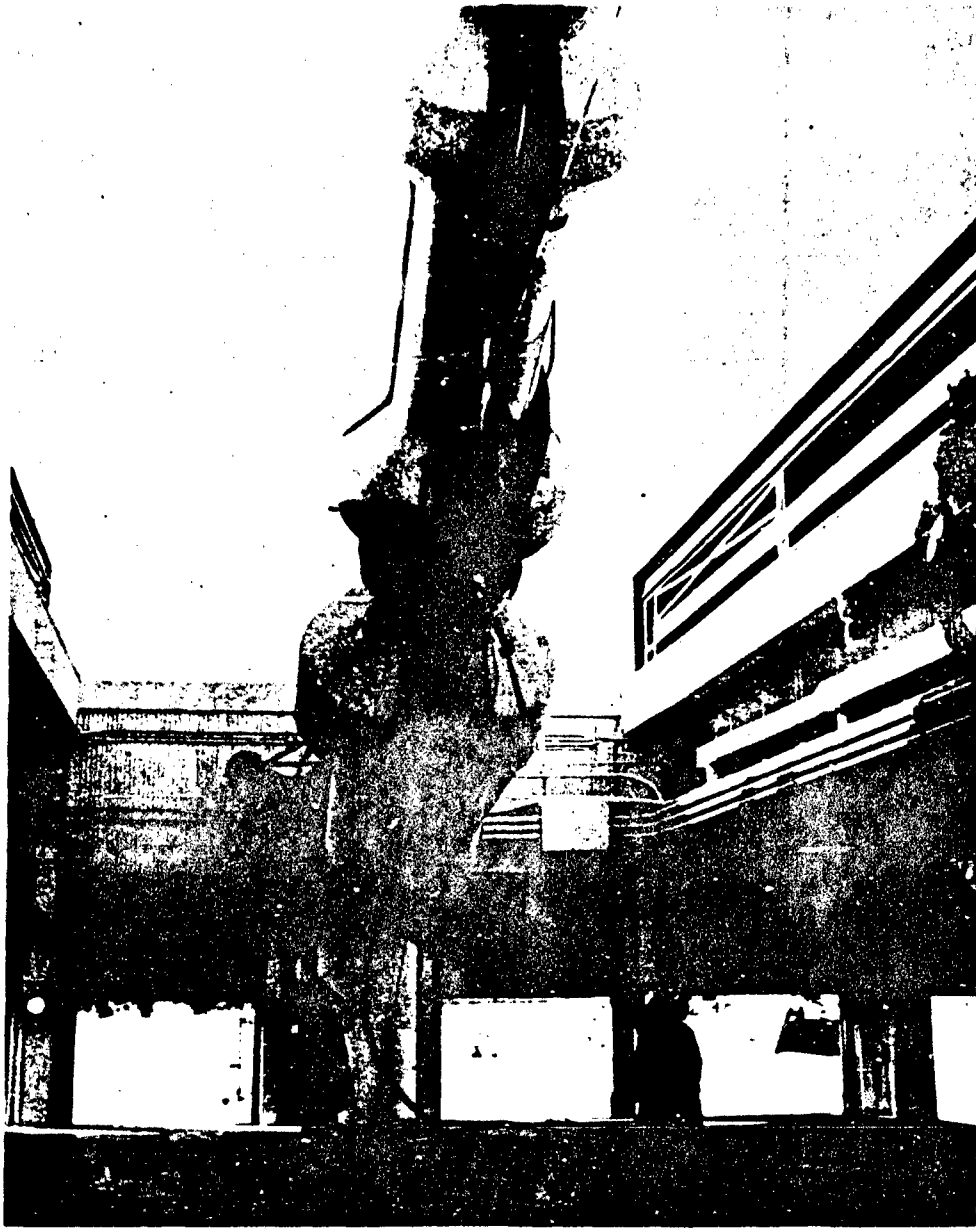


FIG. 49 LAUNCHER IN AN ELEVATED POSITION WITH THE HEAT SHIELD CLOSED AROUND THE ROCKET

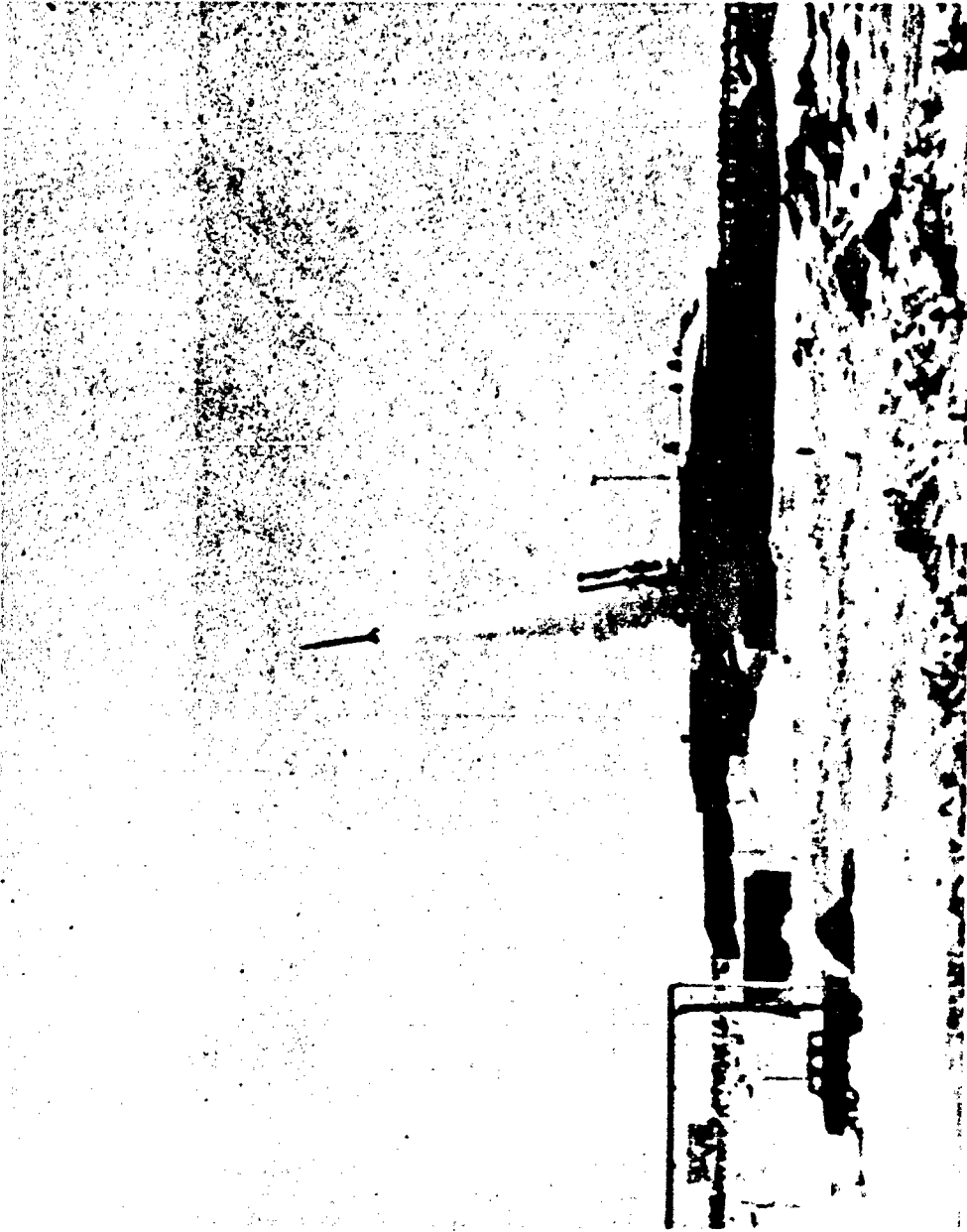


FIG. 50 LIFT-OFF OF THE UNIVERSITY OF TORONTO ROCKET

TIME

COMMUTATOR

LONG. ACCELEROMETER

LONG. MAGNETOMETER  
+ 65° SUN SENSOR

LATERAL MAGNETOMETER  
+ 45° SUN SENSOR

TIME

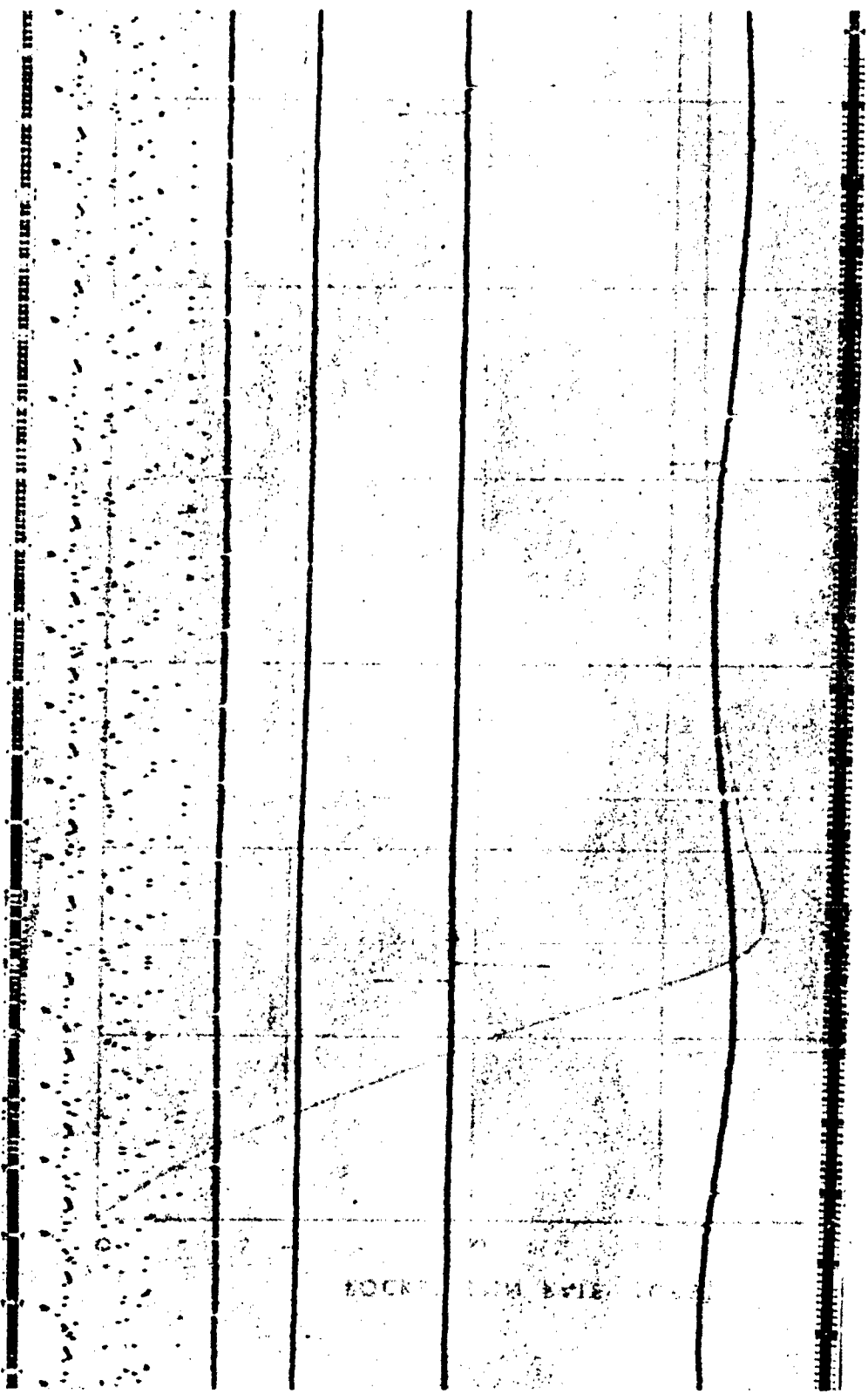


FIG. 51 | TELEMETRY RECORD OF THE SUN SENSOR AND MAGNETOMETER SIGNALS

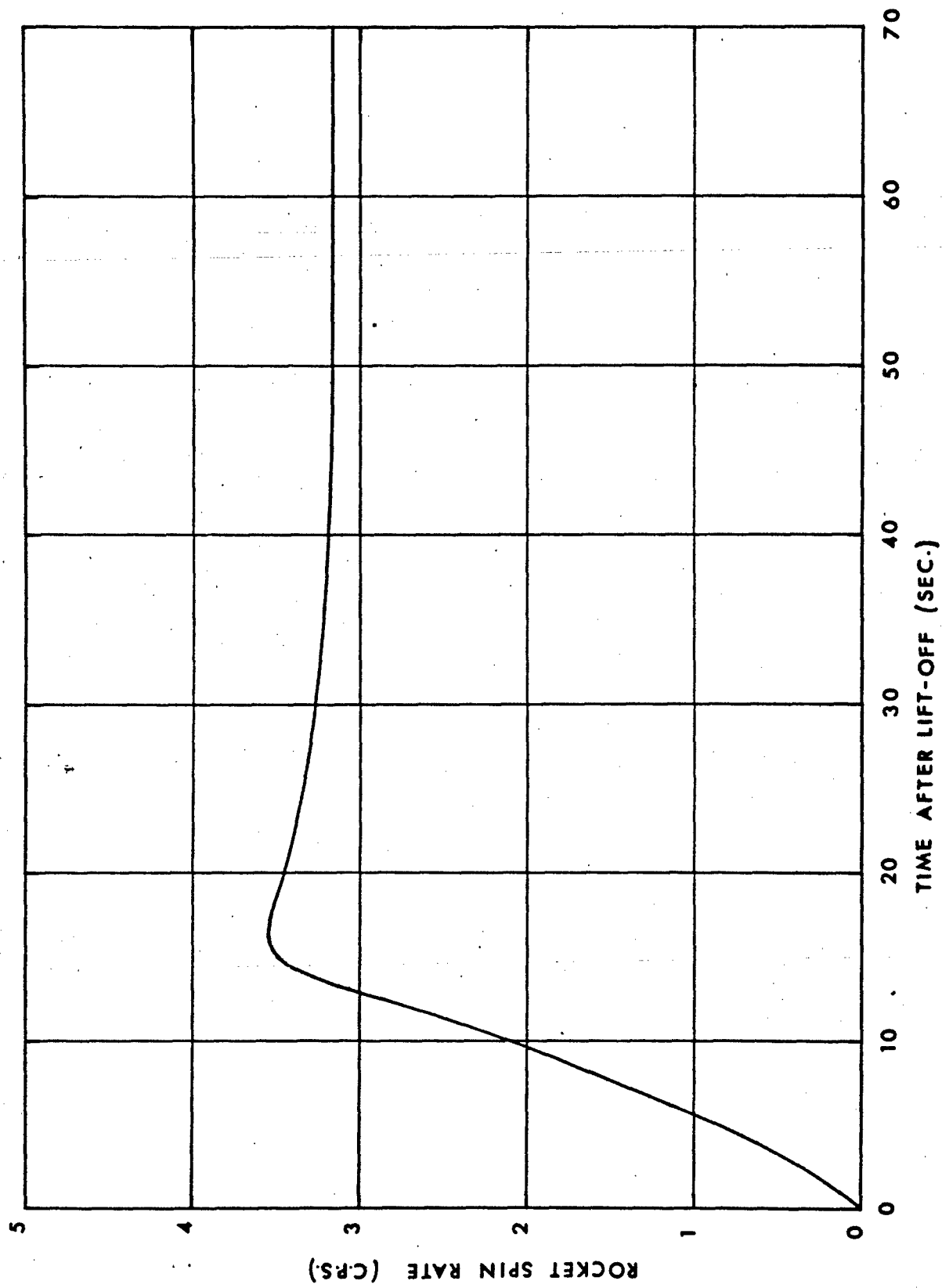


FIG. 52 VARIATION OF ROCKET SPIN RATE

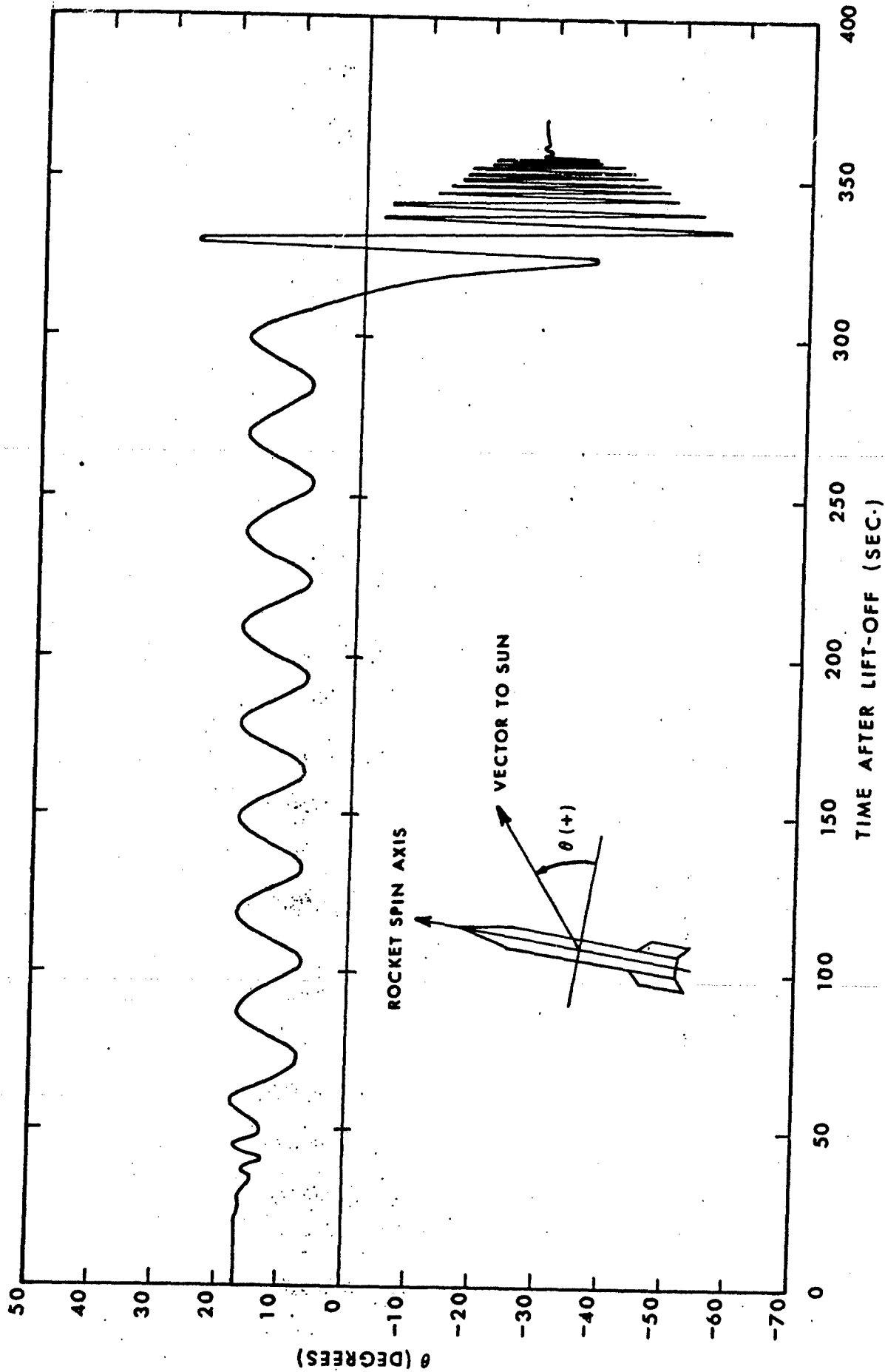


FIG. 53 VARIATION OF THE ANGLE BETWEEN THE ROCKET AXIS AND THE SUN'S DIRECTION.

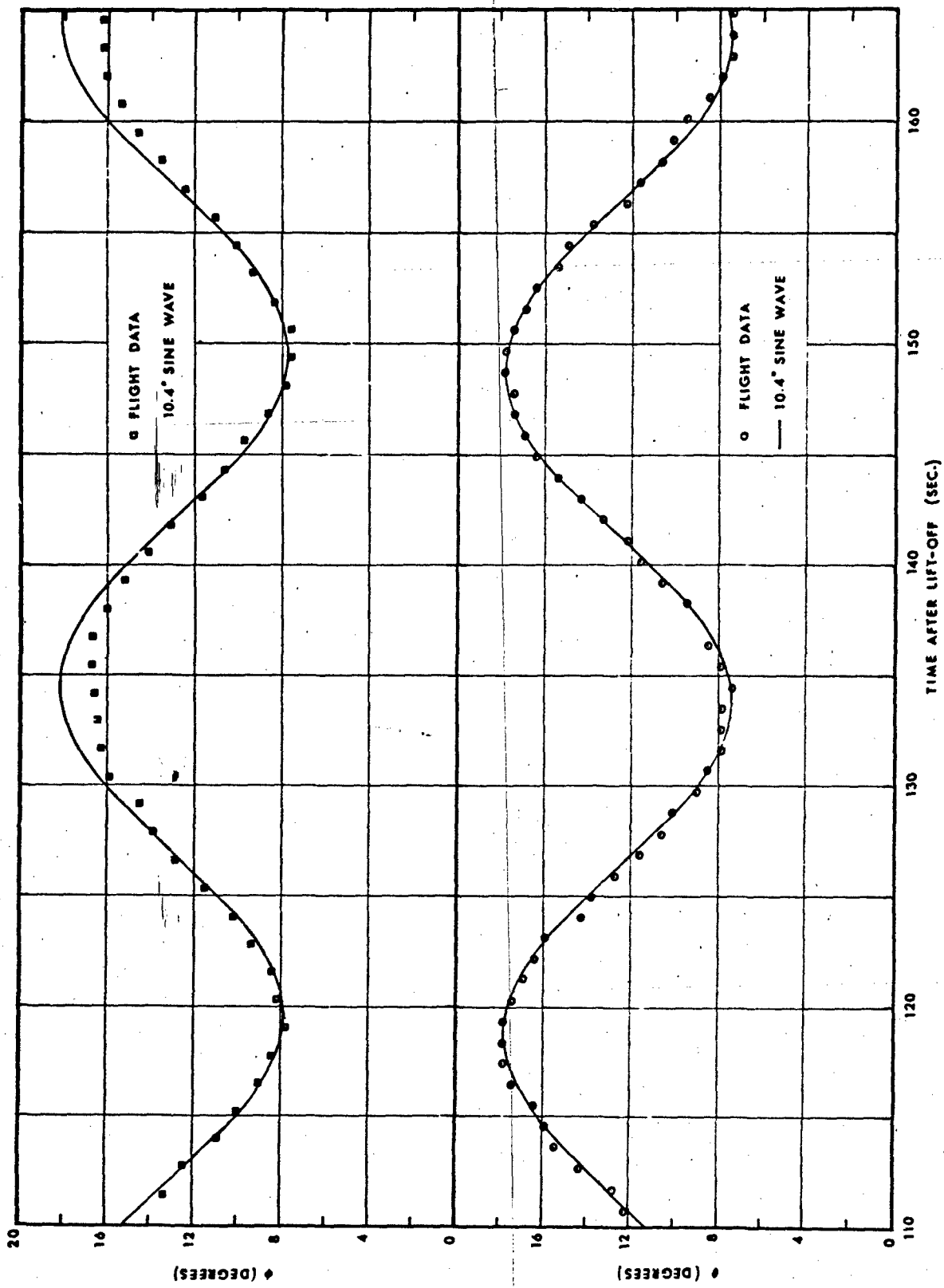


FIG. 54 VARIATION OF  $\theta$  AFTER THE ROCKET SPIN RATE HAD STABILIZED

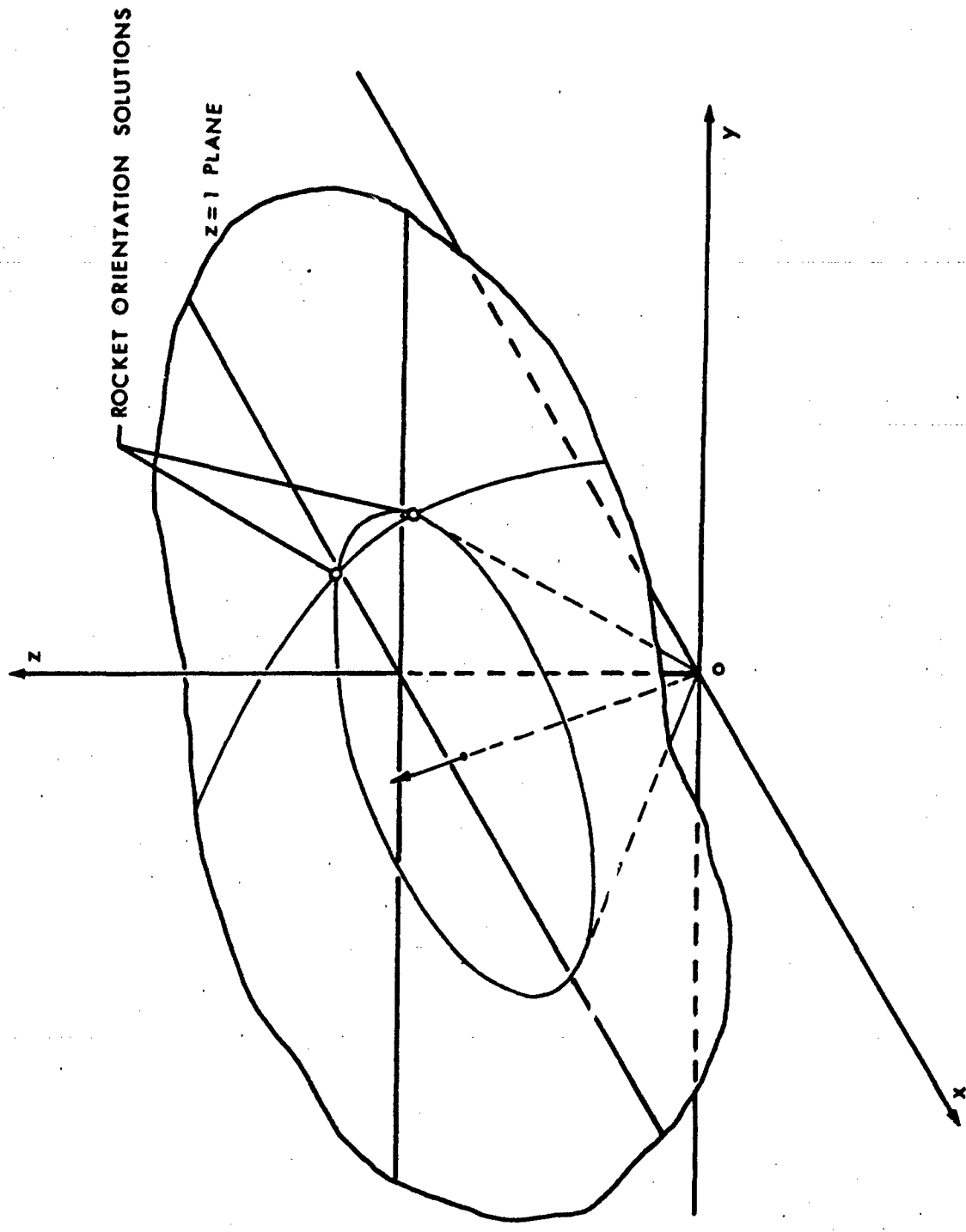


FIG. 55 PICTORIAL VIEW OF THE INTERSECTION OF THE TWO CONES DEFINED BY  $\theta$  AND  $\phi$

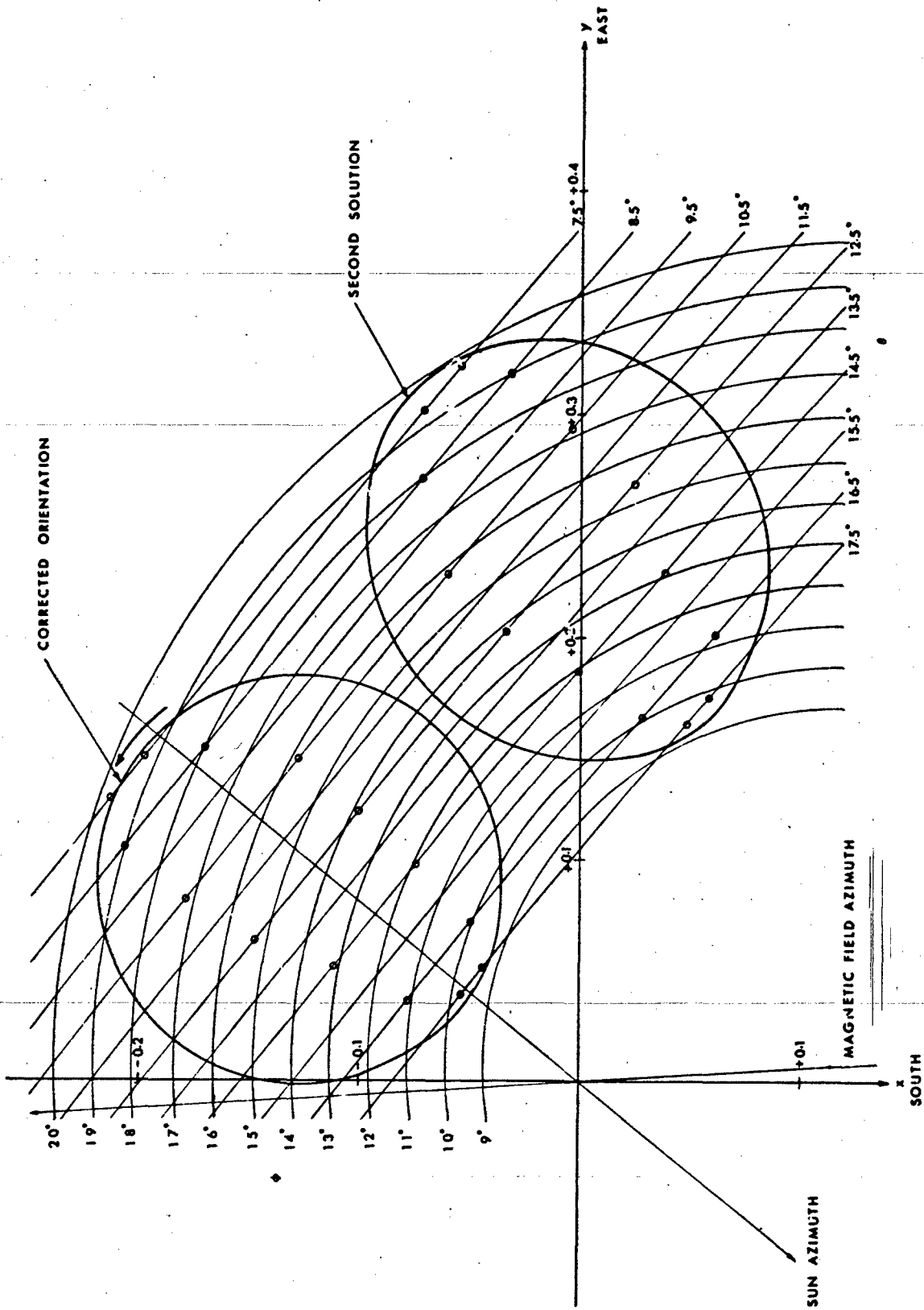


FIG. 56 GRAPHICAL SOLUTION FOR THE ORIENTATION OF THE ROCKET AXIS

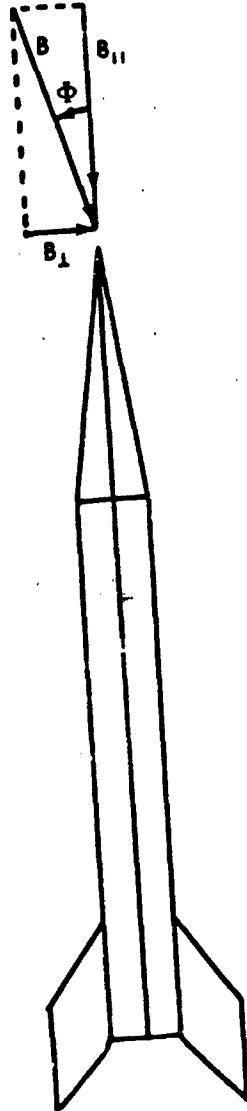
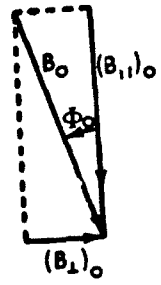


FIG. 57 DISTORTION OF THE MAGNETIC FIELD BY THE ROCKET

VIEW LOOKING AFT

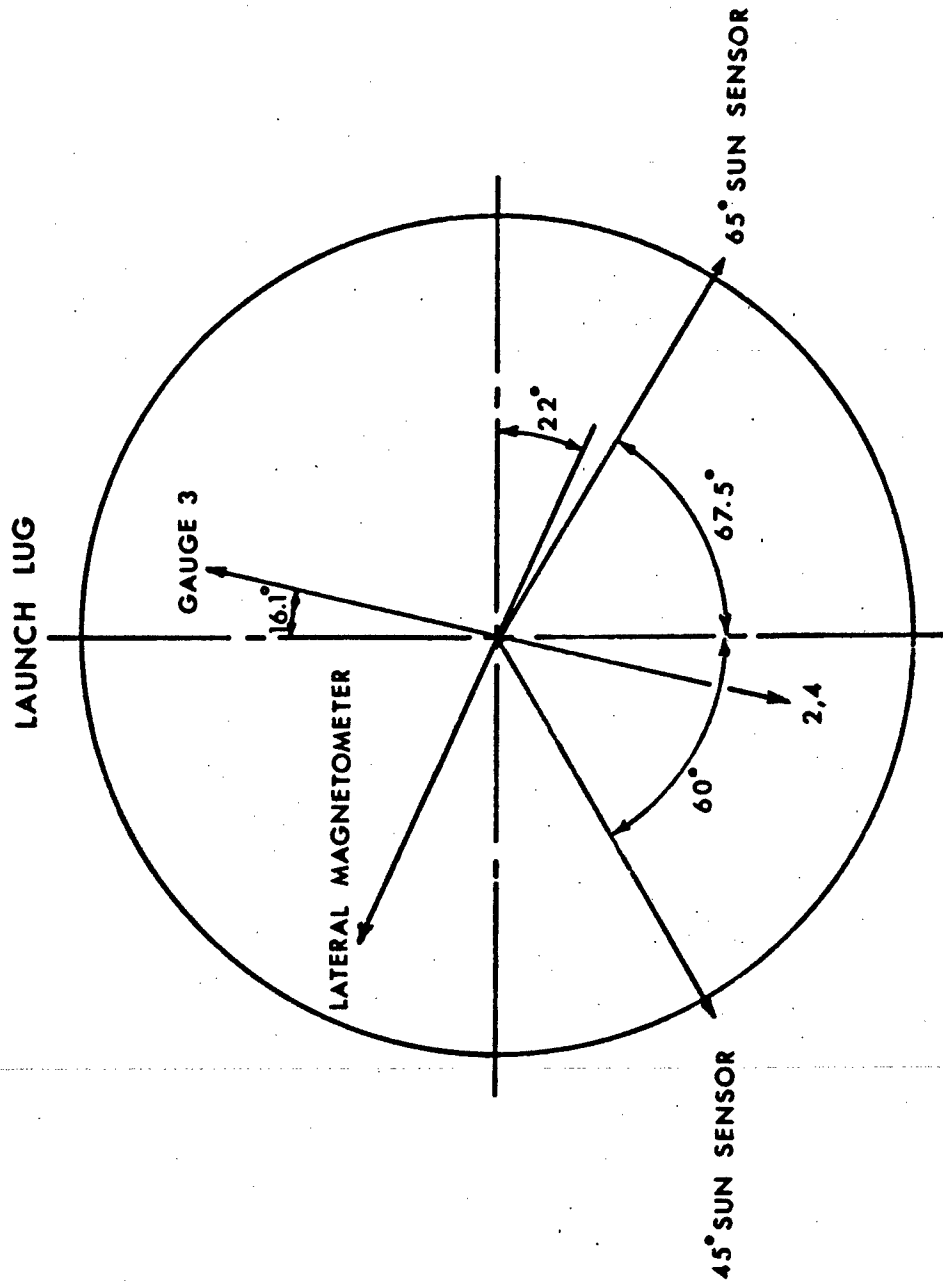


FIG. 58 ANGULAR ORIENTATION OF THE SUN SENSORS AND MAGNETOMETERS IN THE NOSE CONE

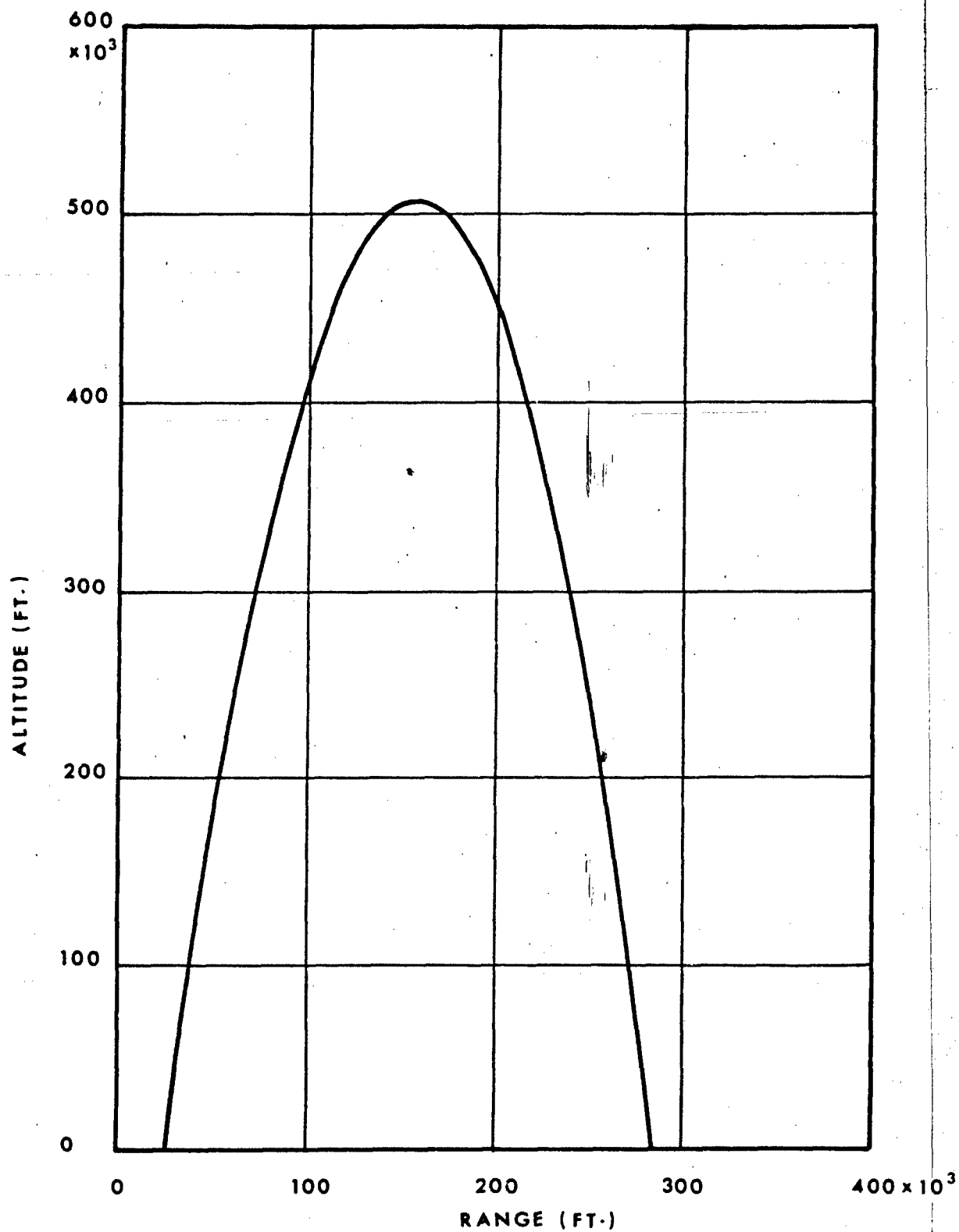


FIG. 59 HEIGHT VS RANGE PLOT OF THE ROCKET TRAJECTORY

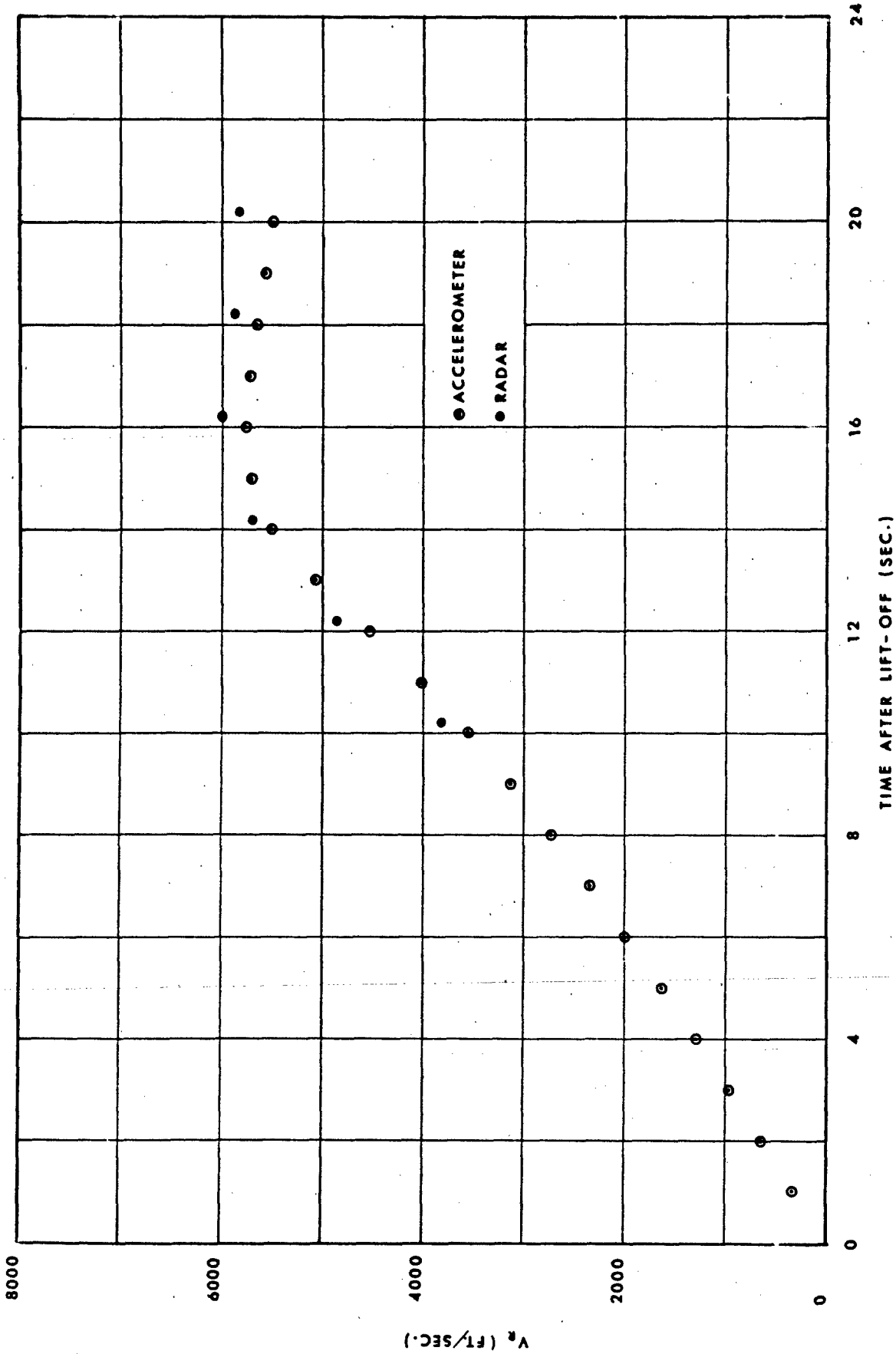


FIG. 60 COMPARISON OF ROCKET VELOCITY AS DETERMINED BY RADAR AND FROM ACCELEROMETER RECORDS

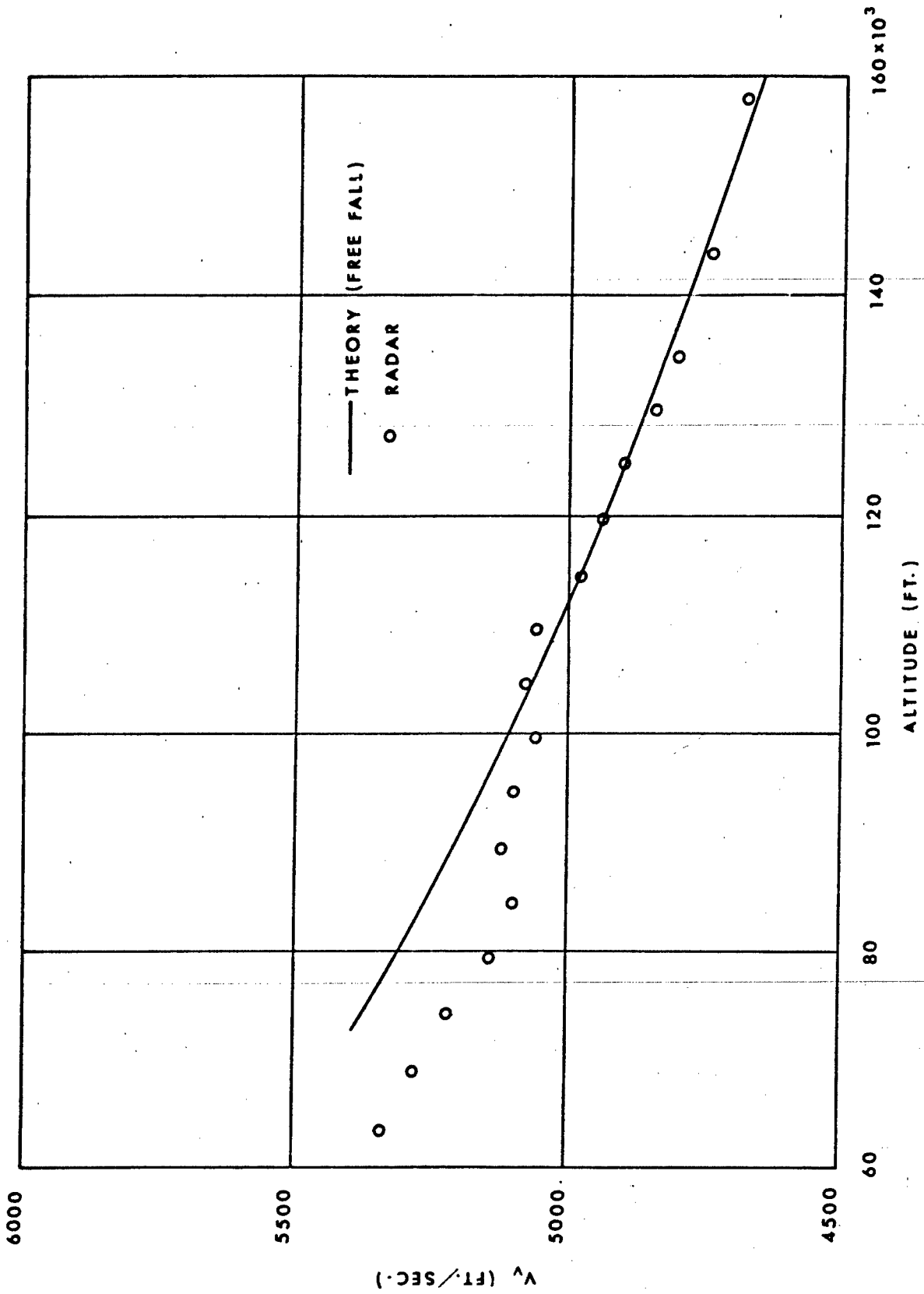


FIG. 61 COMPARISON OF THE VERTICAL COMPONENT OF ROCKET VELOCITY DETERMINED BY RADAR AND COMPUTED ASSUMING FREE FALL AND NO AIR DRAG

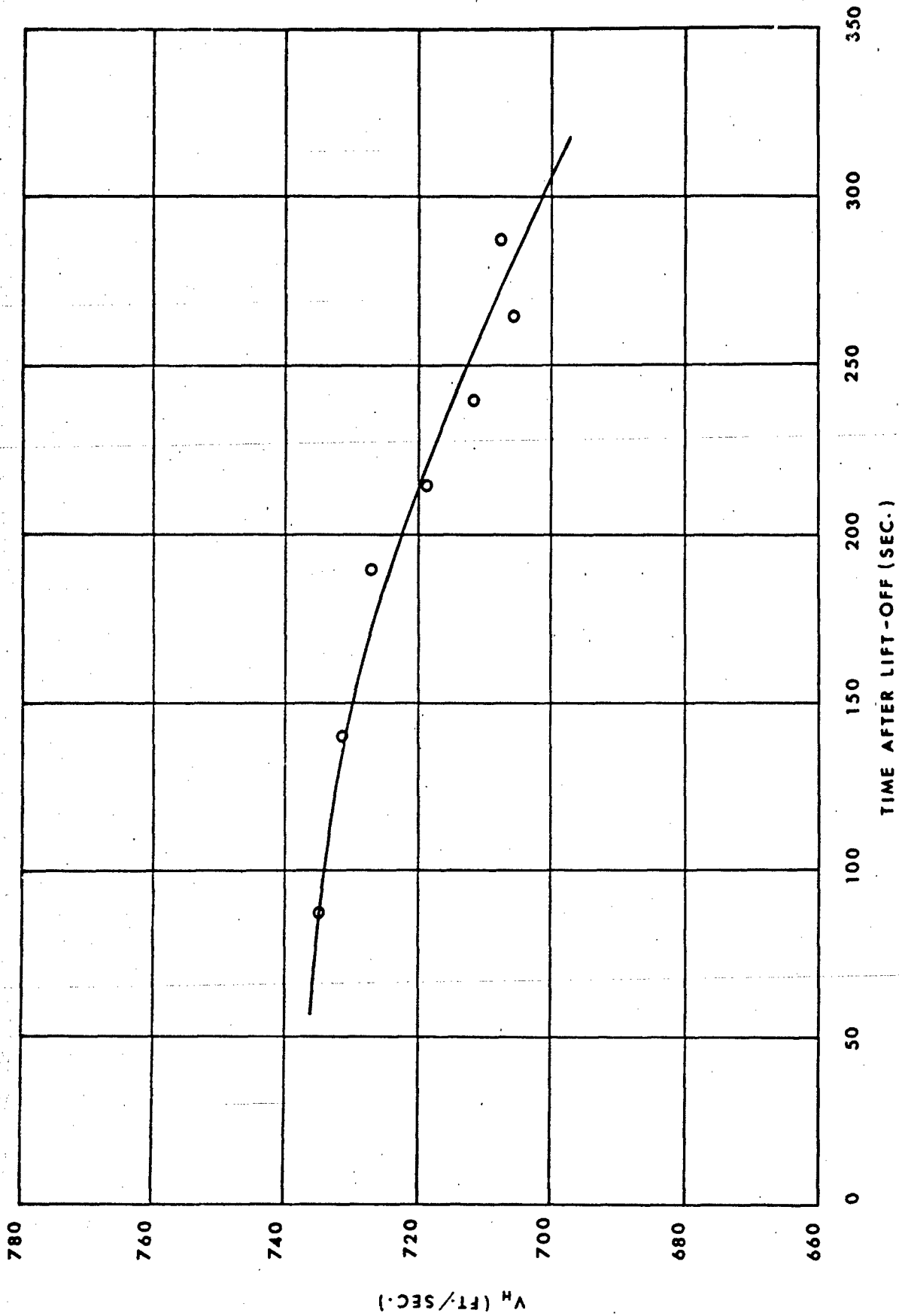


FIG. 62 HORIZONTAL COMPONENT OF THE ROCKET VELOCITY DETERMINED BY RADAR

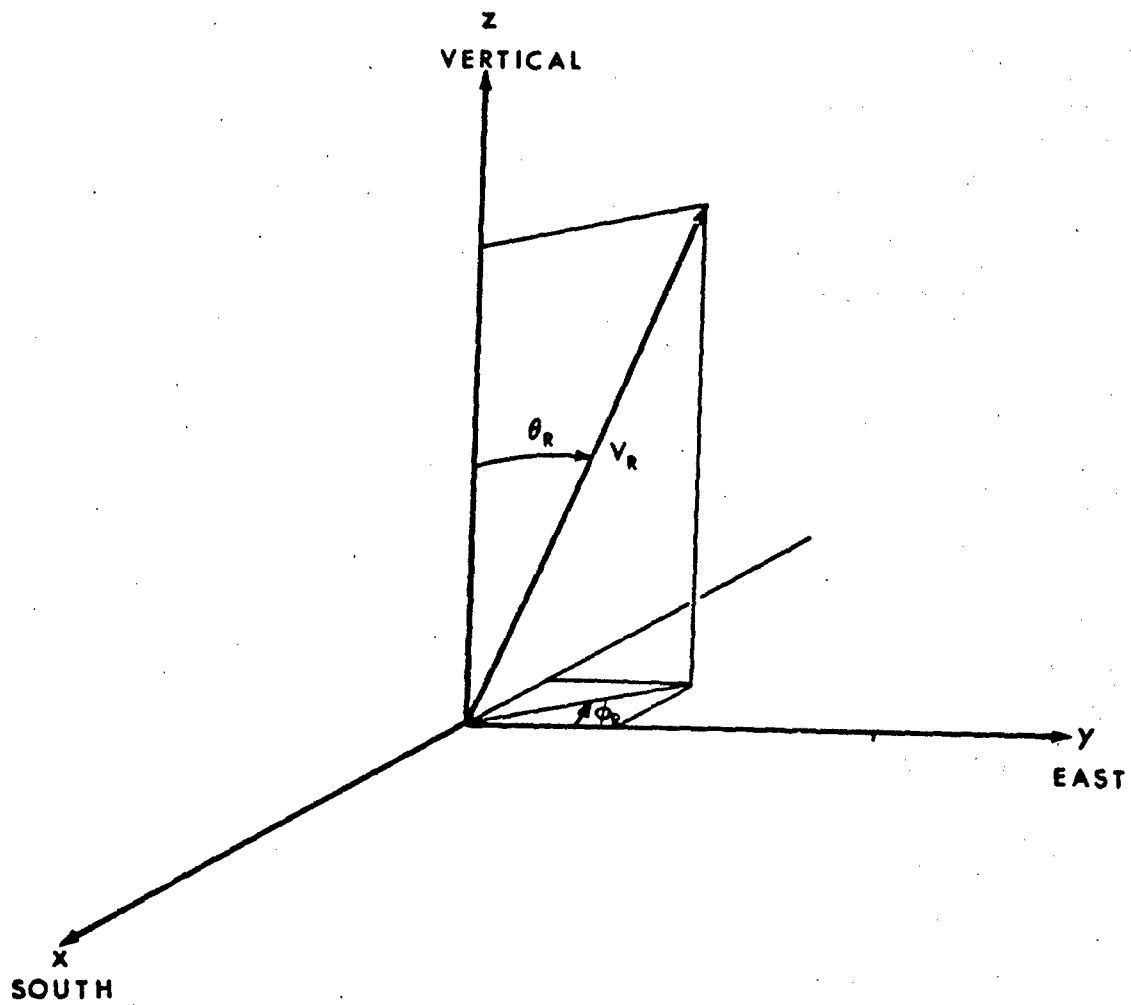


FIG. 63 COORDINATE SYSTEM USED FOR THE DATA REDUCTION

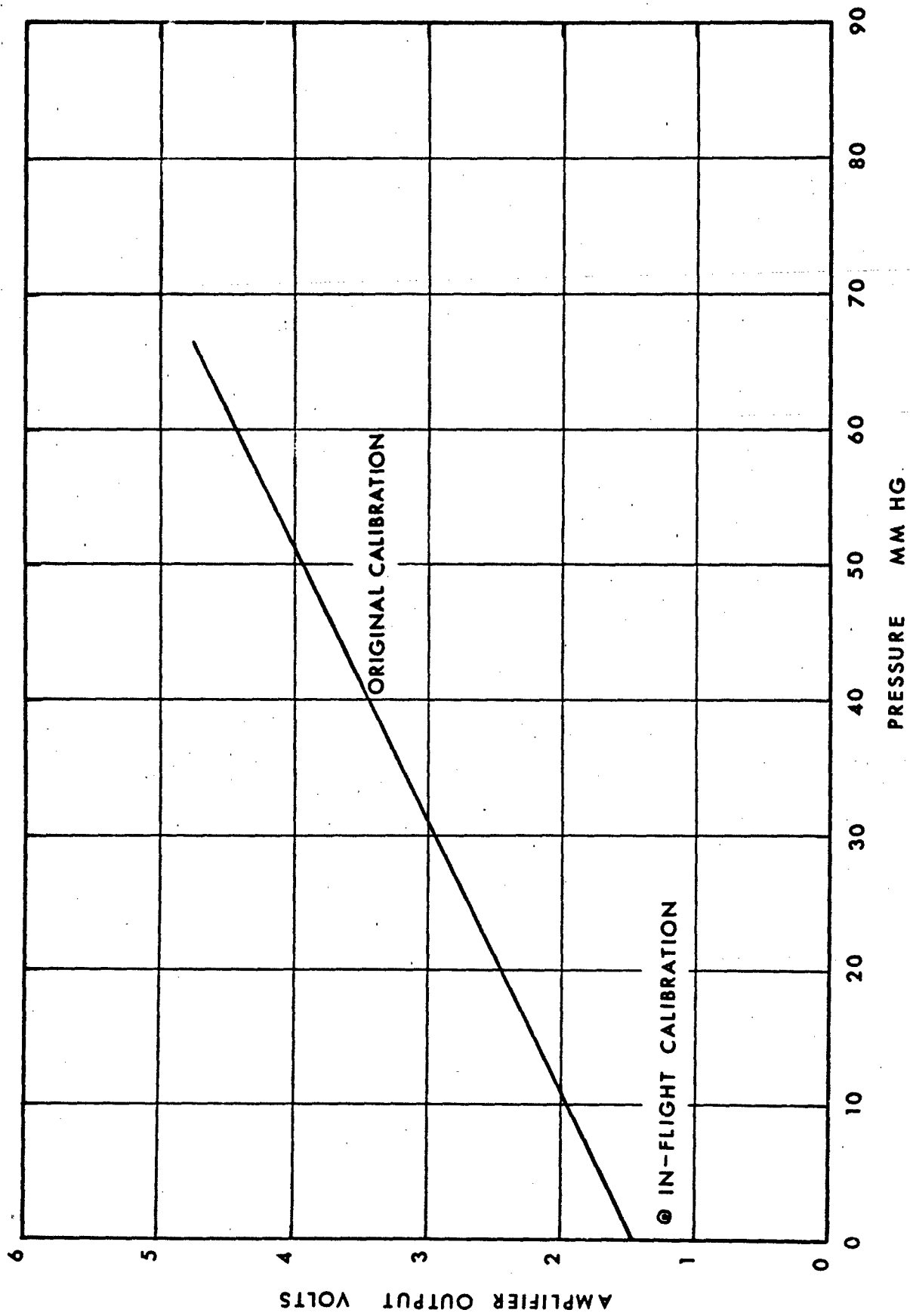


FIG. 64a CHANGE IN THE CALIBRATION FOR THE STRAIN GAUGE SURFACE PRESSURE TRANSDUCER (H.P. 2) IN RANGE 2

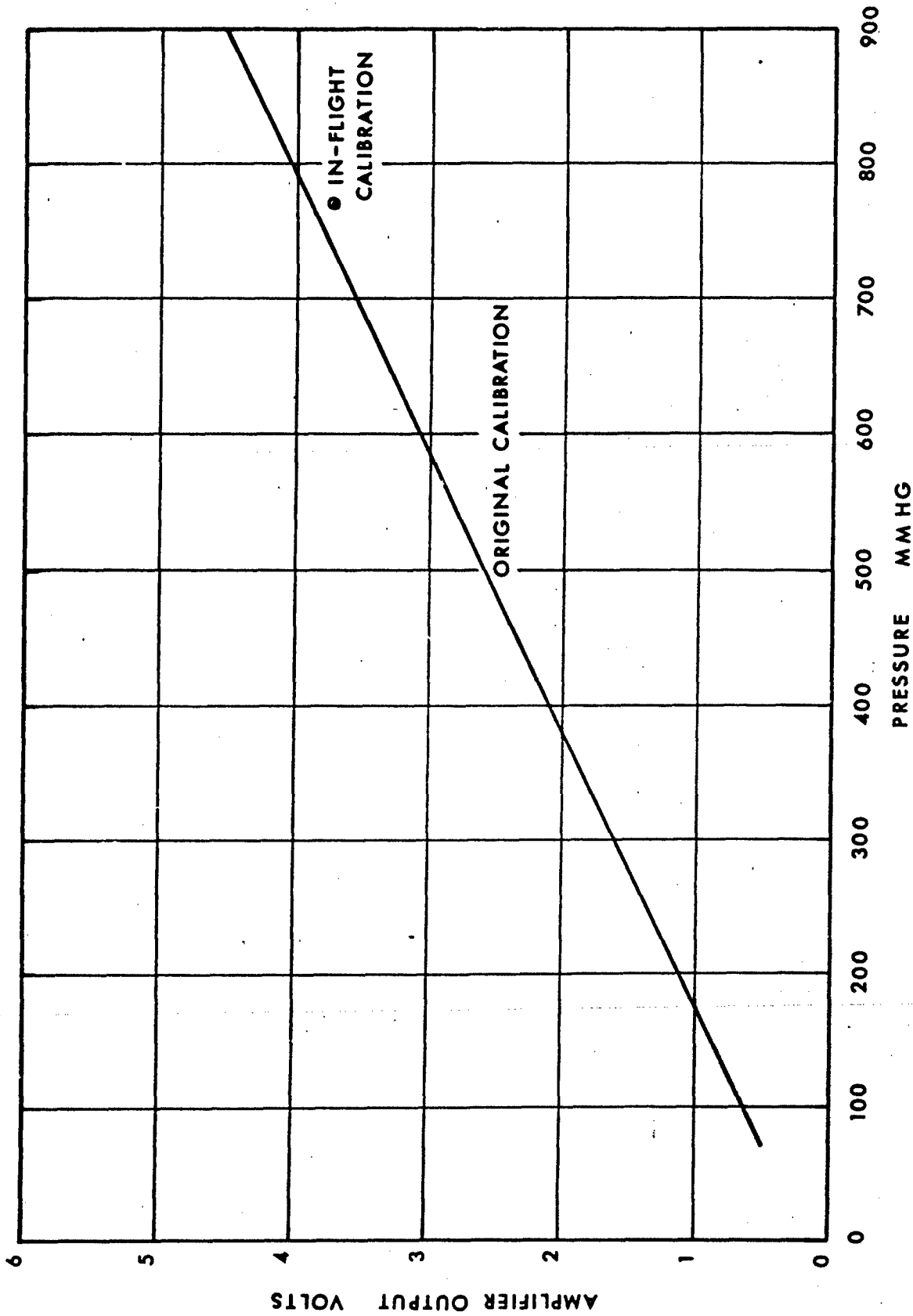


FIG. 64b CHANGE IN THE CALIBRATION FOR THE STRAIN GAUGE SURFACE PRESSURE TRANSDUCER (H.P.2) IN RANGE 4

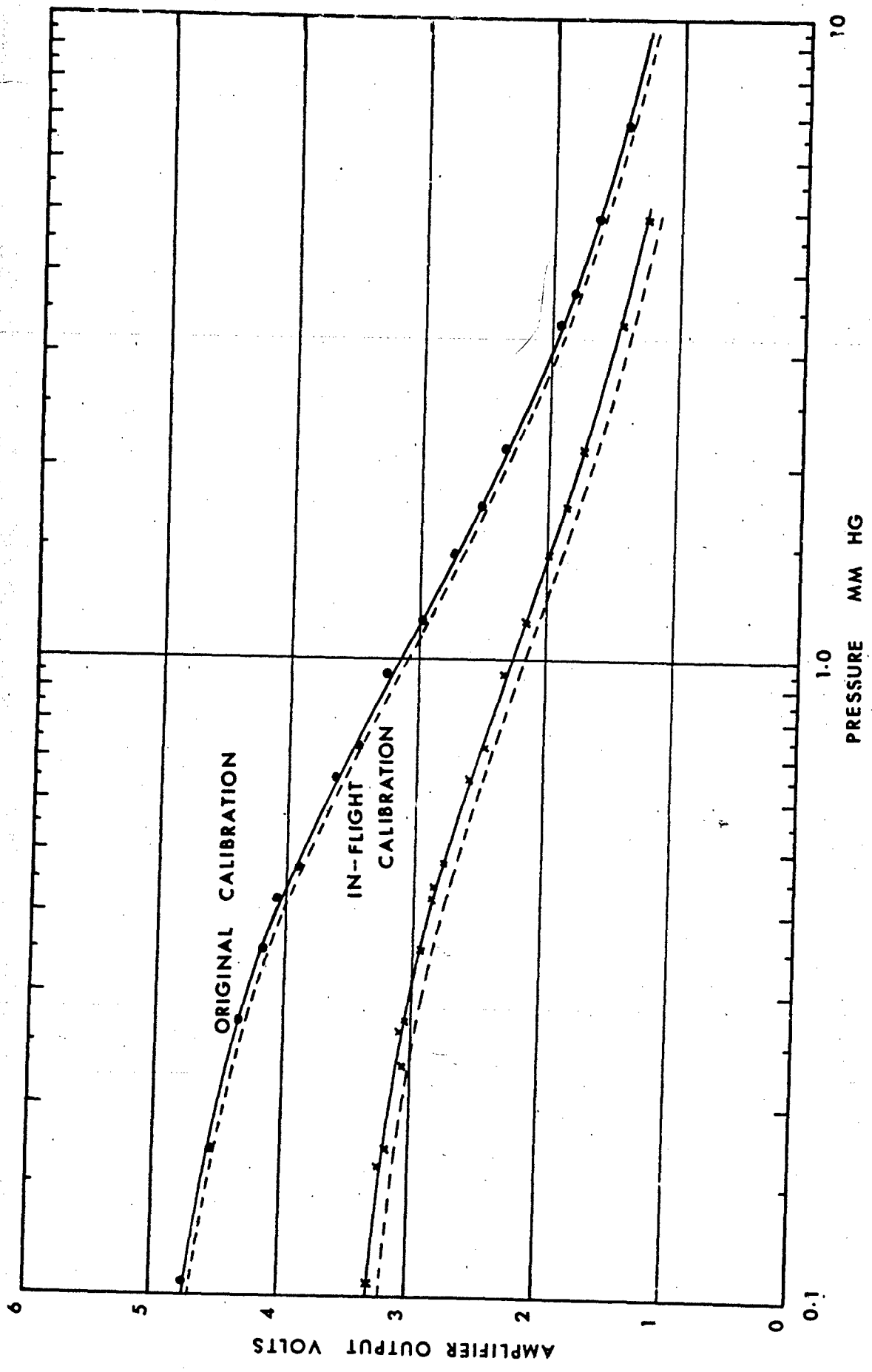


FIG. 65 CHANGE IN THE CALIBRATION FOR THE THERMOCOUPLE TYPE PRESSURE TRANSDUCERS

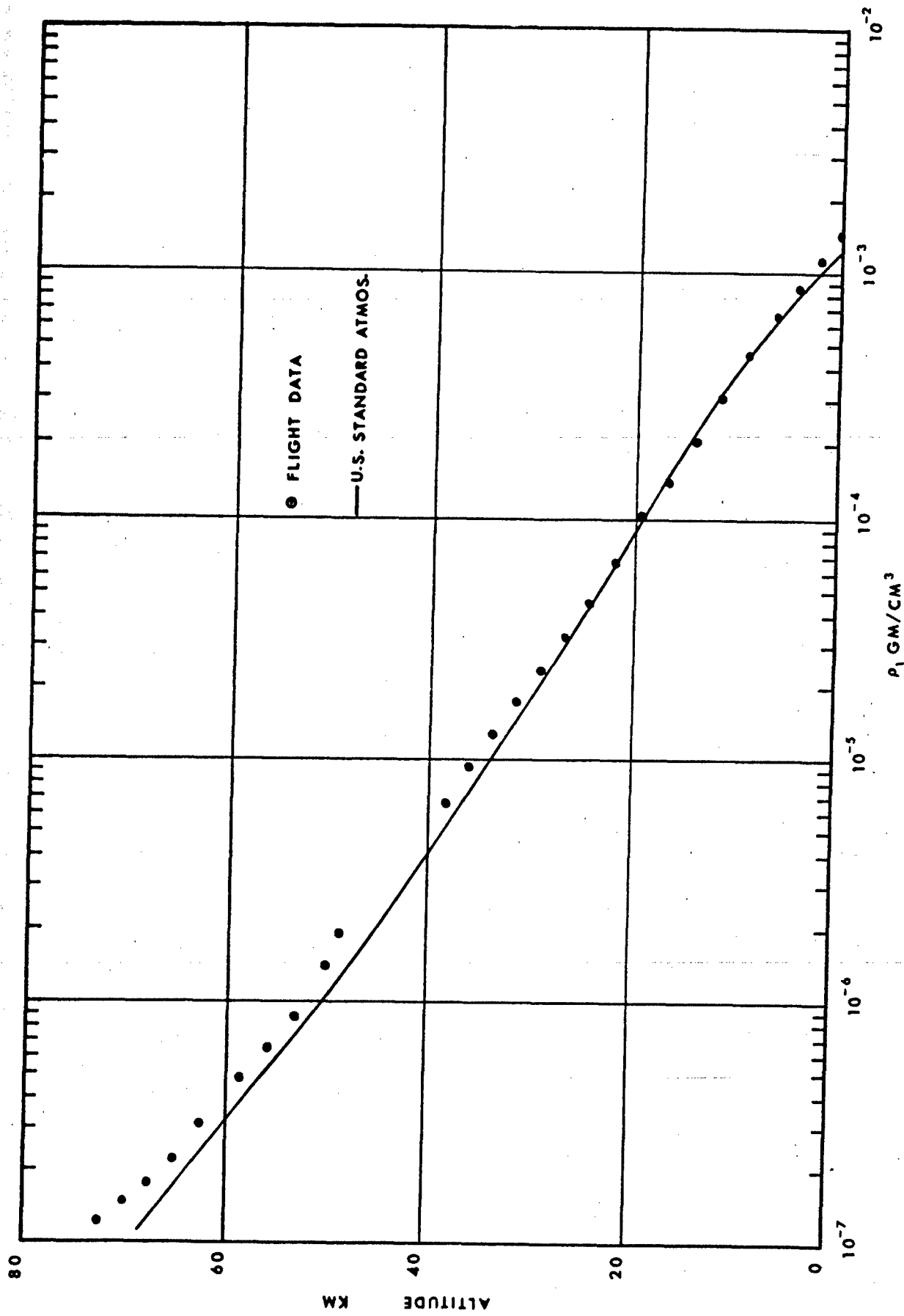


FIG. 66 ATMOSPHERIC DENSITY COMPUTED FROM IMPACT PRESSURE DATA

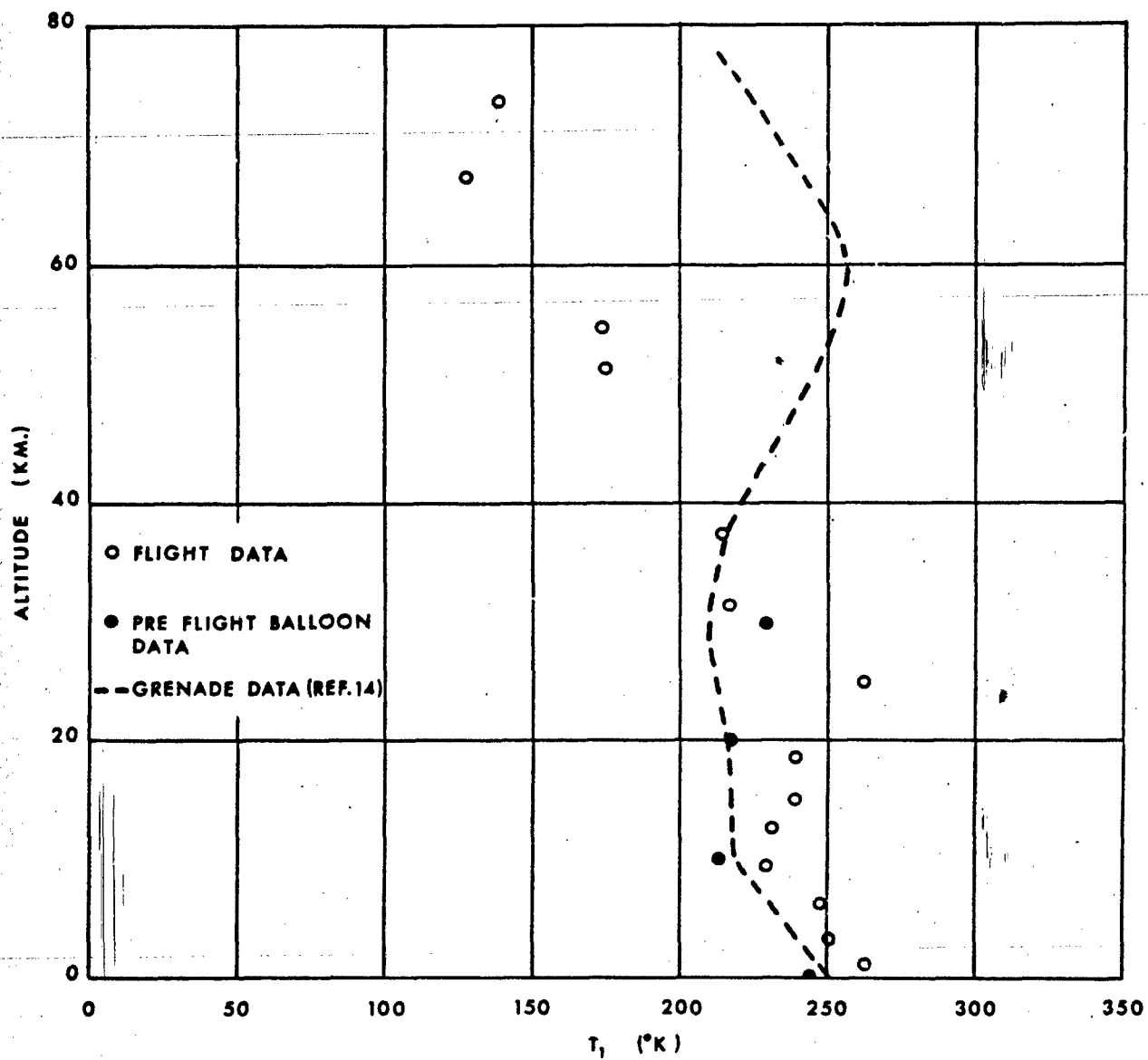


FIG. 67 ATMOSPHERIC TEMPERATURE PROFILE COMPUTED FROM IMPACT AND SURFACE PRESSURE DATA

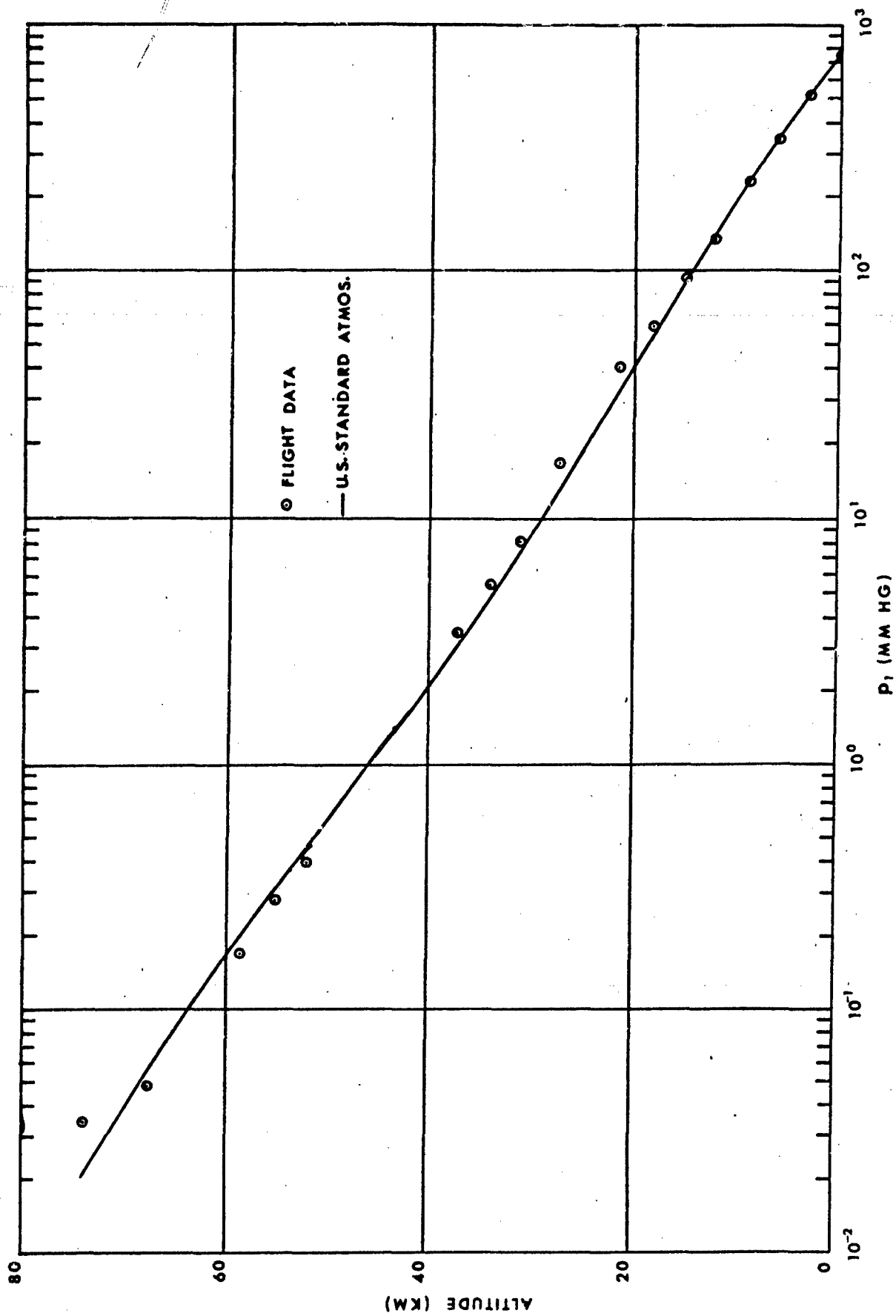


FIG. 68 ATMOSPHERIC PRESSURE PROFILE COMPUTED FROM THE DATA IN FIGS. 66 AND 67.

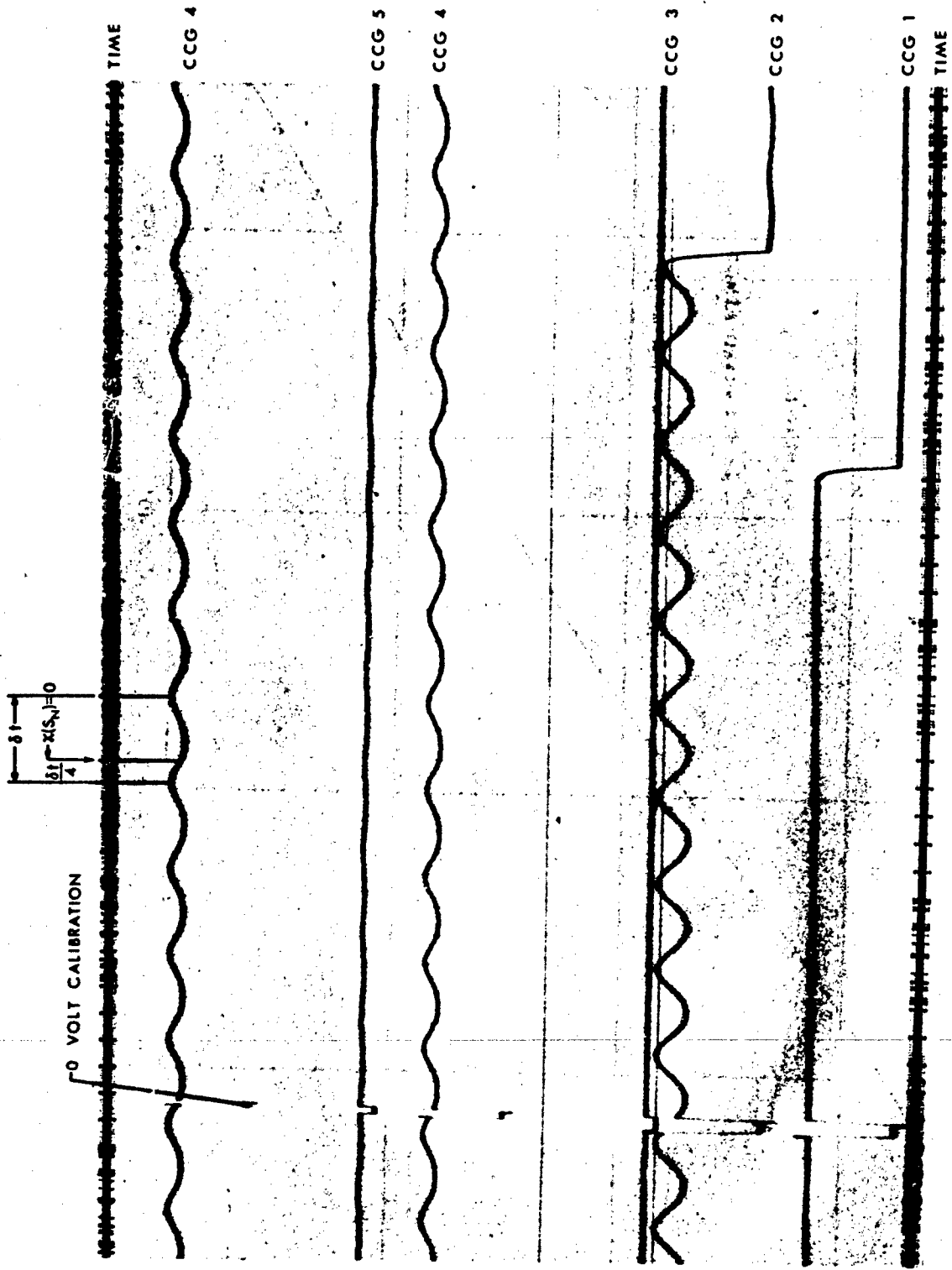


FIG. 69 TELEMETRY RECORD OF THE MODULATED SIGNALS FROM THE DC AMPLIFIERS ON THE IONIZATION GAUGES

VERTICAL

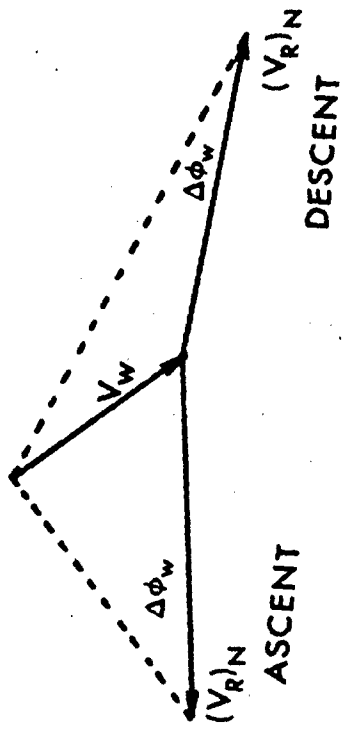
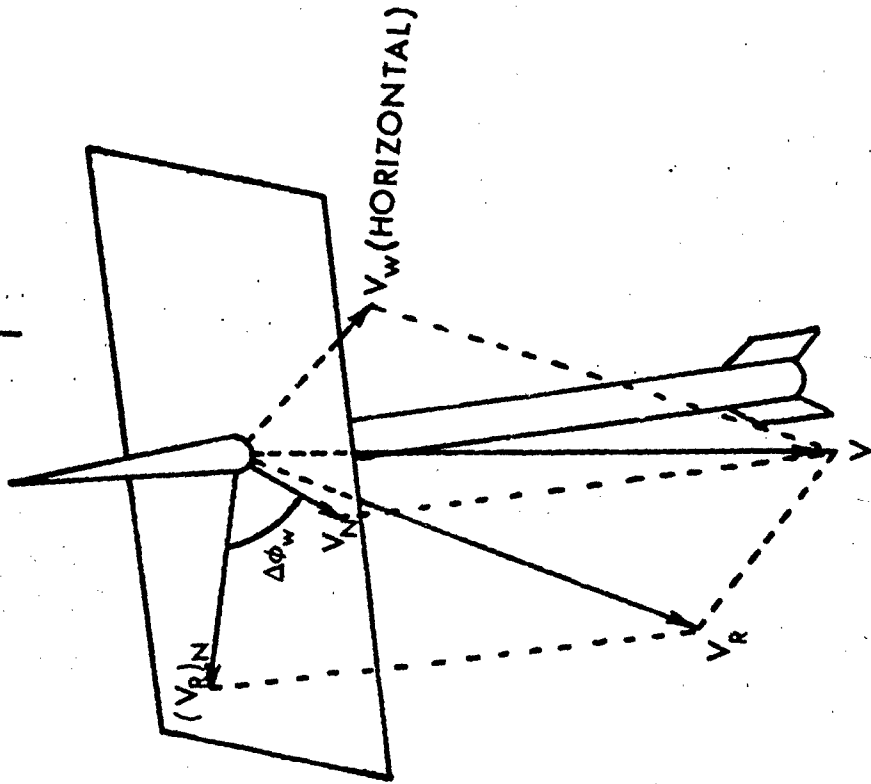


FIG. 70 GRAPHICAL METHOD OF SOLUTION FOR THE WIND VELOCITY

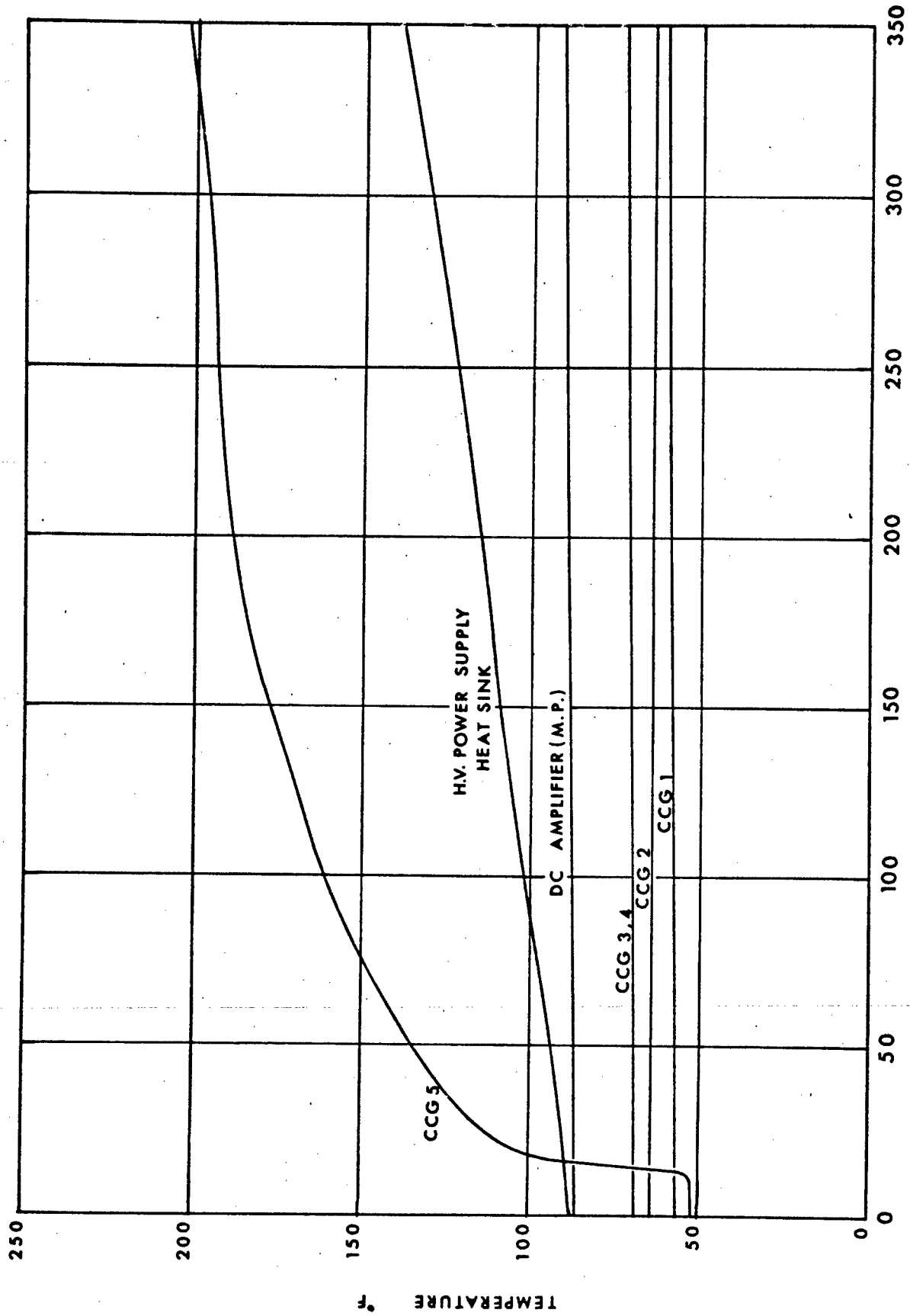


FIG. 71 IONIZATION GAUGE VOLUME, AND ELECTRONICS TEMPERATURES

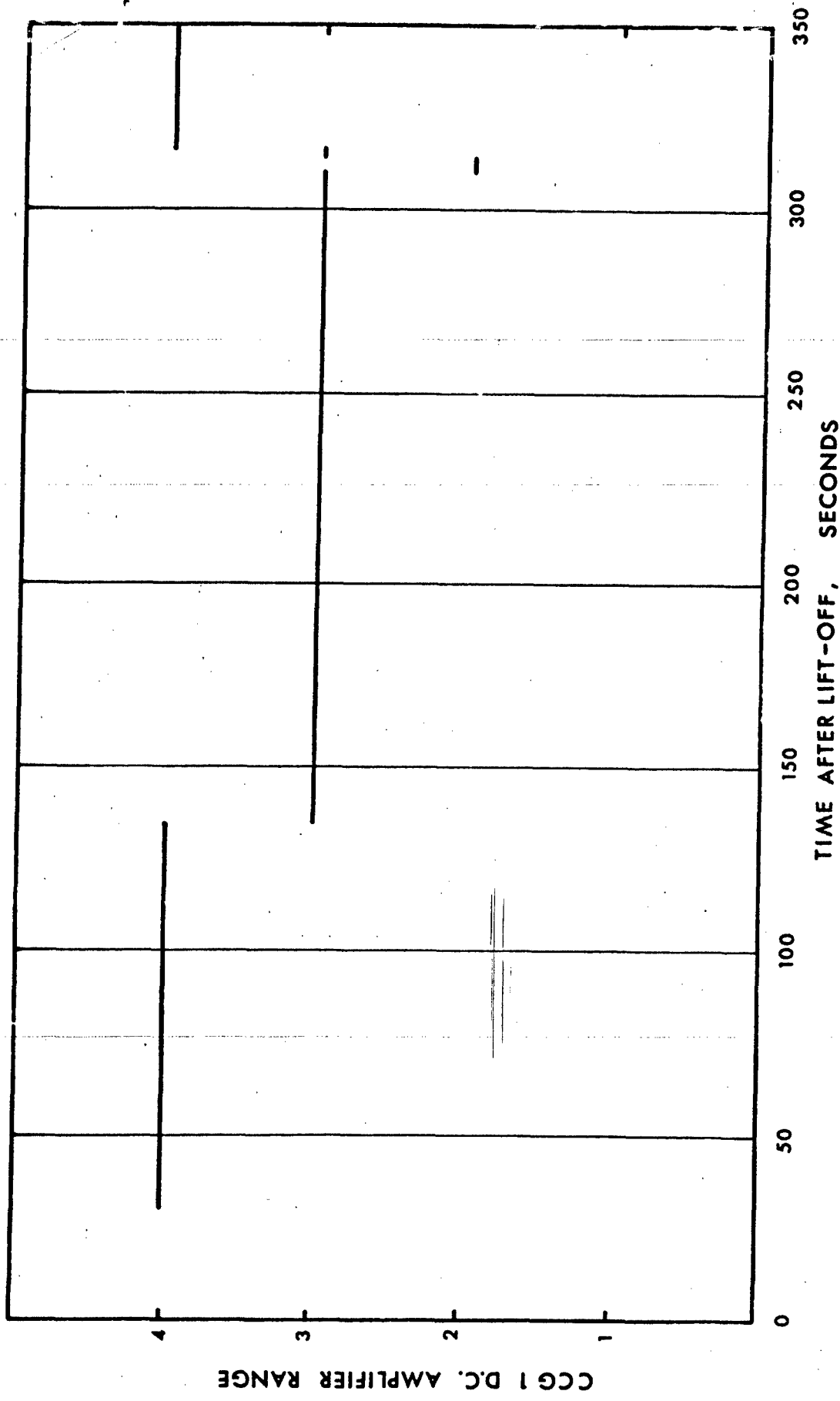


FIG. 72 TYPICAL D.C. AMPLIFIER RANGE INDICATION DURING THE FLIGHT

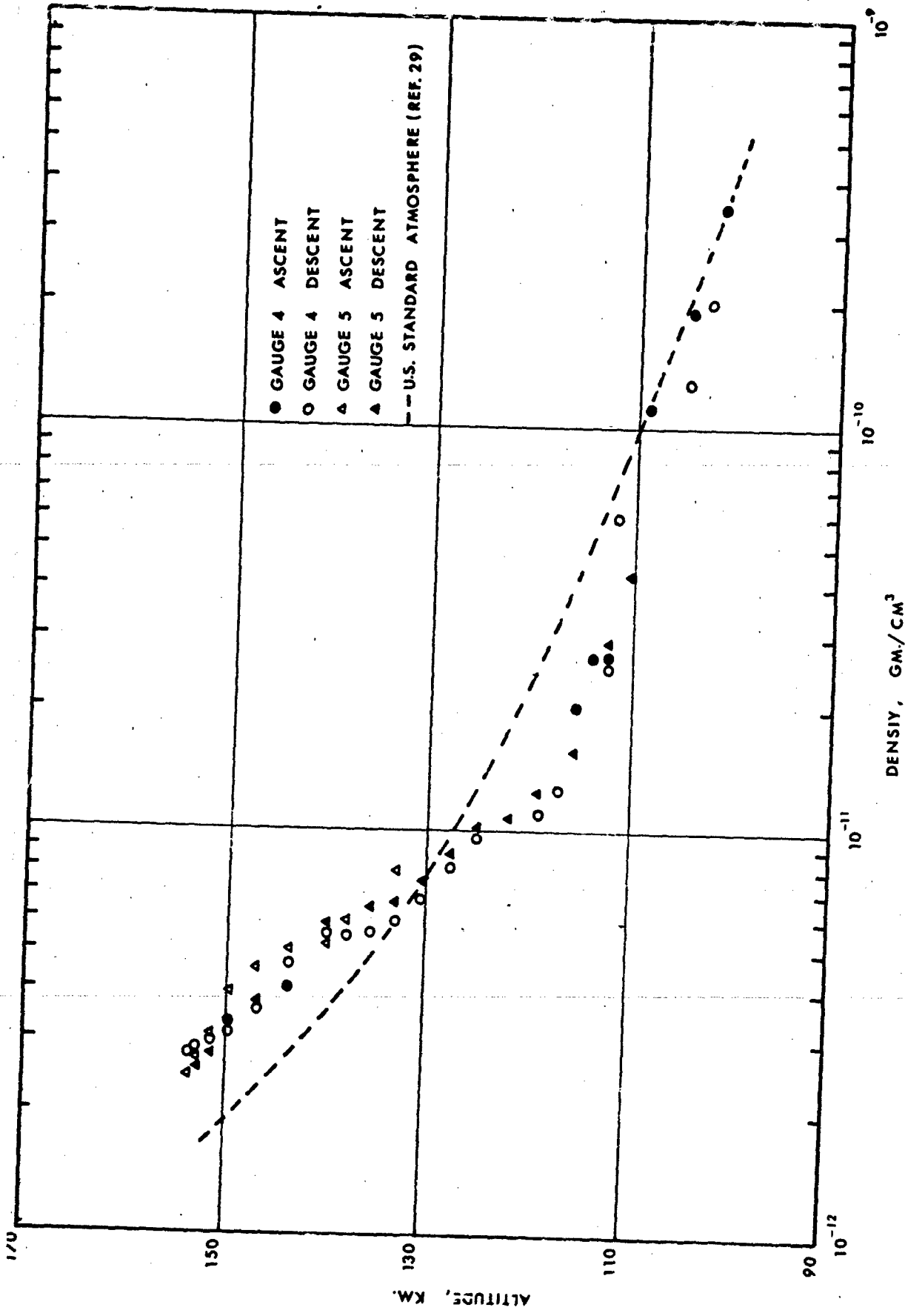


FIG. 73 ATMOSPHERIC DENSITY COMPUTED FROM GAUGES 4 AND 5 DURING ROCKET ASCENT AND DESCENT

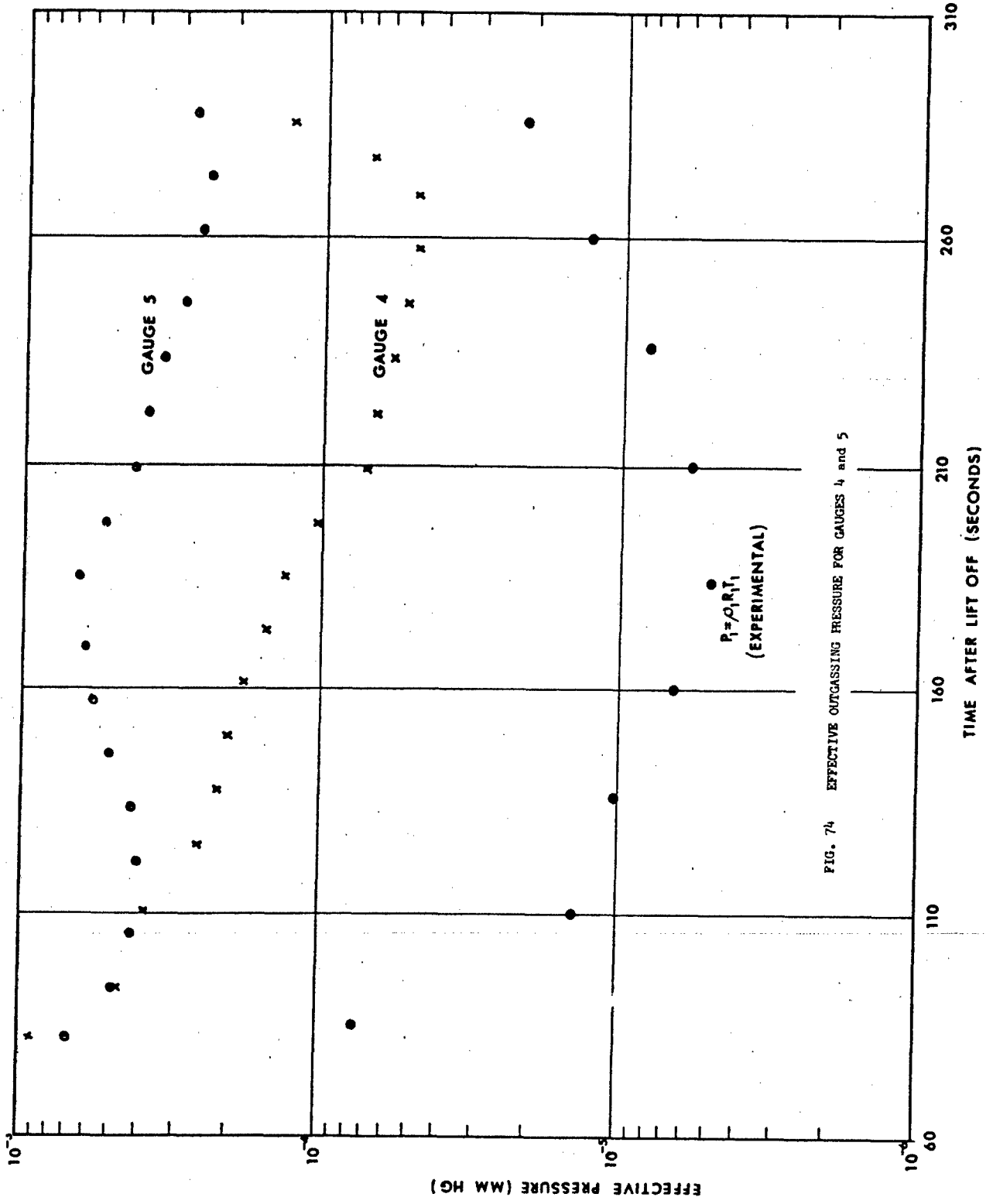


FIG. 74 EFFECTIVE OUTGASSING PRESSURE FOR GAUGES 4 and 5

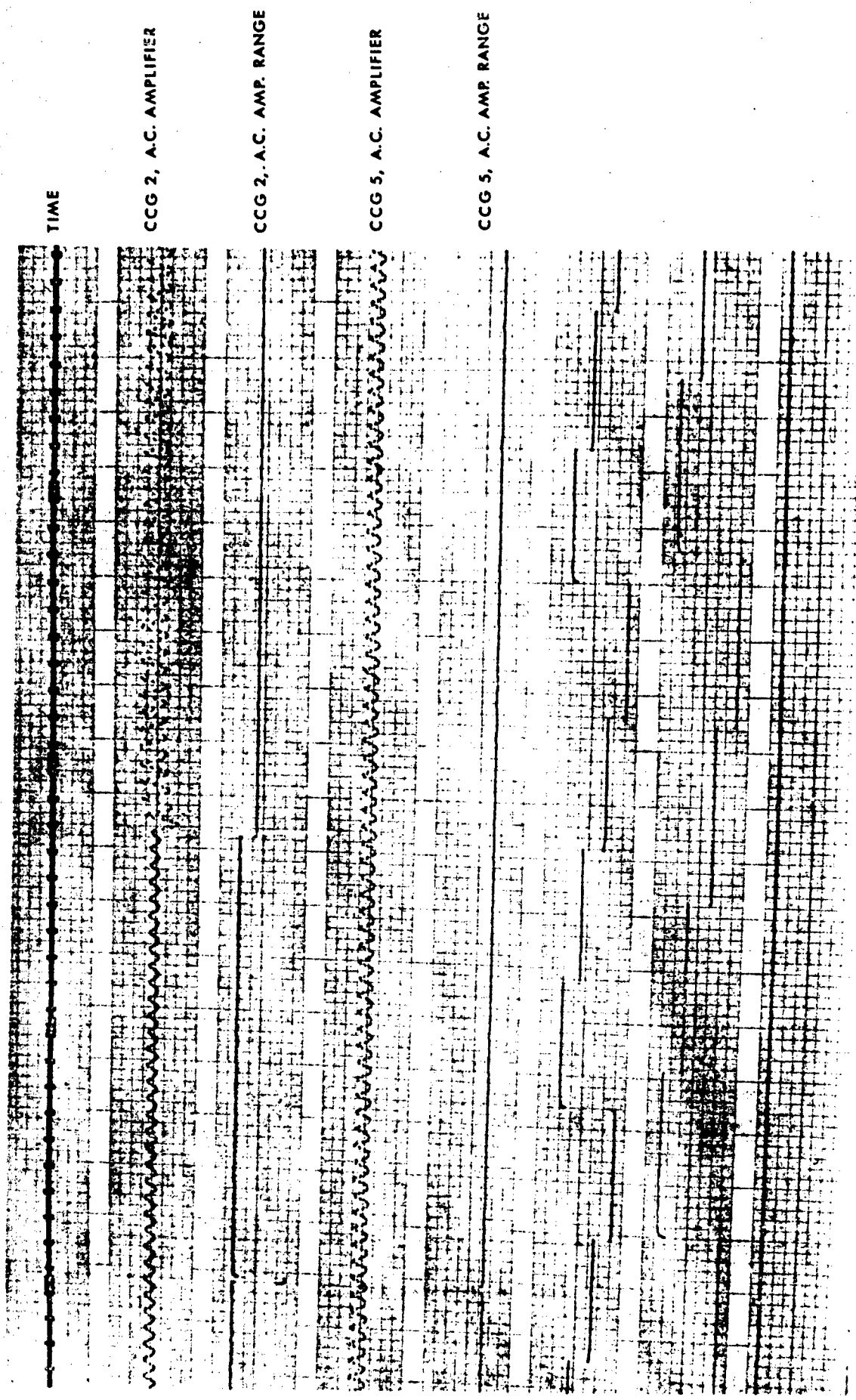


FIG. 75 TELEMETRY RECORD OF THE AC AMPLIFIER SIGNAL

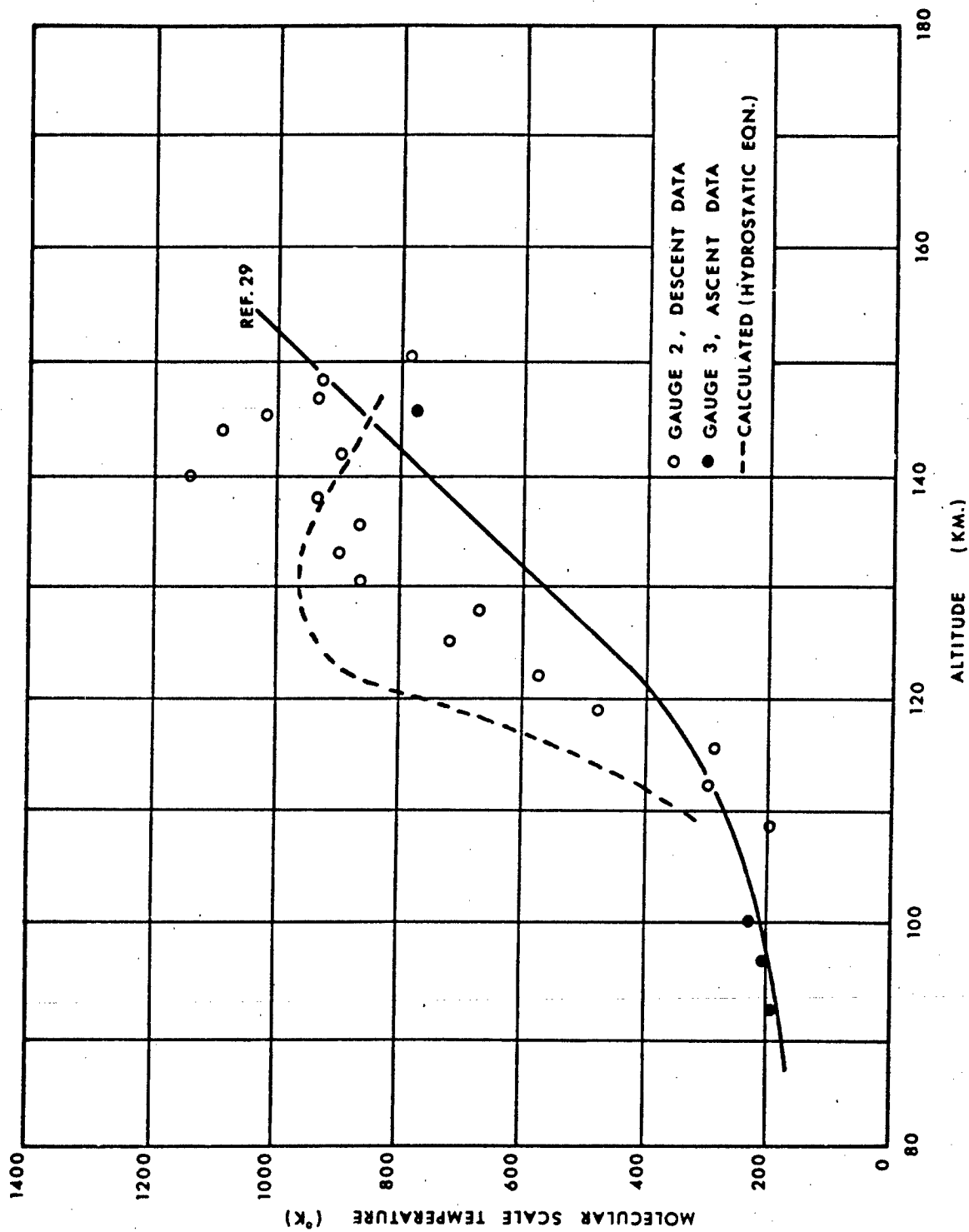


FIG. 76 MOLECULAR SCALE TEMPERATURE COMPUTED FROM THE MODULATED SIGNAL ON IONIZATION GAUGES 2 AND 3

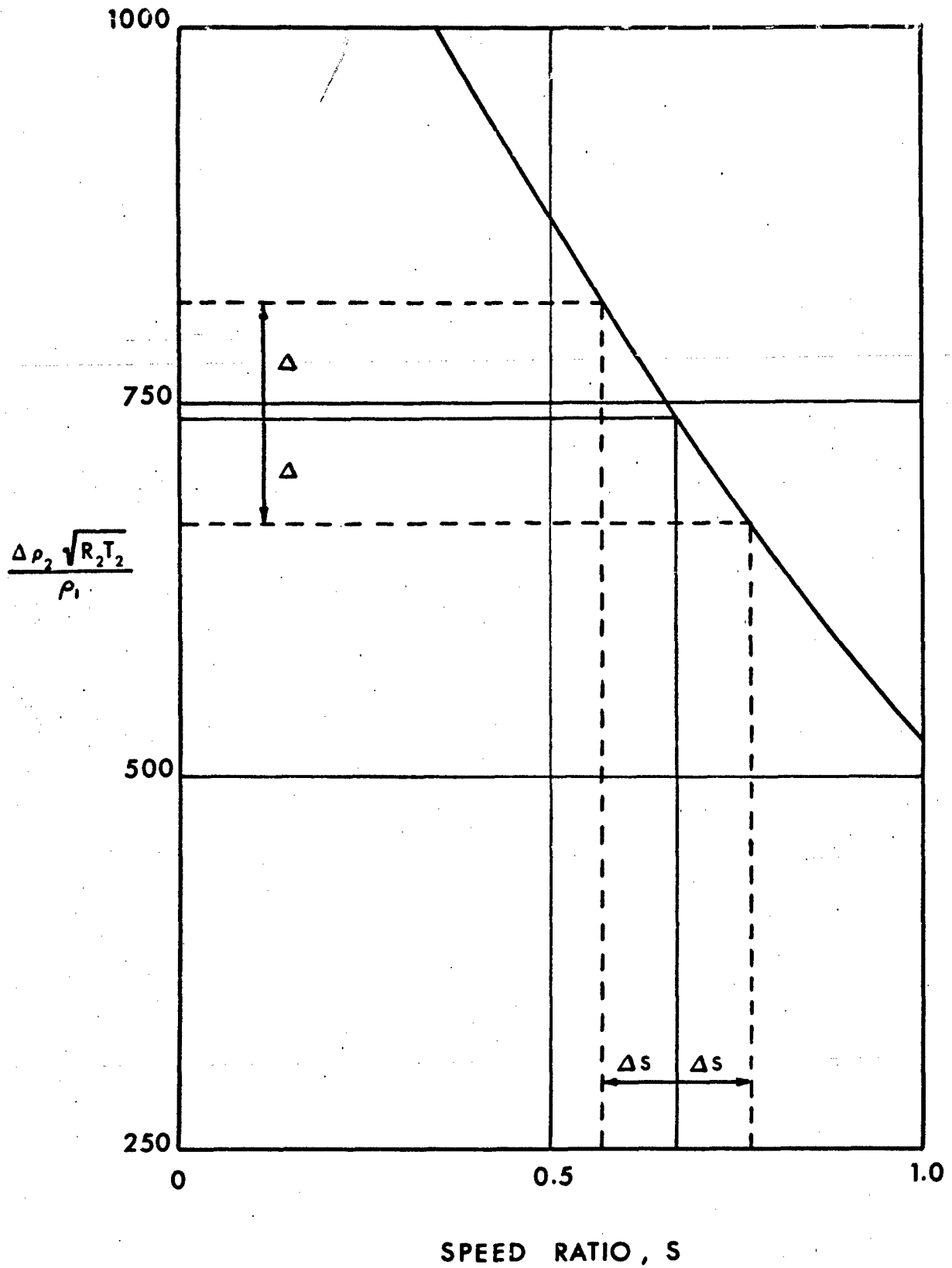


FIG. 77 TYPICAL SOLUTION FOR  $R_1 T_1$  FOR AN ALTITUDE NEAR APOGEE

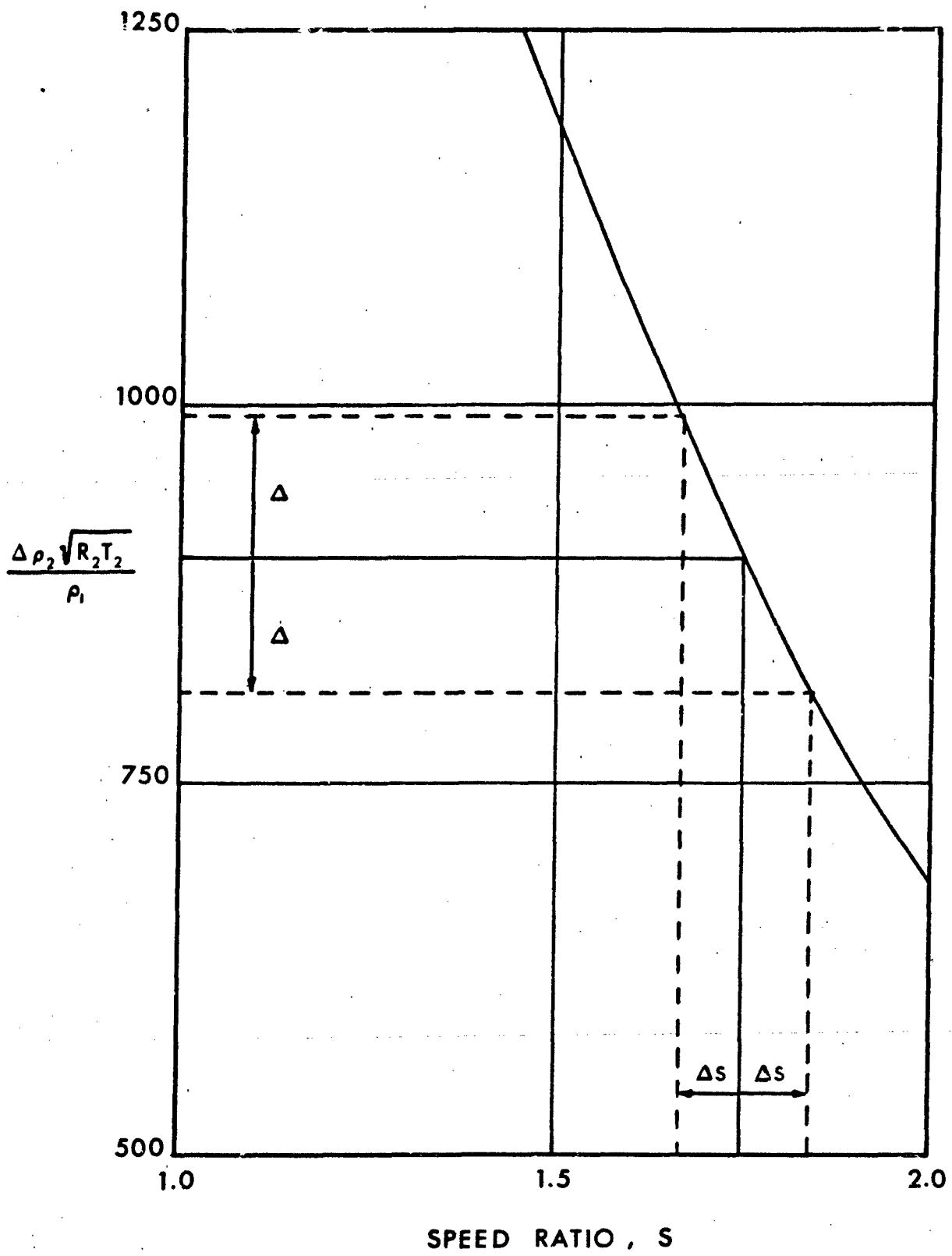


FIG. 78 TYPICAL SOLUTION FOR  $R_1 T_1$  FOR AN ALTITUDE NEAR 110 km.

**BLANK PAGE**

## DOCUMENT CONTROL DATA - R&amp;D

(Security classification of title, body of abstract and indexing annotation must be entered when the overall report is classified)

1. ORIGINATING ACTIVITY (Corporate author) Institute for Aerospace Studies, University of Toronto, Toronto 5, Ontario, Canada		2a. REPORT SECURITY CLASSIFICATION Unclassified	
		2b. GROUP	
3. REPORT TITLE  ROCKET MEASUREMENTS OF UPPER ATMOSPHERE DENSITY AND TEMPERATURE OVER FORT CHURCHILL, MANITOBA.			
4. DESCRIPTIVE NOTES (Type of report and inclusive dates) UTIAS Technical Report			
5. AUTHOR(S) (Last name, first name, initial)  Grenda, Robert, N.			
6. REPORT DATE September, 1966		7a. TOTAL NO. OF PAGES 75 pgs + 78 Figs.	7b. NO. OF REFS 65
8a. CONTRACT OR GRANT NO. AF-AFOSR 276-65		8a. ORIGINATOR'S REPORT NUMBER(S) UTIAS Report No. 117	
8b. PROJECT NO.		8b. OTHER REPORT NO(S) (Any other numbers that may be assigned this report)	
c.			
d.			
10. AVAILABILITY/LIMITATION NOTICES Institute for Aerospace Studies, University of Toronto, Toronto 5, Canada			
11. SUPPLEMENTARY NOTES		12. SPONSORING MILITARY / Y Air Force Office Scientific Research SREM	
3. ABSTRACT <p>This report describes a rocket experiment designed to measure density and molecular scale temperature above 100 km by means of a free molecule flow analysis of the data. In addition, pressure, temperature, and density were measured in the lower atmosphere by conventional methods.</p> <p>A theoretical analysis under conditions of continuum and free-molecule flow is included. The desired atmospheric parameters are given in terms of the quantities measured by the rocket-borne instruments.</p> <p>The mechanical design of the payload, and the electronics and electrical system are discussed.</p> <p>The data is reduced and the atmospheric parameters based on the data are presented. The experiment is discussed and modifications are suggested to improve the experiment and obtain better data.</p>			

14.	KEY WORDS	LINK A		LINK B		LINK C	
		ROLE	WT	ROLE	WT	ROLE	WT
Free Molecular Pressure Probe Upper Atmospheric Density Upper Atmospheric Scale Height Rocket Experiment							

**INSTRUCTIONS**

1. **ORIGINATING ACTIVITY:** Enter the name and address of the contractor, subcontractor, grantee, Department of Defense activity or other organization (*corporate author*) issuing the report.
- 2a. **REPORT SECURITY CLASSIFICATION:** Enter the overall security classification of the report. Indicate whether "Restricted Data" is included. Marking is to be in accordance with appropriate security regulations.
- 2b. **GROUP:** Automatic downgrading is specified in DoD Directive 5200.10 and Armed Forces Industrial Manual. Enter the group number. Also, when applicable, show that optional markings have been used for Group 3 and Group 4 as authorized.
3. **REPORT TITLE:** Enter the complete report title in all capital letters. Titles in all cases should be unclassified. If a meaningful title cannot be selected without classification, show title classification in all capitals in parenthesis immediately following the title.
4. **DESCRIPTIVE NOTES:** If appropriate, enter the type of report, e.g., interim, progress, summary, annual, or final. Give the inclusive dates when a specific reporting period is covered.
5. **AUTHOR(S):** Enter the name(s) of author(s) as shown on or in the report. Enter last name, first name, middle initial. If military, show rank and branch of service. The name of the principal author is an absolute minimum requirement.
6. **REPORT DATE:** Enter the date of the report as day, month, year, or month, year. If more than one date appears on the report, use date of publication.
- 7a. **TOTAL NUMBER OF PAGES:** The total page count should follow normal pagination procedures, i.e., enter the number of pages containing information.
- 7b. **NUMBER OF REFERENCES:** Enter the total number of references cited in the report.
- 8a. **CONTRACT OR GRANT NUMBER:** If appropriate, enter the applicable number of the contract or grant under which the report was written.
- 8b, 8c, & 8d. **PROJECT NUMBER:** Enter the appropriate military department identification, such as project number, subproject number, system numbers, task number, etc.
- 9a. **ORIGINATOR'S REPORT NUMBER(S):** Enter the official report number by which the document will be identified and controlled by the originating activity. This number must be unique to this report.
- 9b. **OTHER REPORT NUMBER(S):** If the report has been assigned any other report numbers (*either by the originator or by the sponsor*), also enter this number(s).
10. **AVAILABILITY/LIMITATION NOTICES:** Enter any limitations on further dissemination of the report, other than those

imposed by security classification, using standard statements such as:

- (1) "Qualified requesters may obtain copies of this report from DDC."
- (2) "Foreign announcement and dissemination of this report by DDC is not authorized."
- (3) "U. S. Government agencies may obtain copies of this report directly from DDC. Other qualified DDC users shall request through \_\_\_\_\_."
- (4) "U. S. military agencies may obtain copies of this report directly from DDC. Other qualified users shall request through \_\_\_\_\_."
- (5) "All distribution of this report is controlled. Qualified DDC users shall request through \_\_\_\_\_."

If the report has been furnished to the Office of Technical Services, Department of Commerce, for sale to the public, indicate this fact and enter the price, if known.

11. **SUPPLEMENTARY NOTES:** Use for additional explanatory notes.
12. **SPONSORING MILITARY ACTIVITY:** Enter the name of the departmental project office or laboratory sponsoring (*paying for*) the research and development. Include address.
13. **ABSTRACT:** Enter an abstract giving a brief and factual summary of the document indicative of the report, even though it may also appear elsewhere in the body of the technical report. If additional space is required, a continuation sheet shall be attached.

It is highly desirable that the abstract of classified reports be unclassified. Each paragraph of the abstract shall end with an indication of the military security classification of the information in the paragraph, represented as (TS), (S), (C), or (U).

There is no limitation on the length of the abstract. However, the suggested length is from 150 to 225 words.

14. **KEY WORDS:** Key words are technically meaningful terms or short phrases that characterize a report and may be used as index entries for cataloging the report. Key words must be selected so that no security classification is required. Identifiers, such as equipment model designation, trade name, military project code name, geographic location, may be used as key words but will be followed by an indication of technical context. The assignment of links, rules, and weights is optional.